UNIVERSIDAD AUTONOMA DE MADRID

FACULTAD DE CIENCIAS

DEPARTAMENTO DE QUÍMICA INORGÁNICA

# INTERRELATIONSHIP BETWEEN TRANSPORT PROPERTIES IN PHOSPHATE GLASSES THROUGH THEIR ATOMIC STRUCTURE

Memoria presentada por:

**Laura Muñoz Senovilla**

para optar al grado de

**DOCTORA EN CIENCIAS QUÍMICAS**

Director:

**Dr. Francisco Muñoz Fraile**

Instituto de Cerámica y Vidrio

CSIC

CONSEJO SUPERIOR DE INVESTIGACIONES CIENTÍFICAS

Esta tesis doctoral ha sido realizada en el Instituto de Cerámica y Vidrio (ICV-CSIC) y ha sido desarrollada en el marco del proyecto nacional MAT2010-20459: Bases estructurales de las propiedades de transporte en vidrios con interés tecnológico y financiada por el programa Formación de Personal Investigador (FPI) BES-2011-044130 del Ministerio de Economía y Competitividad.

Las estancias de investigación realizadas en el extranjero han sido financiadas por el Deutscher Akademischer Austauschdienst (DAAD) (A/13/71565) y por el Programa Estatal de Promoción del Talento y su Empleabilidad en I+D+i, Subprograma Estatal de movilidad del Ministerio de Economia y Competitividad EEBB-I-14-08513 y EEBB-I-15-10036, así como por el Consejo Superior de Investigaciones Científicas dentro del Programa para la colaboración científica internacional del CSIC con instituciones extranjeras (CSIC-i-Link 0959). El autor agradece al Consejo Superior de Investigaciones Científicas (CSIC) y a la dirección del Instituto de Cerámica y Vidrio (ICV) por permitir la realización de esta memoria.

Esta memoria de tesis doctoral cumple con los requisitos necesarios para obtener la mención internacional en el Título de Doctor que se describen en la normativa de enseñanzas universitarias de doctorado de la Universidad Autónoma de Madrid y que han sido establecidos en el artículo 15 del Real Decreto 99/2011 que establece la Ordenación de las Enseñanzas Universitarias Oficiales (BOE nº 35 de 28 de enero de 2011, páginas 13909-13926). La presente memoria de tesis doctoral ha sido informada por dos doctores que pertenecen a Instituciones de Educación Superior de Francia y Dinamarca:

**Dr. Gregory Tricot**

LASIR UMR-CNRS 8516,

Institución: Université de Lille 1

Francia

**Prof. Yuanzheng Yue**

Department of Chemistry and Bioscience

Institución: Aalborg Universitet

Dinamarca

**A mis padres y hermano,**

**A Jose**

# Agradecimientos/ Acknowledgements

Esta tesis no hubiese sido posible sin la ayuda de todas las personas que han contribuido y ayudado a la realización de la misma. En primer lugar me gustaría agradecer a mi director de tesis, Dr. Francisco Muñoz Fraile, por la dedicación y la confianza puesta en mí desde un primer momento. Muchas gracias por el tiempo que me has dedicado y por todo lo que he aprendido estos años.

A la Prof. Mª José Macazaga Porlan del Departamento de Química Inorgánica de la Universidad Autónoma de Madrid por aceptar la tutela de esta tesis.

Al Prof. Vicente Fernández, por darme la primera oportunidad en el mundo de la investigación, y por su apoyo e interés en mi trabajo a lo largo de todos estos años.

A la Prof. Alicia Durán, por su total disposición y dedicación en el trabajo, por su inestimable apoyo y ayuda en las discusiones de los resultados, por sus ideas inagotables, por la energía y motivación que tiene.

I want to thank all the international supervisors of the short-stays developed during these years: thanks to Prof. Leo Van Wüllen (Universität Augsburg (Gemany)), thanks to Prof. Tanguy Rouxel (Université de Rennes 1 (France)), thanks to Prof. Ifty Ahmed (University of Nottingham (UK)) and finally Prof. Gregory Tricot (Université de Lille 1 (France)).

Al personal técnico del ICV, en especial a Eva y Juan por su gran ayuda en el trabajo experimental. Al departamento de vidrios, a mis compañeros y amigos del instituto, en especial a Chelo, Benito, Yhasmin, Mónica, Nerea, Juli, Yolanda, Juan, Ana, Zoilo, Miguel, Carlos, Giulio, José, Sonia y Esther. Ha sido un placer compartir estos años con todos vosotros.

A mis amigos de siempre, y por supuesto a mi familia, a mis padres y hermano.

Y a Jose.

A todos, muchas gracias.

# Prólogo

A lo largo de la historia han sido numerosos los ejemplos en los que la humanidad ha visto limitada la puesta en práctica de los conocimientos científicos adquiridos fundamentalmente a través de la observación de su entorno, no por unos desarrollos teóricos incorrectos o por una falta de solidez en los planteamientos, si no por el mero hecho de que los materiales conocidos hasta el momento no eran capaces de soportar y hacer viables los avances tecnológicos demandados por una creciente población mundial con nuevas necesidades a las que dar respuesta.

Gran parte de lo que en siglos pasados se fiaba a la intuición o a la buena suerte con una ciencia basada esencialmente en la prueba y el error, actualmente se fundamenta en la aplicación de los constantes descubrimientos en física y química básica al diseño de nuevos materiales que den respuesta al vertiginoso avance de la tecnología del que somos testigos hoy en día y, que además, tanto su fabricación como su uso sean sostenibles desde el punto de vista medioambiental. Hoy en día, este diseño a medida conlleva modelizar las estructuras moleculares a partir de las cuales se puedan deducir las propiedades físicas y químicas que permitan la producción de prototipos reales de aquellos modelos con mayores posibilidades de poseer las características adecuadas para una aplicación determinada con el consiguiente ahorro de tiempo, costes y recursos naturales.

El vidrio, lejos de ser un material de nueva creación remonta sus orígenes a varios milenios con técnicas convencionales de producción bien establecidas. Se trata de un material con una presencia importante en nuestra sociedad que ha sido empleado tradicionalmente como elemento arquitectónico o para la fabricación de envases. Sin embargo, las constantes innovaciones llevadas a cabo en el campo de los materiales vítreos a lo largo del siglo XX han tenido como principal objetivo reinventar este material tradicional gracias a la versatilidad de composiciones que puede presentar dotándole de un alto valor añadido. Así, está presente en muchas de las áreas más relevantes de la Ciencia de los Materiales y la Tecnología, con aplicaciones que van desde la construcción al más alto nivel a la biomedicina, desde la microelectrónica hasta la óptica o la astronomía.

La gran mayoría de los vidrios producidos a nivel industrial, envases y vidrio plano, son vidrios basados en $SiO_2$ debido a su alta estabilidad mecánica y química. La adición de $B_2O_3$ a vidrios de silicato, donde el boro actúa como un segundo formador de red, dio lugar a un nuevo grupo de vidrios con mejores propiedades, como los vidrios de laboratorio Pyrex®. Pero es el $P_2O_5$, tercer formador de red, el que ha originado un extenso campo de investigación de materiales vítreos dedicados fundamentalmente a aplicaciones especiales.

Es llamativa la abundancia de datos que se encuentra en la literatura sobre vidrios de silicatos y borosilicatos que copan las bases de datos de materiales vítreos si lo comparamos con los vidrios de fosfato, de los que apenas se encuentran referencias remontándose muchas de ellas a los años cincuenta y sesenta o limitándose en muchos casos a composiciones muy concretas y habitualmente complejas a las que se ha encontrado una aplicación muy específica que ha hecho necesario su estudio. Probablemente, algunas de las razones sean, entre otras, tanto las dificultades que conlleva la obtención de los vidrios de fosfato, como el posterior procesamiento y manipulación debido a la alta tendencia a desvitrificar y a su alta higroscopicidad las que han impedido en muchos casos su producción a nivel industrial y han frenado posiblemente el estudio de sus propiedades fisicoquímicas en profundidad. Es por ello que a lo largo de esta tesis se ha hecho un esfuerzo por completar y en muchos casos actualizar los datos relativos a las propiedades de transporte y a la estructura de una gran variedad de vidrios de fosfato binarios y ternarios, porque creo firmemente en que los resultados que se derivan de la investigación básica juegan un papel crucial, y así lo han demostrado los recientes premios Nobel otorgados, sentando las bases sobre las que cimentar el diseño y modelización en este caso de materiales vítreos de fosfato con nuevas aplicaciones que quizás estén aún por descubrir.

# INDEX



[1] El acrónimo proviene de las siglas en inglés Magic-Angle sample Spinning

# Abstract

The development of the processing and design of phosphate glasses in a wide range of new technological applications requires the complete understanding of their physical and chemical properties.

The progress on science and glass technology increasingly depends on the ability to optimize the glass composition and on controlling the structure of the materials, through the characterization of the structure and the physico-chemical properties. The relationship between composition, structure and properties is an essential methodology in the modern glass science.

The aim of this thesis has been to study the full process that runs from the generation of basic knowledge, to its application, in this case on their processing as bioactive phosphate glass fibres. For this porpoise, the relationships between chemical composition, structure and dynamics of the processes taking place within the phosphate glass network, which directly influence the processing and design of new glasses, has been investigated in depth.

This assumption is based on the hypothesis that it is possible the modelling of the transport properties from structural data, and that a common model for the viscosity-T curves can be obtained through the study of the rheology of phosphate glasses when a certain composition is given.

The particular milestone has been to establish a relationship between the main structural parameters, such as glass network polymerization degree, coordination number of the modifying cations or the nature of the metal-oxygen bonds; and the properties, such as electrical conductivity, chemical durability and fragility. To that end, a series of binary and ternary metaphosphate glasses with different modifying oxides of alkali, alkaline earth and zinc elements have been studied together with glasses with different glass former content ($P_2O_5$) and with more than one network former ($P_2O_5$ and $B_2O_3$).

First of all, in order to get more insights into the compositional and structural influence on transport properties in pure phosphate glasses, different glass systems have been prepared to determine the role played by the different modifying oxides and by the proportion of $P_2O_5$ present in the glass. The ionic conductivity ($\sigma$) and viscosity have been studied and related with the short and medium range order structure by means of Nuclear Magnetic Resonance and Raman spectroscopies. The kinetic fragility (m) of each glass has been determined by fitting the viscosity experimental data to Vogel-Fulcher-Tamman (VFT), Avramov-Milchev

(AM) and Mauro-Yue-Ellison-Gupta-Allan (MYEGA) equations. Finally, the activation energy of viscous flow, and its correlation with composition and structure, has also been studied.

It has been found that the presence of cations with lower cationic potential (Z/a) in the glass network, leads to less covalent $M^{n+}O^{m-}$ bonds. The decrease on the covalent character of the glass network and, therefore, the weakening and subsequent decrease of the overall network's rigidity, are reflected on the short and medium range order structure and, as a consequence, the main glass properties will also be influenced up to some extent by those. On the other hand, variations on the glass network connectivity, especially the appearance of $Q^1$ units in the glass network, causes a more pronounced increase on the NBO per tetrahedral unit, which seems to provoke a preferential arrangement of the $Q^2$ groups units in chains instead of rings. A higher proportion of chains seems to lead to a denser glass network that influences on the flow of the $PO_4$ units through it and thus on the properties.

The prediction of properties with enough accuracy has been for many years one of the most important goals that the glass science community wanted to achieve in order to offer an alternative to the time consuming experimental studies. On the basis of the relationships found between the structure and properties, the first steps towards the modelling of glass compositions with desired fragility trough the prediction of the viscosity-temperature curves in the whole temperature range has been achieved. In particular, the similarity found between the calculated and experimental viscosity points in the melt has validated the use of the relationships found and allowed establishing an alternative to the experimental determination of viscosity data at high temperatures.

Once the influence of the addition of different modifying oxides and variation on the connectivity degree of the glass network has been investigated and established, studies on glasses with more than one network former oxide were carried out. In recent years, borophosphate glasses have received increasing attention because of their interesting optical and electrical properties. It is well known that these glasses, where two glass formers are mixed, show a pronounced non-linear change in their properties, which is commonly known as the so-called mixed network former effect (MGFE). In the light of the wide existing literature found about structural studies in borophosphate glasses, it is noteworthy the effort made by the glass community to better understand the effect of composition on structure and on physical properties, and to bring some light to the MGFE in order to predict the compositional dependence of the properties. Nevertheless, to the best of the author´s knowledge just few works address a systematic study on the rheological properties of alkali borophosphate glasses through the determination of their fragility. In this thesis, the

structural characterization of a series of lithium and sodium borophosphate glasses has been studied by means of MAS-NMR experiments performed at a very high field, which has distinguishing between different types of boron fourfold coordinated in the glass network, and to corroborate the presence of boron in trigonal coordination previously detected by means of Raman spectroscopy. These structural changes in the short and medium range order structure caused by the mixing of two glass former network oxides have been related with the variation of kinetic fragility and activation energy for viscous flow with increasing boron content.

To conclude, the basic knowledge acquired from the systematic study of structure and properties in binary and ternary phosphate glasses, and the relationships found between them, has been applied to the fibre drawing processing of phosphate glasses that present good cytocompatibility. Macroscopic properties such as kinetic fragility (m) and molar volume ($V_m$) have been related with the structure directly determined on the fibres by means of Raman and $^{31}P$ and $^{23}Na$ Nuclear Magnetic Resonance. It has been observed that the replacement of $P_2O_5$ by $Na_2O$ causes the glass network depolymerisation and seems to favour the presence of chain arrangements that become shorter resulting in a denser glass network with lower connectivity. This is reflected in a lower molar volume, kinetic fragility and dissolution rate with increasing $Na_2O$ content that facilitate fibre drawing processing. The good mechanical properties observed in these fibres, leads to the conclusion that a structure orientation on the fibres is likely taking place, although it was not possible to elucidate whether the chains of $PO_4$ tetrahedra in the glass fibres are randomly distributed or lie along the fibre main axis direction.

## Resumen

El diseño y procesamiento de vidrios de fosfato para un amplio rango de nuevas aplicaciones tecnológicas, requiere de un completo conocimiento de sus propiedades físicas y químicas.

El progreso en la ciencia y tecnología del vidrio depende cada vez más de la optimización de las composiciones de los vidrios y del control de la estructura de los materiales, a través de la caracterización de las propiedades físico-químicas.

El objetivo de esta tesis ha sido estudiar el proceso completo que va desde la generación de conocimiento fundamental hasta su aplicación, en este caso, como fibras de vidrio de fosfato bioactivos. Para lograr este objetivo, se han investigado en profundidad las relaciones entre la composición, estructura y dinámica de los procesos que tienen lugar en el seno de la red vítrea y que directamente influyen sobre el procesamiento y diseño de nuevos vidrios.

Esta suposición se basa en la hipótesis de que es posible modelizar las propiedades de transporte a través de datos estructurales, y que se puede obtener un modelo común para las curvas de viscosidad-temperatura a través del estudio de la reología de los vidrios de fosfato a partir de una composición dada.

Los objetivos parciales de esta tesis han sido establecer una relación entre los principales parámetros estructurales como son el grado de polimerización de la red, el índice de coordinación de los cationes modificadores o la naturaleza de los enlaces metal-oxígeno; y las propiedades como la conductividad eléctrica, la durabilidad química o la fragilidad. Con esta finalidad, se han estudiado vidrios de metafosfato binarios y ternarios con diferentes óxidos modificadores de metales alcalinos, alcalinoterreos y zinc junto con vidrios que presentan diferentes contenidos de $P_2O_5$ y con más de un oxido formador ($P_2O_5$ y $B_2O_3$).

En primer lugar, con el objetivo de lograr una mayor compresión sobre la influencia de la estructura y la composición en las propiedades de transporte en vidrios de fosfato, se han preparado diferentes sistemas vítreos con el objetivo de determinar el papel que juegan los distintos óxidos modificadores y la proporción de $P_2O_5$ presente en el vidrio. Se han estudiado la conductividad iónica y la viscosidad y se ha relacionado con el orden estructural a corto y medio alcanza a través de espectroscopias de resonancia magnética nuclear y Raman. La fragilidad cinética (m) de cada vidrio se ha determinado a través del ajuste de los datos experimentales a las ecuaciones de Vogel-Fulcher-Tamman (VFT),

Avramov-Milchev (AM) y Mauro-Yue- Ellison-Gupta-Allan (MYEGA). Por último se ha estudiado la activación de flujo viscoso y su correlación con la composición y la estructura.

Se ha observado que la presencia de cationes con menor potencial catiónico (Z/a) en la red vítrea, da lugar a enlaces metal-oxigeno de menor carácter covalente. La disminución del carácter covalente de la red vítrea y por tanto el debilitamiento y consiguiente disminución del grado de rigidez total de la red, se refleja en el orden estructural a corto y medio alcance, y en consecuencia en las principales propiedades de los vidrios.

Por otro lado variaciones en la conectividad de la red vítrea, en especial la aparición de unidades $Q^1$ en la red vítrea, producen un aumento más pronunciado de los oxígenos no puente por unidad tetraédrica, lo que parece provocar un ordenamiento preferencial de los grupos $Q^2$ en forma de cadena en vez de anillos. La mayor proporción de cadenas da lugar a una red vítrea más densificada que influye en la fluencia de las unidades de $PO_4$ a través de ella y por tanto en las propiedades.

La predicción de propiedades con suficiente exactitud ha sido durante muchos años uno de los objetivos más importantes que la comunidad científica del vidrio ha buscado alcanzar como alternativa a los estudios experimentales. En base a las relaciones encontradas entre la estructura y las propiedades, se han alcanzado los primeros pasos hacia la modelización de las composiciones vítreas con una fragilidad deseada a través de la predicción de las curvas de viscosidad en el rango completo de temperaturas. En particular, la similitud encontrada entre los datos de viscosidad calculados y los determinados experimentalmente en el fundido ha validado el empleo de las relaciones encontradas y ha permitido establecer una alternativa a la determinación experimental de la viscosidad a altas temperaturas.

Una vez que se ha investigado y establecido como influye la adicione de diferentes óxidos modificadores y la variación del grado de conectividad de la red vítrea, se han podido llevar a cabo estudios con más de un oxido formador. En los últimos años, los vidrios de borofosfato han suscitado un gran interés debido a sus interesantes propiedades ópticas y eléctricas. Es bien conocido, que estos vidrios en el que dos óxidos modificadores están mezclados muestran una pronunciada variación no lineal de las propiedades, lo que comúnmente se conoce como el efecto mezcla de dos óxidos formadores. A la vista de la gran bibliografía existente sobre estudios estructurales en vidrios de borofosfato, es notable el esfuerzo llevado a cabo por la comunidad del vidrio para llegar a entender el efecto de la composición en la estructura y en las propiedades físicas. Sin embargo, solo se han encontrado unos pocos trabajos dedicados al estudio sistemático de las propiedades reológicas de vidrios de borofosfato alcalinos a través de la determinación de su fragilidad.

En esta tesis la caracterización estructural de vidrios de borofosfato de litio y sodio, se han estudiado a través de experimentos de RMN-MAS llevados a cabo en un espectrómetro de alto campo magnético lo que ha permitido distinguir entre diferentes tipos de boro tetracoordinado en la red vítrea, y corroborar la presencia de boro en coordinación trigonal. Estos cambios estructurales en el orden estructural a corto y medio alcance producidos por la mezcla de dos óxidos formadores se han relacionado con la variación de la fragilidad cinética y la energía de activación de flujo viscoso.

Para concluir, el conocimiento fundamental adquirido a través del estudio sistemático de la estructura y propiedades en vidrios de fosfatos binarios y ternarios, y la relaciones encontradas entre ellos se han podido aplicar al fibrado de vidrios de fosfato bioactivos. Se han relacionado las propiedades macroscópicas como la fragilidad cinética y el volumen molar con la estructura directamente determinada en las fibras a través de espectroscopia de RMN y Raman. Se ha observado que la sustitución de $P_2O_5$ por $Na_2O$ produce la despolimerización de la red vítrea y parece favorecer la presencia de cadenas cortas que dan lugar a la densificación de la red vítrea. Esto se refleja en un menor volumen molar, fragilidad cinética y velocidad de disolución con el aumento del contenido de $Na_2O$ que facilita el procesamiento de los vidrios de fosfato en fibras. Sin embargo, las buenas propiedades mecánicas observadas en estas fibras permite concluir que se ha producido una orientación en la estructura de las fibras aunque no haya sido posible dilucidar si las cadenas de unidades PO4 se encuentran distribuidas aleatoriamente u orientadas al eje principal de las fibras.

# Chapter I

# Motivation, objectives and thesis layout

## Chapter I: Motivation, objectives and thesis layout

The development of the processing and design of phosphate glasses in a wide range of new technological applications requires the complete understanding of their physical and chemical properties.

The progress on science and glass technology increasingly depends on the ability to optimize the glass composition and on controlling the structure of the materials, through the characterization of the structure and the physico-chemical properties. The relationship between composition, structure and properties is an essential methodology in the modern glass science.

In this regard, there are nowadays many studies that address the structure-properties relationship as a function of composition, not only from a fundamental point of view that allows to move forward in the knowledge of basic aspects in glass science, but also as a means to control the behavior of these glassy materials and to search new applications.

The aim of this thesis is to study in depth the relationships between chemical composition, structure and dynamics of the processes taking place within the phosphate glass network, which directly influence the processing and design of new glasses. This assumption is based on the hypothesis that it is possible the modelling of the transport properties from structural data in phosphate glasses.

The particular milestone is to establish a relationship between the main structural parameters, such as glass network polymerization degree, coordination number of the modifying cations or the nature of the metal-oxygen bonds, and the properties, such as electrical conductivity, chemical durability and fragility. Furthermore, it is thought that a common model for the viscosity-T curves can be obtained through the study of the rheology of phosphate glasses when a certain composition is given.

For this purpose, this thesis is focused on the following objectives that constitute the full process that runs from the generation of basic knowledge, to its application on the processing of phosphate glasses for their real application as bioactive materials:

**I.** Preparation of the following binary and ternary phosphate glass systems for characterization:

a) Different modifying cations and constant network former content in order to study the influence of the nature of M cation:
   - $50MO.50P_2O_5$ (M=Mg,Ca,Sr,Ba,Zn) and $50M'_2O.50P_2O_5$ (M'=Li,Na)

- $xLi_2O.(50-x)ZnO.50P_2O_5$ and $xNa_2O.(50-x)ZnO.50P_2O_5$ (x=0-50)

b) Different network polymerization degrees depending on $P_2O_5$ content in order to study the influence of the glass network connectivity :
   - $x/2Li_2O.x/2ZnO.(100-x)P_2O_5$ (x=30-60)
   - $xNa_2O.16CaO.24MgO.(60-x)P_2O_5$ (x=5-20)

c) More than one network former component in order to elucidate the effect of mixing two glass former oxides:

   - $50Li_2O.xB_2O_3.(50-x)P_2O_5$ (x= 5-15; 50)
   - $50Na_2O.xB_2O_3.(50-x)P_2O_5$ (x= 5-25)

**II.** Detailed study of the compositional influence on the short and medium range order structure in phosphate glasses through Raman and Nuclear Magnetic Resonance spectroscopies. FTIR spectroscopy has been employed to determinate the water content on glasses.

**III.** Characterization of the thermal and transport properties, particularly glass transition temperature, viscosity and ionic conductivity, in order to elucidate the mechanisms that govern their variation with composition.

**IV.** Interpretation of the relationship between the short and medium range order structure and molar volume, glass transition temperature, kinetic and fragility, Doremus ratio and activation energy of viscous flow.

**V.** Modelling of viscosity-temperature curves.

**VI.** Application of the relationships found between properties and structure in phosphate glasses to fibre drawing processing of bioactive phosphate glasses.

The objectives listed above have been divided into respective chapters as follows. All of them include a brief introduction of the topic and the particular objectives to be achieved as well as partial conclusions and the references of the chapter.

**Chapter II** gathers an introduction to phosphate glasses and their structure, as well the state of the art on viscosity and fragility for these glass systems. It also reviews the viscosity models commonly used for the glass science community as well as the different parameters employed to define the variation of viscosity with temperature. It has been written in Spanish according with University regulation for manuscripts written in a foreign language.

**Chapter III** illustrates a brief description of the experimental techniques employed. The experimental conditions employed to run the experiments as well as the specifications of the equipments are included in the Materials and experimental methods section of each of the following chapters devoted to the obtained results.

**Chapter IV** presents most of the work carried out throughout the first years of the thesis period and has given rise to two publications: "*Behaviour of viscosity in metaphosphate glasses".* J. of Non-Cryst. Solids, 385 (2014) 9-16 *and "Study of viscosity and structure in alkali zinc phosphate glasses*". J. of Non-Cryst. Solids. 428 (2015) 54-61.

It is devoted to the structural and properties characterization of binary and ternary metaphosphate glasses as well as ternary phosphate glasses with different former oxide content. It includes the experimental work carried out in collaboration with the research groups of Prof. L. Van Wüllen in Universität Augsburg (Gemany) and Prof. T. Rouxel in Université de Rennes 1 (France) during two short-term stays.

**Chapter V** discusses the preliminary results of the viscosity- temperature curves modellization in phosphate glasses taking as starting point the relationships found from the systematic study of structure and rheology in the previous chapter.

**Chapter VI** describes the structural and properties characterization of a series of alkali borophosphate glasses. The mixed former effect of the so-called mixed former on kinetic fragility is studied.

**Chapter VII** illustrates the fabrication and characterization of phosphate glass fibres as well as the relationship between fragility and the fibre drawing process. The experimental work described in this chapter was entirely carried out during a short-term stay in the research group of Prof. Ahmed in The University of Nottingham (UK).

# Capítulo II

## Introducción

## Capítulo II: Introducción. Vidrios de fosfato

Los vidrios de fosfato han dado lugar a un amplio campo de investigación en el seno de los materiales vítreos. Principalmente se han desarrollado principalmente para una gran variedad de aplicaciones especiales debido a las propiedades particulares que les confiere su estructura. Sin embargo, muchas de las aplicaciones tecnológicas de los vidrios de fosfato se han visto limitadas por su baja durabilidad química debido a una elevada higroscopicidad. Una forma de mejorar sustancialmente su resistencia a la hidrólisis ha sido mediante la introducción de cationes modificadores con alta intensidad de campo, como alcalinotérreos o metales de transición, u otros óxidos que actúen como formadores secundarios o elementos de carácter intermedio, como el aluminio o el boro.

En general, los vidrios de fosfato presentan bajas temperaturas de transición vítrea y de reblandecimiento dilatométrico, así como mayores coeficientes de expansión térmica si los comparamos con los vidrios de silicato y borosilicato. Estas características permiten su aplicación como elementos de unión en sellos estables y herméticos entre ciertos metales o entre vidrio y metal cuando la temperatura de sellado no puede exceder en muchos casos de los 300 ºC [1]. En cuanto a las propiedades ópticas especiales de los vidrios de fosfato, éstos poseen una alta transparencia en la región del ultravioleta (UV) y son capaces de disolver una gran cantidad de elementos de tierras raras, como por ejemplo Neodimio. Además, presentan una amplia sección transversal de emisión y bajos índices de refracción no lineal, lo que permite su uso como matrices en estado sólido para la emisión de radiación laser de alta potencia [2]. Por otro lado, vidrios de fosfato con composiciones que presentan una alta durabilidad química y temperaturas de procesamiento bajas, como es el caso de vidrios de fosfato de hierro, se usan como matrices para la vitrificación de residuos nucleares [3]. Los vidrios de fosfato también están presentes en el campo de la medicina debido a su carácter biocompatible. Especial interés despierta el procesado de estos vidrios en fibras para su utilización como material de refuerzo de matrices poliméricas para la fabricación de implantes. Una de las principales ventajas que presentan estos materiales frente a otros implantes metálicos es que son completamente biocompatibles y que su reabsorción por el organismo puede llevarse a cabo de forma controlada. De esta forma se promueve la soldadura del hueso fracturado a través de la regeneración en vez la sustitución, evitando la necesidad de practicar operaciones posteriores para llevar a cabo la retirada de los implantes [4]. Por otro lado, la búsqueda de electrolitos en estado sólido para baterías recargables de litio ha abierto nuevas posibilidades en las aplicaciones tecnológicas de los materiales vítreos. Su aplicación busca solventar los problemas

derivados del uso de electrolitos líquidos, como la contaminación de los electrodos por el disolvente, el riesgo de explosiones o las dificultades en el procesamiento de las baterías. En concreto, los vidrios de fosfato de litio y oxinitruros presentan altas conductividades eléctricas puramente iónicas a temperatura ambiente que han permitido su aplicación como electrolitos sólidos en dispositivos totalmente sólidos para la obtención y almacenamiento de energía [5, 6].

## 2.1 Estructura de los vidrios de fosfato

A diferencia de los vidrios de silicato, los vidrios de fosfato presentan tetraedros $[PO_4]^{n-}$ como unidad estructural básica. En dichas unidades, el átomo de fósforo se encuentra unido a cuatro átomos de oxígeno formando enlaces sencillos $sp^3$ con tres de ellos. Al promover uno de sus cinco electrones de valencia ($3s^2$ $3p^3$) a un orbital 3d, se forma el enlace π restante con los electrones del orbital 2p del oxígeno [7, 8]. Estos tetraedros se unen entre sí a través de enlaces covalentes mediante oxígenos puente (OP).

Su clasificación se lleva a cabo mediante la nomenclatura $Q^i$ establecida por Lippmaa *et al.*, donde el superíndice i indica el número de oxígenos puente [9]. En la Figura 2.1 se han representado las distintas unidades tetraédricas básicas que pueden estar presentes en los vidrios de fosfato en función del número enlaces a través de oxígenos puente que formen con otras unidades tetraédricas.

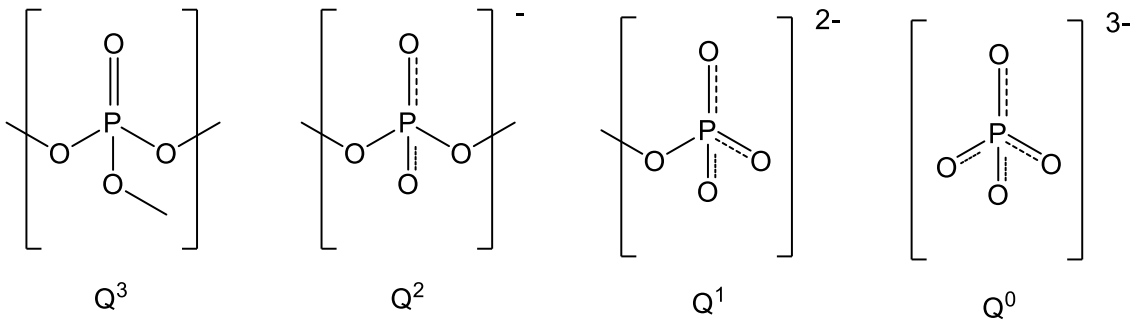


. Figura 2.1: Unidades tetraédricas básicas en vidrios de fosfato

Para describir la estructura de los vidrios tanto a corto como a largo alcance, además del entorno de coordinación de los iones, se debe tener en cuenta el modo de unión entre poliedros para formar la red vítrea. Es por ello que las redes de los vidrios de fosfato pueden clasificarse mediante la relación existente entre oxígeno y fósforo, la cual, fija el número de uniones tetraédricas vecinas a través de oxígenos puente. Así, para una relación [O]/

[P]=2,5 hablamos de pentóxido de fósforo vítreo (v-$P_2O_5$) con una estructura formada enteramente por unidades $Q^3$ como puede verse en la Figura 2. 2:

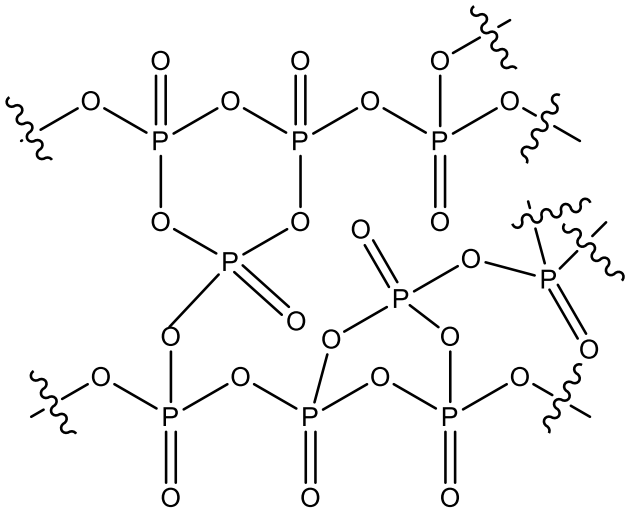

Figura 2.2: Estructura del v-$P_2O_5$ formada enteramente por unidades $Q^3$

Zachariasen fue el primero en clasificar a los óxidos en formadores y modificadores de red [10]. La adición de uno o más óxidos modificadores, en este caso a v-$P_2O_5$, provoca la despolimerización de la red como resultado de la ruptura de enlaces de oxígeno puente al situarse dichos cationes modificadores en los huecos reticulares que quedan libres entre los poliedros de coordinación.

La concentración de tetraedros $Q^i$ puede predecirse en base a la composición del vidrio [11]. Para vidrios donde 2,5≤ [O]/[P]<3, denominados ultrafosfatos, la fracción de tetraedros $Q^3$ y $Q^2$ viene dada por las ecuacións (2.1).

$$f(Q^2)=\frac{x}{1-x};f(Q^3)=\frac{1-2x}{1-x} \qquad \text{Donde } 0\leq x\leq 0{,}5 \qquad (2.1)$$

Los vidrios de composición metafosfato que se muestran en la Figura 2.3, donde la relación [O]/[P]=3 y x=0,5 presentan redes poliméricas formadas por anillos y cadenas de unidades $Q^2$, dos enlaces a través de oxígenos puente y otros dos no puente (ONP), que se unen entre sí a través de los enlaces iónicos que se establecen entre los cationes modificadores (M) y los ONP.

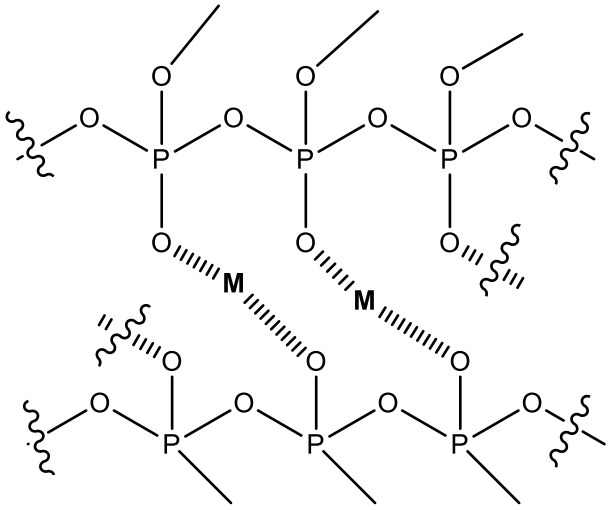


Figura 2.3: Estructura de un vidrio de composición metafosfato

Por último, los vidrios de polifosfato en los que la relación [O]/[P]>3 para concentraciones de x>0,5, presentan estructuras basadas en cadenas de $Q^2$ con unidades $Q^1$en los extremos, cuyas fracciones vienen dadas por las ecuaciónes (2. 2).

$$f(Q^1)=\frac{2x-1}{1-x};f(Q^2)=\frac{2-3x}{1-x} \quad \text{Donde } 0{,}5\leq x\leq 0{,}67 \tag{2.2}$$

A medida que aumenta la relación [O]/[P], o lo que es lo mismo, el número de oxígenos no puente por unidad tetraédrica, disminuye la longitud media de las cadenas. Así, para estequiometrias [O]/[P]=3,5; x=0,67, la estructura de la red está dominada por dímeros de grupos $PO_4$, o pirofosfato que constan de dos unidades $Q^1$ unidas mediante un OP. Vidrios cuya estequiometria [O]/[P]>3,5 presentan unidades aisladas de ortofosfato ($Q^0$).

Para las composiciones que presentan una concentración de óxidos modificadores comprendida entre la región del pirofosfato (x=0,67) y la de ortofosfato (x=0,75) la fracción de grupos Q1 y Q0 viene dada por las ecuaciones (2.3).

$$f(Q^0)=\frac{3x-2}{1-x};f(Q^1)=\frac{3-4x}{1-x} \quad \text{Donde } 0{,}67\leq x\leq 0{,}75 \tag{2.3}$$

Cabe destacar que la formación de estos vidrios mediante métodos convencionales es muy complicada debido a la alta tendencia que presentan a cristalizar. En la literatura se recogen ejemplos de obtención de vidrios con presencia de especies $Q^1$ y $Q^0$, bien con óxidos modificadores metálicos que presentan bajos índices de coordinación como es el caso de SnO, ZnO, CdO, PbO y $Fe_2O_3$, o bien obtenidos mediante técnicas de enfriamiento

ultrarrápido. Estos últimos vidrios serían análogos a los denominados vidrios invertidos de silicato que presentan composiciones estables con estequiometria [O]/[S]>3 [12].

A modo de resumen, la progresión de una red de unidades $Q^3$, pasando por una estructura tipo cadenas de unidades $Q^2$, a vidrios despolimerizados de unidades $Q^1$ y $Q^0$, tiene lugar a medida que aumenta la relación [O]/[P], es decir, a medida que aumenta la proporción de óxidos modificadores en la composición del vidrio.

El agua se comporta como otro modificador estructural al reaccionar con los tetraedros de fosfato a través del doble enlace con el oxígeno dando lugar a enlaces P-OH. Es por ello que, cuanto mayor es la fracción molar de pentóxido de fósforo en el vidrio (región del ultrafosfato), mayor es el número de enlaces P=O potencialmente hidrolizables y por tanto, menor es su durabilidad química [12].

### 2.2. Propiedades de transporte

Los avances en la Ciencia y Tecnología del vidrio dependen cada vez más del estudio de la relación entre la composición, la estructura y las propiedades fisicoquímicas de los vidrios, no sólo desde el punto de vista fundamental, sino también como medio a través del cual controlar la estructura y posibilitar el diseño de nuevas composiciones que amplíen el abanico de aplicaciones.

Algunas propiedades de los vidrios, como la densidad o el índice de refracción, pueden expresarse como una función lineal de las fracciones molares de los óxidos presentes en la composición. La adición de nuevos componentes en proporción variable permite el ajuste de la propiedad con gran fidelidad, conformando el grupo de propiedades aditivas de los vidrios en las que se pone de manifiesto la relación directa entre composición y propiedades. Sin embargo, aunque los materiales vítreos presentan un orden estructural a corto alcance, las diferentes ordenaciones atómicas de la red, así como la naturaleza de los diferentes elementos químicos y las interrelaciones entre ellos dan lugar a variaciones no lineales de determinadas propiedades. Como ejemplos clásicos de influencia de la estructura sobre las propiedades de transporte se pueden citar el efecto de álcali mixto y la anomalía bórica, esta última basada en el cambio de coordinación del boro, de grupos $[BO_3]$ a $[BO_4]$, y que en función de la concentración de alcalinos dan lugar a variaciones no lineales de dichas propiedades.

En particular, en las propiedades de transporte, aquéllas que dependen de los fenómenos de difusión y que implican desplazamiento de materia o de carga en el seno de la red vítrea,

como es el caso de las propiedades eléctricas, químicas y reológicas, son en las que generalmente se observan variaciones no lineales.

### 2.2.1 Propiedades reológicas: viscosidad

Las principales características de los vidrios derivan de que son materiales homogéneos e isótropos y pueden ser definidos como sólidos rígidos que presentan una transición continúa entre el estado subenfriado o forma visco-plástica y el estado vítreo o forma visco-elástica, que ocurre de forma reversible y sin cambios de fase [13]. Este intervalo de transición es la característica principal de un vidrio siendo la viscosidad su propiedad fundamental. Dicho intervalo viene determinado por la temperatura de transición vítrea ($T_g$), a la que generalmente se le asigna una viscosidad de cizalla de $10^{12}$ Pa.s independientemente de la composición [14,15]. La viscosidad gobierna todas y cada una de las etapas de la fabricación del vidrio, como la fusión y el afinado, la desvitrificación, su conformación y la eficacia de los tratamientos de recocido para llevar a cabo la relajación de las tensiones generadas por el rápido enfriamiento. Durante los procesos de fusión y conformado del vidrio, como por ejemplo en la producción de fibra de vidrio, el modelado de lentes esféricas o en el sellado vidrio-metal, la viscosidad ha de mantenerse controlada en todo momento para asegurar la obtención de productos de alta calidad. Además, el conocimiento de la dependencia de la viscosidad con la temperatura permite ajustar de forma precisa la temperatura que se ha de alcanzar en los hornos de fusión, dando lugar a una producción más eficiente y sostenible energéticamente.

Sin embargo, la viscosidad en vidrios de fosfato ha sido mucho menos estudiada y, en su caso, no de forma sistemática, debido a su menor producción a escala industrial con respecto a los vidrios de silicato. Además, la variación más pronunciada de la viscosidad con la temperatura, debido de nuevo a sus especiales características estructurales, así como la mayor tendencia a desvitrificar conlleva ciertas dificultades en su determinación experimental.

En la literatura se encuentran relativamente pocos datos experimentales sobre viscosidad en vidrios de fosfato. Varios estudios profundizan en la influencia de la adición de óxidos metálicos, como $Al_2O_3$, ZnO y PbO entre otros, u óxidos de metales alcalinotérreos en las propiedades térmicas y en la dependencia de la viscosidad con la temperatura [16-22]. El entrecruzamiento de las cadenas de fosfato a través de los cationes metálicos fortalece la red vítrea e influye no sólo en las propiedades de los vidrios si no que mejora su durabilidad química.

También se han llevado a cabo estudios sobre la relación entre la relajación estructural y el flujo viscoso en vidrios de fosfato [23-27]. La dependencia de la viscosidad con el tiempo se ha estudiado mediante experimentos de flujo oscilatorios en los que ha determinado la viscosidad dinámica compleja ($\eta^*$) [28, 29]. En el libro *Handbook of glass data* se puede encontrar una recopilación de los resultados de viscosidad obtenidos hasta 1985, principalmente sobre vidrios de metafosfato binarios de metales alcalinos y alcalinotérreos medidos mediante elongación de fibras [30]. Recientemente se han publicado sendos trabajos en los que se ha estudiado la viscosidad de vidrios de fosfato biocompatibles con el objetivo de establecer las condiciones óptimas de temperatura para llevar a cabo su fibrado, poniendo de manifiesto la gran importancia práctica que tiene conocer la viscosidad en el estudio de estos vidrios [31, 32].

Desde el fundido hasta la temperatura de transición vítrea, la viscosidad varía en más de 15 órdenes de magnitud a lo largo de un amplio rango de temperaturas, de forma que su determinación experimental requiere de la combinación de varias técnicas y por tanto del uso de varios equipos. Adicionalmente, las altas temperaturas a las que se determina la viscosidad en el fundido suponen un gran reto debido a la escasez de equipos y sobre todo de materiales disponibles que soporten dichas temperaturas sin verse alterados, mientras que los largos tiempos de medida necesarios para determinar viscosidades de entre $10^{10}$ y $10^{15}$ Pa.s a bajas temperaturas hacen que su medida experimental sea muy costosa desde el punto de vista económico. Además la viscosidad es muy sensible incluso a pequeñas variaciones de composición. Por esta razón, ha resultado siempre de gran interés entre la comunidad científica el desarrollo de un modelo que permita predecir con precisión el comportamiento del flujo viscoso en función de la temperatura y la composición.

Con este objetivo, han sido numerosos los modelos, predominantemente empíricos, que se han propuesto para modelizar la viscosidad en todo el rango de temperaturas. Además de que reproduzcan con la mayor precisión posible los valores experimentales, se busca que presenten el menor número de parámetros ajustables dotados de significado físico, que además sean independientes de la temperatura.

El primer modelo fue postulado por Frenkel y asumió que la viscosidad era un proceso activado térmicamente y que podía por tanto describirse mediante una simple ecuación exponencial con una sola energía de activación de flujo viscoso que se mantedría constante [33]. La simplicidad de este modelo que hace que no pueda dar respuesta al comportamiento de la viscosidad en el intervalo intermedio de temperaturas, muy importantes en la industria del vidrio, dio lugar al desarrollo de numerosos modelos

posteriores de los que tan solo unos pocos se han convertido en los más conocidos y por tanto, utilizados con mayor frecuencia. M. I. Ojovan en su revisión sobre viscosidad y flujo viscoso en vidrios [34] recoge la mayor parte de las teorías desarrolladas, como el modelo de Adam-Gibbs [35] o el de Douglas [36] entre otros.

Destaca sobre el resto, por la popularidad que goza entre la comunidad científica del vidrio, la ecuación empírica de Vogel, Fulcher & Tamman (VFT) (2.4) [37] ya que a pesar de no ajustarse correctamente al comportamiento asintótico de los extremos de la curva de viscosidad, proporciona con gran precisión una descripción de su variación en el intervalo de temperaturas intermedias, a lo largo de muchos órdenes de magnitud y con tan solo tres parámetros ajustables, A, B y $T_0$, como se observa en la ecuación 2.4.

$$\log \eta(T) = A_{VFT} + \frac{B_{VFT}}{T - T_0} \qquad (2.4)$$

La ecuación de VFT se puede deducir del modelo del volumen libre, que relaciona la viscosidad del fundido con el volumen libre por molécula, siendo éste el volumen especifico del líquido menos el volumen de sus moléculas constituidas por átomos que se comportan idealmente como esferas rígidas. Con el aumento de la temperatura se produce también un aumento de la cantidad de volumen libre, dando lugar a un incremento del transporte y ésto a su vez a una relación exponencial entre la viscosidad y el volumen libre [38]. El problema con la teoría del volumen libre es que el volumen específico de un material amorfo en función de la temperatura muestra una discontinuidad en la pendiente a la temperatura de transición vítrea, mientras que la viscosidad en el vidrio y en el fundido no, como se observa en las curvas de viscosidad representadas en la Figura 2.4.

El modelo de Adam-Gibbs [35] describe la relación entre la viscosidad y la temperatura de un líquido asumiendo que éste está formado por un número de regiones o subsistemas independientes. Cada una de las regiones está compuesta por un grupo de átomos o de moléculas que pueden reorganizarse de manera cooperativa. Cuando el líquido se enfría, la entropía configuracional del sistema disminuye y el tamaño de los subsistemas que se reorganizan de forma cooperativa aumenta progresivamente haciendo que los modos flexibles se vuelvan rígidos. Finalmente, en el estado vítreo no hay grados de libertad y por lo tanto la entalpía configuracional desaparece.

La ecuación de AG (2.5) se obtiene asumiendo que por encima de la temperatura de transición vítrea las moléculas en el fundido pueden estar en diferentes estados configuracionales con el tiempo y, a medida que la temperatura aumenta, se pueden

explorar mayores estados de energía configuracional. Por el contrario, por debajo de la temperatura de transición vítrea se asume que las moléculas en el vidrio se encuentran atrapadas en un estado configuracional único. La ecuación resultante es similar a la ecuación VFT [37]:

$$\log \eta(T) = A_{AG} + \frac{B_{AG}}{TS_{conf}(T)} \qquad (2.5)$$

Donde $A_{AG}$ y $B_{AG}$ son parámetros constantes ajustables similares a los del resto de los modelos que se describen e independientes de la temperatura. $B_{AG}$ es una barrera de activación efectiva y $S_{conf}$ (T) representa la entropía configuracional del fundido. $S_{conf}$ (T) se obtiene comúnmente integrando las curvas de capacidad calorífica obtenidas experimentalmente asumiendo que $S_{conf}$ (T) = $\Delta C_p$ (T-$T_v$)/T, donde $\Delta C_p$ es el incremento en el calor específico.

La ecuación de AG ajusta un gran número de datos de viscosidad pero no proporciona un ajuste preciso sobre todo el rango de temperaturas. A altas y bajas viscosidades la ecuación (2.5) no describe la dependencia experimental de la viscosidad con la temperatura y cada vez se producen mayores desviaciones de los valores experimentales.

El modelo de Adam-Gibbs (AG) es la base teórica sobre la que recientemente se ha desarrollado el modelo de restricciones topológicas dependiente de la temperatura (traducción al español de "Topological Constraint Theory") formulado por Gupta y Mauro [14] en el que $S_C$ se relaciona con los grados de libertad topológicos por átomo y depende de la temperatura de los líquidos. Se obtienen tres grados de libertad por átomo en el límite de alta temperatura a partir de los que se deduce[2] el modelo de viscosidad Mauro-Yue-Ellison-Gupta-Allan (MYEGA) (2.6) dependiente de tres parámetros ajustables, $A_{MYEGA}$, K y C [39]:

$$\log \eta(T) = A_{MYEGA} + \frac{K}{T}\exp\left(\frac{C}{T}\right) \qquad (2.6)$$

Este modelo consigue mejorar la descripción de la viscosidad en el rango de bajas temperaturas.

Por último, el modelo de Avramov–Milchev (AM) [40-43] asume que debido al desorden existente, hay barreras de energía de activación de diferentes alturas y que la función de

[2] El desarrollo matemático en detalle que tiene como resultado la ecuación (2.6) puede encontrarse en la publicación [43] referenciada en este trabajo.

distribución de las alturas de estas barreras depende de la entropía. Por tanto, la viscosidad se asume como una función de la entropía total del sistema que da lugar a que la viscosidad en el equilibrio dependa exponencialmente de la temperatura (ecuación 2.7):

$$\log \eta(T) = A_{AM} + 2.3(13.5 - A_{AM})\left(\frac{T_g}{T}\right)^{\alpha} \tag{2.7}$$

En este caso $T_g$, con un valor de 13.5 dPa.s viene definido por la ecuación (2.8):

$$\frac{\ln \eta(T_g)}{2.3} = 13.5 \tag{2.8}$$

Donde, $A_{AM}$ es una constante, y α es el parámetro adimensional de fragilidad de Avramov. Cuanto mayor es α, menos fuerte es un fluido, por tanto los líquidos fuertes tendrán un valor de α próximo a la unidad.

A excepción del modelo de MYEGA, ninguno de los modelos descritos anteriormente, tampoco el de Adam-Gibbs [35], describe la viscosidad fuera de intervalo de temperaturas intermedias, es decir, en los límites de baja y alta temperaturas cuando la energía de activación del flujo viscoso se mantiene prácticamente constante.

En esta tesis, los datos de viscosidad experimentales se ajustarán a los tres modelos descritos VFT, AM y MYEGA, con el objetivo de evaluar la adecuación de cada una de las tres ecuaciones para el estudio de la viscosidad en vidrios de fosfato y comparar los parámetros ajustables obtenidos mediante cada análisis.

### 2.2.2 Concepto de fragilidad

El concepto de fragilidad ha demostrado ser útil como base para la organización de datos de los líquidos formadores de vidrio y por tanto ha ayudado en el estudio de los procesos de relajación y de la temperatura de transición vítrea en el estado líquido subenfriado. Sin embargo, la cuantificación de la fragilidad ha resultado siempre un problema, y aun habiéndose propuesto varias formas para determinarla los factores que la determinan continúan sin entenderse bien, por lo que resulta una propiedad prácticamente impredecible. Por esta razón se ha intentado mejorar su determinación empírica mediante el desarrollo de medidas simples y directas que a su vez sean aplicables a cualquier líquido vitrificable.

A continuación se pasa a recopilar los métodos más comúnmente utilizados.

La definición de temperatura de transición vítrea, $T_g$, descrita anteriormente, fue utilizada por Angell para representar la dependencia de la viscosidad con la temperatura en función de la temperatura reducida ($T_g$/T), con el objetivo de normalizar las curvas η-T y facilitar la comparativa entre vidrios con diferentes $T_g$. Esta representación permite su clasificación en función de la variación que presente la viscosidad con la temperatura en el intervalo de transición según el parámetro de fragilidad cinética[3] de Angell [44], expresado como la pendiente de la curva log η frente a $T_g$/T cuando la temperatura es igual a $T_g$ según la ecuación (2.9).

$$m = \left[ \frac{\partial \log \eta}{\partial \frac{T_g}{T}} \right]_{T=T_g} \tag{2.9}$$

En la Figura 1.4 se puede observar dicha representación gráfica para vidrios de distintas composiciones.

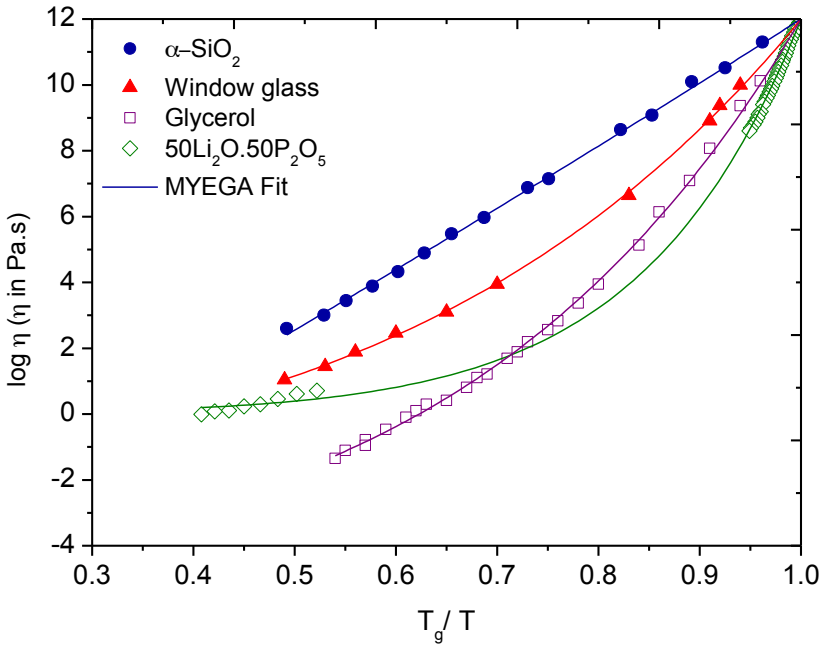


Figura 2.4: Curvas completas viscosidad *vs*. temperatura reducida para sílice vítrea (α- $SiO_2$) [45], vidrio de silicato sodo-cálcico (window glass en la gráfica) [39], vidrio de metafosfato de litio [46], y glicerol [47] como ejemplo de un vidrio orgánico con una alta viscosidad a temperatura ambiente. Las líneas continuas corresponden al ajuste de los datos experimentales a la ecuación MYEGA para facilitar la visualización de su variación.

[3] El término de fragilidad cinética se relaciona con la rápida pérdida de energía cinética cuando un líquido se enfría por debajo de su temperatura de fusión, lo que da lugar a un considerable aumento de la viscosidad de cizalla.

Observamos en la Figura 2.4 que en la sílice vítrea (v-$SiO_2$) la variación de la viscosidad respecto de la temperatura reducida ($T_g/T$) se puede aproximar a una ecuación de tipo Arrhenius de la que se extrae una única energía de activación para el flujo viscoso que es constante con la temperatura y por tanto independiente de ésta [48]. Sin embargo, en la práctica, la mayor parte de los vidrios, se alejan en mayor o menor medida de este comportamiento. Muestra de ello es el vidrio de silicato sodocálcico de la figura, donde la viscosidad muestra una dependencia no lineal con la temperatura.

De acuerdo con la definición de Angell [44], estos vidrios se clasifican como vidrios "fuertes", siendo la sílice vítrea, el vidrio de referencia. Por el contrario, los vidrios de fosfato, de nuevo debido a sus características estructurales, presentan una variación más brusca de la viscosidad con la temperatura, denominándose vidrios "frágiles" como puede observarse en la figura 1.4. En general, tienden a ser "fuertes" los vidrios de $Si_2O$, $GeO_2$ y $BeF_2$, mientras que los de fosfato, calcogenuros y vidrios orgánicos son generalmente "frágiles" y por tanto su energía de activación aumenta considerablemente al aproximarse a la temperatura de transición vítrea.

A lo largo de esta tesis, y con el objetivo de ser capaces de comparar los resultados de viscosidad obtenidos experimentalmente a través del ajuste de los mismos a los modelos VFT, AM y MYEGA, los distintos parámetros ajustables de cada una de las tres ecuaciones anteriores van a expresarse en términos del mismo número de variables con significado físico, como son la temperatura de transición vítrea ($T_g$), la fragilidad cinética de Angell (m) y la extrapolación de la viscosidad a temperatura infinita ($\eta_\infty$) [39], quedando las ecuaciones (2.4), (2.6) y (2.7) reescritas de la siguiente forma (2.10), (2.11) y (2.12) al incluir la ecuación (2.8) en las mismas [43]:

$$\log\eta(T) = \log\eta_\infty + \frac{(12-\log\eta_\infty)^2}{m\left(\frac{T}{T_g}-1\right)+(12-\log\eta_\infty)} \tag{2.10}$$

$$\log\eta(T) = \log\eta_\infty + (12-\log\eta_\infty)\frac{T_g^{\left(\frac{m}{12-\log\eta_\infty}\right)}}{T} \tag{2.11}$$

$$\log\eta(T) = \log\eta_\infty + (12-\log\eta_\infty)\frac{T_g}{T}\exp\left(\frac{m}{12-\log\eta_\infty}-1\right)\left(\frac{T_g}{T}-1\right)$$

(2.12)

La segunda aproximación utilizada por Richert y Angell para calcular la fragilidad [49], es medir la desviación del comportamiento de tipo Arrhenius, cuantificada mediante el parámetro $F_{1/2}$ y calculado a través de la ecuación (2.13):

$$F_{1/2} = \frac{2T_g}{T_{1/2}} - 1 \qquad (2.13)$$

donde $T_{1/2}$ es el valor de temperatura al que el tiempo de relajación es la mitad (en escala logarítmica) entre el límite del tiempo de relajación a alta temperatura ($10^{-14}$ s) y $T_g$, donde el tiempo de relajación es igual a $10^2$ s. En la práctica, mide la distancia que se aleja la curva de un comportamiento ideal en el punto medio del intervalo comprendido entre los límites superior e inferior de viscosidad, generalmente considerados como $10^{12}$ y $10^{-5}$ Pa.s. $F_{1/2}$ adquiere un valor igual a 0 para vidrios idealmente fuertes y de 1 para vidrios idealmente frágiles. Pero esta expresión ha resultado ser inexacta, dando valores de fragilidad subestimados [50].

Como se ha indicado anteriormente, la viscosidad tiene un comportamiento asintótico de tipo Arrhenius a temperaturas suficientemente altas y bajas comparadas con $T_g$, por lo que en estos rangos de temperatura las energías de activación del flujo viscoso ($E_a$) son constantes y se pueden calcular mediante la ecuación (2.14):

$$\eta = A \exp \frac{E_a}{RT} \qquad (2.14)$$

donde A es el factor preexponencial y R es la constante universal de los gases.

Basándose en este comportamiento, Doremus propone [51, 52] otra forma de evaluar la fragilidad del fundido basándose en la relación entre las energías de activación de flujo viscoso en el intervalo de alta ($Q_H$) y baja ($Q_L$) viscosidad (ecuación 2.15):

$$R_D = \frac{Q_H}{Q_L} \qquad (2.15)$$

A diferencia de los métodos anteriormente descritos para determinar de forma cuantitativa el grado de fragilidad, este nuevo criterio de fragilidad implica todos o la mayoría de los rangos de temperatura en los que se lleva a cabo las medidas de viscosidad y no solo las temperaturas próximas a la temperatura de transición vítrea o el punto medio de las curvas.

Cuanto mayor es el radio de Doremus ($R_D$), más frágil es el material, presentando valores

iguales o superiores a 2 ($R_D \geq 2$), como es el caso del óxido de boro ($R_D$=3.28) o la anortita, un silicoaluminato de cálcico con un $R_D$=4. 52. La sílice vítrea ($SiO_2$) o el óxido de germanio ($GeO_2$), presentan valores de $R_D$=1.45 y $R_D$=1.47, respectivamente, radios que los clasifican como vidrios fuertes [34]. Lamentablemente no se encuentran en la literatura referencias de vidrios de fosfato.

Según Doremus, la similitud entre la energía de activación de relajación de la viscosidad en vidrios de silicato sodo-cálcicos y la de flujo viscoso a alta viscosidad pone de manifiesto que la viscosidad controla el proceso de relajación cerca del intervalo de transición, mientras que la viscosidad en sí misma está determinada por varios factores como la estructura y las uniones de los elementos estructurales.

Inicialmente, los líquidos frágiles fueron denominados así haciendo referencia a la rápida ruptura de su configuración estructural, asociada con el orden estructural a medio alcance que involucra a la primera esfera de coordinación, con el aumento de la temperatura cerca y por encima de la temperatura de transición ($T_g$), y por tanto la estructura es térmicamente frágil [53]. Esta clasificación de los materiales vítreos en fuerte-frágil hizo que llevara asociado el concepto de materiales con enlaces fuertes-débiles, Doremus advirtió [51, 52] del uso extendido de estos términos, que aunque convenientes, eran engañosos. Por ejemplo, los vidrios de silicato binarios son fuertes pese a tener numerosos oxígenos no puente. Por el contrario, la anortita, como hemos indicado anteriormente, tiene energías de activación muy altas y, sin embargo, se la clasifica como frágil.

Los datos experimentales de viscosidad obtenidos a lo largo de esta tesis para vidrios de fosfato de distintas composiciones, muestran que la viscosidad en los rangos de alta y baja temperatura presentan una dependencia de tipo Arrhenius por lo que es posible obtener dos valores diferentes de energía de activación de flujo viscoso y, por lo tanto evaluar la fragilidad de los vidrios de fosfato mediante el radio de Doremus. De esta forma, todos los datos experimentales obtenidos están involucrados en el análisis y no solo aquellos valores cercanos a la temperatura de transición vítrea como ocurre con el parámetro de fragilidad cinética de Angell (m), por lo que en esta tesis la fragilidad, y su relación con la composición y la estructura, va a ser estudiada mediante ambos métodos con el objetivo de llegar a establecer una comparación entre ellos y evaluar su adecuación al estudio de los vidrios de fosfato.

### 2.2.3 Importancia de la fragilidad

La fragilidad no es solo un parámetro con interés puramente académico sino que las

consecuencias de la fragilidad siguen siendo un motivo de preocupación para la fabricación de vidrio comercial durante la que se necesita un control preciso de la viscosidad. Por lo tanto, no sorprende encontrar numerosos estudios en la literatura que han explorado correlaciones entre la fragilidad y otras propiedades a temperaturas iguales o inferiores a $T_g$, como son la capacidad calorífica [53, 54] y más recientemente con el coeficiente de Poisson [55]. Incluso ya en el modelo clásico de Adam-Gibbs la fragilidad aparece como una medida directa de la velocidad a la que la entropía configuracional disminuye a medida que se almacena progresivamente en la fase no-ergódica.

La fragilidad normalmente se ha definido en clave de propiedades dinámicas, como la viscosidad o la velocidad de relajación, aunque evidencias tanto teóricas como experimentales indican que la fragilidad se relaciona fundamentalmente con propiedades termodinámicas [54, 56, 57], incluyendo el exceso de entropía y la capacidad calorífica, y sugiriendo que debería tener un efecto estructural, es decir, que la fragilidad depende principalmente de factores estructurales. Esta presunta conexión con el orden estructural es utilizada normalmente para describir la fragilidad de forma cualitativa. Mauro y colaboradores han demostrado utilizando datos experimentales de la estructura y la viscosidad, que la fragilidad refleja la velocidad de ordenación estructural cerca de $T_g$, lo que demostraría la conexión entre fragilidad y estructura, y ésta a su vez con la dinámica de la red vítrea [58].

## 2.3 Referencias

[1] R. K. Brow, L. Kovacic, R. E. Loehman, Ceram. Trans. 70 (1996) 177.

[2] J. H. Campbell, J. S. Hayden, A. Marker, Int. J. App. Glass Sci. 2 (1) (2011) 3.

[3] D. E. Day, z. Wu, C. S. Ray, P. Hrma, J. Non-Cryst. Solids 241 (1998) 1.

[4] J. C.Knowles, J. Mater. Chem. 13 (10) (2003) 2395.

[5] J. Fu, J. Mater. Sci. 33 (6) (1998) 1549.

[6] J. B. Bates, N. J. Dudney, G. R. Gruzalski, R. A. Zuhr, A. Choudhury, C. F. Luck, J. D. Robertson, Solid State Ionics 53-56 (1992) 647.

[7] D. W. J. Cruickshank, J. Chem. Soc. (1961) 5486.

[8] K. A. R. Mitchell., Chem. Rev. 69 (2) (1969) 157.

[9] E. Lippmaa, M. Maegi, A. Samoson, G. Engelhardt, A. Grimmer, J. Am. Chem. Soc. 102 (1980) 4889.

[10] W. H. Zachariasen, J.Am. Chem. Soc. 54 (1932) 3841.

[11] J. R. Van Wazer, Phosphorus and its Compounds, vol. 1,Interscience, New York, (1958).

[12] R. K. Brow, J. Non-Cryst. Solids 263 & 264 (2000) 1.

[13] J. M. Fdez. Navarro, El Vidrio, Consejo Superior de Investigaciones Científicas; Madrid (2003).

[14] P. K. Gupta, J. C. Mauro; J. Chem Phys. 130: 094503 (2009).

[15] Y. Z. Yue , J. Non-Cryst. Solids 355 (2009) 737.

[16] S.I.S. Shaharuddin, I. Ahmed, D. Furniss, A.J. Parsons, C.D. Rudd, Glass Technol. Eur. J. Glass Sci. Technol. Part A 53 (6) (2012) 245.

[17] S. Striepe, J. Deubener, J. Non-Cryst.Solids 358 (12–13) (2012) 1480.

[18] P. Wange, J. Vogel, S. Knoche, C. Russel, Glas. Sci. Technol. 77 (4) (2004) 172.

[19] J.E. Shelby, J. Non-Cryst. Solids 263 (2000) 271.

[20] S.V. Nemilov, N.E. Volkova, Fiz. Khim. Stekla 18 (6) (1992) 88.

[21] N.V. Komarova, S.V. Nemilov, Sov. J. Glass Phys. Chem. 17 (1) (1991) 13.

[22] J. Kitheri, K.V. GovindanKutty, M.C. Goswami, P.R. VasudevaRao, Thermoch.Acta 587 (2014) 42.

[23] M. Chromčíková, M. Liška, J. Macháček, J. Therm. Anal. Calorim. (2013) 1.

[24] I. Avramov, C. Tzvetkova, T. Vassilev, J. Non-Cryst. Solids 355 (1) (2009) 23.

[25] P.F. Green, E.F. Brown, R.K. Brow, J. Non-Cryst. Solids 263 (2000) 195.

[26] D.L. Sidebottom, P.F. Green, R.K. Brow, J. Mol. Struct. 479 (2–3) (1999) 219.

[27] Y. Hiki, H. Kobayashi, H. Takahashi, Y. Kogure, Solid State Ionics 113–115 (1998) 659.

[28] J.U. Otaigbe, J. Non-Cryst. Solids 263 (2000) 202.

[29] R.L. Sammler, J.U. Otaigbe, M.L. Lapham, N.L. Bradley, B.C. Monahan, C.J. Quinn, J. Rheol. 40 (2) (1996) 285.

[30] O.V. Mazurin, M.V. Streltsina, Handbook of glass data, Elsevier, Amsterdam, 1985.

[31] F. Döhler, D. Groh, S. Chiba, J. Bierlich, J. Kobelke, D. S. BrauerJ. Non-Cryst. Solids xxx (2015) xxx (in press).

[32] A.J. Parsons, N. Sharmin, Sharifah I.S. Shaharuddin, M.Marshall, J. Non-Cryst.Solids 408 (2015) 76.

[33] Y. I. Frenkel, *Kinetic theory of liquids*, Oxford University Press, Oxford, (1946).

[34] M.I. Ojovan, Phys. Chem. Glasses: Eur. J. Glass Sci. Technol. B, 53 (4) (2012) 143.

[35] G. Adam, J. H. Gibbs, *J. Chem. Phys.*, 43 (1965) 139.

[36] R. W. Douglas, *J. Soc. Glass Technol.*, 33 (1949) 138.

[37] G.S. Fulcher, J. Am. Ceram. Soc. 75 (1992) 1060.

[38] D. Turnbull, M. H Cohen, *J. Chem. Phys.*, 34 (1961)120.

[39] J.C. Mauro, Y.Z. Yue, A.J. Ellison, P.K. Gupta, D.C. Allan, Proc. Natl. Acad. Sci. U. S. A. 106 (2009) 19780.

[40] I. Avramov, A. Milchev, *J. Non-Cryst. Solids*, 104 (1988)253.

[41] I. Avramov, *J. Non-Cryst.Solids*, 262 (2000) 258.

[42] I. Avramov, *J. Non-Cryst. Solids*, 351 (2005) 3163

[43] I. Avramov, *J. Non-Cryst. Solid, 357 (2011) 391*

[44] C.A. Angell, Science 267 (1995) 1924.

[45] G. Hetherington, K. H. Jack, J. C. Kennedy, Phys. Chem. Glasses 5 130 (1964)

[46] L. Muñoz-Senovilla, F. Muñoz, J. Non-Cryst. Solids 385 (2014) 9.

[47] K. Schröter, E. Dorth, J. Chem. Phys. 113 9101 (2000)

[48] C.A. Angell, J. Phys. Chem. Solids 49 (1988) 863.

[49] R. Richert, C. A. Angell, J. Chem. Phys. 108 (1998) 9016

[50] L. Wang, V.Velikov, C. A. Angell, J. Chem. Phys., 117 (22) (2002) 10184

[51] R. H. Doremus, Am. Ceram. Soc. Bull. 82 (3) (2003) 59

[52] R. H. Doremus, J. Appl. Phys., 92 (2002) 7619

[53] C.A. Angell, Relaxations in complex systems, K. Ngai and G.B. Wright (Eds.), Natl. Technol. Inform. Service, US Dept. of Commerce, Springfield, V.A. (1985) 3

[54] L. M. Martinez, C. A. Angell, Nature 410 (2001) 663

[55] V.N. Novikov, A.P. Sokolov, Nature 431 (2004) 961

[56] K. Ito, C. T. Moynihan, C.A. Angell, Nature 398 (1999) 492

[57] S. Sastry, P. G. Debenedetti, F. H. Stillinger, Nature 393 (1998) 554

[58] N. A. Mauro, M. Blodgett, M. L. Johnson, A. J. Vogt, K. F. Kelton, Nat. Commun. 5:4616 doi: 1. 1038/ncomms5616 (2014)

# Capítulo III

# Técnicas y métodos experimentales

## Capítulo III: Técnicas y métodos experimentales

En este capítulo se van a describir brevemente las técnicas utilizadas a lo largo de esta tesis para llevar a cabo la caracterización de las propiedades fundamentales del vidrio así como de su estructura atómica a corto y medio alcance. Las condiciones experimentales utilizadas en cada técnica así como las especificaciones del equipo utilizado vienen brevemente recogidas en el apartado de trabajo experimental en cada uno de los capítulos en los que se describen los resultados obtenidos.

### 3.1 Determinación de la composición

#### 3.1.1 Cálculo del contenido de agua mediante FTIR

Debido al carácter higroscópico de los vidrios de fosfatos es importante determinar el contenido en agua en los mismos. En este trabajo la espectroscopia de infrarrojo en el modo de transmisión (FTIR) ha sido utilizada para determinar el contenido en agua en muestras de vidrio de unos 2 mm de espesor en un espectrómetro *PerkinElmer Spectrum 100* en el rango de 950 to 5500 $cm^{-1}$.

Los vidrios de fosfato presentan una banda de absorción a 3000$cm^{-1}$ correspondiente a los grupos hidroxilo [1]. El contenido de agua en los vidrios se puede expresar en términos del coeficiente de absorción de los grupos –OH ($r_{OH}$) a 3000$cm^{-1}$ que determina la concentración relativa de OH en los vidrios según la ecuación (3.1)

$$r_{OH} = \frac{-\log \frac{T_{3000}}{T_{5000}}}{l} \qquad (3.1)$$

donde l es el espesor de la muestra y $T_{3000}$ y $T_{5000}$ son la transmisión a 3000 and 5000 $cm^{-1}$, respectivamente, como se puede observar en la Figura 3.1 para dos vidrios de diferente composición a modo de ejemplo.

El valor de $T_{5000}$ sirve como valor máximo de la transmisión del vidrio e incluye las pérdidas de reflexión de Fresnel. Para la calcular el contenido absoluto de grupos –OH en ppm se ha seguido la ecuación (3.2) donde $r_{OH}$ viene expresado en $cm^{-1}$ [2].

$$OH_{content}(ppm) = 30 \cdot r_{OH} \qquad (3.2)$$

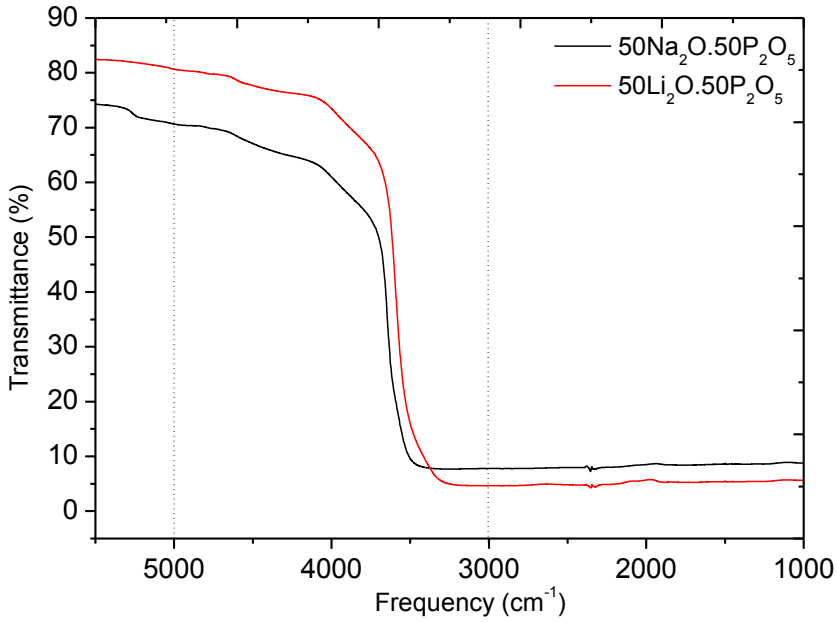


Figura 3.1 Transmitancia en la región del infrarrojo cercano para vidrios de composición $M_2O.P_2O_5$ donde M= Li, Na.

### 3.1.2 Cálculo del contenido en fosforo mediante Resonancia Magnética Nuclear de $^{31}P$

La composición de los vidrios se estudió primeramente mediante análisis químico utilizando distintas técnicas en función del elemento a utilizar. El litio se analizó por fotometría de llama y el fósforo por espectrometría de plasma. Debido a que los resultados obtenidos fueron similares a los nominales y a la simplicidad de las composiciones de los vidrios estudiados (sistemas binarios o ternarios), se determinó estudiar la composición mediante resonancia magnética nuclear de $^{31}P$ como se explicara en más detalle en el apartado 3.3 de este capítulo con el objetivo de optimizar recursos.

## 3.2 Caracterización de las propiedades

### 3.2.1 Análisis térmico diferencial (ATD)

El Análisis Térmico Diferencial (ATD) consiste en determinar las variaciones calorimétricas producidas en la muestra estudiada en función de la temperatura por comparación con una muestra inerte de referencia, normalmente α-alúmina calcinada cuando ambas están sometidas a un programa de calentamiento controlado. Estas variaciones se manifiestan por la aparición de efectos endotérmicos y exotérmicos, cuando

las reacciones que tienen lugar transcurren con absorción de calor (como la fusión), o desprendimiento (cristalización), respectivamente.

La técnica de ATD se ha empleado para determinar la temperatura de transición vítrea ($T_g$) previa al tratamiento de recocido para eliminar las tensiones internas del vidrio. Dichas tensiones se han creado al pasar del estado plástico al estado rígido, debido al rápido enfriamiento y a la baja conductividad térmica del vidrio. Esto hace que se establezca un gradiente de temperatura desde el centro de la pieza hasta la superficie. Al ir desapareciendo dicho gradiente, las capas externas se contraen en primer lugar limitando la contracción de las internas [3].

En la Figura 3.2 se muestra como ejemplo uno de los diagramas obtenidos. Se puede observar cómo se obtiene geométricamente $T_g$ a partir del intervalo de transición que se corresponde con el primer efecto endotérmico que se observa en el diagrama.

Las medidas se han llevado a cabo en el equipo SEIKO–6300 DTA/TG utilizando crisoles de platino a una velocidad de calentamiento constante de 10ºC/min en aire, hasta 900ºC.

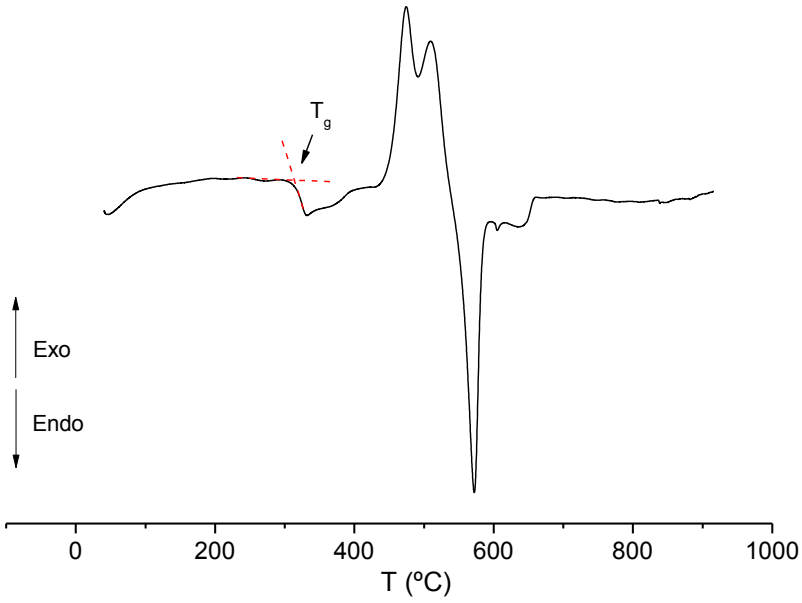


Figura 3.2: Termograma del vidrio $30Li_2O.30ZnO.40P_2O_5$ (x=40) a modo de ejemplo

### 3.2.2 Dilatación térmica

La dilatación térmica es el aumento dimensional que experimentan los materiales con la temperatura al aumentar la distancia entre sus constituyentes estructurales, como consecuencia de un aumento de su energía interna [3].

Este aumento dimensional viene dado para cada material por un factor característico dependiente de la temperatura, denominado coeficiente de dilatación referido al volumen (β), a la superficie (γ) o a una sola dimensión (α).

El coeficiente de dilatación medio entre dos temperaturas viene dado por la ecuación (3.3):

$$\alpha_{T2\text{-}T1} = \frac{1}{l} \cdot \frac{\Delta l}{\Delta t} \qquad (3.3)$$

Donde la longitud l de un cuerpo sólido sufre un alargamiento Δl cuando su temperatura se eleva de T hasta T+ΔT.

En los vidrios, el coeficiente de dilatación es independiente de la dirección de medida al tratarse de cuerpos isótropos y es una de las características de mayor importancia tecnológica ya que influye sobre algunas de sus propiedades, como la resistencia al choque térmico.

El comportamiento dilatométrico de los vidrios depende fundamentalmente de sus características reticulares, como son el índice de coordinación de los iones formadores, el número de oxígenos puente, o la intensidad de los enlaces entre oxígenos e iones formadores y modificadores. Por tanto, va a depender de la composición. Por otro lado, la curva de dilatación térmica pone de manifiesto el grado de relajación estructural del vidrio y las desviaciones de su volumen específico con respecto al que alcanzaría en un enfriamiento ideal, por lo que las características dilatométricas del vidrio van a depender también de su historia térmica. En la Figura 3.3 se ha representado la curva dilatométrica de uno de los vidrios estudiados en esta tesis a modo de ejemplo.

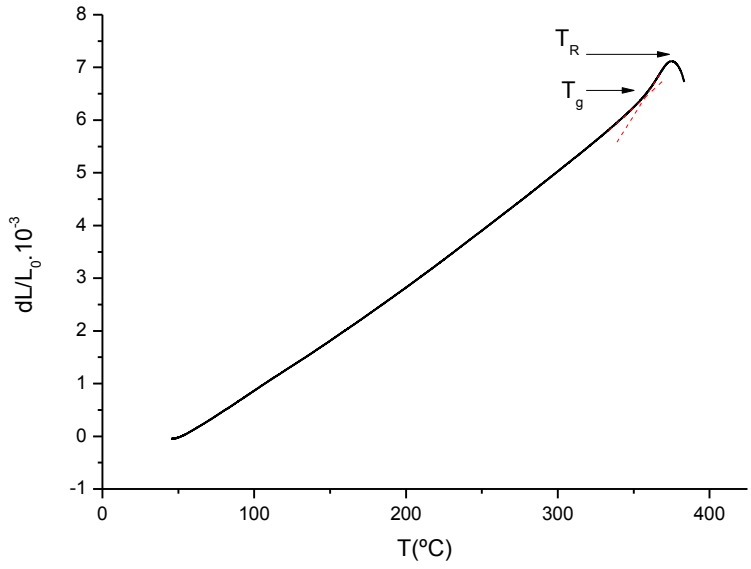

Figura 3.3: Ejemplo de curva de expansión dilatométrica.

En la curva dilatométrica podemos distinguir la temperatura de transición vítrea ($T_g$) que se determina geométricamente como se ve en la Figura 3.2 a partir del intervalo de transición y que corresponde a un punto fijo de viscosidad ($\eta=10^{12}$ Pa.s), y la temperatura de reblandecimiento dilatométrico ($T_R$), que corresponde al máximo de la curva de dilatación, con una viscosidad de $10^{10}$ Pa.s, así como el coeficiente de expansión térmica ($\alpha_{T1-T2}$).

Siempre que no se produzcan cambios estructurales, la variación dimensional en función de la temperatura va a transcurrir de un modo continuo, sin presentar por tanto discontinuidades en la curva dilatométrica.

En este trabajo, las curvas dilatométricas se han obtenido mediante el método diferencial para determinar la temperatura de transición vítrea en el vidrio en masa tras llevar a cabo el tratamiento de recocido. Este método consiste en un tubo de cuarzo en el que se aloja la probeta de ensayo, cuyo alargamiento es transmitido mediante una varilla, también de sílice, a un micrómetro donde se obtiene la dilatación aparente de la muestra por lectura directa como resultado de la diferencia entre su dilatación real y la del tubo de cuarzo. El equipo utilizado es un dilatómetro Netzsch Gerätebau, modelo 402 EP, con una velocidad de calentamiento de 2 K $min^{-1}$ en aire. En este trabajo, se han preparado muestras en forma de prisma con las dos caras plano paralelas pulidas y perpendiculares a su eje de 10 a 20 mm de longitud.

### 3.2.3 Picnometría de helio

La densidad es una propiedad intrínseca del material y es probablemente una de las medidas más importantes en un vidrio. Se define como la cantidad de masa contenida por unidad de volumen. Por su simplicidad y economicidad, el método más comúnmente utilizado para determinar la densidad es por el principio de Arquímedes con agua destilada como medio en el que se lleva a cabo la inmersión. Sin embargo, una de las limitaciones son los materiales higroscópicos, como los vidrios de fosfato, por razones obvias. La picnometría de helio constituye una buena alternativa para este tipo de materiales. En este trabajo la densidad se ha determinado mediante picnometría de helio en un multipicnómetro *Quantachrome Corp*. a partir de muestras de vidrio en masa, homogéneo y exento de tensiones. El método se basa en la medida de la diferencia de presión ejercida por una cantidad de helio en una célula de referencia ($P_1$) de volumen conocido ($V_R$) y la presión ejercida por el helio en una célula de medida ($P_2$) de volumen ($V_c$) que contiene la muestra.

Una vez conocidos estos datos se calcula la densidad de los vidrios utilizando la masa de muestra utilizada y el volumen de muestra calculado según la ecuación (3.4):

$$V_{vidrio} = V_C - V_R\left(\frac{P_1}{P_2} - 1\right) \tag{3.4}$$

La determinación de la densidad se lleva a cabo para determinar el grado de interconectividad estructural, y por tanto el volumen intersticial que está libre, por lo que es más indicativo determinar el volumen ocupado por un mol de vidrio mediante la ecuación (3.5):

$$V_M = \frac{\sum x_i M_i}{\rho} \tag{3.5}$$

donde, ρ es la densidad, $x_i$ la fracción molar y $M_i$ la masa molecular de cada componente i.

### 3.2.4 Determinación de la viscosidad

La viscosidad es una de las propiedades más importantes de un fluido, por ejemplo, en la industria del vidrio la viscosidad determina las condiciones de fusión, de trabajo y las temperaturas de recocido, la velocidad de afinamiento o de cristalización. El vidrio se obtiene comúnmente a partir de fundidos homogéneos obtenidos por reacción a alta temperatura de mezclas vitrificables de óxidos, calcogenuros, halogenuros, metales o sales, que han de enfriarse a una velocidad adecuada para evitar su cristalización, por lo que la viscosidad es una propiedad de una importancia fundamental para los materiales amorfos tanto fundidos como en estado sólido [4]. La viscosidad cuantifica la resistencia que opone el material a fluir e indica la habilidad para disipar el momento lineal o *momentum*. El momento de equilibrio de un fluido Newtoniano se describe a nivel macroscópico por las ecuaciones de Navier-Stokes [5]. A nivel microscópico la viscosidad aumenta debido a la transferencia del momento lineal entre capas del fluido que se mueven a diferente velocidad como se describe en la teoría cinética de Maxwell [5].

Por definición, la viscosidad es la resistencia al deslizamiento o a la deformación que existe entre las moléculas de un fluido no ideal. Ésta viene representada por el coeficiente de viscosidad característico para cada líquido (η), calculado a partir del cociente entre la tensión de cizalla y el gradiente de velocidad (ver Figura 3.4) según la ecuación (3.6):

$$\eta = \frac{F}{A} \cdot \frac{H}{v} \tag{3.6}$$

donde F es la fuerza aplicada a una superficie de área A, V es la velocidad and H es la separación entre dos planos. La viscosidad viene expresada en Poise (P) equivalente a los dPa en el sistema cgs, o en Pascales por segundo en el S.I. (Pa.s).

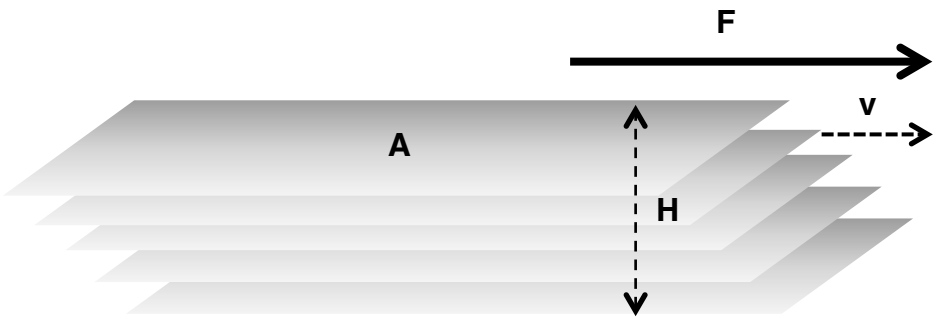


Figura 3.4: Esquema de las capas imaginarias en movimiento en un material que fluye.

La viscosidad gobierna los procesos de relajación como el tiempo de relajación de Maxwell ($\tau_M$) y es directamente proporcional al coeficiente de viscosidad $\tau_M \approx \eta/G$, donde G es el módulo de cizalla [4-9]. Cuanto mayor es la viscosidad mayor es el tiempo de relajación, que para el vidrio puede ser enorme, por ejemplo para la sílice a temperatura ambiente es de $\tau_M \approx 10^{98}$ años. Cabe destacar que estas escalas de tiempo son inconmensurablemente más largas que el tiempo de vida del Universo $\approx 1.5 \times 10^{10}$ años.

La viscosidad depende de la composición química del material y de la temperatura, por ejemplo a temperatura ambiente en los sistemas de silicato la viscosidad alcanza los valores más altos para la sílice vítrea. La viscosidad se encuentra altamente influida por la temperatura, además comúnmente se asume que la viscosidad es un proceso activado térmicamente. Al someter a un vidrio a un aumento progresivo de la temperatura, se observa una pérdida creciente de rigidez al debilitarse los enlaces interatómicos en orden creciente de energía reticular, como consecuencia de la energía calorífica aportada. Esto hace que aumente su fluencia y por tanto que disminuya la viscosidad del sistema.

La viscosidad experimenta una variación de 16 a 18 órdenes de magnitud a lo largo del rango de temperaturas por el que pasa el vidrio desde el fundido hasta temperatura ambiente [3]. Los viscosímetros de alta temperatura, se dividen en aquellos que miden viscosidades menores de $10^6$ Pa.s y los que miden mayores de $10^6$ Pa.s, por lo que la obtención de la curva completa de viscosidad-temperatura de los vidrios requiere la combinación de medidas realizadas por equipos de ambos tipos.

El vidrio es un material con un comportamiento de tipo Newtoniano por lo que la viscosidad ha de determinarse mediante métodos adecuados a este comportamiento. A temperaturas superiores a la temperatura de transición vítrea, en el intervalo de reblandecimiento ($10^{12}$ Pa.s <η< $10^{5}$ Pa.s), las técnicas de flexión de barras, elongación de fibras, medidas cuasiestáticas o de deformación bajo compresión, en inlgés *parallel plate*, son las comúnmente usadas para determinar la viscosidad en vidrios. Por otro lado, en el intervalo de temperaturas en el que el vidrio se encuentra fundido y que corresponde al rango de viscosidades comprendido entre y $10^{3}$ Pa.s y 1 Pa.s, las técnicas utilizadas con mayor frecuencia son, o bien los viscosímetros en los que se determina la velocidad de caída de una bola en el seno del fundido mantenido a una temperatura constante, o bien mediante el comúnmente denominado viscosímetro de rotación.

A lo largo de esta tesis las curvas de viscosidad-temperatura de los vidrios se han determinado mediante la combinación de los métodos de rotación y de flexión de barras de vidrio. La viscosidad en el fundido se ha determinado mediante el método de rotación en el intervalo de viscosidad de $10^{2}$–1 Pa.s. El viscosímetro empleado es de tipo Searle cilíndrico de alta temperatura equipado con un Sistema Sensor ME 1700 (Modelo RV30 Rotovisco/TP1700, Haake, Karlsruhe, Germany). El método de rotación se basa en determinar la fuerza de cizalla necesaria para para imprimir una rotación determinada a una varilla de platino sumergida en el fundido mientras el crisol que lo contiene se mantiene inmóvil. Todas las medidas se han realizado en modo estático, para ello antes de realizar la medida, la temperatura del fundido debe estabilizarse aunque no durante tiempos muy prolongados para evitar, tanto la volatilización de componentes, como la aparición de fases cristalinas en el fundido. Una vez la temperatura está estabilizada se han realizado tres medidas a velocidades de entre 3 a 15 rpm durante 15 min según el estándar internacional ISO 7884-2. En la Figura 3.5 se ha representado un esquema del equipo utilizado.

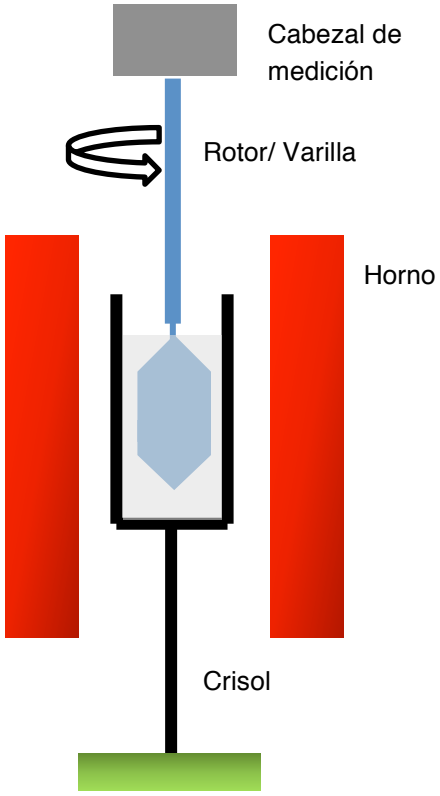


Figura 3.5: Esquema de un viscosímetro de rotación cilíndrico de alta temperatura.

La viscosidad (η) se calcula a partir del cociente entre tensión de cizalla (τ) y la velocidad de cizalla ($\dot{\gamma}$) aplicada a un fluido viscoso según la relación (3.7):

$$\eta = \frac{\tau}{\dot{\gamma}} \tag{3.7}$$

En el intervalo de viscosidad de $10^{11,5}$–$10^{8}$ Pa.s la viscosidad se ha determinado por flexión de barras de vidrio (en inglés beam bending). Esta técnica permite determinar viscosidades por encima de las obtenidas mediante *parallel plate* o mediante el método de rotación. La técnica se basa en medir la velocidad de flexión de una muestra de vidrio mecanizada en forma de barra de dimensiones conocidas. La muestra se encuentra soportada en una barra de sílice con tres puntos de apoyoen posiciones simétricas para permitir la flexión por acción del peso al que la muestra es sometida en función de la temperatura. El viscosímetro empleado es *VIS401 (BährThermoanalyse, Germany*) con un vano de 40 mm. La viscosidad (η) se ha medido en modo dinámico siguiendo las condiciones de medida estándar según la norma DIN ISO 7884-4 a través de la ecuación (3.8). La velocidad de calentamiento se ha fijado en 2K.min$^{-1}$ y los pesos utilizados han sido de 10-200 g.

$$\eta = \frac{g}{1440 I_C (dh/dt)} \left( M + \frac{\rho A L}{1.6} \right) \tag{3.8}$$

M es el peso total aplicado, dh/dt es la velocidad de flexión en el punto medio de la muestra, g es la aceleración dela gravedad, $I_C$ es momento de inercia de la sección transversal de la muestra, ρ es la densidad del vidrio, A es el área de la sección transversal de la barra de vidrio Y L es la longitud del vano que existe entre los soportes en los que se sostiene la muestra.

En la Figura 3.6 se ha representado un esquema del equipo utilizado.

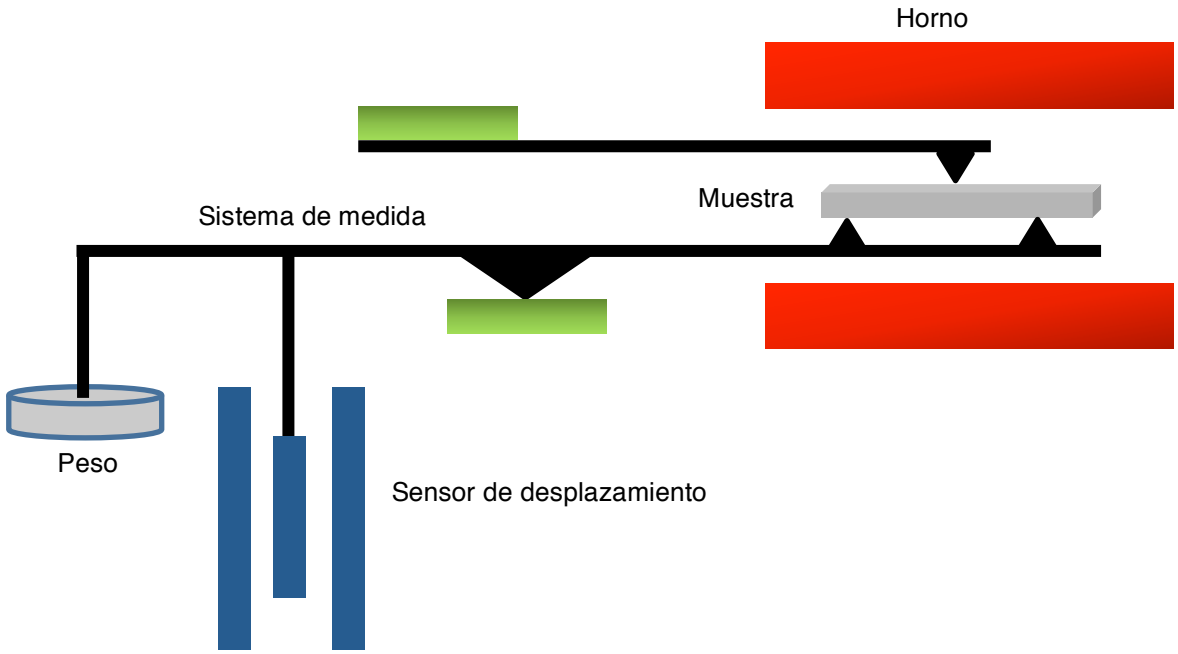


Figura 3.6: Esquema de un viscosímetro de flexión de alta temperatura.

### 3.2.4 Espectroscopia de impedancia electroquímica (EIS)

En los materiales cerámicos y vítreos para evitar los problemas que generalmente lleva asociada la aplicación de una corriente continua (métodos D. C.), como los de polarización en las interfases entre los electrodos y la muestra, la conductividad de estos materiales se determina mediante la aplicación de métodos basados en la aplicación de un potencial de corriente alterna (métodos A. C.) sobre un determinado intervalo de frecuencias. Una de las técnicas electroquímicas A.C comúnmente utilizadas para determinar la impedancia en vidrios es la Espectroscopia de Impedancia Electroquímica (EIS). La impedancia se define como una magnitud compleja que se obtiene al aplicar una corriente alterna y responde a la ecuación $Z(\omega)=Z' + \exp(j\pi/2)\, Z''$ [10]. En la Figura 3.7 se ha

representado el diagrama de Nyquist de la impedancia Z. La parte real de Z como vector plano es la componente en x de dicho vector (Z´) mientras que la parte imaginaria es la componente en y (Z´´).

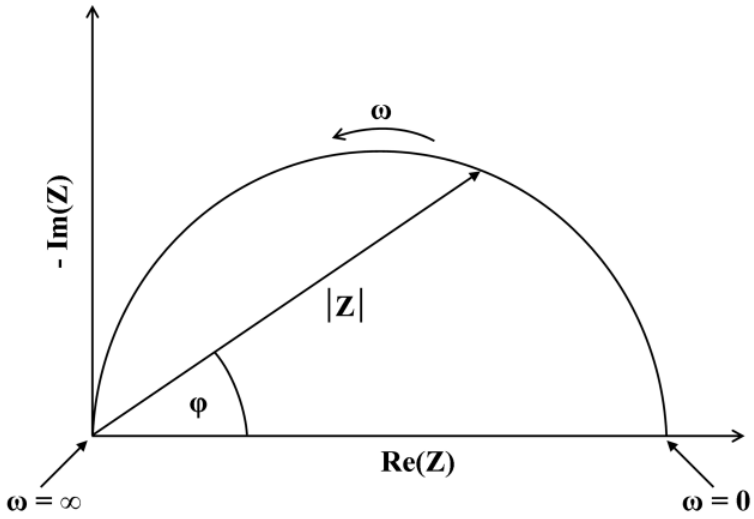


Figura 3.7: Representación de la impedancia mediante un diagrama de Nyquist.

La componente imaginaria del vector Z se hace cero cuando ϕ=0 y por tanto el comportamiento de la muestra es puramente resistivo siendo la impedancia independiente de la frecuencia Z'=R. Para determinar la resistencia (R) los datos experimentales se ajustan a un circuito equivalente que en esta tesis es un circuito simple formado por una resistencia $R_1$ y un capacitor $C_1$ ya que no se observan fenómenos de interfase electrodo/electrolito. En la figura 3.8 se muestra el esquema del montaje experimental utilizado para medir la resistencia de las muestras en función de la temperatura.

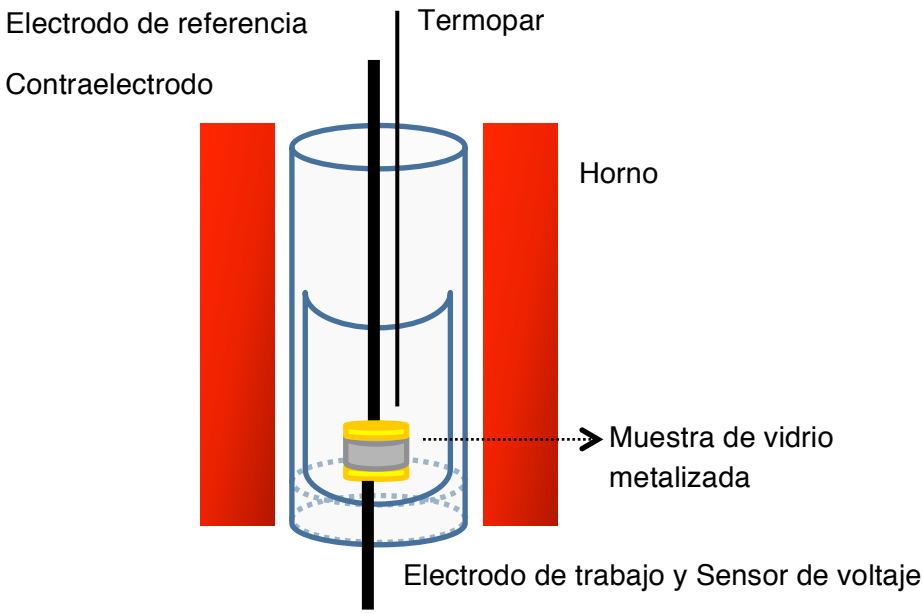

Figura 3.8 Esquema del montaje experimental para medir impedancia con variación de la temperatura.

### 3.3 Caracterización de la estructura:

Uno de los aspectos más complejos de estudio en los vidrios es la caracterización de su estructura. Es de sobra conocida la falta de orden estructural a largo alcance en los vidrios y que conlleva la ausencia de patrones de difracción. Sin embargo, tanto el orden estructural tanto a corto como a medio alcance puede quedar bien definido mediante diferentes técnicas espectroscópicas, como son la Resonancia Magnética Nuclear o las espectroscopias vibracionales Raman y de infrarrojos. Cada una de estas técnicas tiene características específicas que las permite aportar datos complementarios con el objetico de construir una instantánea de la estructura del vidrio. La Resonancia Magnética Nuclear por ejemplo, es muy potente en la determinación de la estructura atómica local y de la conectividad de la red vítrea. Además, esta técnica se puede utilizar para la mayor parte de los núcleos que forman parte de la composición del vidrio y es selectiva del núcleo bajo estudio. De esta forma es posible obtener una imagen real de todos y cada uno de los componentes del vidrio.

#### 3.3.1 Resonancia Magnética Nuclear en solidos con rotación en el ángulo mágico (RMN-MAS[4])

La Resonancia magnética nuclear se fundamenta en las interacciones entre los momentos magnéticos dipolares ($\mu$) de núcleos atómicos cuyo número cuántico de espín sea distinto de cero ($I \neq 0$) y un campo magnético externo ($B_0$).

En presencia del campo $B_0$, el momento magnético dipolar solo puede tomar determinadas orientaciones especificadas por el número cuántico de espín $m_I = I, I-1, \ldots, -I+1, -I$ y que van asociadas cada una de ellas a una energía diferente. Este desdoblamiento de los niveles energéticos por acción de un campo magnético se denomina efecto Zeeman [11].

En el equilibrio térmico, el exceso poblacional se generará en el estado menos energético, que corresponde a la orientación de $\mu$ que se alinea lo más paralelamente a $B_0$, según la ecuación de Boltzmann (3.9), lo que puede traducirse en términos macroscópicos en una magnetización neta $M_0$, que en el estado de equilibrio tendrá la misma dirección y sentido que $B_0$.

[4] El acrónimo proviene de las siglas en inglés Magic-Angle sample Spinning

$$\frac{n_s}{n_i} = \exp\left(-\frac{\Delta E}{kT}\right) \approx 1 - \frac{\Delta E}{kT} \tag{3.9}$$

donde $n_s$ y $n_i$ es el número de núcleos en el estado superior e inferior de energía, respectivamente; ΔE es la diferencia de energía entre ambos estados, k, es la constante de Boltzmann y T es la temperatura absoluta.

Es por lo tanto posible inducir transiciones energéticas entre dos niveles de energía mediante radiación energética de la frecuencia adecuada dada por la ecuación (3.10)

$$\Delta E = \hbar \nu \tag{3.10}$$

donde $\hbar$ es la constante de Planck y $\nu$ es la frecuencia de la radiación utilizada para inducir la transición.

Además de adquirir diferentes orientaciones, los momentos magnéticos nucleares sufren adicionalmente un par de fuerzas que les obliga a girar alrededor de $B_0$ con una velocidad angular $\omega_0$ y una frecuencia $\nu_0$ (frecuencia de precesión de Larmor) directamente proporcional a $B_0$, donde $\gamma$ es la constante giromagnética característica de cada núcleo (ecuación 3.11). Este movimiento se denomina de precesión de Larmor.

$$\nu_0 = \frac{\gamma}{2\pi} B_0 \tag{3.11}$$

La aplicación de una radiación electromagnética con objeto de producir transiciones permitidas entre los distintos niveles de energía adyacentes genera una perturbación en $M_0$ desviándola de su posición de equilibrio.

La transición se producirá cuando la frecuencia de la radiación empleada para perturbar el equilibrio sea igual a la del movimiento de precesión del núcleo en estudio, es decir, cuando la radiofrecuencia y la frecuencia de precesión estén en resonancia.

En la práctica, la muestra es sometida a pulsos de radiofrecuencia durante intervalos de tiempo controlado que desalinean $M_0$ de $B_0$ un ángulo de 90º o de 180º denominados respectivamente pulsos de 90º o 180º de irradiación de la muestra. El resultado final de la aplicación del pulso es generar una magnetización transversal para obtener la señal de RMN.

La técnica de resonancia magnética nuclear permite no sólo diferenciar entre señales producidas por diferentes núcleos sino también, y más importante, distinguir un núcleo

particular con respecto a su entorno químico. Este entorno químico viene determinado por la diferente distribución de electrones y enlaces químicos que rodean al núcleo, de forma que el campo efectivo local al que se ve sometido el núcleo es diferente del campo externo aplicado (ecuación (3.12))

$$B_{efectivo} = B_0(1-\sigma) \tag{3.12}$$

donde σ es la constante de apantallamiento característica del núcleo debido a su entorno químico particular. El resultado es una frecuencia de resonancia diferente para cada tipo de núcleo o desplazamiento químico δ calculado en partes por millón (ppm) siguiendo la ecuación (3.13).

$$\delta(ppm) = \frac{\nu - \nu_{ref}}{\nu_{ref}} 10^6 \tag{3.13}$$

siendo $\nu$ y $\nu_{ref}$ las frecuencias de resonancia del núcleo y de la referencia frente a la que se realiza el experimento, respectivamente.

Posteriormente, los procesos de relajación, conducen a la restauración de las poblaciones del equilibrio, distinguiéndose dos tiempos de relajación: tiempo de relajación longitudinal o espín-red ($T_1$) y tiempo de relajación transversal o spin-spin ($T_2$). El primero implica procesos donde se produce intercambio de energía entre el sistema de spin y la red, y mide la velocidad a la que $M_0$ se aproxima al valor en el equilibrio. Mientras que el segundo mide la velocidad a la que la magnetización en el plano perpendicular a $B_0$ se aproxima al equilibrio. De forma que lo que se mide es el denominado decaimiento libre inducido o FID de la que se obtienen los espectros al aplicar la transformada de Fourier (FT).

Además de las interacciones Zeeman resultantes al aplicar $B_0$ y el desplazamiento químico, existen una serie de interacciones internas, cuyos parámetros reflejan los detalles de la estructura local del entorno. En estado sólido, estas interacciones son todas anisótropas y causan el ensanchamiento de las señales. Estas son:

- Apantallamiento químico o magnético: se trata de las interacciones magnéticas del núcleo con los electrones vecinos. Al aplicar el fuerte campo magnético externo ($B_0$), se inducen corrientes electrónicas que producen un campo magnético inducido $B'$ proporcional a $B_0$ y diamagnético normalmente, que modifica el campo magnético local ($B_{loc}$) y por tanto sus frecuencias de precesión, provocando la anisotropía de los desplazamientos químicos (δ) respecto de la referencia.

- Interacciones magnéticas dipolo-dipolo entre espines nucleares (acoplamiento dipolar) que a su vez se dividen en directas, aquellas que sólo reflejan la proximidad espacial, e indirectas, donde el acoplamiento es transmitido a través de la polarización de electrones enlazantes.
- Interacciones cuadrupolares: se dan entre los momentos electrónicos cuadrupolares de espín de los núcleos mayores de ½ y el gradiente de campo electrostático que rodea a dichos núcleos.

En los líquidos, los movimientos moleculares son suficientemente rápidos como para promediar las interacciones anisótropas internas y los espectros de RMN muestran bandas de resonancia estrechas. Sin embargo, en un sólido estas interacciones anisótropas no son promediadas por el movimiento y la parte espacial de estas interacciones depende de todas las orientaciones presentes, dando lugar a espectros cuyas líneas resultas de la superposición de todas las contribuciones posibles, dando lugar a un fuerte ensanchamiento de las bandas de resonancia que hacen que los espectros sean difícilmente resolubles.

El espectro de RMN de las especies nucleares en estado sólido está influenciado por todas estas interacciones simultáneamente. Sin embargo, aplicando ciertas técnicas de promedio selectivas es posible eliminar algunas de ellas.

La técnica de rotación en el ángulo mágico permite eliminar las interacciones anisótropas de primer orden (acoplamiento dipolar y la anisotropía del desplazamiento químico) ya que la parte espacial del Hamiltoniano pasa a ser independiente del tiempo. La denominación de ángulo mágico, se debe a la importante reducción del ancho de pico en el espectro de RMN, comparable a la observada para muestras líquidas ya que produce un efecto análogo a la rotación molecular rápida y al azar que tiene lugar en una muestra líquida.

Durante la adquisición del espectro la muestra es introducida en un rotor y es girada sobre un eje con una inclinación θ de 54.74º respecto del campo magnético externo que hace cero el factor ($3\cos^2\theta - 1$) que representa las interacciones dipolares. Si la velocidad de giro es suficientemente rápida, permite además reducir el ensanchamiento de las bandas al intervenir solamente la componente isótropa, dando lugar a bandas estrechas centradas en las posiciones de desplazamiento químico isótropo.

Para eliminar las interacciones de segundo orden como el acoplamiento cuadrupolar ($I > 1/2$) sería necesario aplicar otras técnicas mono- o bidimensionales más complejas.

### 3.3.2 Espectroscopia Raman

La espectroscopia Raman se ha utilizado para estudiar el orden estructural a corto y medio alcance. La mayoría de los fotones de un haz de luz que incide sobre una molécula son dispersados elásticamente. Los fotones dispersados tienen la misma energía (frecuencia) y por tanto número de onda que los fotones de la radiación incidente, esta dispersión se denomina Rayleigh y no da información estructural. Sin embargo, una pequeña fracción de luz (aproximadamente 1 de $10^7$ fotones) es dispersada a frecuencias mayores o menores a la frecuencia de los fotones incidentes. El proceso que da lugar a esta dispersión inelástica se denomina efecto Raman. La espectroscopia Raman se basa en la excitación de los modos vibracionales y rotaciones de los grupos de átomos enlazados entre sí y que forman la estructura del material. Para asegurar un mayor número de fotones dispersados, se utiliza radiación láser.

### 3.4 Referencias:

[1] R.V. Adams, Phys.Chem. Glasses 2 (1961) 39

[2] H. Toratani, H. E. Meissner, T. Izumitani and S. E. Stokowoski, J. Non-Cryst. Solids 95&96 (1987) 701.

[3] J. M. Fdez. Navarro, El Vidrio, Consejo Superior de Investigaciones Científicas; Madrid (2003)

[4] M. I. Ojovan, *Phys. Chem. Glasses: Eur. J. Glass Sci. Technol. B*, 53 (4) (2012) 143–150

[5] L.D. Landau, E.M. Lifshitz, Fluid Mechanics, Vol.6 Butterworth-Heinemann, 2nd ed. , Oxford, 1987

[6] C. Kittel, Introduction to solid state physics, J. Wiley and Sons Inc., Bew York, 1996.

[7] A. R. West, Basic solid state chemistry, J. Wiley and Sons Ltd., Chichester, 1999.

[8] A. K. Varshneya, Fundamentals of inorganic glasses, Society of Glass Technology, Sheffield, 682p., 2006.

[9] J. Zarzycki, Glasses and the vitreous state, Cambridge University Press, New York, 1982.

[10] J. R. Macdonald, Impedance Spectroscopy, 2005.

[11] I.N. Levine, Química Cuántica. Ed. AC, Madrid 1977.

# Chapter IV

# Behaviour of viscosity in a series of binary and ternary phosphate glass systems

## Chapter IV: Behaviour of viscosity in a series of binary and ternary phosphate glass systems

In the last years, the study of the kinetic fragility and its relationship with the glass structure in binary and mixed glass former phosphate glasses with potential applications [1, 2] is getting a renewed interest, fostered in part because of the topological constraint theory [3-5]. However, even though much progress has been achieved in this respect [6, 7], there is still a lack of experimental data, which can support the existing theories.

In order to get more insights into the compositional and structural influence on transport properties in pure phosphate glasses, different glass systems have been prepared to determine the role played by the different modifying oxides and by the proportion of $P_2O_5$ present in the glass. The ionic conductivity (σ) and viscosity have been studied and related with the short and medium range order structure by means of Nuclear Magnetic Resonance and Raman spectroscopies. The kinetic fragility (m) of each glass has been determined by fitting the viscosity experimental data to Vogel-Fulcher-Tamman (VFT), Avramov-Milchev (AM) and Mauro-Yue-Ellison-Gupta-Allan (MYEGA) equations. Finally, the activation energy of viscous flow, and its correlation with composition and structure, has been followed through Doremus ratio.

This chapter is going to be divided into three sections (4.3, 4.4 and 4.5), each of them devoted to every glass compositional system studied.

### 4.1. Materials and methods

#### 4.1.1 Glass melting

A series of phosphate glasses with the following compositions were prepared by conventional melt-quenching procedure:

- Alkali, alkaline earth and zinc metaphosphate glasses with compositions $50MO.50P_2O_5$ (M=Mg,Ca,Sr,Ba,Zn) and $50M'_2O.50P_2O_5$ (M'=Li,Na)
- Lithium and sodium zinc metaphosphate glasses with compositions $xLi_2O.(50-x)ZnO.50P_2O_5$ and $xNa_2O.(50-x)ZnO.50P_2O_5$ (x=0-50)
- Lithium zinc phosphate glasses with compositions $x/2Li_2O.x/2ZnO.(100-x)P_2O_5$ (x=30-60)

Reagent grade raw materials analytically pure $Na_2CO_3$, MgO, $CaCO_3$ and ZnO (Panreac); $SrCO_3$ and $BaCO_3$ (Alfa Aesar); $(NH_4)_2HPO_4$ and $Li_2CO_3$ (Sharlau, ACS), were mixed and the

batches were calcined in porcelain crucibles up to 450ºC, in an electric furnace, and then melted during 2 h at temperatures ranging from 900ºC to 1200ºC depending on composition.

The melts were poured onto brass moulds and annealed slightly above their glass transition temperature after determination of their $T_g$ by DTA. Since the experimental data may critically depend on the exact composition and thermal history of the samples, all measurements have been performed on samples from the same batch.

### 4.1.2 Structural characterization

#### 4.1.2.1 Magic Angle Spinning Nuclear Magnetic Resonance spectroscopy (MAS-NMR)

Magic Angle Spinning (MAS) $^{31}P$ Nuclear Magnetic Resonance (NMR) spectra were recorded on a *Bruker ASX 400* spectrometer operating at 161.96 MHz (9.4T). The pulse length was 2.5 µs and 60 s delay time was used. A total number of 128 scans were accumulated with a spinning rate of 10 kHz. MAS NMR spectra were fitted to Gaussian functions, in accordance with the chemical shift distribution of the amorphous state. Solid $(NH_4)$ $H_2PO_4$ was used as secondary reference with a chemical shift of 0.82 ppm with respect to $H_3PO_4$ (85%). The error in the determination of the chemical shift is taken as ± 1 ppm.

$^{7}Li$ MAS NMR was performed on a Bruker ASX 400 spectrometer operating at 155.51 MHz (9.4 T). The pulse length was 2 µs and 2 s delay time was used. A total number of 256 scans were accumulated under a spinning rate of 10 kHz. Solid LiCl was used as secondary reference with chemical shift of 1.06 with respect to LiCl 1 M solution.

The high-temperature in situ $^{31}P$ MAS NMR experiments were performed employing a Bruker LASER MAS probe at 7.04 T ($\nu_0$=121.53 MHz) and a Bruker Avance III console. Magic Angle Spinning was applied at frequencies of 4-4.5 kHz using dry $N_2$ for sample spinning. The sample is contained in an AlN container placed in a LASER MAS 7 mm spinner. The magic angle proved to be stable over the entire experimental temperature range employed in this study, from room temperature to 600 ºC. The radiofrequency (rf) used was 50 kHz, corresponding to a π/2-pulse length of 5 µs. Repetition times of 5 s to 1000 s, depending on the sample and temperature, were employed.

The radiofrequency field (rf) strength used was 50 kHz, corresponding to a π/2-pulse length of 5 µs. Repetition times of 5 s to 1000 s, depending on the sample and temperature employed. The $^{31}P$ chemical shift is referenced to 85% $H_3PO_4$.

#### 4.1.2.2 Raman Spectroscopy

Raman spectroscopy analyses were performed on a *WItec Alpha300RA* Raman-AFM confocal spectrometer with 532 nm laser wavelength excitation and 39 mW power in the range of 220-3800 $cm^{-1}$. The laser polarization angle was in x axis. Polished glass samples around 2 mm thick were used. The precision in the determination of the Raman shifts is ± 1 $cm^{-1}$. The spectra were fitted using Origin Pro software and residual after first derivative was settled as method for finding hidden peaks. The tolerance was fixed to $10^{-15}$ and the number of iterations to the maximum allowed by the software. The tolerance criterion was satisfied in all cases and the number of iterations needed to get the lowest reduced chi-square value was always less than the maximum fixed. The regression coefficient of the fits ($R^2$) was 0.9997 or better for all the spectra. The standard errors of the Gaussian bands positions attributed to chains and rings are of the size of the points.

### 4.1.3 Properties characterization

Glass transition temperature ($T_g$) was determined from the thermal expansion curves of the glasses obtained in air with a *Netzsch Gerätebau* dilatometer, *model 402 PC/1* at a heating rate of 2 $K.min^{-1}$. Prismatic samples around 10 mm in length were used for the measurements. The estimated error in $T_g$ is ± 1K.

The density of the glasses was measured by helium pycnometry in a *Quantachrome Corp*. multipycnometer on bulk samples (±0.01$g.cm^{-3}$). The molar volume ($V_m$) was calculated from the relation between the molar mass (M) and the density ($\rho$) of the glass ($V_m$=M. $\rho^{-1}$).

Fourier Transformed Infrared (FT-IR) spectroscopy was performed on mirror-like polished glass samples around 2 mm in thickness in a *PerkinElmer Spectrum 100* spectrometer operating in the transmission mode within the wave number range of 950 to 5500 $cm^{-1}$. The water content of the metaphosphate glasses can be expressed in terms of the OH absorption coefficient ($r_{OH}$) that determines the relative concentration of OH in the glasses as described in Chapter III of this thesis.

The viscosity-temperature curves of the glasses were determined using the rotation and beam-bending methods at high and low temperature ranges, respectively. The viscosity of the melts in the range $10^3$–$10^1$ dPa.s was determined employing a high-temperature Haake viscometer of the cylindrical Searle type (*Haake, Karlsruhe, Germany*) equipped with a ME

1700 sensor. Rotation speeds of 3 to 15 rpm were used for 15 min, following the International Standard ISO 7884-2.

Within the viscosity range $10^{12.5}$–$10^{9}$ dPa.s viscosity was measured by bending glass beams heated at 2K.min$^{-1}$ and using weights of 10 to 200 g. A viscometer *VIS401 (Bähr Thermoanalyse, Germany*) with a 40 mm open span in symmetric three point mode was employed. The viscosity was calculated according to the standard testing conditions DIN ISO 7884-4. For further details about the experimental procedure followed to determine the viscosity, the reader is referred to the Chapter III of this thesis.

The shear viscosity has been also derived from creep testing in compression mode using dedicated in-house facility of *Mechanics and Glass* research group in Université de Rennes 1 (France). Constant temperature tests were carried out applying a constant load at a particular temperature. The specimen and the set-up were kept at each testing temperature until a thermal equilibrium was achieved. The error on the temperature registered by the thermocouple situated at the glass sample is considered to be ± 3ºC. Parallel plane prismatic samples around 7mm length and ca. 20 mm$^2$ base area were employed. In creep experiments, the viscosity is calculated from the strain-rate (dε/dt) associated with the stationary creep regime, following the standard viscosity relationship (Equation (4.1))

$$\eta = \frac{\sigma}{\left[2\left(1+\nu\right)\frac{d\varepsilon}{dt}\right]} \tag{4.1}$$

where σ is the normal stress and v is Poisson's ratio.

Under the assumption of an isochoric flow, the former equation reduces to the classical Trouton's law:

$$\eta = \frac{\sigma}{3\frac{d\varepsilon}{dt}} = \frac{\sigma}{3\dot{\varepsilon}} \tag{4.2}$$

When high deformations occur (ε > 10%), as it is the case, a magnitude called true strain ($\varepsilon_t$) should be employed. A solid with a high h, which varies (dh) under compression conditions and leads to deformation in a time dt is considered. $\varepsilon_t$ is then obtained from its integration:

$$d\varepsilon_t = -\frac{dh}{h}; \varepsilon_t = \ln\left(\frac{h_0}{h}\right) \tag{4.3}$$

where $h_0$ is the high of the sample at a stable temperature and h= $h_0$-ε

The expression for σ depends on the loading configuration. For a compressive experiment, as this case, σ=P/S where P is the axial force and S the cross section area. During a real test, samples do not deform uniformly and sample cross section varies with deformation. Variations on the sample's shape such as cracks and those caused by the resulting friction between the compressed faces of the sample and the creep machine pistons make the sample to get a "barrel shape". Thus, as the strain, the normal stress ($\sigma$) has been corrected with the instantaneous section of the sample (S') and a new magnitude called true stress ($\sigma_t$) is defined to describe the real process. To simplify, a constant volume deformation and no friction conditions are assumed. Thus a straight prism sample that keeps its shape under deformation is considered. The creep equipment works with a dead load, therefore the default load ($P_0$) has to be subtracted to the measured load (P). These approximations lead to equation (4.4):

$$\sigma' = \frac{P'}{S'} = \frac{P - P_0}{S'} \tag{4.4}$$

Electrical conductivity of the glasses was calculated through the determination of the bulk resistance by Electrochemical Impedance Spectroscopy in a VMP3 potentiostat from BioLogic, within the frequency range of 10 Hz to 1 MHz and between room temperature to the glass transition of the glasses. For the measurements, gold electrodes were deposited onto both faces of ca. 10 $mm^2$ square samples of 1-2 mm in thickness (e). The resistance of the sample (R) is read in the Nyquist plot of the complex *versus* real impedance at the intersection point with the horizontal axis. The conductivity ($\sigma$) is calculated through the sample geometric factor ($e \cdot A^{-1}$), where A is sample area, following the equation $\sigma = e \cdot (R \cdot A)^{-1}$.

## 4.2 Alkali, alkaline-earth and zinc metaphosphate glasses

Alkali, alkaline-earth and zinc metaphosphate glasses were the systems selected to study the effect of the modifying cations on a phosphate glass network mainly formed by $Q^2$ units and thus with the same connectivity degree. Additional viscosity data have been obtained for these glasses along and above the glass transition range on a controlled-stress rheometer through creep testing technique.

### 4.2.1 Structural characterization

#### 4.2.1.1 $^{31}$P MAS NMR spectroscopy

The different $Q^i$ tetrahedra shows isotropic $^{31}P$ chemical shift peaks in MAS NMR spectra. The resonance due to $Q^3$ groups appears at about -51 ppm, $Q^2$ tetrahedra usually at -22ppm, while signals due to $Q^1$ and $Q^0$ units appear at -10 ppm and 0 ppm, respectively.

Figure 4.1 shows the $^{31}P$ MAS NMR spectra of the metaphosphate glasses.

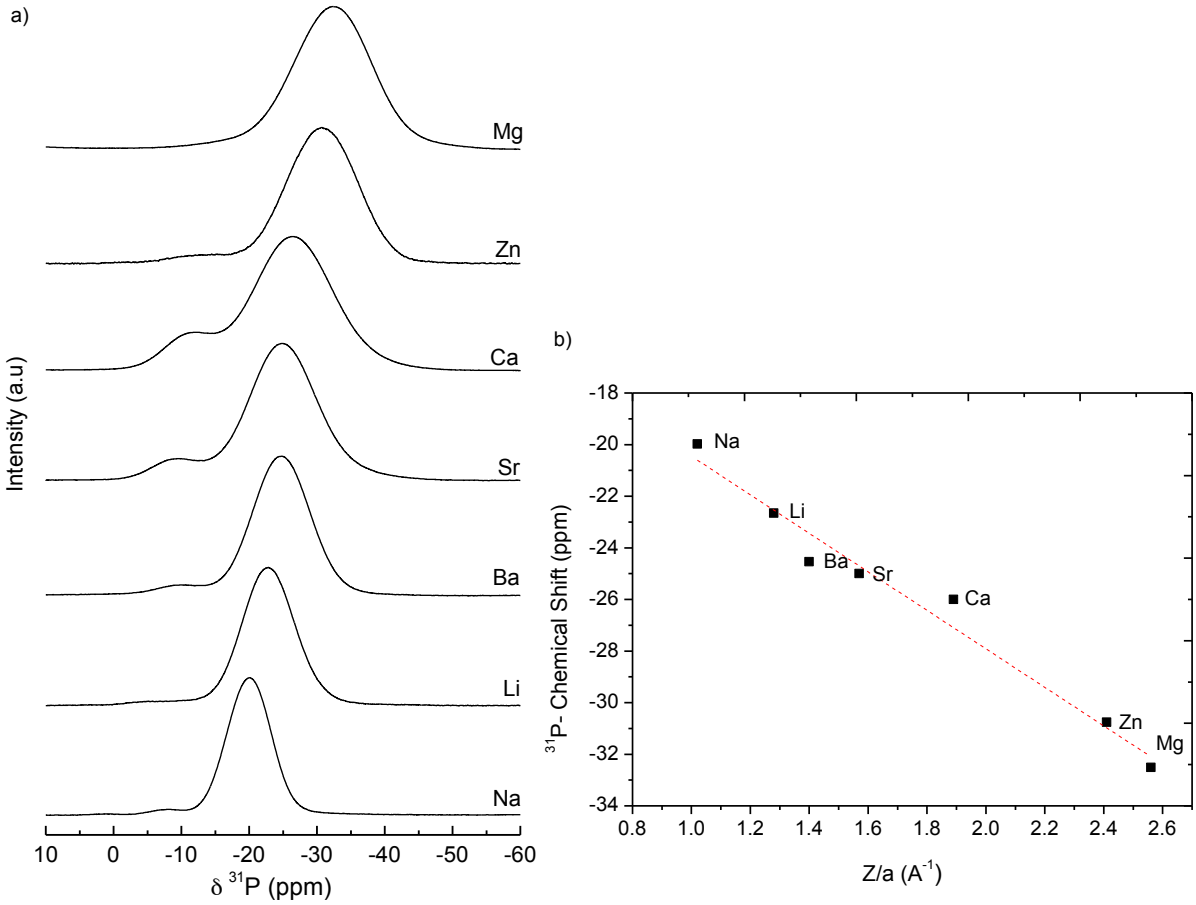


Figure 4.1: a) Isotropic signal of $^{31}P$ MAS NMR spectra of $50MO.50P_2O_5$ (M=Mg,Ca,Sr,Ba,Zn) and $50M'_2O.50P_2O_5$ (M'=Li,Na) glasses. b) $^{31}P$-NMR chemical shifts of the glasses as a function of cationic potential (Z/a). Dotted line is the linear fit with a regression coefficient ($R^2$) of 0.97.

It can be observed that the main resonance corresponds to $Q^2$ tetrahedra at about -20 ppm, which shifts high-field with the cationic potential of the modifier. There is also a small amount of $Q^1$ groups due to a non-stoichiometric composition, probably as a result of some phosphorous volatilization because of the higher temperatures employed during alkaline-earth glass melting. These units are present in the glass as terminal and pyrophosphate groups.

From the integration of $^{31}P$-NMR peaks using dmfit [8], the fraction of $Q^i$ tetrahedra [9] can be determined and the glass composition derived using equation (2.2) replicated here for convenience.

$$f(Q^2) = \frac{2-3x}{1-x} \qquad (2.2)$$

The highest deviation from the nominal composition corresponds to $Ba(PO_3)_2$, $Ca(PO_3)_2$, and $Mg(PO_3)_2$ with 47 mol % of $P_2O_5$, while $LiPO_3$ and $Zn(PO_3)_2$ present 49 mol% of $P_2O_5$; and 48 and 50 mol% for $Sr(PO_3)_2$ and $NaPO_3$, respectively. Since the difference in the $P_2O_5$ molar fraction indirectly determined through $^{31}P$ NMR decomposition is not greater than 3 mol % with respect to the nominal composition, it can be assumed that there should not be a relevant influence on the glass properties. Due to the hygroscopic character of phosphate glasses and in order to determine if the proportion of $Q^1$ is due to the presence of water in the glass composition, the water content has been determined by FTIR spectroscopy as described above. The water concentration is lower than $2.10^{-2}$ wt. % ± $5.10^{-3}$ for all glasses, thus it is consider that this water is present on the glass surface as a consequence of the unavoidable exposure to moisture during glasses manipulation.

Structure and properties of metaphosphate glasses will be influenced mainly by composition. We have selected the cationic potential (Z/a) as the parameter employed to show the effect of composition through the modifying cation. (Z/a) reflects the most important characteristics that defines a counterion, the charge (Z), and the ionic radius (a) [10]. Figure 4.1 b) shows the variation of the isotropic $^{31}P$ NMR chemical shift with the cationic potential. It is well known [11] that the peaks shift high-field with Z/a due to the increase on the covalent character of M-O bonds that decreases the electronic density on phosphorous atoms, thus increasing the shielding.

The chemical shift anisotropy ($\delta_{CSA}$), which gives information about the conformation of the $Q^i$ units, was determined using the dmfit software [8]. Larger values of this tensor are found in structures in which there is a prevalence of ring arrangements instead of phosphate chains [12, 13]. Figure 4.2 plots the $\delta_{CSA}$ as function of the modifier´s cationic potential.

The obtained values are in agreement with the ones reported by Brow et al. [11]. The chemical shift anisotropy decreases with cationic potential up to $Ca(PO_3)_2$ composition, thus the higher covalent character of the $M^+O^-$ bond, the higher the proportion of chains in the glass network. This is in accordance with the higher proportion of $Q^1$ groups detected for these compositions as terminal chain units.

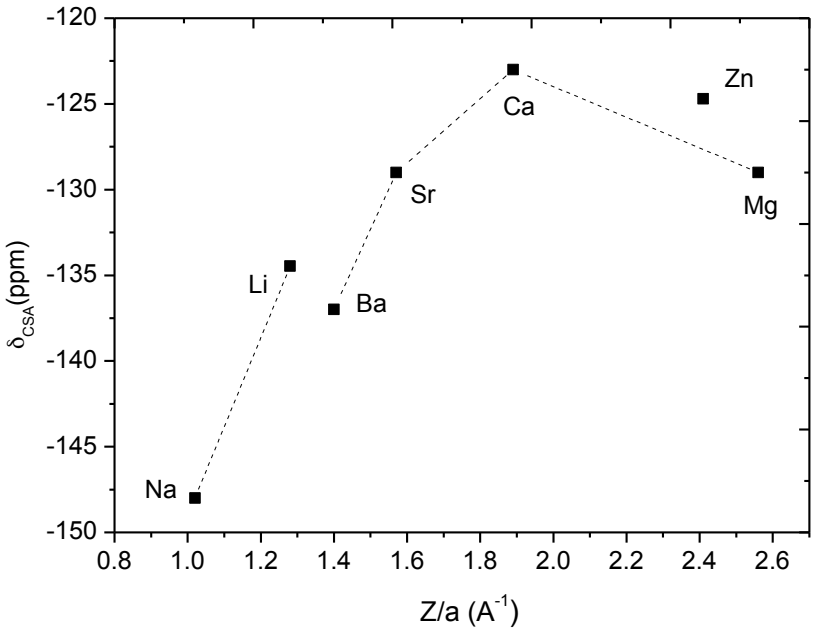


Figure 4.2: Variation of $\delta_{CSA}$ of $50MO.50P_2O_5$ (M=Mg,Ca,Sr,Ba,Zn) and $50M'_2O.50P_2O_5$ (M'=Li,Na) glasses with cationic potential. Dotted lines are drawn as guide for the eyes.

#### 4.2.1.2 Raman spectroscopy

Raman spectroscopy has also been employed to study the short and medium range order structure. Figure 4.3 shows the Raman spectra collected for the metaphosphate series.

All the spectra were normalized to the band with major intensity and decomposed into Gaussian contributions from 600 $cm^{-1}$ to 1400 $cm^{-1}$. The spectra are all dominated by two main bands appearing at about 650-750 $cm^{-1}$ and 1150-1250 $cm^{-1}$ and attributed to the symmetric stretching modes of P-O-P and O-P-O bonds (i.e. bridging and non-bridging oxygens respectively) [14, 15]. The P-O bending mode of $Q^2$ units appears as a broad peak in the range of 200 $cm^{-1}$ to 400 $cm^{-1}$. A smaller band can be observed around 1000 $cm^{-1}$, which is due to the small proportion of $Q^1$ groups present on barium, calcium and strontium metaphosphate glasses. The bands attributed to the corresponding asymmetric stretching modes of the O-P-O and P-O-P bonds in $Q^2$ groups are located around 1280 $cm^{-1}$ and 780 $cm^{-1}$ respectively [14, 15].

It is also possible to study the medium range order structure by means of Raman spectroscopy. In order to obtain the proportion between rings and chains in the glass network the relative intensity was calculated following equation (4.5):

$$I_{relative} = \frac{I_{rings}}{I_{rings} + I_{chains}} \tag{4.5}$$

where $I_{rings}$ and $I_{chains}$ correspond to the intensities of the bands obtained from the deconvolution of the $\nu_s$ $Q^2$ (O-P-O) band into two Gaussians. Each of it is related with the presence of rings and chains in the glass network [16].

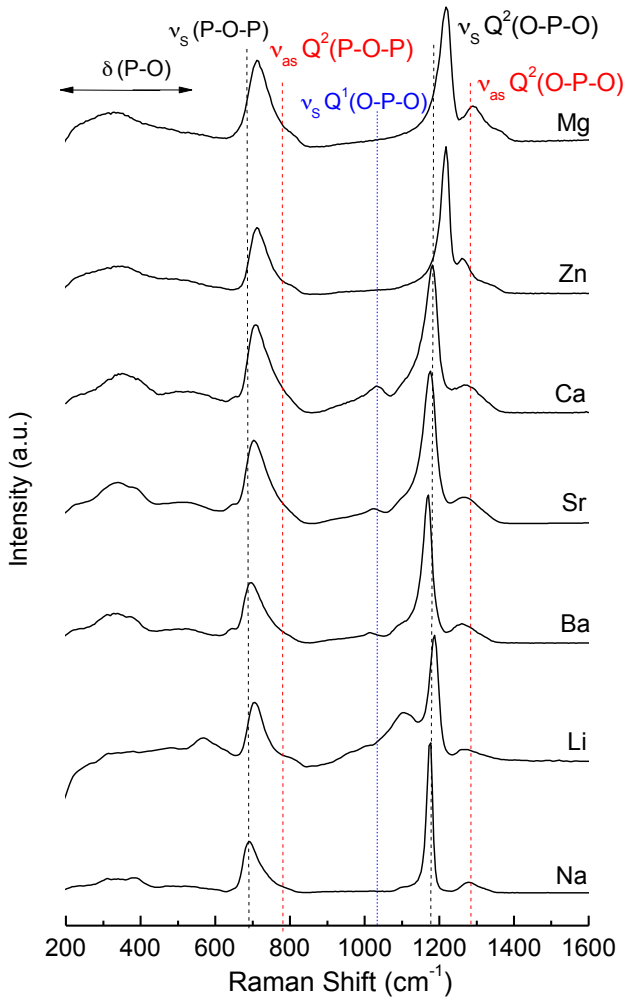


Figure 4.3: Raman spectra of $50MO.50P_2O_5$ (M=Mg,Ca,Sr,Ba,Zn) and $50M'_2O.50P_2O_5$ (M'=Li,Na) glasses. Dotted lines show the bands attributed to bending (δ) and stretching (ν) vibrational modes of P-O bonds.

In Figure 4.4 the relative intensity is plotted as a function of cationic potential.

The inset in Figure 4.4 shows the deconvolution of $\nu_s$ $Q^2$ (O-P-O) band for $Sr(PO_3)_2$ glass as an example. The proportion of chains increases with the modifying ion cationic potential until $Ca(PO_3)_2$ thus corroborating the results from $^{31}P$ MAS NMR.

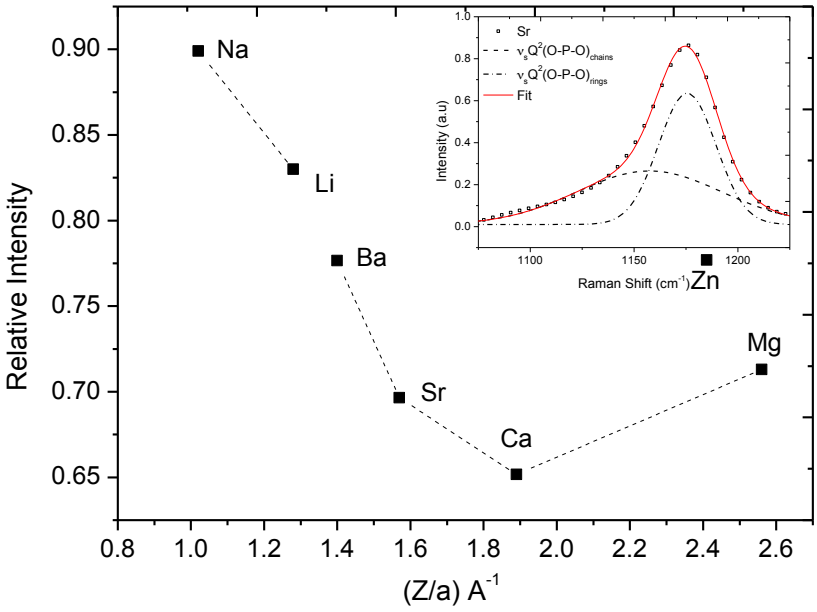


Figure 4.4: Relative intensity of $50MO.50P_2O_5$ (M=Mg,Ca,Sr,Ba,Zn) and $50M'_2O.50P_2O_5$ (M'=Li,Na) glasses as a function of cationic potential. The inset shows the deconvolution of $v_s$ $Q^2$ (O-P-O) band into two Gaussians attribute each of it to the presence of chains and rings arrangements in the glass network. Dotted lines are drawn as guide for the eyes.

Figure 4.5 presents the Raman shifts of the bands attributed to the symmetric stretching modes of P-O-P and O-P-O bonds as a function of the cationic potential.

The peak frequency of O-P-O band shifts to higher values from Na to Li and from Ba to Mg with cationic potential including zinc, while P-O-P Raman shift increases for alkali and decreases for alkaline earth phosphate glasses.

To summarize the results presented in this section, it has been observed by means of NMR and Raman spectroscopies that the atomic structure is influenced by the composition, at both short and medium range orders and, as a consequence, the main glass properties will also be influenced up to some extent by those as it will be discussed in the following section.

The short range order structure is determined through the modifying cation influence directly onto the P-O bonds. The medium range order structure is then subject to the effect of modifier's cationic potential on the organization of the tetrahedral units in rings and chains. Although the results obtained from both spectroscopies do not allow the quantification of the proportion of each arrangement, it seems that the increase on the covalent character of $M^+O^-$ bond increases the proportion of chains arrangements in the glass network.

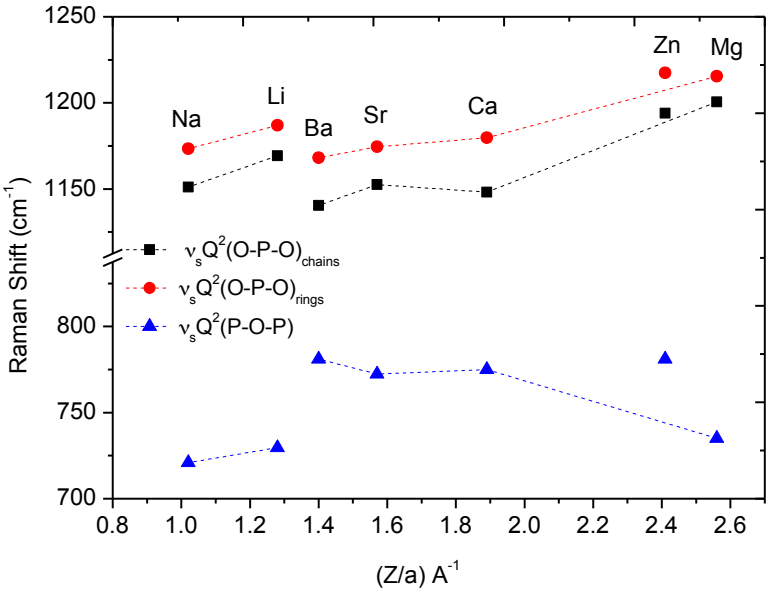


Figure 4.5: Raman shifts of the symmetric bands attributed to $Q^2$ units of $50MO.50P_2O_5$ (M=Mg,Ca,Sr,Ba,Zn) and $50M'_2O.50P_2O_5$ (M'=Li,Na) glasses as function of the cationic potential. Dotted lines are drawn as guides for the eyes.

### 4.2.2 Transport properties

#### 4.2.2.1 Viscosity

As a macroscopic transport property, the viscosity will be affected by the organization of the glass network and how this organization varies with temperature throughout the deformation process that allows the structural arrangements to flow along the whole temperature range.

The viscosity data obtained by beam bending and rotation techniques have been fitted to VFT, AM and MYEGA models (equations (2.3), (2.5) and (2.6)). In order to be able to compare the results obtained through the three models, the adjustable parameters have been expressed in terms of $T_g$, as defined for a shear viscosity equal to $10^{12}$ Pa.s [17, 18], of fragility and of extrapolated infinite temperature viscosity following equations (2.9), (2.10) and (2.11).

The temperature and reduced temperature dependence of experimental viscosity data as well as the best fit to the VFT, AM and MYEGA models are plotted in Figure 4.6.

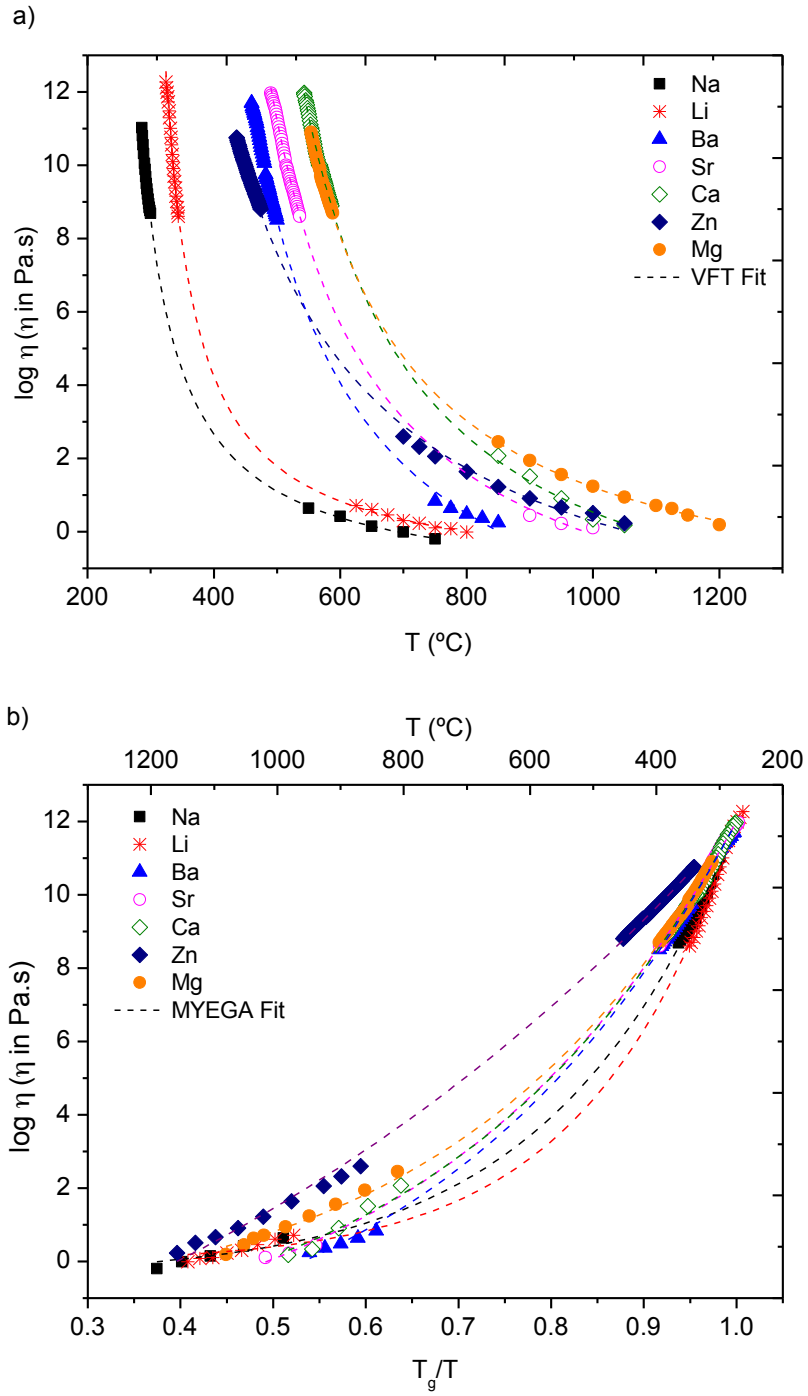


Figure 4.6: a) Temperature dependence of viscosity of $50MO.50P_2O_5$ (M=Mg,Ca,Sr,Ba,Zn) and $50M'_2O.50P_2O_5$ (M'=Li,Na) glasses and best fits (dotted lines) of the experimental values to VFT. b) Viscosity data points and best fits (dotted lines) to MYEGA equation as function of the reduced temperature ($T_g/T$). Error bars are of the size of the points. The regression coefficient ($R^2$) in all fits was of 0.999 or better.

Glass transition temperature measured by dilatometry and $T_g$ values obtained from the best fits to viscosity models are both very similar for all glass compositions as seen in Figure 4.7 a). This correspondence shows a good agreement between the definition of $T_g$ by DSC and the results obtained by dilatometry.

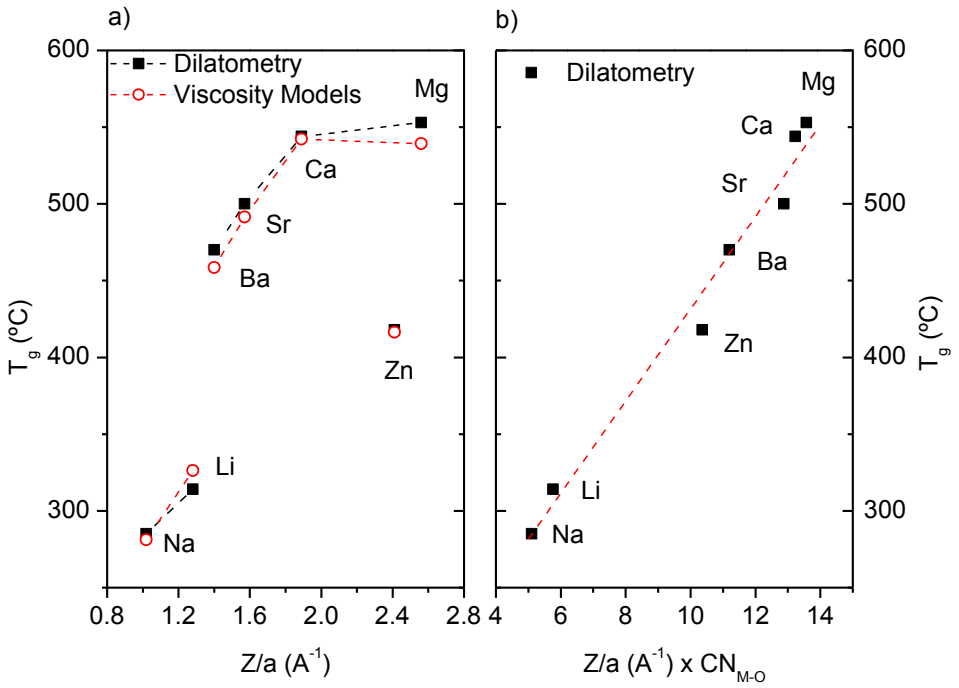


Figure 4.7: a) $T_g$ of $50MO.50P_2O_5$ (M=Mg,Ca,Sr,Ba,Zn) and $50M'_2O.50P_2O_5$ (M'=Li,Na) glasses obtained by dilatometry and by models as function of cationic potential. b) Linear correlation between $T_g$ obtained by dilatometry and the product of cationic potential with coordination number ($CN_{M-O}$). Dotted lines are drawn as guides for the eyes.

Glass transition temperature seems to increase for alkali and alkaline earth phosphate glasses with cationic potential except for $Zn(PO_3)$, which shows a lower value than the one expected attending to its Z/a. Although the variation of $T_g$ with Z/a is not straightforward, a linear correlation was found between $T_g$ and the product of cationic potential and the coordination number of the modifying ion (Z/a x $CN_{M-O}$[5]) as Figure 4.7 b) shows. Thus, the increase of $T_g$ with Z/a x $CN_{M-O}$ seems to be due to the increase of the glass network strength, as a consequence of the increase on the covalence character of $M^+O^-$ bond, and on connectivity as a result of the higher coordination number of the modifying ion.

The average of the kinetic fragility values obtained through the three models for each composition are illustrated as a function of cationic potential in Figure 4.8.

illustrated as a function of cationic potential in Figure 4.8.

[5] Cation coordination numbers: $CN_{Na}$=5, $CN_{Li}$=4-5, $CN_{Ba}$=8, $CN_{Sr}$=8.2, $CN_{Ca}$=7, $CN_{Zn}$=4.3 and $CN_{Mg}$=5.3 [19-22]

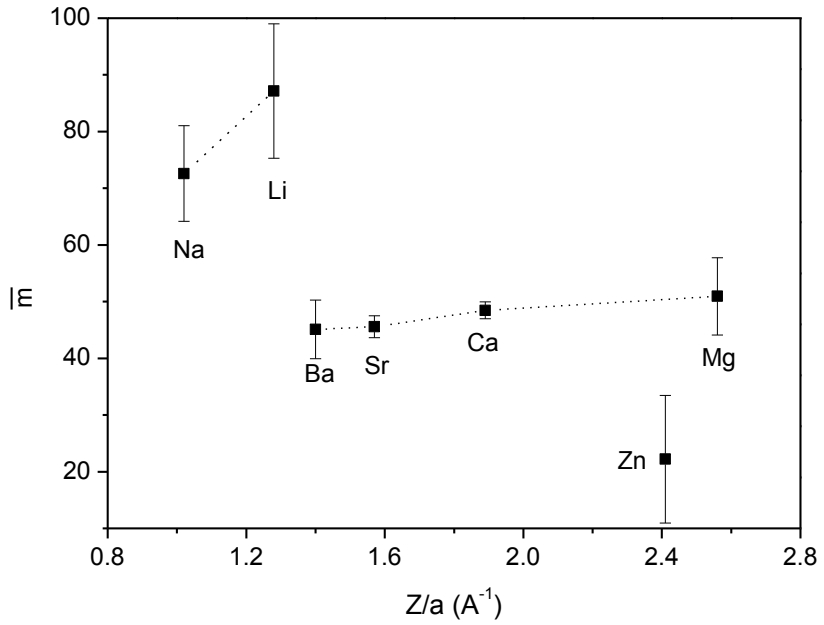


Figure 4.8: Kinetic fragility of $50MO.50P_2O_5$ (M=Mg,Ca,Sr,Ba,Zn) and $50M'_2O.50P_2O_5$ (M'=Li,Na) glasses as function of cationic potential. Dotted lines are drawn as guide for the eyes.

As it can be observed in Table 4.1, where all the values are collected, fragility parameter depends on the model used to determine it. The greater the Z/a, the higher is the kinetic fragility in both, alkali and alkaline-earth metaphosphate series. Zinc metaphosphate glass shows once more the lowest value of the series. $Zn^{2+}$ electronic configuration include completely filled d orbitals ($[Ar]3d^{10}$), the same configuration as the Gallium cation ($Ga^{3+}$). This last element is affected by the so-called d-block contraction, a term used in chemistry to describe the effect of having full d orbitals on the period 4 elements. The cause of the d-block contraction is the poor shielding of the nuclear charge by the electrons in the d orbitals which leads to a more polarizing cation and thus to a higher covalent character of the Zn-O bond than the one reflected attending to its cationic potential. A higher covalent character of the M-O bond would lead to the strengthening of the glass network and thus to lower fragility. However, this assumption could be one of the possible explanations in an attempt to explain the trend observed for fragility.

Table 4.1: Kinetic fragility parameter of $50MO.50P_2O_5$ (M=Mg,Ca,Sr,Ba,Zn) and $50M'_2O.50P_2O_5$ (M'=Li,Na) glasses obtained from VFT, AM and MYEGA models.

| **Glass Composition** | **Glass Code** | **m** | | |
|---|---|---|---|---|
| | | **VFT** | **AM** | **MYEGA** |
| **$NaPO_3$** | Na | 72 | 81 | 65 |
| **$LiPO_3$** | Li | 83 | 101 | 78 |

| | | | | |
|---|---|---|---|---|
| **$Ba(PO_3)_2$** | Ba | 49 | 39 | 48 |
| **$Sr(PO_3)_2$** | Sr | 47 | 44 | 46 |
| **$Ca(PO_3)_2$** | Ca | 49 | 50 | 47 |
| **$Zn(PO_3)_2$** | Zn | 29 | 9 | 29 |
| **$Mg(PO_3)_2$** | Mg | 49 | 59 | 46 |

The Doremus ratio has also been calculated in order to evaluate the fragility using another approach, the ratio between the activation energy of viscous flow at high and low viscosity ranges. The values obtained are plotted in Figure 4.9 as a function of the modifier´s cationic potential.

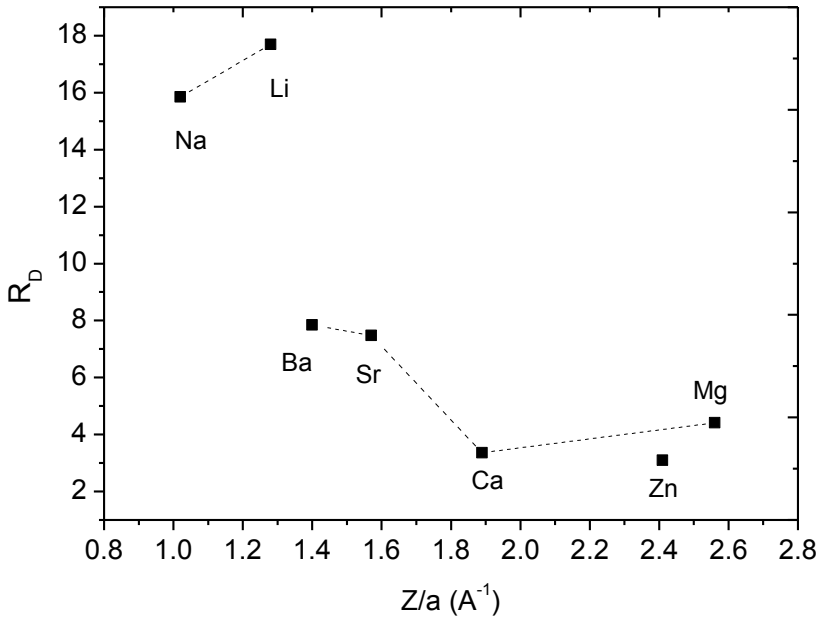


Figure 4.9: Doremus ratio of $50MO.50P_2O_5$ (M=Mg,Ca,Sr,Ba,Zn) and $50M'_2O.50P_2O_5$ (M'=Li,Na) glasses as a function of cationic potential. Dotted lines are drawn as guides for the eyes.

Doremus ratio increases slightly with Z/a for the alkali metaphosphate glasses and decreases for the alkaline earth ones. It can be seen that the bigger the gap between the high and low viscosity activation energies, the greater the Doremus ratio. Zinc metaphosphate glass shows now an $R_D$ value more in accordance with its cationic potential.

In an attempt of going forward into the relationship between medium range order structure and the viscosity of the glasses, the correlation between Doremus ratio and the chemical shift anisotropy as well as the Raman bands intensity attributed to rings has been studied as shown in Figure 4.10 a) and b), respectively.

Even though the number of data points studied in this first case is still small, both plots show the same tendency. Doremus ratio decreases with the increase of the proportion of chains in

the glass network in an approximately linear trend, except for lithium metaphosphate glass that deviates from the general trend. It can be derived from this correlation that the gap between both activation energies will be lower if the proportion of chains in the glass network is higher.

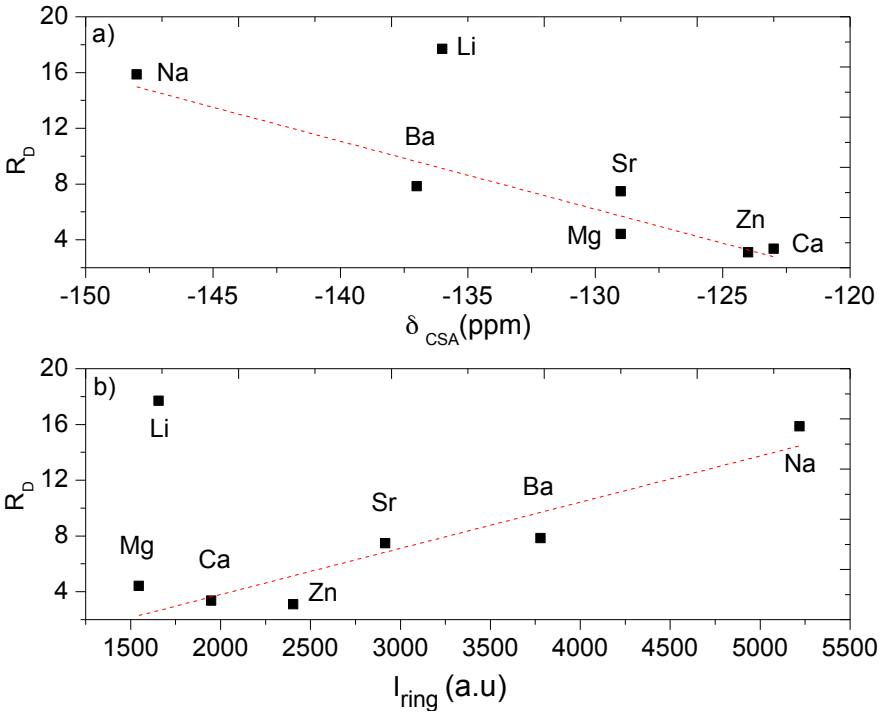


Figure 4.10: Doremus ratio as a function of the chemical shift anisotropy (a) and of the Ramn bans intensities attributed to rings arrangements (b) of 50MO.50$P_2O_5$ (M=Mg,Ca,Sr,Ba,Zn) and 50M'$_2$O.50$P_2O_5$ (M'=Li,Na) glasses. Dotted lines are drawn as guides for the eyes.

The activation energy of viscous flow at low ($E_a^{low\text{-}T}$) and high temperature ($E_a^{high\text{-}T}$) (i.e. high and low viscosity ranges respectively) have been calculated by fitting separately the experimental values in each temperature range to an Arrhenius-type equation. As it can be observed in Figure 4.11, the variation of the activation energy of viscous flow is different in the low and high temperature range with cationic potential. This may imply two different mechanisms controlling the viscous flow through a different evolution of the structure with temperature in each of them. Thus the $E_a$ is going to be influenced not only by composition and structure, but on temperature.

At low temperatures the variation with cationic potential is similar to that observed for the kinetic fragility. It sharply increases for alkali cations, while from Ba to Mg practically does not vary, or the increase is very low. $Zn(PO_3)_2$ composition shows again a lower value than it would be expected according to its cationic potential.

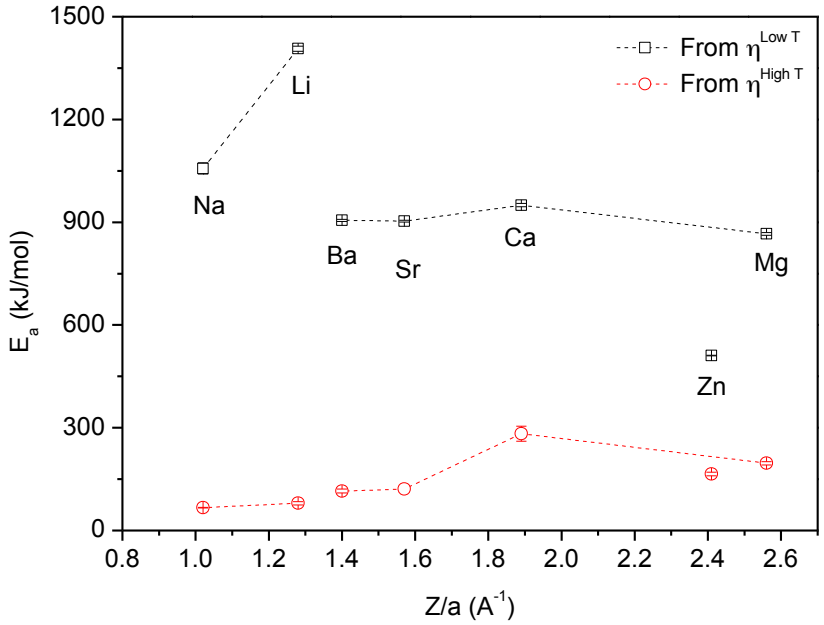


Figure 4.11: Activation energy of viscous flow at low and high temperatures of $50MO.50P_2O_5$ (M=Mg,Ca,Sr,Ba,Zn) and $50M'_2O.50P_2O_5$ (M'=Li,Na) glasses as function of cationic potential. Dotted lines are drawn as guide for the eyes.

In search of further insights to be able to explain the behaviour of $E_a$ $^{low\text{-}T}$, we have interpreted it in terms of molar volume and the average single bond strength (B) for each binary glass.

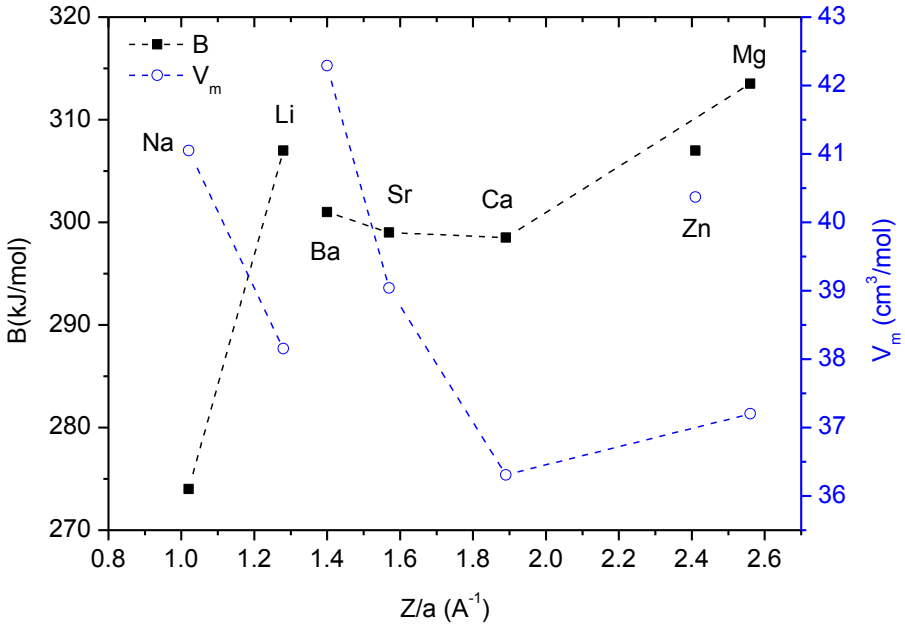


Figure 4.12: Molar volume and average single bond strength in the glass network of $50MO.50\ P_2O_5$ (M=Mg,Ca,Sr,Ba,Zn) and $50M'_2O.50P_2O_5$ (M'=Li,Na) glasses as function of cationic potential. Dotted lines are drawn as guide for the eyes.

It is expressed by the following equation according with the approach proposed in [23], where $B_{M-O}$ is the corresponding single bond strength in each oxide and $n_i$ is the molar fraction:

$$B = \sum\left(n_i B_{M-O}\right) \tag{4.6}$$

It can be observed that the activation energy of viscous flow increases with the decrease of the molar volume and with the rise of average single bond strength in the glass network. In order to see more clearly the effect of both intrinsic properties on the activation energy the variation of the ratio between bond strength and molar volume ($B/V_m$) has been calculated and represented together with the $E_a^{low\text{-}T}$ in Figure 4.13.

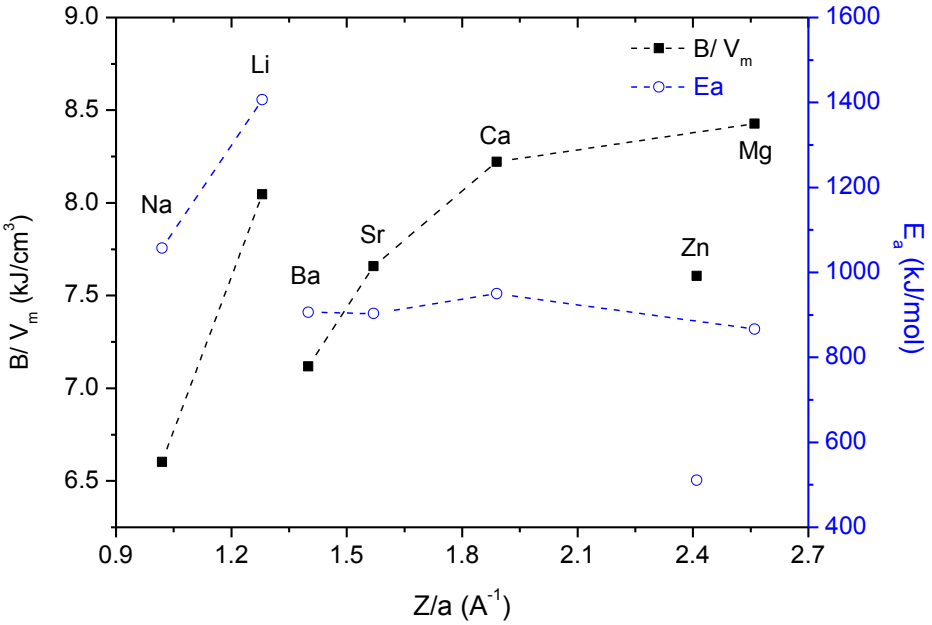


Figure 4.13: Variation of the ratio between single bond strength ($B_{M-O}$) and molar volume ($V_m$), and activation energy of viscous flow at low temperature ($E_a^{low\text{-}T}$) with cationic potential of $50MO.50P_2O_5$ (M=Mg,Ca,Sr,Ba,Zn) and $50M'_2O.50P_2O_5$ (M'=Li,Na) glasses. Dotted lines are drawn as guide for the eyes.

The higher the ratio between bond strength and molar volume, the higher is the activation energy. It can be seen that $E_a^{low\text{-}T}$ and $B/V_m$ behave in a very similar way. However, the variation between barium and magnesium glasses is less pronounced compared with $B/V_m$ ratio, which could necessitate of additional factors like the medium range order in the glass network. As seen through the analysis of the chemical shift anisotropy and the Raman spectra deconvolution, there would be a pronounced increase of the proportion of chains against that of rings from the sodium to the calcium metaphosphate glasses. A higher proportion of chains together with higher molar volume can be related to lower activation

energies due to an easier flow of these arrangements through the glass network as a response to the deformation applied. Zinc metaphosphate glass takes the lowest value for both the $E_a^{low\text{-}T}$ and $B/V_m$ ratio, thus showing the strong influence of this last parameter on the activation energy. As seen in Figure 4.12 $Zn(PO_3)_2$ glass presents a high $V_m$ compared with the alkaline earth metaphosphate glasses but a B value similar to $LiPO_3$ glass. However, $E_a^{low\text{-}T}$ presents a minima for $Zn(PO_3)_2$ glass, thus the $V_m$ seems to be the driving factor on $E_a^{low\text{-}T}$ behaviour. A higher molar volume may facilitate the flow of the structural units through a more open glass network that would lead in turn to minima on the activation energies for viscous flow (c.f. Figure 4.11).

On the contrary, at high temperature the activation energy in general increases with the increased covalent character of the $M^+O^-$ bonds. Thus, it seems that the medium range order structure as well as the ratio between bond strength and molar volume do not influence on the activation energy at high temperature in the same degree as they do on $E_a^{low\text{-}T}$. The more or less linear increase of activation energy, except with a small decrease observed for magnesium and zinc glasses, seems to be dominated through the cationic potential of the modifier.

Additional experimental viscosity data has been obtained from 0.9 to 1.1 $T_g$ through creep measurements for Li, Sr, Ca, Mg and Zn metaphosphate glasses. This viscosity range include values that are not possible to arise with beam bending measurements and also values already determined by this technique in order to compare both experimental methods. In general, creep denotes the evolution undergone by the geometry of a body (i.e. irreversible deformation) over a length of time, under the effect of stresses. It is a thermally activated process, that is, it is faster with higher temperatures. Thus, it is known as a time dependent, thermally assisted plastic deformation under constant load (stress) [24].

The speed of deformation or creep rate ($\dot{\varepsilon}$) increases quickly when the temperature approaches the softening temperature of the glass. Typically, while studying creep, the progressive curve of deformation against time presents successively three regions of creep. First is the primary creep stage, were dε/dt decreases with time, followed by secondary creep regime (or stationary) at constant dε/dt. Although several mechanisms are proposed for this stage, overall four categories can be defined: diffusion, viscous, grain boundary and dislocation related creep [25]. For amorphous materials, as our case, the only mechanism is viscous creep. Finally, the tertiary creep regime is characterized by a rapid increase in dε/dt. In the first stage, an instantaneous elastic and plastic strain occurs as the load is applied followed by the plastic strain in which the creep resistance increases with strain leading to a

decreasing creep strain rate. The anelasticity (also called delayed elasticity) is responsible for this primary stage of creep (transitory viscoelastic behaviour) which precedes the stationary yield. The anelasticity manifests itself by a delayed response to stress: the return to non-deformed state on load removal may necessitate an infinite time. As a first approximation, the anelasticity can be described with the help of linear viscoelastic models. The secondary stage is known as the steady-state creep with the strain increasing linearly with time. The tertiary stage reflects the rapid progress of the accumulating damage and thus occurs before failure, with rather fast increasing strain stress [26] (cf. Figure 4.14).

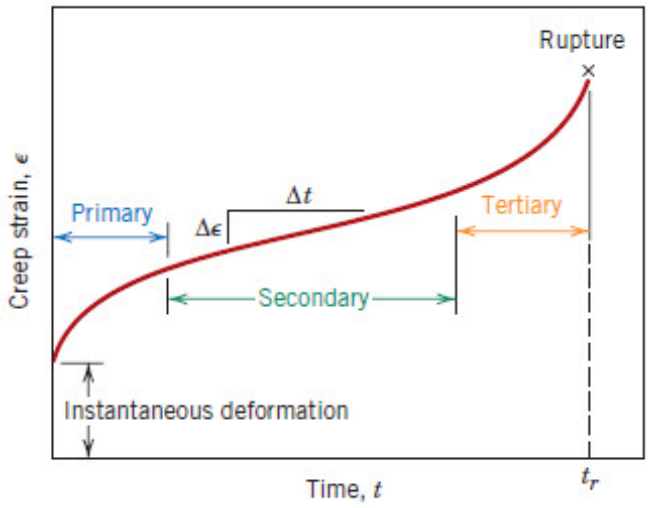


Figure 4.14: Typical creep strain versus time curve

At relatively high temperatures, considering the flow behaviour of the glass materials, the viscosity should decrease and viscous flow can lead to creep.

In Figure 4.15 the recorded deformation (ε) and the true strain ($\varepsilon_t$) of $(MgPO_3)_2$ has been plotted as an example.

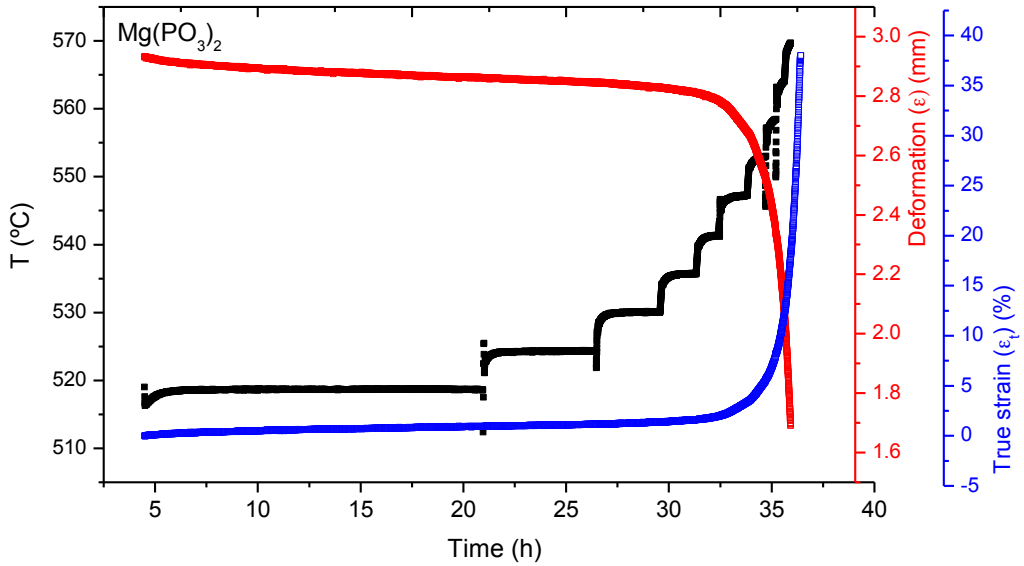


Figure 4.15: Temperature program (in black), displacement (in red) and true strain (in blue) as a function of time for $(MgPO_3)_2$ glass.

The strain-rate or the speed of creep ($\dot{\varepsilon}$) has been calculated from the slope of the true strain $\varepsilon_t$ as a function of time, when deformation stabilizes with time and viscosity was derived following equation (4.2) and plotted in Figure 4.16.

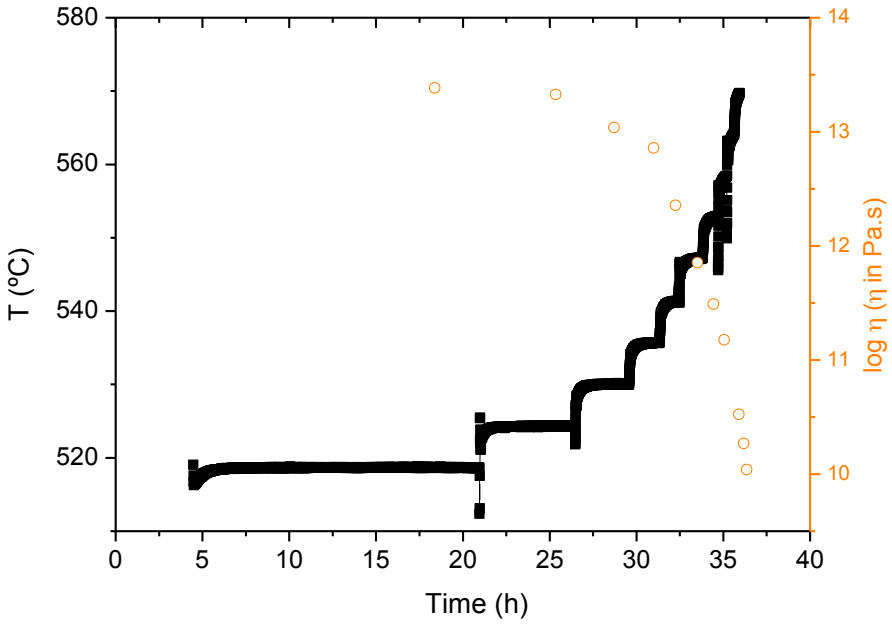


Figure 4.16: Temperature program (in black) and viscosity (in green) as a function of time for $(SrPO_3)_2$ glass.

At viscosities above $T_g$ (i.e. $10^{12}$ Pa.s) due to the thermal history of the glass, the viscosity may not represent conditions of thermal equilibrium. In order to minimize these effects by allowing the glass to approach equilibrium structural conditions, measurements were carried out over higher time intervals. Notwithstanding, high noise is still observed in the high end of

the measured viscosity range. In figure 4.17 viscosity values obtained at approximately every 10ºC from 0.9 to 1.1 $T_g$ have been plotted together with the viscosity data points obtained for these glasses by beam bending and rotation measurements.

In general, viscosity data obtained for alkali and alkaline-earth metaphosphate glasses by creep and by beam bending techniques are in good agreement. The higher difference is found for the glass that shows the lowest fragility value within the glass series, and thus the lower variation of viscosity with temperature, $Zn(PO_3)_2$ glass. This deviation may come from the different creep stages where viscosity data are calculated from. The deflection data obtained by beam bending have been taken under heating at controlled rates of $2ºC.min^{-1}$ as recommended by ASTM C1350M standard in order to avoid delayed elastic strain. However, by this technique viscosity is essentially calculated from the deformation that takes place in the primary stage where the delayed elastic strain and thus the higher deformation rate ($d\varepsilon/dt$) could lead to lower viscosity values compared with creep measurements, where the viscosity data are taken under isothermal conditions at long test times in the secondary stage to ensure stabilization of equilibrium structure and elimination of delayed elastic strain. It is considered that this effect would be stronger in glasses with lower kinetic fragility, where the change of viscosity with temperature is lower, such as $Zn(PO_3)_2$ glass.

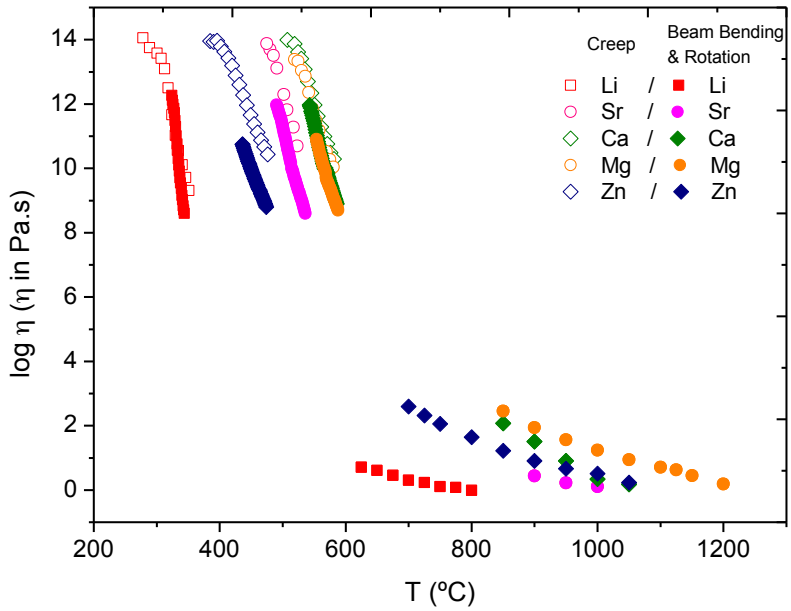


Figure 4.17: Temperature dependence of viscosity of $50MO.50P_2O_5$ (M=Mg,Ca,Sr,Zn) and $50M'_2O.50P_2O_5$ (M'=Li) glasses determined by creep (open symbols) and beam bending and rotation measurements (filled symbols).

In order to compare the dependence of kinetic fragility on the method used to determine viscosity in the low temperature range, and thus the possibility to obtain viscosity values well

below $T_g$, kinetic fragility calculated from viscosity values obtained by creep and by beam bending and rotation methods have been represented in Figure 4.18.

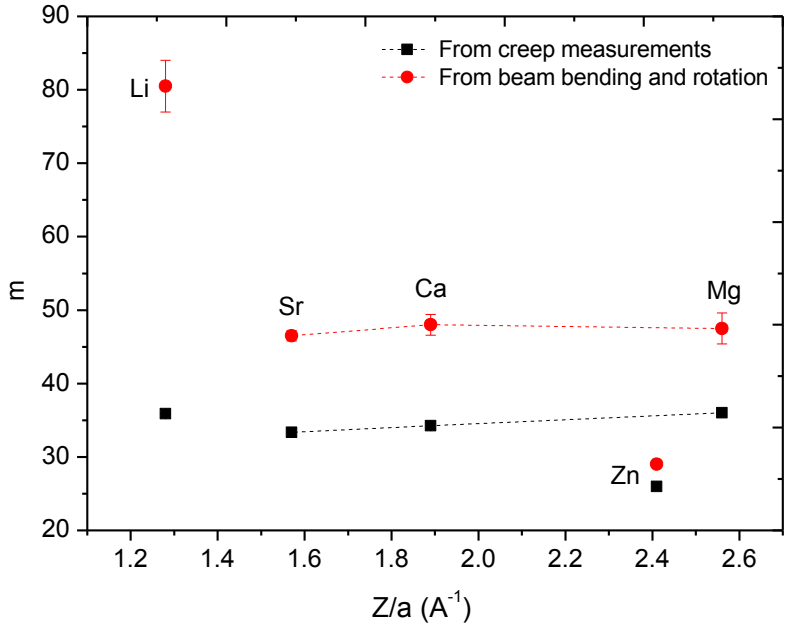


Figure 4.18: Kinetic fragility of $50MO.50P_2O_5$ (M=Mg, Ca, Sr, Zn) and $50M'_2O.50P_2O_5$ (M'=Li) glasses as function of cationic potential. The average values are obtained from VFT and MYEGA fits. M parameter obtained by AM has been neglected due to the very low values obtained (m≈2) in comparison with the other two models. Dotted lines are drawn as guide for the eyes.

As it can be observed, m values obtained from creep measurements are in all cases lower than the ones obtained from beam bending. In the case of $LiPO_3$ glass, a dramatic decrease on m is observed. On the other hand, the trend followed by m values obtained by different methods with cationic potential is the same for alkaline-earth and zinc metaphosphate glasses. The absence of values for $NaPO_3$ glass does not allow corroborating if the tendency is similar also for the alkali metaphosphate glasses. Therefore, is evidenced that kinetic fragility strongly depends on the available experimentally determined viscosity data in the viscosity range above glass transition, than on the high temperature range. The higher the viscosity values obtained in the upper limit viscosity curve seems to lead to lower kinetic fragility values. $LiPO_3$ glass is the perfect example of it since the viscosity data obtained by beam bending and by creep are so similar for viscosities under $10^{12}$ Pa.s, but the kinetic fragility values so different depending on the data selected for the fits. However, to obtain experimental viscosity values from $10^{12}$ to $10^{14}$ Pa.s is time consuming and thus costly due to the long test times needed to obtain reliable data because of the high relaxation times, therefore it is important to get a compromise between the most convenient combination of techniques to measure viscosity in glass materials that covers the widest viscosity range with enough accuracy but also with efficiency on the experimental techniques employed.

### 4.2.2.2 Ionic conductivity

Ionic conductivity values have been obtained as the inverse of the glass sample's resistance calculated through the Nyquist diagrams at each temperature. Figure 4.19 depicts the logarithm of the electrical conductivity as a function of the reciprocal absolute temperature for the metaphosphate glass series under study. It can be clearly seen that the alkali containing glasses present the highest values of conductivity among all the compositions followed by $Zn(PO_3)_2$ glass showing higher conductivity values than alkaline earth phosphate glasses.

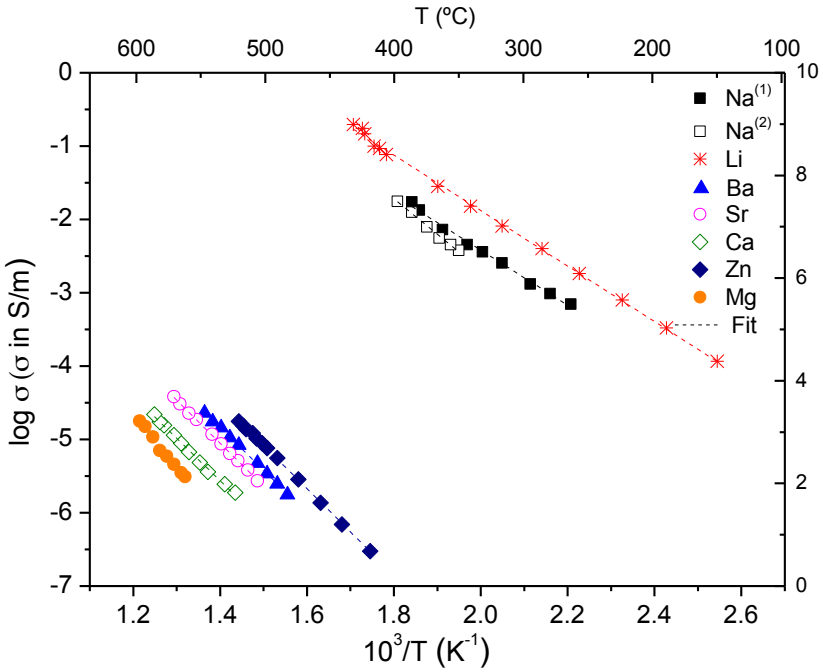


Figure 4.19: Logarithm of conductivity of $50MO.50P_2O_5$ (M=Mg,Ca,Sr,Ba,Zn) and $50M'_2O.50P_2O_5$ (M'=Li,Na) glasses as a function of the reciprocal temperature. Experimental data points have been fitted to an Arrhenius type equation through the least squares method obtaining correlation coefficients ($R^2$) greater than 0.99, from which $E_a$ for ionic conduction has been calculated. $Na^{(1)}$ and $Na^{(2)}$ are the two samples measured of $NaPO_3$ glass.

The activation energy for conduction has been obtained from the Arrhenius fits to these values and the results are plotted against the cationic potential of the modifying ion in each composition in Figure 4.20.

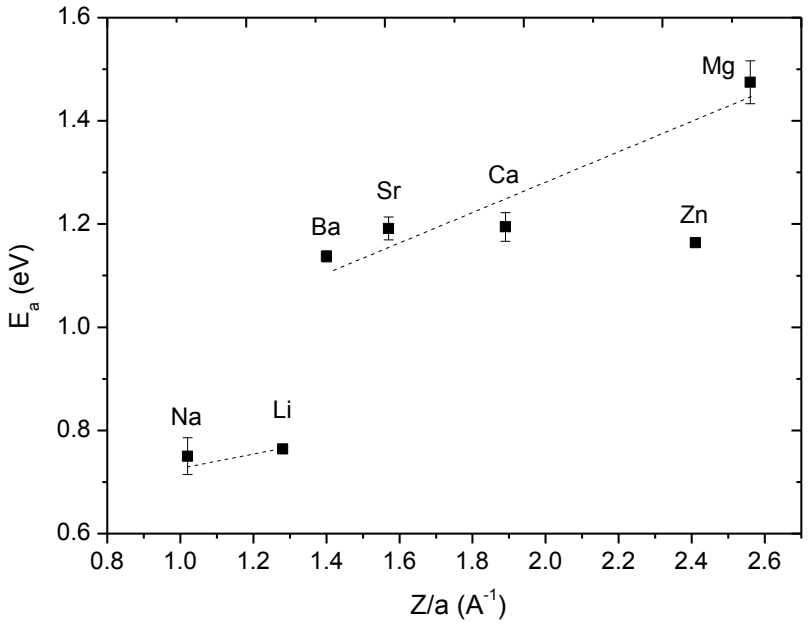


Figure 4.20: Activation energy of ionic conductivity of $50MO.50P_2O_5$ (M=Mg,Ca,Sr,Ba,Zn) and $50M'_2O.50P_2O_5$ (M'=Li,Na) glasses as a function of cationic potential. Dotted lines are drawn as guide for the eyes.

It is noteworthy that the determination of conductivity on $NaPO_3$ glass has been difficult to perform due to the high hygroscopic character of the sample (i.e. 86 ppm of water on the surface determined by FTIR). This hygroscopicity hinders somehow the Au deposition on the glass surface that acts as an electrode during impedance measurements which probably leads to the electrode effect observed when fitting the Nyquist plot to different circuits. As a result, conductivity values obtained in this thesis for different samples but coming from the same $NaPO_3$ batch are different. This experimental observation is in agreement with the dispersion of $E_a$ values found in the literature (i.e $E_a$=0.16 eV in Martin [27], $E_a$=0.95 eV in Hezzat et al. [28] and $E_a$=0.75 eV in Bhide et al. [29]. Following the model of Anderson & Stuart [30], according with $Na^+$ and $Li^+$ cationic radii, activation energy for ionic conduction should be lower for $NaPO_3$ glass than for $LiPO_3$. Thus, taking into account the data found in the literature, the conductivity values for the two samples measured of $NaPO_3$ glass (i.e. $Na^{(1)}$ and $Na^{(2)}$) have been plotted in Figure 4.19. From the two $E_a$ obtained from each of it (i.e. $E_a$=0.75 and $E_a$= 0.91 respectively) it has been selected the first one according with the prediction of Anderson & Stuart model based on the ionic radii of the cation.

The range of the values obtained for activation energy indicates that conductivity is of ionic type, through a hopping mechanism where the cations carrying the charge hop between vacant sites.

Except for $Zn(PO_3)_2$ glass there appears to be a correlation between the activation energy for ionic conduction and the cationic potential, i.e. the higher the cationic potential, the higher the $E_a$ for ionic conduction. The variation of the activation energy for the ionic conduction process can be explained using the model of Anderson & Stuart [30], which uses a decomposition of the total activation energy for the conduction in two parts, one arising from the bond strength of the ion to the surrounding oxygens (i.e. electrostatic energy), and a second one influenced by the glass network strength determining the easiness for the diffusion of the charge carriers. Thus, a higher cationic potential of the modifying cation would lead to an increase of the covalent character of the glass network and therefore to the strengthening and subsequent increase of the overall network's rigidity. The mobility of the cations is then reduced increasing the energy barrier that the cations need to overcome for the site hopping, and thus the total activation energy for ionic conduction increases. Attending to the exceptions observed for zinc cation, the higher polarizability of the $Zn^{2+}$ ions that is going to facilitate the deformation of the electronic density around the nuclei is thought to be the responsible factor for the lowest activation energy for conduction found in the zinc metaphosphate glass, when compared to the bivalent alkaline-earth modifiers.

### 4.3 Alkali zinc metaphosphate glasses

In the recent years the ionic conductivity of glasses has been investigated due to their potential application as electrolytes in solid state ionic devices. Special attention has been devoted to lithium conducting glasses. Moreover, alkali zinc phosphate glasses show a high chemical durability and low processing temperatures which make these glasses good candidates to be co-formed with high temperature polymers to produce organic/inorganic composites. On the other hand, the insulating character of glasses make them suitable candidates for their application as low temperature hermetic seals in order to avoid unwanted current leaks through the seal. These applications required the study of the conduction process based on the structure, and a complete knowledge of the viscosity variation with temperature in order to obtain high quality products during their manufacture. Accordingly, we have selected a series of lithium and sodium zinc metaphosphate[6] glasses in order to determine the role played of a transition metal modifying ion with an intermediate character between forming and modifier, due to its high field strength, in combination with an

[6] The results of lithium, zinc and sodium metaphosphate glasses already presented and discussed in the previous section 4.1, are going to be incorporated here in order to study two full series of composition.

element with a completely different nature. The effect of the replacement of a divalent cation, $Zn^{2+}$, by monovalent $Li^{+}$ or $Na^{+}$ cations on the structure and properties is going to be studied in a glass series where the proportion of $P_2O_5$ does not vary. Additionally, since phosphate glasses could be employed on applications where elevated temperatures are required, such as hermetic sealants, the glass network reorganization and the dynamic processes at temperatures above the glass transition temperature ($T_g$) were followed with in situ solid state high temperature MAS-NMR spectroscopy for the lithium zinc metaphosphate glass series.

### 4.3.1 Structural characterization

#### 4.3.1.1 $^{31}$P and $^{7}$Li MAS NMR spectroscopy

The $^{31}$P MAS NMR spectra of the lithium zinc metaphosphate glasses are depicted in Figure 4.21 a). It can be observed that the main resonance corresponds to $Q^2$ tetrahedra, which is located between -20 and -30 ppm, shifting monotonically low field with the substitution of zinc oxide by lithium oxide.

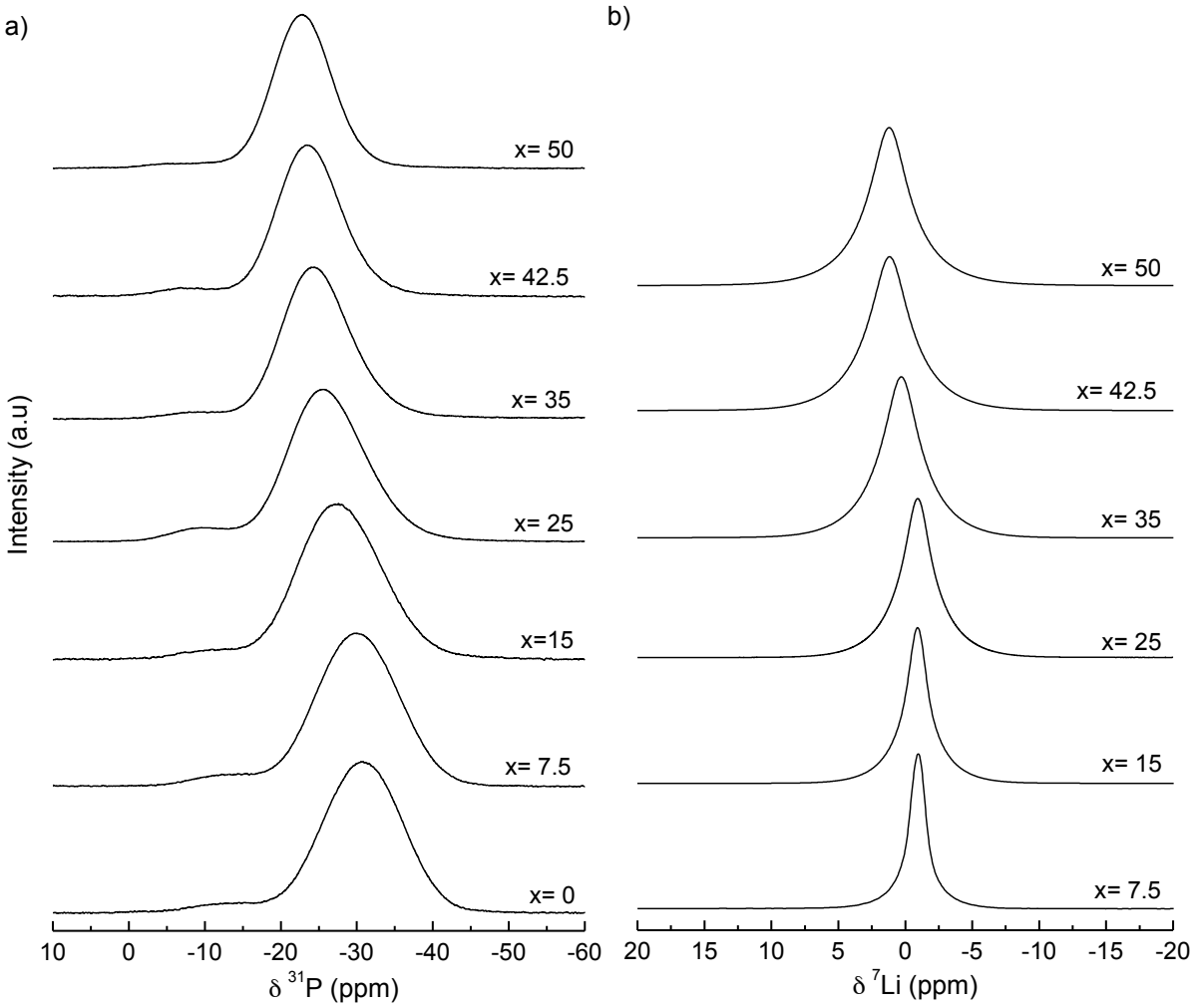


Figure 4.21: a) Isotropic signal of $^{31}$P MAS NMR spectra of $xLi_2O$. (50-x) $ZnO.50P_2O_5$ glasses where x denotes the $Li_2O$ content in each glass. b) Isotropic signal of $^{7}$Li MAS NMR spectra of $xLi_2O$. (50-x) $ZnO.50P_2O_5$ glasses where x denotes the $Li_2O$ content in each glass.

The chemical shift values of x=0 and x=50 glasses are in agreement with literature data for $Zn(PO_3)_2$ and $LiPO_3$ glasses [14, 31]. $Li^+$ with lower field strength causes an increase on the electronic density of phosphorous atoms that reduces the shielding.

The $^{31}$P MAS NMR spectra of sodium zinc metaphosphate glasses are represented in Figure 4.22.

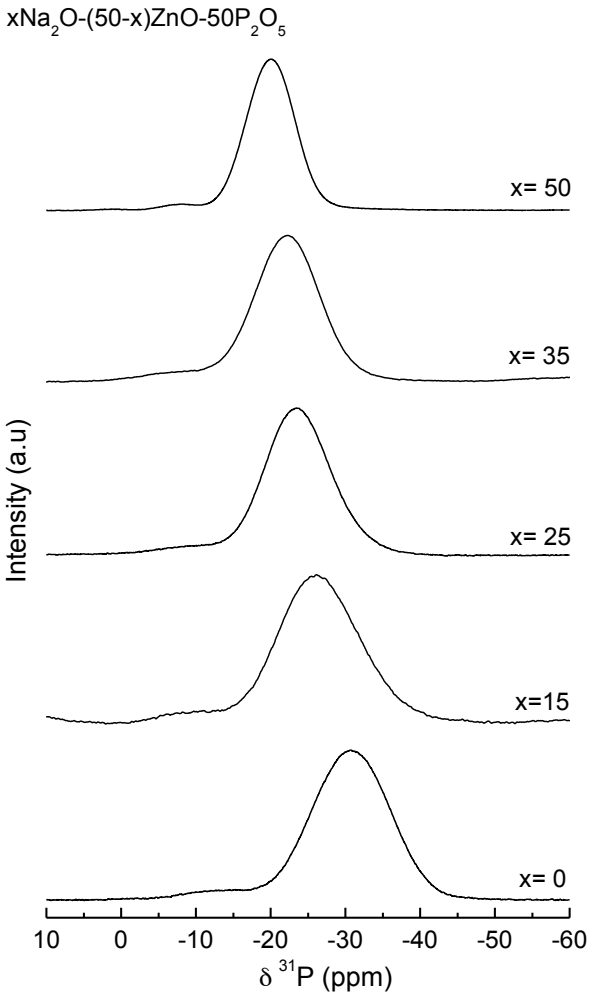


Figure 4.22: Isotropic signal of $^{31}P$ MAS NMR spectra of $xNa_2O$. (50-x) $ZnO.50P_2O_5$ glasses where x denotes the $Na_2O$ content in each glass.

The evolution of the isotropic chemical shift when ZnO is replaced by $Na_2O$ is the same as the observed before, as it could be expected. For both glass systems there is an unavoidable small amount of $Q^1$ groups. The fraction of $Q^2$ tetrahedra, $f$ ($Q^2$), can be determined and the glass composition derived using equation (2.2). Deviations from the nominal composition indirectly determined through the $^{31}P$ MAS NMR decomposition, for both glass series, is not larger than 1 mol %, and the water concentration present in all glasses is lower than $1.10^{-2}$ wt. % for the lithium zinc metaphosphate glass series and lower than $9.10^{-3}$ wt. % for the glass series with $Na_2O$. These water contents are found for $LiPO_3$ and $NaPO_3$ glasses, respectively. Therefore it can be assumed that there should not be a relevant influence of these two factors on the glass properties.

The chemical shift anisotropy ($\delta_{CSA}$) was determined for both glass systems using the dmfit software [8].

According to our results, the Zn rich glass compositions favour chain structures, whereas for the Li and Na rich glasses the proportion of ring structures is found to strongly increase (cf. Figure 4.23). In comparison with the lithium zinc metaphosphate glasses, the metaphosphate series with sodium presents higher proportion of rings in all the compositional range, which corroborates the tendency observed for both pure metaphosphate glasses (i.e. $NaPO_3$ and $LiPO_3$) discussed in the previous section.

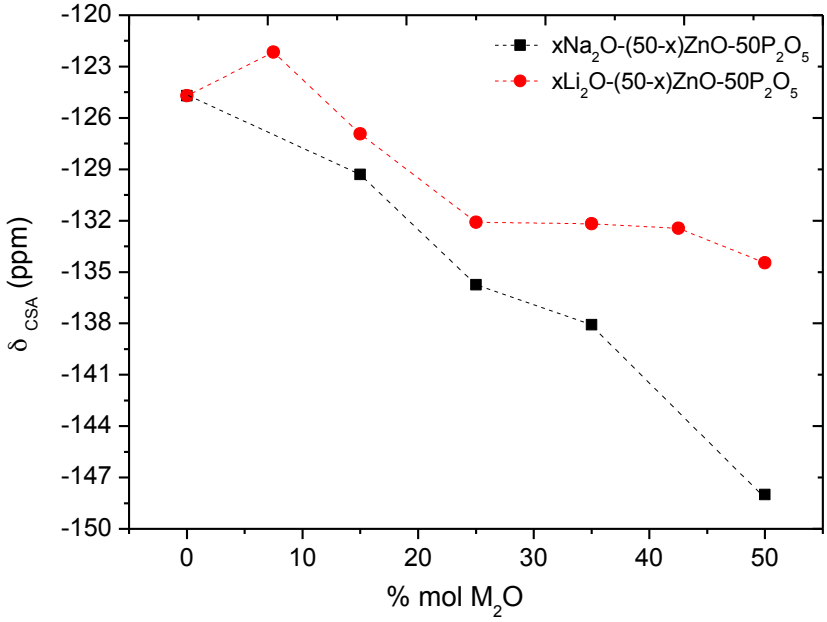


Figure 4.23: Variation of $\delta_{CSA}$ of $xNa_2O.(50\text{-}x)ZnO.50P_2O_5$ and $xLi_2O.(50\text{-}x)ZnO.50P_2O_5$ glasses as function of alkali oxyde content. Dotted lines are drawn as a guide for the eyes.

The $^7Li$ MAS NMR spectra of the $xLi_2O.(50\text{-}x)ZnO.50P_2O_5$ glasses are illustrated in Figure 4.21 b). They all present a single resonance centered about -1 ppm that broadens and shifts low field showing a decreasing shielding and a more disordered $Li^+$ environment as the lithium oxide content increases (cf. Figure 4.24).

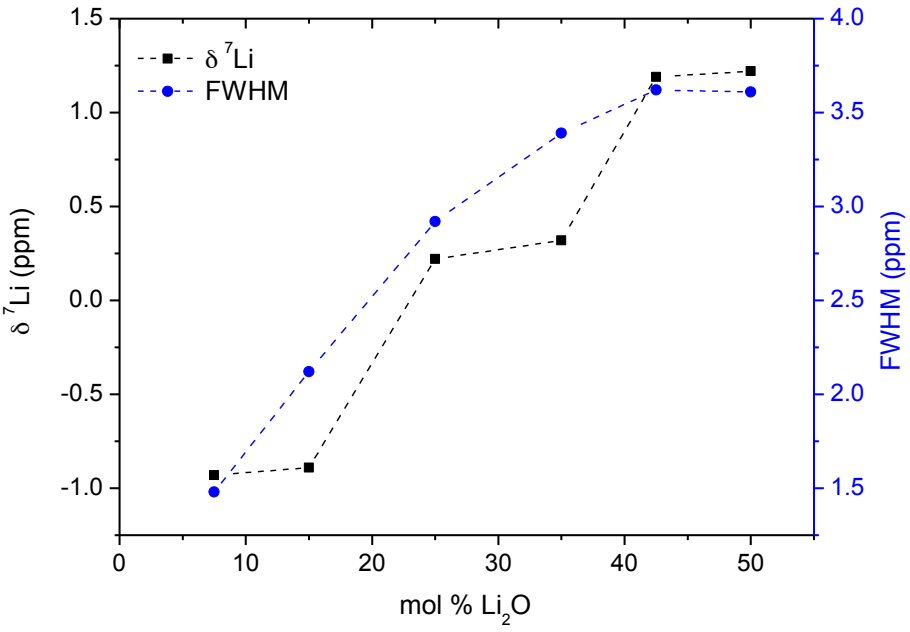


Figure 4.24: $^{7}Li$ NMR chemical shifts and the full width at half maximum of $xLi_2O.(50\text{-}x)ZnO.50P_2O_5$ glasses as a function of $Li_2O$ content. The lines are drawn as a guide for the eyes.

Previous investigations in binary lithium phosphate glasses [23] have demonstrated that correlation between the observed chemical shift and the structure usually does not depend only on one factor. A variety of structural parameters such as coordination numbers, bond length and nature of the modifying ion are involved. We have observed that evolution of the $^{7}Li$ chemical shift closely follows that of the $^{31}P$ CSA anisotropy suggesting that the medium range order structure of the anionic network, i.e. the increment of rings in the glass network, could be another structural factor reflected on the $Li^{+}$ environment.

#### 4.3.1.2 Raman spectroscopy

Figure 4.25 a) and b) shows the Raman spectra collected for the lithium and sodium zinc metaphosphate series respectively.

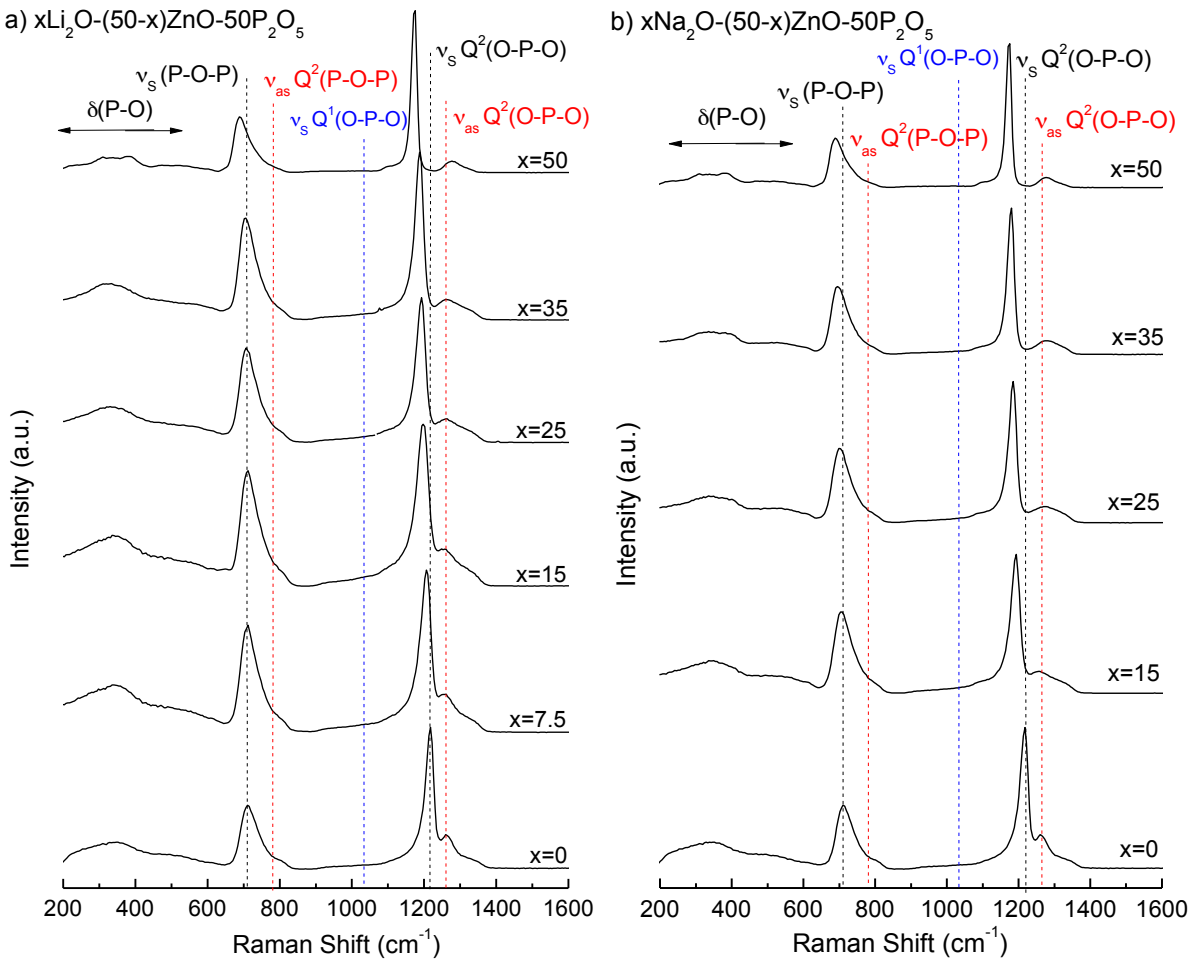


Figure 4.25: a) Raman spectra of $xLi_2O.(50-x)ZnO.50P_2O_5$ glasses.b) Raman spectra of $xNa_2O.(50-x)ZnO.50P_2O_5$ glasses. Dotted lines show the bands attributed to bending (δ) and stretching ($\nu_S$) vibrational modes of P-O bonds.

The spectra of both systems were decomposed into Gaussian contributions from 600 $cm^{-1}$ to 1400 $cm^{-1}$. Two main bands dominate all the spectra appearing at about 650-750 $cm^{-1}$ and 1150-1250 $cm^{-1}$ and are attributed to the symmetric stretching modes of P-O-P and O-P-O bonds, respectively [15, 16]. The P-O bond bending mode of $Q^2$ units emerges as a broad signal in the range of 150 $cm^{-1}$ to 450 $cm^{-1}$. The band attributed to $Q^1$ groups around 1000 $cm^{-1}$ is almost negligible due to the small proportion of these units in the glass structure. The band located around 1280 $cm^{-1}$ can be assigned to the asymmetric stretching mode of the O-P-O bonds in $Q^2$ groups.

The relative intensity between the bands attributed to the presence of rings and chains in the glass network in both alkali zinc metaphosphate glasses is presented in Figure 4.26 as a function of alkali oxide molar percentage. The values have been calculated following Equation 4.2.

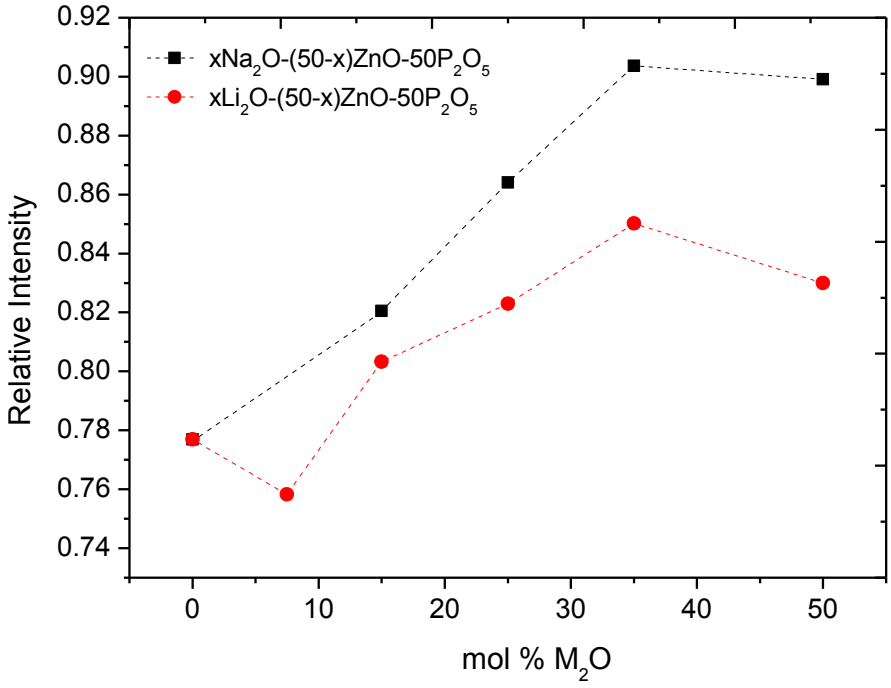


Figure 4.26: Relative intensity of $xNa_2O.(50\text{-}x)\ ZnO.50P_2O_5$ and $xLi_2O.(50\text{-}x)ZnO.50P_2O_5$ glasses as function of alkali oxide content. Dotted lines are drawn as a guide for the eyes.

The proportion of rings increases with the substitution of ZnO by the alkali oxide, thus corroborating the results from $^{31}P$ MAS NMR for both glass series. For pure zinc metaphosphate glass it can be observed that the relative intensity is higher than it would be expected. This behaviour is also detected in the chemical shift anisotropy values of lithium zinc metaphosphate glasses, where $\delta_{CSA}$ of $ZnPO_3$ is also higher than glasses with both modifiers. Figure 4.27 shows the Raman shifts of the bands attributed to the symmetric stretching modes of P-O-P and O-P-O bonds in rings and chains as a function of alkali oxide content for both glass systems.

The bands shift to lower frequencies as the molar proportion of $M_2O$ on the glass composition increases according with previous studies [32,16]. The substitution of $Zn^{2+}$ by a cation with lower field strength gives rise to a reduction of the overall network's rigidity as a result of the P-O bonds lengthening.

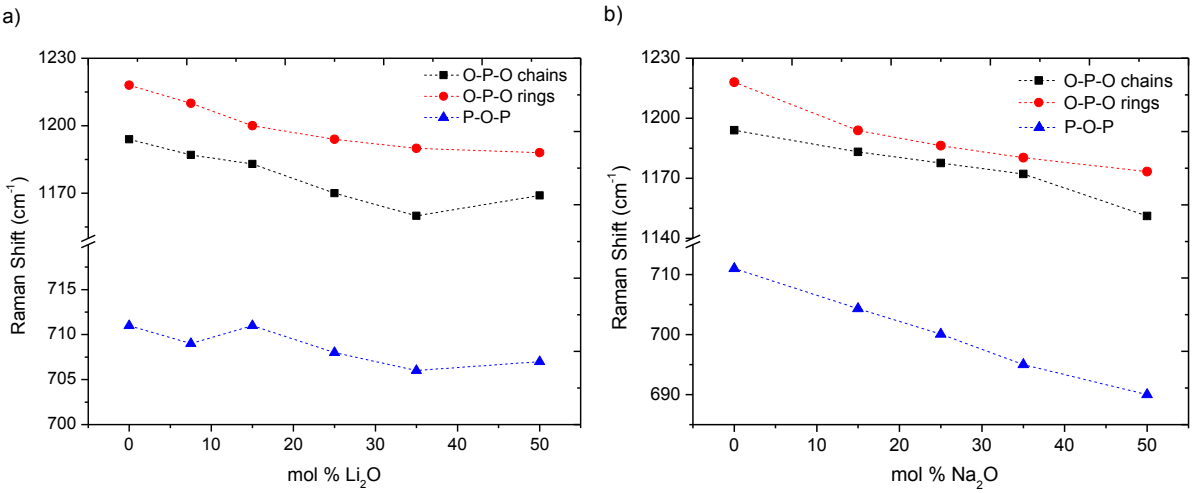


Figure 4.27: a) Raman shifts of the symmetric bands attributed to $Q^2$ units of $xLi_2O$. (50-x) $ZnO.50P_2O_5$ glasses as function of $Li_2O$ content. b) Raman shifts of the symmetric bands attributed to $Q^2$ units of $xNa_2O$. (50-x) $ZnO.50P_2O_5$ glasses as function of $Na_2O$ content. Dotted lines are drawn as a guide for the eyes.

#### 4.3.1.3 $^{31}$P LASER MAS NMR spectroscopy

Macroscopic properties in glasses, such as viscosity and bulk thermodynamic quantities, are primarily controlled by processes at the microscopic level, specially the transition to glass which is controlled by the dynamics of structural changes deeply linked, in turn, to viscosity and diffusivity. Thus, it is important to obtain atomic scale information on both structure and dynamics with changing temperature. Most spectroscopic techniques (e.g. infrared and Raman spectroscopy) provide a “photograph” view of the structure of the material because the time scale of the techniques is of the order of lattice vibrations. However, nuclear magnetic resonance (NMR) can probe much lower frequency motions which are important in the glass transition and the viscosity behaviour. *In situ* high-T methods can directly address the atomic scale dynamics that control structural relaxation and transport properties. Implemented to NMR spectroscopy can be especially useful for probing in detail changes in structure and dynamics in glass-forming liquids through the measurement of the relaxation times and line shapes over a range of temperatures as it takes place [33].

*In situ* high-T NMR can either study the rate of interchange among certain structural species from the temperature-dependent changes in the NMR spectra, or it can be used to characterize atomic-scale motions by measuring nuclear spin relaxation. The advantage of line-shape analysis compared with studies determining the spin-lattice relaxation times ($T^1$) is a greater degree of confidence since the later may be affected by small changes in the nature or concentration of an impurity. This may mean, in the worst case, that any activation energies inferred from $T^1$ data cannot be uniquely attributed to the motions of interest [34].

Additionally, magic angle spinning (MAS) NMR can provide much higher resolution and narrower peaks than static methods, and it can routinely be conducted at temperatures as high as 700ºC, and thus slower exchange can be observed. This allows dynamics closer to the glass transition temperature to be quantified. At temperatures below the glass transition the distributions of bond angle and length broadened the spectra line shape. With increasing temperature, the different sites begin to exchange at a rate which is significantly greater than the difference in NMR frequencies of the different sites, and the motional narrowing effects commonly observed in NMR at high temperature commence, eventually resulting in complete motional narrowing. This exchange between sites can be modeled to obtain the rate of exchange to be capable of relate it to the time scale of processes occurring in glass through the shear relaxation time. Because this exchange involves breaking the strongest bonds in the system (P-O), it is likely that process is closely related to transport properties and to configurational entropy. Bulk viscosity can be directly calculated from species exchange rates measured by NMR, including values for intermediate viscosities that are very rare since the viscosity of glasses are usually measured at high and low viscosity regions using conventional viscosity determination methods [33].

However, unlike silicate glasses [34-37], only sparse of phosphate based glasses [38-40] are available, probably due to the strong crystallization tendency of these glasses.

The temperature dependent $^{31}P$ MAS-NMR spectra of glasses in the lithium zinc metaphosphate series at temperatures ranging from room temperature up to 600 ºC, depending on the composition, are depicted in Figure 4.28 a).

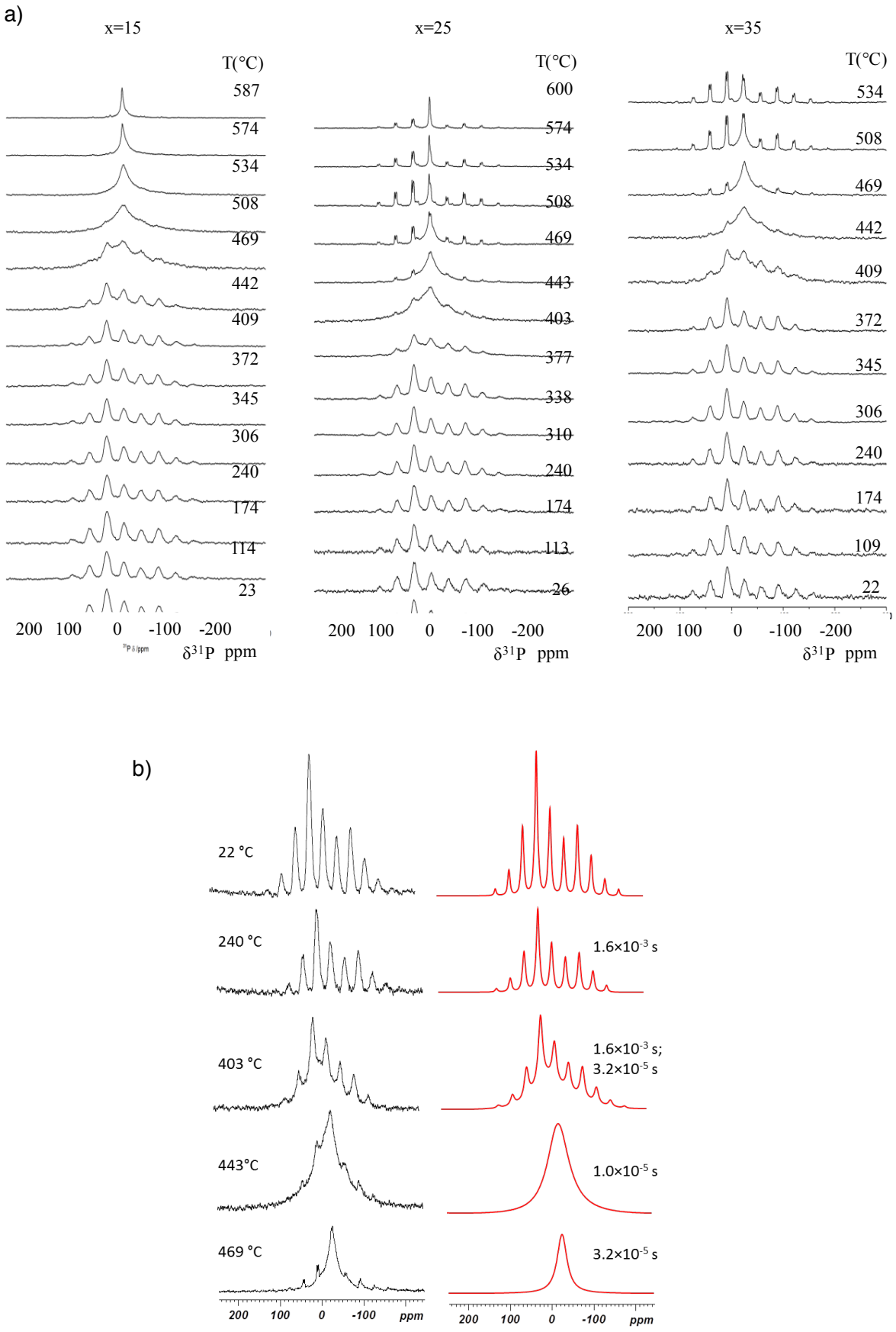


Figure 4.28: a) In situ high temperature $^{31}P$ MAS NMR spectra of $xLi_2O.(50\text{-}x)ZnO.50P_2O_5$ glasses with x = 15, 25 and 35; b) Simulation of the spectra for x = 25. For details of the simulation procedure, the reader is referred to the text.

The spectra exhibit a single resonance line indicative of $Q^2$ units centred at -28 ppm, -26 ppm and -25 ppm, respectively, accompanied by numerous spinning sidebands. The spinning sidebands occur as a consequence of a large chemical shift anisotropy, which is not completely averaged by the MAS process and is accentuated in these spectra due to the 4kHz spinning speed used during acquisition. The room temperature spectra could be fitted using the following parameters: x=15:$\delta_{iso}$ = -27.7 ppm; $\delta_{CS}$ = -125.1 ppm; $\delta_{CS}$ = 0.47; x=25:$\delta_{iso}$ = -26.0 ppm; $d_{CS}$ = -128.3 ppm; $\delta_{CS}$ = 052; x=35:$\delta_{iso}$ = -24.7 ppm; $\delta_{CS}$ = -130.5 ppm; $\delta_{CS}$ = 0.52. At temperatures above the glass transition, the dynamics of the glass network imparts a (partial) averaging of the chemical shift interaction, and hence induces a narrowing of the overall spectral width. In the studied glasses, since only a single phosphate species is present (i.e. $Q^2$), the dynamics cannot be modelled by a simple chemical exchange model as e.g. in [39, 40]. For a simulation of the evolution of the line shape with temperature, we used a home-built MATHEMATICA code. Since no specific dynamics with well-defined axis and angles is involved, the best we can do is assuming exchange between all possible orientations, i.e. between all frequencies of the spectrum. To simulate the effect of such a dynamic, we first calculated the room temperature spectrum using the parameters for the CSA tensors as given above, with the necessary rotations of the tensor according to equation (4.5):

$$\sigma = M^{-1}(\omega_{rot}t,\theta_M,0)R^{-1}(\alpha,\beta,\gamma)M(\omega_{rot}t,\theta_M,0) \tag{4.5}$$

with $\omega_{rot}$ denoting the MAS frequency and $\theta_M$ the magic angle (54.7°). $\alpha$, $\beta$ and $\gamma$ are the Eulerian angles, obtained from a ZCW3 file, as available e.g. from [41, 42]. After generating the FID (FID(t) = FID(t) + exp(I$\omega$dw) with dw denoting the dwell time of the experiment and Fourier transformation, the number of occurrences of the present frequencies is counted and used as the input for a standard exchange dynamics calculation, in which the exchange between all possible orientations (i.e. frequencies) is modelled using equation (4.6):

$$g(t) = \vec{g}(0)\exp(i\omega + \pi)t\,\mathbf{1} \tag{4.6}$$

in which $\vec{g}(0)$ contains the occupancies of the n involved sites, $\pi$ denotes the exchange matrix, containing the exchange frequencies, **1** denotes the unity vector of length n and $\omega$ represents a diagonal matrix containing the resonance frequencies as calculated above. Typically, the dimension of the matrices are 500…1500. Following this procedure, it was possible to obtain an estimate for the correlation times of the glass dynamics at the given

temperatures. In Figure 4.28 b), the spectra and the results of the simulations are given exemplarily for glass x=25. The correlation times, as obtained from these simulations, may now be compared to the results from the viscosity measurements (cf. Figure 4.29).

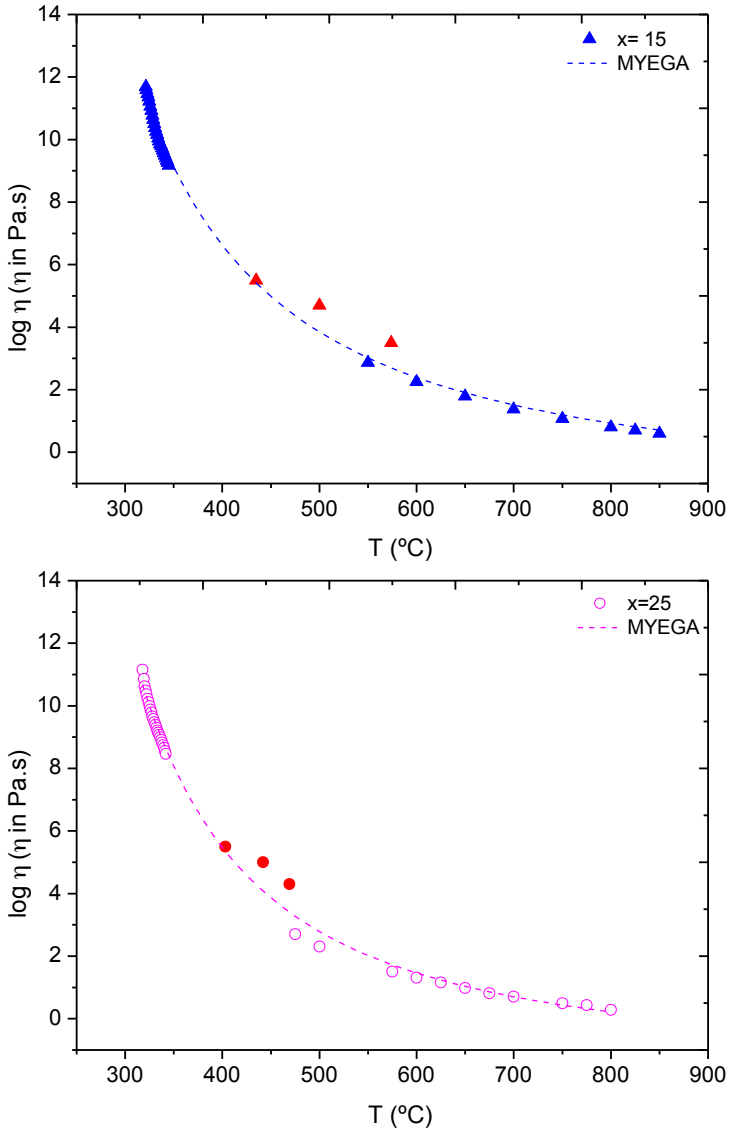

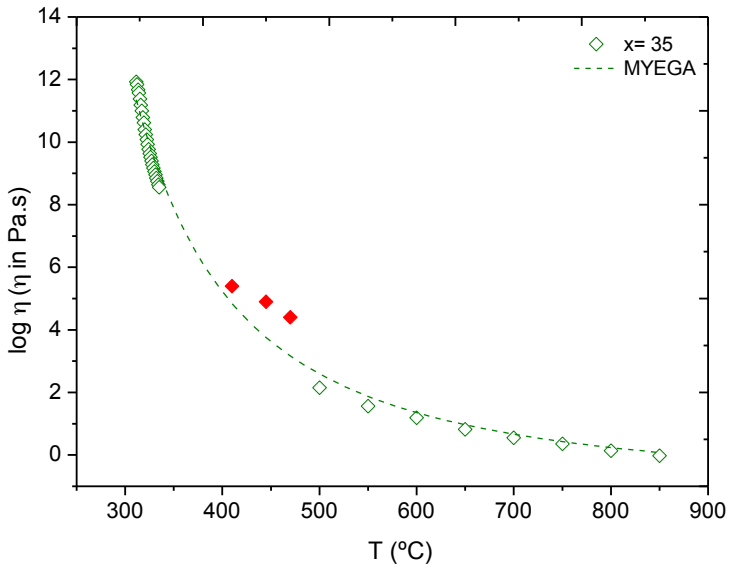


Figure 4.29: Viscosity data as determined from viscosity measurements and NMR line shape evolution (points filled in red) for glass samples with x = 15, 25 and 35 of $xLi_2O.(50\text{-}x)ZnO.50P_2O_5$ glass series.

Dingwall and Webb [43] have pointed out that the shear relaxation time (τ) can be determined from the zero-frequency viscosity and the shear modulus at infinite frequency ($G^{\infty}$) via the Maxwell equations for viscoelastic behaviour (Equation (4.6)) using only the viscosity data and an average value of $G^{\infty}$, ca. $1\times10^{10}$ Pa. [44, 45] because $G^{\infty}$ remains fairly constant compared with the shear viscosity over a large temperature range. In the case under study, viscosity is the property that is going to be calculated from the correlation times using the Maxwell relation (4.7):

$$\eta = G^{\infty}\tau \tag{4.7}$$

Given the uncertainties in the experimental setup (temperature gradient along the sample), the viscosity, as calculated from the temperature dependent evolution of the $^{31}P$ MAS NMR line shape, fits remarkably well within the viscosity data as determined from the rotation and beam-bending methods. The increasing deviation at higher temperatures can be traced back to the crystallization of a fraction of the sample during the in situ MAS NMR experiments, which will induce an overall increase of the viscosity.

From the spectra alone we cannot decide whether the observed glass dynamics is accompanied by local P-O-P bond breaking and making. However, without any bond breaking and making, long metaphosphate chains would probably not exhibit a dynamic process, in which a given $PO_4$ tetrahedron in this chain would move as fast and isotropically as to average all the sidebands, as observed in the spectra. For this reason, we assume a local P-O-P bond breaking and making, as observed for other binary phosphate and ternary

aluminophosphate glasses [39, 40]. Thus, again, local bond breaking and making constitutes the determining microscopic step of the macroscopic viscosity [34-37, 39, 40].

### 4.3.2 Transport properties

#### 4.3.2.1 Viscosity

In this work the temperature dependence of the viscosity in a series of lithium zinc and sodium zinc metaphosphate glasses was evaluated using the equations (1.9) to (1.11) that derive respectively from VFT, AM and MYEGA viscosity models equations (1.3) to (1.5).

Figure 4.30 plots the experimental data of viscosity and the best fits to the MYEGA model as an example for both lithium and sodium zinc metaphosphate glasses.

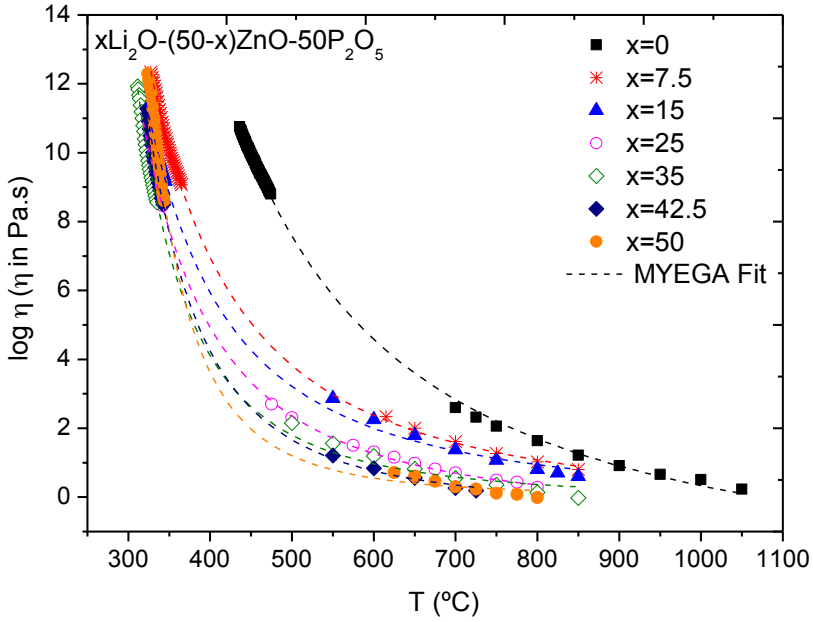

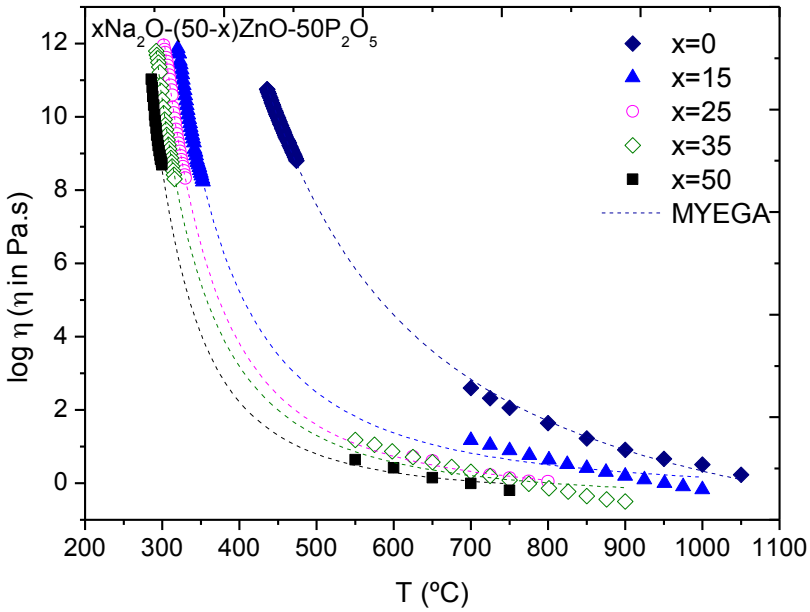


Figure 4.30: Viscosity data points of $xLi_2O.(50-x)ZnO.50P_2O_5$ (top figure) and $xNa_2O.(50-x)ZnO.50P_2O_5$ glasses (bottom) and best fits of the experimental values to MYEGA equation as a function of temperature. Error bars are of the size of the points. The regression coefficient ($R^2$) obtained from the fits to the three models was 0.999, or better.

The average of the kinetic fragility values obtained from VFT, AM and MYEGA equations, except for x=0 and x=50 compositions, where the AM value has been excluded due to the high difference observed between these values and the ones calculated by the other two models that dramatically increases the standard deviation, are collected on Table 4.2 and illustrated in Figure 4.31 as a function of alkali oxide content.

Table 4.2: Kinetic fragility parameter and thermal expansion coefficients of $xLi_2O.(50-x)\ ZnO.50P_2O_5$ and $xNa_2O.(50-x)ZnO.50P_2O_5$ glasses obtained from VFT, AM and MYEGA models.

| $xLi_2O.(50-x)ZnO.50P_2O_5$ | | | | | |
|---|---|---|---|---|---|
| **Glass composition** | **Glass** | $\alpha_{50-200°C}$□$10^{-6}$ ±1 | **m** | | |
| | | | VFT | AM | MYEGA |
| $50ZnO.50P_2O_5$ | **x=0** | 6.6 | 29 | 9 | 29 |
| $7.5Li_2O.42.5ZnO.50P_2O_5$ | **x=7.5** | 8.3 | 37 | 39 | 36 |
| $15Li_2O.15ZnO.50P_2O_5$ | **x=15** | 10 | 43 | 40 | 39 |
| $25Li_2O.25ZnO.50P_2O_5$ | **x=25** | 11.8 | 50 | 40 | 44 |
| $35Li_2O.15ZnO.50P_2O_5$ | **x=35** | 13.4 | 63 | 58 | 55 |
| $42.5Li_2O.7.5ZnO.50P_2O_5$ | **x=42.5** | 13.9 | 64 | 58 | 55 |
| $50Li_2O.50P_2O_5$ | **x=50** | 14.9 | 78 | 100 | 83 |

| $xNa_2O.(50-x)\ ZnO\ .\ 50P_2O_5$ | | | | | |
|---|---|---|---|---|---|
| $50ZnO.50P_2O_5$ | **x=0** | 6.6 | 29 | 9 | 29 |
| $15Na_2O.35ZnO.50P_2O_5$ | **x=15** | 12.3 | 51 | 47 | 47 |
| $25Na_2O.25ZnO.50P_2O_5$ | **x=25** | 14.2 | 56 | 51 | 53 |
| $35Na_2O.15ZnO.50P_2O_5$ | **x=35** | 17.9 | 61 | 49 | 54 |
| $50Na_2O.50P_2O_5$ | **x=50** | 22.0 | 72 | 81 | 65 |

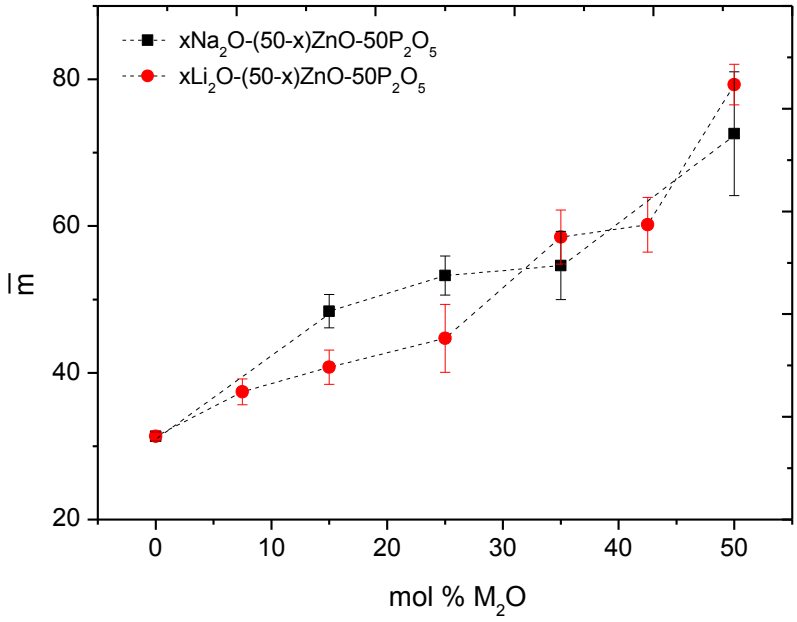


Figure 4.31: Kinetic fragility of $xLi_2O.(50-x)ZnO.50P_2O_5$ and $xNa_2O.(50-x)ZnO.50P_2O_5$ glasses as a function of $Li_2O$ content. Dotted lines are drawn as guide for the eyes.

As it can be observed, the larger the proportion of alkali oxide on the glass, the larger is the kinetic fragility. m rises approximately linearly with increasing lithium or sodium content, which could mean that the intermediate range order structure, based either in chains or rings, apparently does not influence the fragility results. Therefore, the higher fragility for the Li-Zn and Na-Zn metaphosphate glasses would only depend on the character of the bonds involved in the glass network and on the connectivity degree. Since in the glass series under study all phosphate units are of the $Q^2$ type and therefore all present the same degree of connectivity, the decrease on the overall covalent character of the glass network and its lower rigidity, as ZnO is replaced by $Li_2O$ or $Na_2O$, is going to facilitate the flow of $PO_4$ units through the glass network increasing kinetic fragility.

Comparing both glass systems, fragility of sodium zinc phosphate glasses is higher up to x=35 composition, when this trend seems to be somehow reversed. In any case, the values

are similar between both glass series and the standard deviation coming from the average value of the different kinetic fragility overlap for theses high alkali oxide content compositions, thus this change on the trend cannot be confirmed.

The insertion of the calculated viscosity points obtained from the $^{31}P$ MAS-NMR spectra simulation leads to lower fragility values (c.f. Figure 4.29), as a result of the deviation previously mentioned. The fragility values obtained through equation (4.6) for the lithium zinc metaphosphate glasses are m=30 for sample with x=15; m=36 for sample with x=25 and m=38 for sample with x=35. However, there is still a clearly increase of fragility with lithium content.

In Figure 4.32 it can be observed that Doremus ratio increases with alkali content. Thus, the bigger the gap between the high and low viscosity activation energies the greater is the Doremus ratio. This variation with composition is in accordance with kinetic fragility.

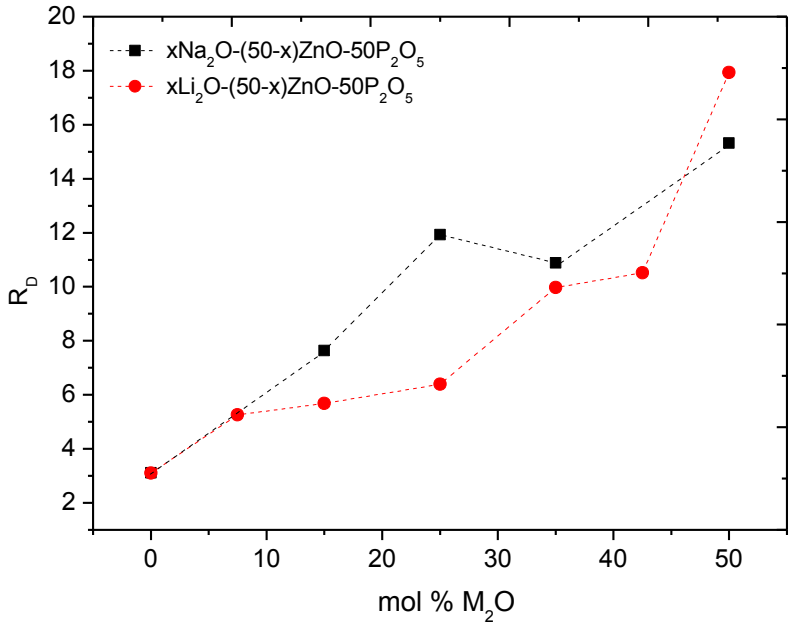


Figure 4.32: Doremus ratio as a function of the $M_2O$ mol content of $xLi_2O.(50\text{-}x)ZnO.50P_2O_5$ and $xNa_2O.(50\text{-}x)ZnO.50P_2O_5$ glasses. Dotted lines are drawn as guides for the eyes.

The thermal expansion coefficient (α) for both glass series are also collected in Table 4.2. α coefficient of a glass depends on the network connectivity features, such as glass network former coordination, number of bridging oxygen within the structure, and modifier to non-bridging oxygen bond strength. In both glass series, where the glass former oxide is kept constant, the thermal expansion coefficient is going to be influenced by the M-O bond nature. For a constant modifying oxide molar fraction in the glass, α increase with increasing alkali oxide content, which is characteristic of an increase on the ionicity of the M-O bonds in

the glass structure and thus of the substitution of $Zn^{2+}$ cations by $Li^+$ and $Na^+$ with lower field strength. The lower field strength of $Na^+$ compared with $Li^+$ is therefore responsible of the higher $\alpha$ coefficients observed in the Na-Zn metaphosphate glass series.

In Figure 4.33 the molar volume, the variation of $T_g$, as measured by dilatometry, and the glass transition temperature values obtained from the fits, are plotted as function of alkali oxide content.

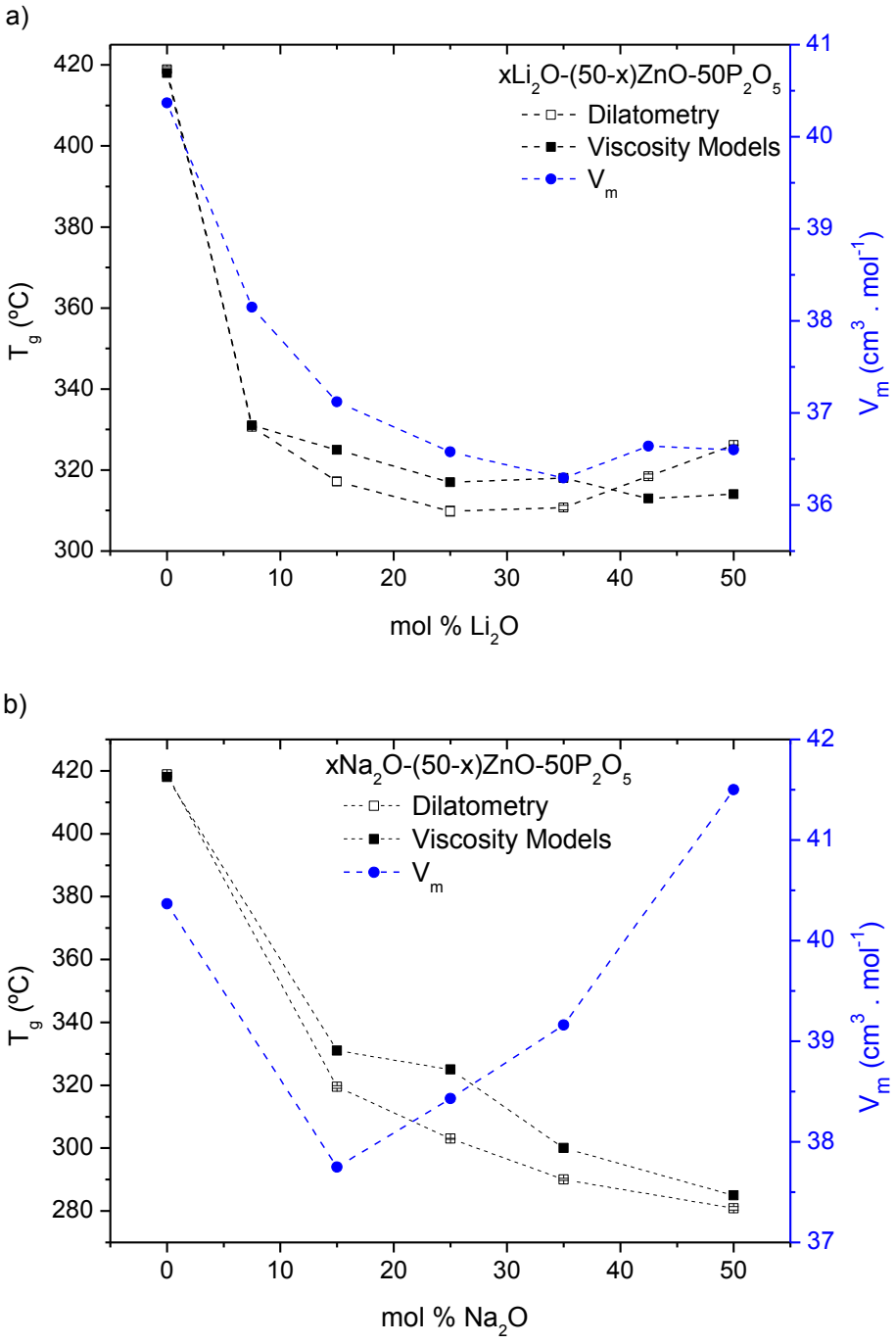


Figure 4.33: Glass transition temperature ($T_g$) obtained by dilatometry and by VFT, AM and MYEGA models and molar volume ($V_m$) of a) $xLi_2O.(50\text{-}x)ZnO.50P_2O_5$ glasses as a function of $Li_2O$ content

and of b) $xNa_2O.(50-x)ZnO.50P_2O_5$ glasses as a function of $Na_2O$ content. Dotted lines are drawn as a guide for the eyes.

The similarity between both $T_g$ values shows a good agreement between the definition of $T_g$ by DSC and by dilatometry as it has been also conclude from the metaphosphate glasses in the previous section.

For Li-Zn metaphosphate glasses, both properties show a non-linear variation with composition, which is in agreement with previous studies on this compositional system [46]. Glass transition temperature and molar volume decrease with the substitution of $Zn^{2+}$ by $Li^+$ up to 25 mol % of $Li_2O$, where a minimum is reached. At higher $Li_2O$ concentrations both properties do not seem to be longer affected by the ratio between the modifying cations. For Na-Zn metaphosphate glasses a similar but less pronounce trend is observed.

The weakening of the glass network with increasing alkali oxide content gives rise to a reduction on the temperature required to activate the rotational motions which make decrease $T_g$. For Li-Zn glasses this decreases is observed up to approximately 25 mol% of $Li_2O$, where a minimum is reached. For higher $Li_2O$ concentration, i.e. x=25-50, $T_g$ remains almost unchanged (c.f. figure 4.32 a)). We have observed from the $\delta_{CSA}$ and the relative Raman intensity results that a reorganization of the glass network from chains to rings occurs in that concentration region for both glass systems .

The structure of zinc metaphosphate glass consists of a more open structure based on chains branched through $Zn^{2+}$ cations [47]. With the replacement of ZnO by $Li_2O$ or $Na_2O$, there would be a progressive formation of rings that are expected to become thermodynamically more stable. This may offset the decrease on $T_g$ due to a higher energetic stability of the glasses with higher $M_2O$ contents.

The non-linear dependence of the molar volume and $T_g$ with composition in Li-Zn metaphosphate glasses is also observed in a previous work of L. Koudelka *et al*. [46]. The almost unchanged values of $V_m$ within the concentration region of x=20-50 mol % $Li_2O$ is attributed in that work to the decisive role of the anionic network, but not further information about its distribution in the medium range scale is given. We have observed from the $\delta_{CSA}$ and the relative Raman intensity results that a reorganization of the glass network from chains to rings occurs in that concentration region. The greater proportion of rings in the glass network could counteract the expected reduction of $V_m$ in the glass, as a result of the substitution of $Zn^{2+}$ by the smaller $Li^+$ cations. This could explain why this property does not follow the same decreasing tendency as for the glasses with the lowest lithium contents. In contrast, for Na-Zn metaphosphate glass series, the molar volume starts to decrease with

the first replacements of ZnO by $Na_2O$ and then increases with higher sodium oxide content. As pointed out before, the structure of $ZnPO_3$ involves an open and branched structure which initially may tend to contract with the first substitutions of $Zn^{2+}$ by $Na^+$ up to x=10 glass composition. Then two factors may affect the evolution of molar volume with composition; in first place the substitution of a divalent cation by two monovalent cations with higher ionic radius [10], and in second place a higher proportion of rings in the glass network compared with Li-Zn metaphosphate glasses.

The transport properties are characterized by their activation energy ($E_a$) and they are influenced not only by the glass network structure but also by the mobility of the modifying cations. The activation energy for viscous flow has been calculated in the low and high temperature ranges, where the viscosity data have been determined, resulting in two activation energies, ($E_a^{low\text{-}T}$) and ($E_a^{high\text{-}T}$), which are plotted in Figure 4.34 for both alkali glass systems.

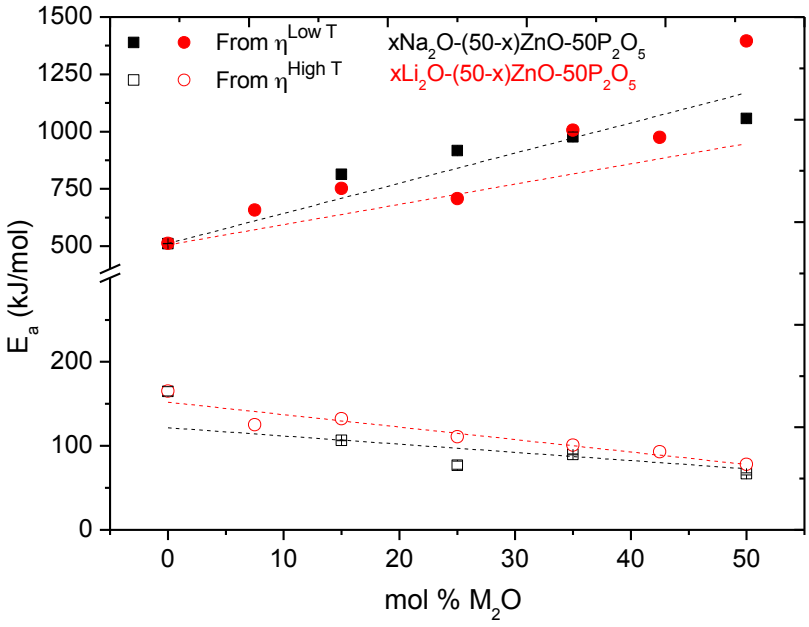


Figure 4.34: Activation energy for viscous flow at low ($E_a^{low\text{-}T}$) and high temperature ($E_a^{high\text{-}T}$) of $xLi_2O.(50\text{-}x)ZnO.50P_2O_5$ and $xNa_2O.(50\text{-}x)ZnO.50P_2O_5$ glasses as a function of alkali oxide content. The lines are drawn as a guide for the eyes and the error bars are within the size of the symbols.

At low temperatures, activation energy rises with the substitution of ZnO by $Li_2O$ or $Na_2O$ while at high temperatures the activation energy for viscous flow decreases for both glass systems.

In the low temperature range the raise on the activation energy ($E_a^{low\text{-}T}$) seems to be determined by cooperative actions between the medium range order structures (i.e. rings and chains). The presence of more stable rings, along with a compaction of the glass

network, as the decrease on the $V_m$ shows, will hinder somehow the cooperative flow of this structural units giving rise to an increase on the energy required to activate this dynamic process. The higher proportion of rings observed for the Na-Zn metaphosphate glass series is in agreement with the higher activation energy of viscous flow in the low temperature range compared with the Li-Zn glass series.

On the other hand, at higher temperatures, when the breaking and re-forming of bonds occurs fast enough due to the high temperature, a single-process action drives the $E_a^{high\text{-}T}$ decrease with the replacement of covalent Zn-O bonds by more ionic $Li^+O^-$ or $Na^+O^-$ bonds. In general, the higher values observed for the Li-Zn glass system agrees with $Li^+$ higher cationic potential (Z/a) compared with $Na^+$ due to the small ionic radius of lithium cation. However, the scattering and the proximity between $E_a^{low\text{-}T}$ and $E_a^{high\text{-}T}$ values of both glass systems only allow elucidating general trends.

#### 4.3.2.2 Ionic conductivity

Following with the study of transport properties, ionic conductivity values have been obtained as the inverse of the glass sample's resistance. Its logarithm is depicted as a function of the reciprocal absolute temperature for the $xLi_2O.(50\text{-}x)ZnO.50P_2O_5$ and $xNa_2O.(50\text{-}x)ZnO.50P_2O_5$ glasses in Figure 4.35 a) and b) respectively.

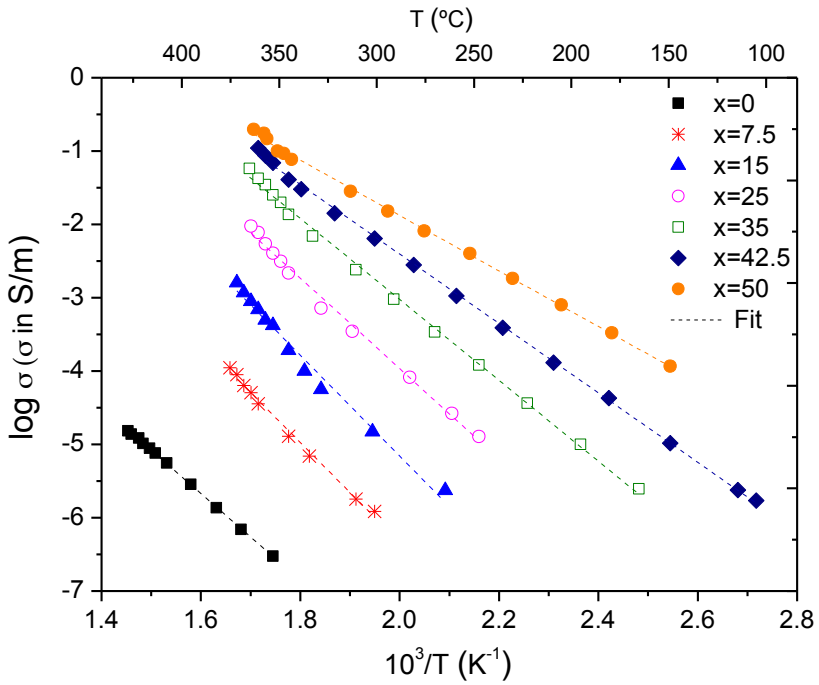

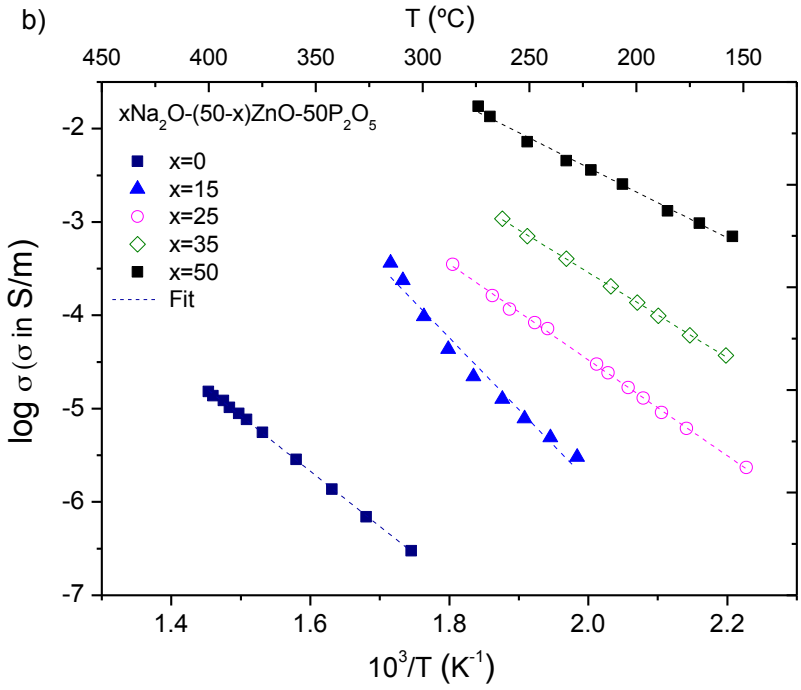


Figure 4.35: Logarithm of conductivity of $xLi_2O.(50\text{-}x)ZnO.50P_2O_5$ (a)) and $xNa_2O.(50\text{-}x)ZnO.50P_2O_5$ glasses (b)) as a function of the reciprocal temperature. Experimental data points have been fitted to an Arrhenius type equation through the least squares method obtaining correlation coefficients ($R^2$) greater than 0.99, from which $E_a$ for ionic conduction has been calculated.

In the previous section devoted to pure metaphosphate glasses it was observed that $LiPO_3$ and $NaPO_3$ glasses were the ones with the higher connectivity followed by $Zn(PO_3)_2$. Is it then expected that the replacement of ZnO by alkali oxide increases the conductivity.

The activation energy for conduction has been obtained from the Arrhenius fits to these values following equation (4.8) and the results are plotted against the alkali oxide content in Figure 4.36.

$$\sigma = \sigma_0 \exp\left(-\frac{E_a}{RT}\right) \tag{4.8}$$

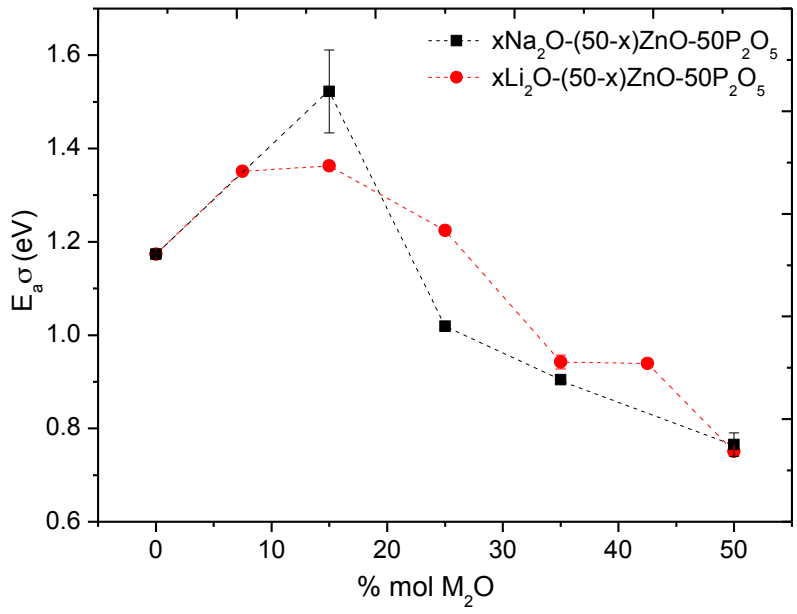


Figure 4.36: Activation energy of ionic conductivity of $xLi_2O.(50-x)ZnO.50P_2O_5$ and $xNa_2O.(50-x)ZnO.50P_2O_5$ glasses as a function of alkali oxide content. Dotted lines are drawn as guide for the eyes.

Again, the values´ range indicates that conductivity is of ionic type, through a hopping mechanism where the cations carrying the charge hop between vacant sites.

For both metaphosphate glass series, $E_a$ of ionic conduction slightly increases with the substitution of ZnO by $Li_2O$ or $Na_2O$ up to x=15. The expected increase on the $E_a$ (σ) as a result of the increment on the number of charge carriers (i.e. every $Zn^{2+}$ cation is replaced by two $Li^+$ or $Na^+$ ions) does not occur with the first replacements of ZnO by $Li_2O$ or $Na_2O$. The initial addition of $M_2O$ starts to replace $Zn^{2+}$ ions that present higher field strength, by cations with higher mobility, but the pathways through the glass network for alkali ion migration are still hindered by the higher proportion of ZnO tetrahedra in the glass network together with the decrease on the molar volume observed up to x=15 for these two compositional systems. Until the concentration of $Li_2O$ or $Na_2O$ is high enough to produce more hopping sites occupied by $Li^+$ or $Na^+$ ions, that enhance its jumps through glass network, and the $V_m$ starts to increase (or it keeps almost constant as in the Li-Zn glass system), the activation energy for ionic conduction does not start to decrease.

If we compare both glass systems, Na-Zn metaphosphate glasses up to x=20 show a higher $E_a$ while for higher alkali content the trend is reversed. This behaviour observed at higher alkali contents is in agreement with Anderson & Stuart model [30]. On the one hand, the higher bond strength between $Li^+$ and the surrounding oxygen atoms compared with $Na^+$, due to its higher field strength, would lead to greater $E_a$ (σ) since their mobility is going to be

more reduced. On the other hand, the higher field strength would lead to a glass network with higher overall covalent character and a higher rigidity increasing the energy barrier that $Li^+$ cations need to overcome for the site hopping leading to a higher total activation energy for ionic conduction compared with Na-Zn metaphosphate glass system.

The different behaviour found between $E_a$ (σ) and $E_a^{low\text{-}T}$ for Li-Zn and Na-Zn metaphosphate glasses reveal that $E_a$ (σ) strictly reflects the energy barrier of the motional process that cations with higher mobility, i.e. $Li^+$ or $Na^+$ in these glasses, need to overcome in order to hop from one site to another, while the viscous flow is mainly related to the network dynamics and thus more influenced by the medium range order structure.

## 4.4 Lithium zinc phosphate glasses

Lastly, to conclude with this systematic study of structure and transport properties in phosphate glasses, and following with the lithium zinc ternary glass system, the effect of the glass network connectivity on the structure and properties is going to be determined through the variation of the glass former oxide proportion in a series of lithium zinc phosphate glasses.

### 4.4.1 Structural characterization

#### 4.4.1.1 $^{31}P$ and $^{7}Li$ MAS NMR spectroscopy

The structural evolution of the lithium zinc phosphate glasses has been followed by means of MAS NMR spectroscopy. Both $^{7}Li$ and $^{31}P$ nuclei are going to be influenced by changes on composition and thus on their local environment. Figure 4.37 a) and b) depicts $^{7}Li$ and $^{31}P$ MAS NMR spectra, respectively. Both isotropic chemical shift experienced variations with composition.

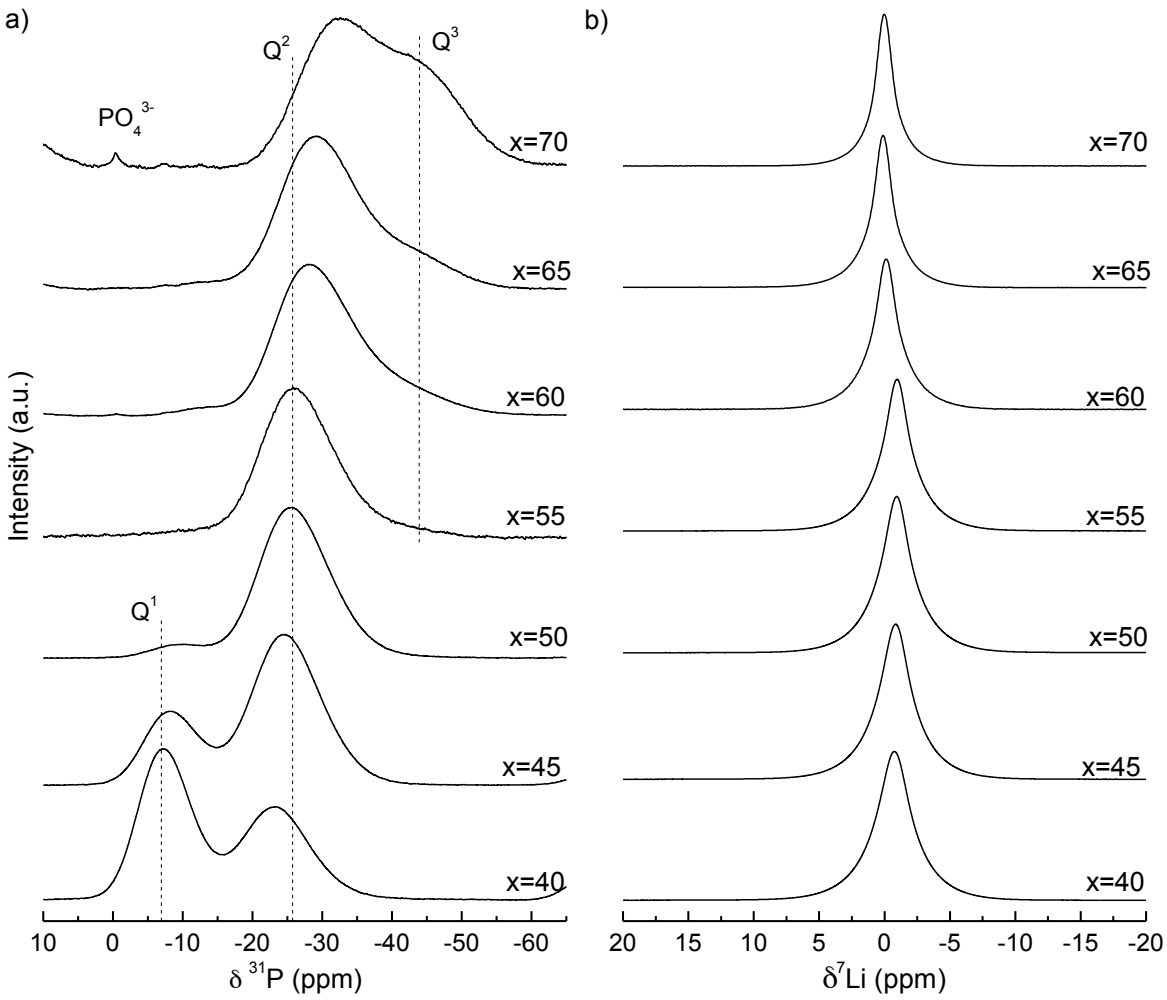


Figure 4.37: a) Isotropic signal of $^{31}$P MAS NMR spectra of x/2$Li_2O$.x/2ZnO.(100-x)$P_2O_5$ glasses where x denotes the $P_2O_5$ content in each glass. b) Isotropic signal of $^{7}$Li MAS NMR spectra of x/2$Li_2O$.x/2ZnO.(100-x)$P_2O_5$ glasses where x denotes the $P_2O_5$ content in each glass.

Spectra line shape varies significantly from the ultraphosphate region to the polyphosphate (from up to bottom in Figure 4.37 a)). With the decrease on the glass former content as it is replaced by the modifying oxides, $Li_2O$ and ZnO, both present in the glass in equimolar proportion, the resonances are less shielded as a result of the redistribution of the electronic density around phosphorous. The higher shift experienced by the resonances attributed to $Q^2$ groups and observed in all the compositional range is detected for the glass compositions in the ultraphosphate region (i.e. for glass former content higher than 55 mol %). A small and narrow peak characteristic of orthophosphate crystalline compound appears in the ultraphosphate glass x=70. Since no crystalline phases were observed on the bulk glass, this crystalline species has been probably formed during the manipulation of the glass powder previous to the NMR acquisition due to the exposure to moisture to this highly hydrolysable phosphate glass. Therefore, this glass composition was excluded from the

study of the properties. The evolution of the $Q^i$ units with composition is followed in Figure 4.38.

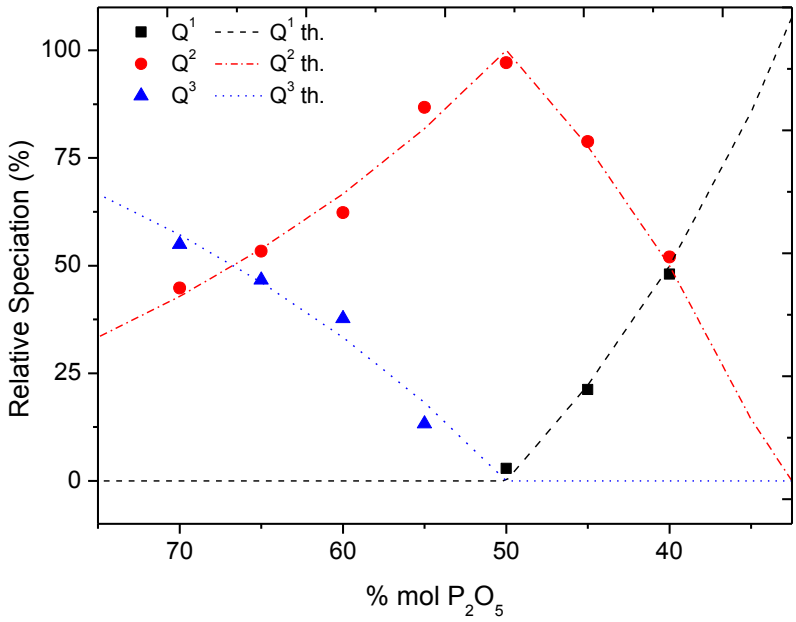


Figure 4.38: Relative speciation of $Q^i$ units of $x/2Li_2O.x/2ZnO.(100-x)P_2O_5$ glasses as function of $P_2O_5$ content. Dotted lines correspond to theoretical values obtained from equations (1.1 and 1.2).

The depolymerization of the glass network can be observed as the total modifying oxide content ($Li_2O$+ZnO) increases. Gradually, the presence of $Q^i$ units with less bridging oxygens (i.e. $Q^1$ as pyrophosphate dimers or end chain groups) occurs at expense of $Q^2$ units arranged either on chains or rings and $Q^3$ groups. The higher deviation from the theoretical values predicted by the structural model based on the nominal composition following equations (2.1) and (2.2), is observed for x=55 and x=60 glasses in the ultraphosphate region which correspond to a deviation from the nominal composition of 1 and 2 mol % respectively .

The relative speciation of $Q^i$ units has been used to calculate the number of non-bridging oxygens per tetrahedral $PO_4$ unit (NBO/P) through equation (4.8), where $f(Q^i)$ are the experimental molar fractions represented in Figure 4.38.

$$\frac{NBO}{P} = 4f(Q^0) + 3f(Q^1) + 2f(Q^2) + fQ^3 \qquad (4.9)$$

In equation (4.9) it is assumed that the terminal oxygen P=O in $Q^3$ units is a NBO. The variation of NBO/P is represented in Figure 4.39.

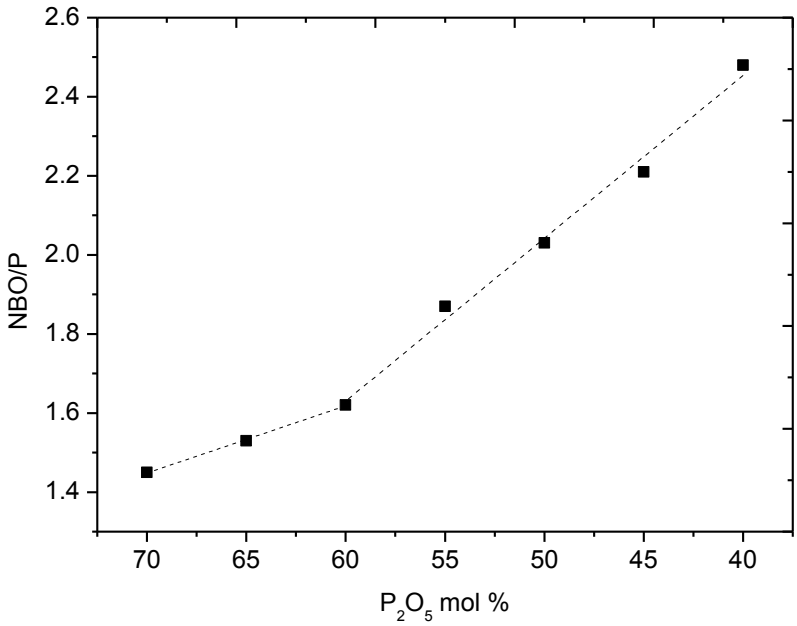


Figure 4.39: Non-bonding oxygens per phosphate tetrahedral unit (NBO/P) as a function of $P_2O_5$ content for $x/2Li_2O.x/2ZnO.(100\text{-}x)P_2O_5$ glasses. Dotted lines are drawn as guide for the eyes.

In general, as the total amount of modifying oxides increases, an increment on the number of non-bridging oxygens per $PO_4$ unit is observed. More in detail, two different regions can be distinguished if the different trends on the variation of NBO/P with $P_2O_5$ mol % are taking into account. The appearance of $Q^1$ units in the glass network as the total modifying oxides content rises causes a more pronounced increase on the NBO per tetrahedral unit as it can be deduced from Figure 4.39. The availability of a higher number of NBO is going to be reflected on the short and medium range order structure within the glass network.

The chemical shift anisotropy ($\delta_{CSA}$) of $Q^2$ species were determined from the spinning side bands using dmfit software and are depicted in Figure 4.40

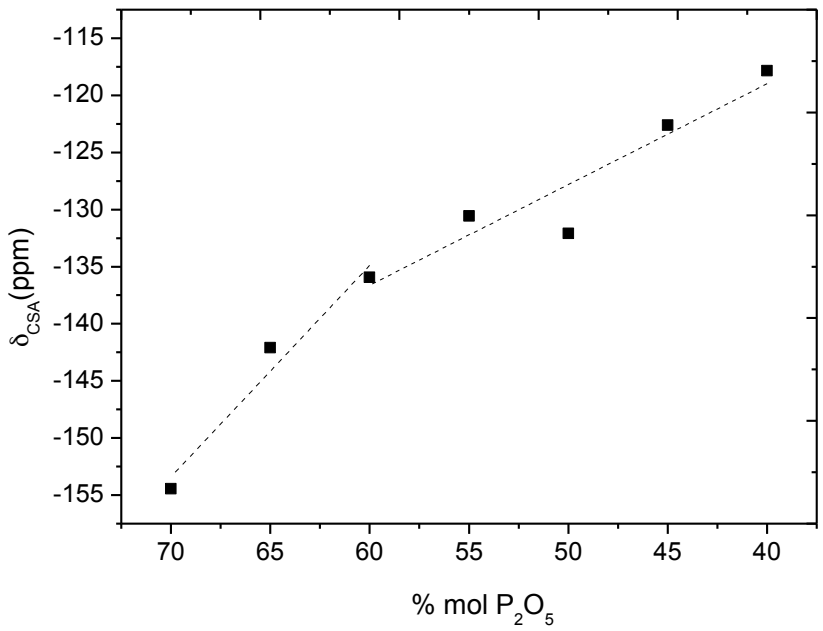


Figure 4.40: Variation of $\delta_{CSA}$ of $x/2Li_2O.x/2ZnO.(100-x)P_2O_5$ glasses as function of $P_2O_5$ content. Dotted lines are drawn as a guide for the eyes.

The variation of the chemical shift anisotropy with increasing modifying oxide content follows a similar trend of that found for the number of non-bridging oxygens per $PO_4$ tetrahedra and two different regions can be again distinguished. As the proportion of $Q^2$ species in the glass network increases (c.f. figure 4.38), $\delta_{CSA}$ decreases and thus the proportion of rings in the glass network, being this variation more pronounced in the ultraphosphate region from x=70 to x=60. The appearance of $Q^1$ species within the glass structure (from x=50 to x=40) seems to provoke a preferential arrangement of the $Q^2$ groups units in chains instead of rings.

The distribution of $Li^+$ ions within the structure of $x/2Li_2O.x/2ZnO.(100-x)P_2O_5$ glasses can be analysed by means of $^7$Li MAS NMR. The spectra are illustrated in Figure 4.37 b). They all present a single resonance centred between 0 and -1 ppm that gets broader as the lithium oxide content increases showing a more disordered $Li^+$ environment. The NMR parameters deduced from the spectra deconvolution, such as chemical shift and full width at half maximum (FWHM) are plotted in Figure 4.41. Two different regions can be differentiating as in the case of $\delta_{CSA}$, suggesting that the medium range order structure of the anionic network, i.e. the increment of chains in the glass network, could be a structural factor reflected on the $Li^+$ environment.

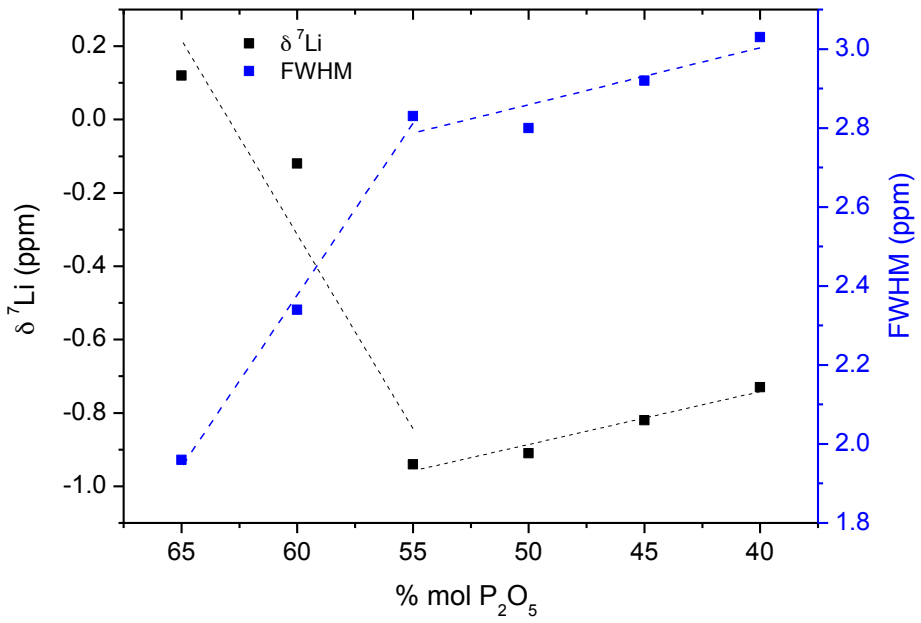


Figure 4.41: $^{7}$Li NMR chemical shifts and the full width at half maximum of x/2$Li_2O$.x/2ZnO.(100-x)$P_2O_5$ glasses as a function of $P_2O_5$ content. Dotted lines are drawn as a guide for the eyes.

Regarding to the chemical shift, the variation with composition follows an opposite variation between the ultraphosphate region from x=55 to x=65 and glass compositions in the range x=40-55. With increasing the modifying oxide content, the $^{7}$Li resonance shifts up-field and down-field in each compositional range, respectively. From the ultraphosphate to the polyphosphate region, a pronounced change on the chemical shift is observed and thus an important variation on the $Li^+$ local environment could be deduce from this behaviour. However, the positive values observed for x=60 and x=65 are anomalous compared with the results of Alam *et al.* [22] where a monotonically shift toward higher frequencies is reported with increasing $Li_2O$ content, as it is observed in the x=40-55 compositional range. This variation is usually related with small and continuous changes on the coordination numbers, bond length and modifying ion nature as discussed in the previous section.

### 4.4.2 Transport properties

#### 4.4.2.1 Viscosity

The temperature dependence of viscosity in the glasses under study was evaluated using the three viscosity models as in the previous sections. The experimental results together with the best fits to VFT model as an example have been represented in Figure 4.42. For the glass compositions x=65 and 60 the experimental viscosity was just determined in the low temperature range. These glasses present very low $T_g$ values, the lowest of all the glasses

that have been studied in this work as it will be presented further on, together with a low chemical durability due to the presence of a high proportion of P=O bonds highly hydrolysable in the glass structure that difficulties their handling. Due to these two features, it was considered that the long time at high temperatures required to perform viscosity measurements in the melt could cause phosphorous volatilization and thus a high deviation from the nominal composition. Experimental inconveniences that could arise as this one, is one of the reasons why it is important to be able to predict properties through modelization.

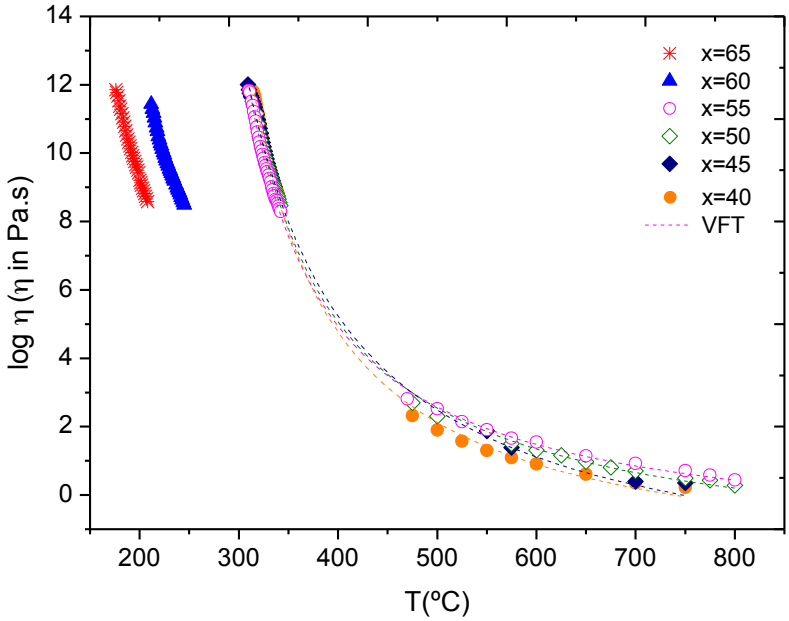


Figure 4.42: Viscosity data points of $x/2Li_2O.x/2ZnO.(100-x)P_2O_5$ glasses and best fits of the experimental values to VFT equation as a function of temperature. Error bars are of the size of the points. The regression coefficient ($R^2$) obtained from the fits to the three models was 0.999, or better.

The kinetic fragility values obtained by VFT, AM and MYEGA equations are collected on Table 4.3.

Table 4.3: Kinetic fragility parameter of $x/2Li_2O.x/2ZnO.(100-x)P_2O_5$ glasses obtained by VFT, AM and MYEGA models.

| Glass composition | Glass code | m | | |
|---|---|---|---|---|
| | | VFT | AM | MYEGA |
| $22.5Li_2O.22.5ZnO.55P_2O_5$ | **x=55** | 51 | 50 | 46 |
| $25Li_2O.25ZnO.50P_2O_5$ | **x=50** | 48 | 39 | 43 |
| $27.5Li_2O.27.5ZnO.55P_2O_5$ | **x=45** | 42 | 31 | 40 |
| $30Li_2O.30ZnO.55P_2O_5$ | **x=40** | 43 | 45 | 49 |

The fragility has been calculated trough the study of the kinetic fragility average value and Doremus ratio approach. Both are illustrated in Figure 4.43.

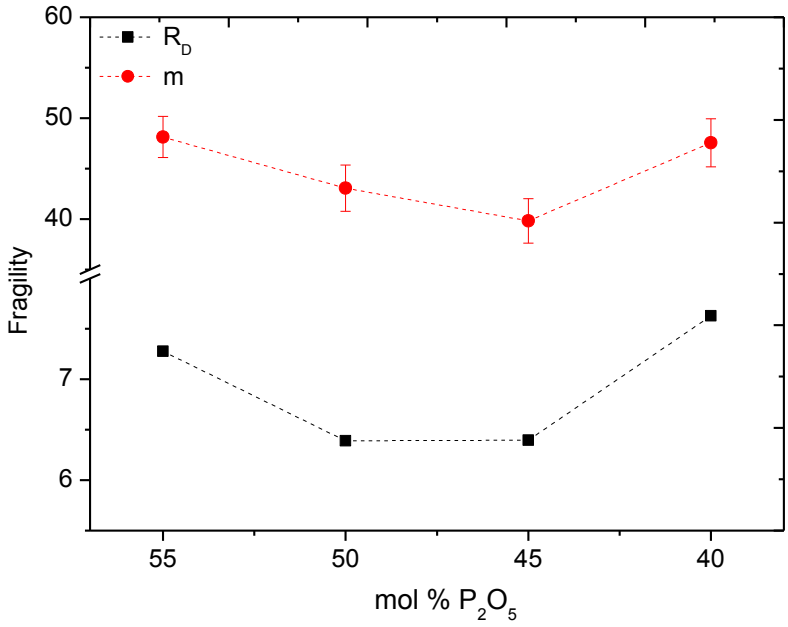


Figure 4.43: Kinetic fragility and Doremus ratio of x/2$Li_2O$.x/2ZnO.(100-x)$P_2O_5$ glasses as a function of $P_2O_5$ content. Dotted lines are drawn as guide for the eyes.

The viscosity *vs.* temperature curve plotted in Figure 4.42 reveals that viscosity does not present a significant variation from one composition to another, neither the kinetic fragility values. Furthermore, $R_D$ follows the same trend as m. Both decrease with increasing modifier content (i.e. $Li_2O$+ZnO) except for x=40 glass composition. One could think that the glass network depolymerization, as a consequence of the increase on the total modifier content (i.e. larger concentration of NBO), may lead to a higher kinetic fragility and $R_D$ ratio. However, an opposite variation with composition is observed, which could be caused by the glass network compaction degree except for x=40. A higher proportion of chains compared to rings as the glass-former oxide content decreases, as seen from $\delta_{CSA}$ values (c.f. Figure 4.40), would lead to a denser glass network, as it is also reflected by the molar volume in Figure 4.44.

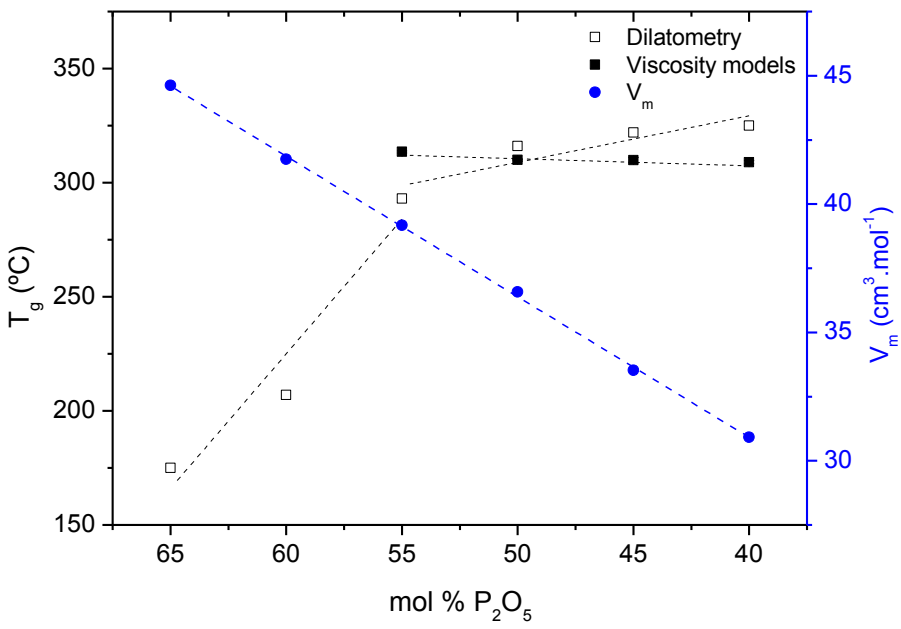


Figure 4.44: Glass transition temperature ($T_g$) obtained by dilatometry and by VFT, AM and MYEGA models and molar volume ($V_m$) of x/2$Li_2O$.x/2ZnO.(100-x)$P_2O_5$ glasses as a function of $P_2O_5$ content. Dotted lines are drawn as guide for the eyes.

Unlike the chemical shift anisotropy and $\delta^7$Li, two different regions cannot be distinguished on $V_m$. It decreases continuously with increasing modifying oxides content. The lower molar volume is going to hinder the cooperative flow of the $PO_4$ units through the glass network and therefore cause a reduction on kinetic fragility and on Doremus ratio. The higher fragility observed for x=40 glass may be caused by the high depolymerization degree of the glass network (i.e. one $Q^1$ group per $Q^2$ unit as seen in Figure 4.38). The organization of $Q^i$ units in dimers facilitates its own flow counteracting the opposite influence of the lower $V_m$ observed for this glass composition.

With regard to the glass transition temperature, it increases with the modifying oxides content. Again two regions can be differentiated attending to the $T_g$ variation with composition. The behaviour in the ultraphosphate region can be explained based on the structural model presented by Hoppe [48], which describes the packing densities in alkaline earth and zinc ultraphosphate glasses based on the coordination environments of the modifying cations and thus on the number of terminal oxygens available for coordination. In the ultraphosphate region, the depolymerization caused by the first additions of modifying oxides (c.f. Figure 4.39) is counteracted by the formation of O-M-O bonds as a result of the sharing of corners and edges between modifying cations, acting as bridges between neighboring $Q^2$ and $Q^3$ polyhedra. The higher covalent character and the consequent bond shortening of these later bonds gives rise to the increase of the overall covalent character of

the glass network together with higher packing densities that cause the glass network strengthening, which balances the depolymerization effect and leads to the pronounced increase on $T_g$ with increasing modifying oxides content as seen in Figure 4.44.

On the meta- and polyphosphate compositional regions, $T_g$ varies slightly with composition, as the kinetic fragility does. Regarding the higher depolymerization degree in this compositional range as a consequence of the appearance of $Q^1$ groups (c.f. increase on the NBO/P ratio in Figure 4.39), a strong decrease on $T_g$ values with decreasing former oxide content would be expected. Nevertheless, the high concentration of modifiers, and thus of O-M-O bonds with higher covalent character, balances the depolymerization effect and leads to a slight increase on $T_g$ with increasing modifying oxides content.

The activation energy of viscous flow in the low and high temperature range has been represented in Figure 4.45.

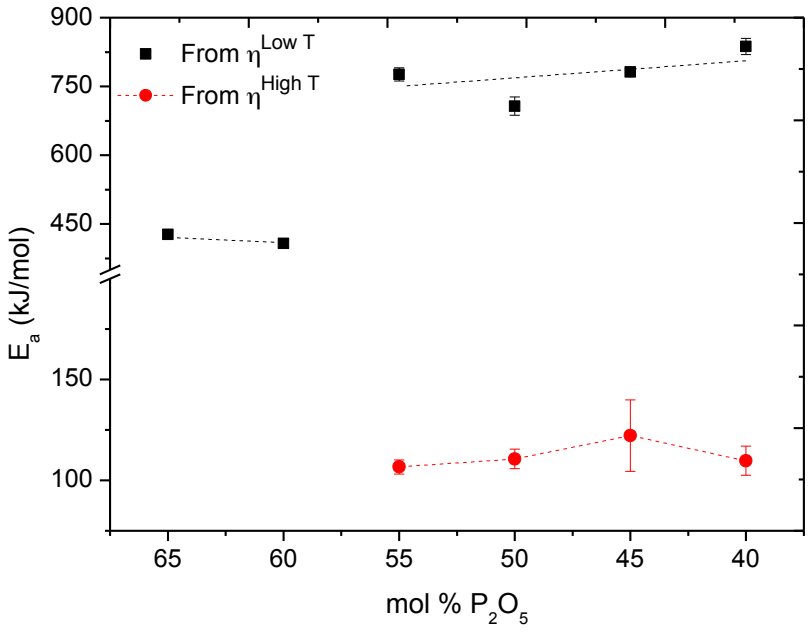


Figure 4.45: Activation energy of viscous flow of $x/2Li_2O.x/2ZnO.(100-x)P_2O_5$ glasses as a function of $P_2O_5$ content. Dotted lines are drawn as guide for the eyes.

The marked gap between the ultraphosphate compositions and the x=55-40 compositional range, contrasts with the small variation observed in the meta- and polyphosphate compositional range.

In both temperature ranges, Ea $^{low\text{-}T}$ and Ea $^{high\text{-}T}$ slightly increase with the increasing modifier content. The variation between compositions is the lowest shown for the phosphate glass series studied. As seen in the previous sections, the preferential arrangement of the $Q^2$ groups units in chains instead of rings is expected to cause a decrease on the Ea $^{low\text{-}T}$ with

increasing modifier content. However, the reduction on the molar volume as a consequence of the lower connectivity degree, may counteract this effect, hindering the cooperative flow of these structural units. Therefore, these two opposite factors would be responsible of the similar values observed.

In the high temperature range, when the breaking and re-forming of bonds occurs fast enough due to the high temperature, the connectivity degree of anionic network may not play an important role. A single-process action drives the $E_a^{high\text{-}T}$ to increase with the increase of the overall covalent character of the glass network and its rigidity.

The lower values of Ea $^{low\text{-}T}$ shown for x=65 and 60 suggest the lowest Doremus ratio and kinetic fragility of the glass series, as both of these two parameters usually vary in the same way. The variation of the proportion of glass former oxide will add another factor to be considered on the discussion of the compositional variations observed in transport properties. The higher number of NBO per $PO_4$ unit available with increasing modifier content, as the proportion of $Q^2$ and $Q^1$ species in the glass network shows, seems to provoke a preferential arrangement of these $Q^2$ units in chains instead of rings, that would lead to a denser glass network as it is also reflected by the decrease of the molar volume.

On the other hand, the kinetic fragility, $R_D$ values and Ea $^{low\text{-}T}$ and Ea $^{high\text{-}T}$ in the meta- and polyphosphate composition range vary slightly with increasing modifier content. The decrease of the $V_m$ seems to play a role on m and $R_D$ decrease with increasing modifier content and on Ea $^{low\text{-}T}$ behaviour, counteracting for this last case the effect caused by the preferential arrangement of the $Q^2$ groups units in chains.

### 4.5 Summary and partial conclusions

Several glass systems have been prepared to determine the role played by the different modifying oxides and by the proportion of $P_2O_5$ present in the glass in order to get more insights into the compositional and structural influence on transport properties in pure phosphate glasses.

The compositional influence on both, properties and atomic structure has been followed through the effect caused on the phosphate glass network by the modifying oxides for those glass compositions where the former oxide content has been kept constant.

On the one hand, the presence of cations with lower cationic potential (Z/a), i.e. $Na^+<Li^+<Ba^{2+}<Sr^{2+}<Ca^{2+}<Zn^{2+}<Mg^{2+}$, or the substitution of ZnO by alkali oxides ($Na_2O$ or $Li_2O$) where $Na^+$ and $Li^+$ cations present lower field strength on the other, lead to less

covalent $M^{n+}O^{m-}$ bonds. The decrease on the covalent character of the glass network and therefore the weakening and subsequent decrease of the overall network's rigidity are reflected on the short and medium range order structure and, as a consequence, the main glass properties will also be influenced up to some extent by those, as explained below.

The short range order structure is determined through the modifying cation influence directly on $^{31}P$ nuclei and on P-O bonds. Both effects have been studied by means of NMR and Raman spectroscopies respectively. It has been observed in all cases that the isotropic chemical shift of the resonance attributed to $Q^2$ units monotonically shifts downfield due to an increase on the electronic density of phosphorous atoms that reduces the shielding as a consequence of the decrease on the covalent character of $M^{n+}O^{m-}$ bonds. Attending to the peak frequencies of O-P-O in $Q^2$ units, a shift to lower frequencies is observed. The presence of cations with lower field strength has given rise to a reduction of the overall network's rigidity as a result of the P-O bonds lengthening.

The medium range order structure, also studied by the mentioned spectroscopies, is subject to the effect of modifying oxides on the organization of the tetrahedral units in rings and chains. The qualitative study of the proportion of each arrangement has been based on the variation observed on the chemical shift anisotropy ($\delta_{CSA}$) and the relative intensity ($I_{rel}$) with composition. According to our results, the decrease on the overall covalent character of the glass network seems to favour rings arrangements.

The analysis of viscosity through the different models where the adjustable parameters have been expressed in terms of $T_g$, fragility (m) and of extrapolated infinite temperature viscosity ($\log \eta_\infty$), has shown that kinetic fragility take different values depending on the model employed; meanwhile $T_g$ values are quite similar between each other and to those determined by dilatometry, independently of the model.

The rate of viscosity variation with temperature has been studied through two approaches, Angell's kinetic fragility (m) and Doremus ratio ($D_R$).

The averaged kinetic fragility increases with Z/a in both, alkali and alkaline-earth metaphosphate series. $Zn(PO_3)_2$ glass shows a lower value among all glasses than it would be expected according to its cationic potential. Doremus ratio follows the same variation as m for the alkali metaphosphate glasses while it decreases for the alkaline earth ones and a $R_D$ value for $Zn(PO_3)_2$ glass more in accordance with its Z/a. The results of the local structure in the glasses, through $\delta_{CSA}$ and Raman band intensities attributed to rings ($I_{ring}$), showed a relatively close relationship with $R_D$, suggesting that a representation of the viscous flow in terms of the atomic structure of the glasses could be done.

For Li-Zn and Na-Zn metaphosphate series, m behaves as an additive property increasing approximately linearly with decreasing covalent character of $M^{n+}O^{m-}$ bonds, from $Zn(PO_3)_2$ minima to $LiPO_3$ as a result of the easier flow of $PO_4$ units through the glass network. In this case, $R_D$ varies accordingly with m. These observations could mean that the intermediate range order structure, based either in chains or rings, apparently does not influence the fragility results.

Additional viscosity points have been obtained by two different and no conventional techniques within the processing and above and below the glass transition range, *In situ* high-T NMR and creep, respectively. In the first case, the viscosity, as calculated from the temperature dependent evolution of the $^{31}P$ MAS NMR line shape, fits remarkably well within the viscosity data as determined from conventional viscosity methods. A good agreement has been also found between the viscosity data obtained by creep and by beam bending techniques. Although fragility values calculated from the viscosity points obtained by these two methods are lower than the previously obtained by the conventional techniques, the tendency followed with composition does not vary. Therefore, is evidenced that kinetic fragility strongly depends on the available experimentally determined viscosity data within the high viscosity range than on the melt. However, to obtain experimental viscosity values by these two techniques are time consuming and costly due to the long test times needed to obtain reliable data because of the high relaxation times by creep, and costly due to the special probe and high power laser required to carry out NMR measurements at high temperature. Therefore, it is important to get a compromise between the most convenient combination of techniques to measure viscosity in glass materials that covers the widest viscosity range with enough accuracy but also with efficiency on the experimental techniques employed.

The transport properties are characterized by their activation energy ($E_a$) and they are influenced not only by the glass network structure but also by the mobility of the modifying cations. The activation energy for viscous flow has been calculated in the low and high temperature ranges, where the viscosity data have been determined, resulting in two activation energies, ($E_a^{low\text{-}T}$) and ($E_a^{high\text{-}T}$) that follow different trends with composition. This may imply two different mechanisms controlling the viscous flow through a different evolution of the structure with temperature in each of them. Thus the $E_a$ is going to be influenced not only by composition and structure, but on temperature range.

The rise on the activation energy for viscous flow observed at temperatures above $T_g$ ($E_a^{low\text{-}T}$) seems to be determined by cooperative actions between the medium range order structure

(i.e. rings and chains). The higher proportion of more stable rings, along with a compaction of the glass network, as the decrease on the molar volume ($V_m$) shows, will hinder somehow the cooperative flow of these structural units giving rise to an increase on the energy required to activate this dynamic process as a response to the deformation applied.

In search of further insights to be able to explain the behaviour of $E_a^{low\text{-}T}$, it was interpreted it in terms of $B/V_m$ ratio. The higher is the ratio between bond strength and molar volume (i.e. lower $V_m$ and higher B), the higher the activation energy. However, the different values observed for $E_a^{low\text{-}T}$ in lithium and zinc metaphosphate glasses while their B value is quite similar (150 and 151 kJ. $mol^{-1}$ respectively), reveals that the medium range order structure is the key factor.

On the contrary, in the melt, when the breaking and re-forming of bonds occurs fast enough due to the high temperature, a single-process action drives the $E_a^{high\text{-}T}$ to decrease with the reduction of the overall covalent character of the glass network and its rigidity. Thus, it seems that the medium range order structure as well as $B/V_m$ ratio do not influence on the activation energy at high temperature.

The range of the values obtained for activation energy of ionic conduction $E_a(\sigma)$ in the metaphosphate glasses studied indicates that conductivity is of ionic type. Following Anderson & Stuart model, it has been observed that a lower Z/a or field strength of the modifying cation and thus a lower bond strength between the cation and the surrounding oxygens, give rise to lower $E_a(\sigma)$. The higher mobility, and thus the easiness for the diffusion of the charge carriers through a weaker and less rigid glass network reduce the energy barrier that cations need to overcome for the site hopping. Additionally, it has been observed the important role played by a higher molar volume ($V_m$) on the $E_a(\sigma)$ decrease.

$Zn(PO_3)_2$ composition shows a lower value for $E_a^{low\text{-}T}$ and $E_a(\sigma)$ than it would be expected according to its cationic potential. The higher $V_m$ of this glass may facilitate the flow of the structural units through a more open glass network that would lead in turn to minima on the activation energies.

On the other hand, the minima observed for kinetic fragility is thought to be cause by the so-called d-block contraction that would lead to a higher covalent character of the Zn-O bond than the one reflected attending to its cationic potential and thus to the strengthening of the glass network and the subsequent lower fragility

Finally, the lower covalent character of $M^+O^-$ bond is going to be also reflected on the thermal properties. The weakening of the glass network with increasing alkali oxide content

gives rise to a reduction on the temperature required to activate the rotational motions which make decrease the glass transition temperature. The medium range order structure, specifically the reorganization of the glass network from chains to rings may be responsible of the discontinuity shown with composition. Additionally, the linear correlation found with the product of cationic potential and the coordination number of the modifying ion ($Z/a \times CN_{M-O}$) in alkali and alkaline earth phosphate glasses reveal the importance of the connectivity of the modifying ionic subnetwork.

Lastly, to conclude with this systematic study of structure and transport properties in phosphate glasses, the effect of the glass network connectivity on the structure and properties has been determined through the variation of the glass former oxide proportion in a series of lithium zinc phosphate glasses.

The depolymerization of the glass network can be observed as the total modifying oxide content ($Li_2O$+ZnO) increases. Gradually, the presence of $Q^i$ units with less bridging oxygens (i.e. $Q^1$ as pyrophosphate dimers or end chain groups) occurs at expense of $Q^2$ units arranged either on chains or rings and $Q^3$ groups.

In general, as the total amount of modifying oxides increases the depolymerization of the glass network occurs, and an increment on the number of non-bridging oxygens per $PO_4$ unit is observed. The appearance of $Q^1$ units in the glass network causes a more pronounced increase on the NBO per tetrahedral unit which seems to provoke a preferential arrangement of the $Q^2$ groups units in chains instead of rings. A higher proportion of chains would lead to a denser glass network as reflected by the continuously decrease on molar volume, that hinders the cooperative flow of the $PO_4$ units through the glass network causing a small reduction on kinetic fragility and on Doremus ratio. The higher fragility observed for x=40 glass may be caused by the organization of $Q^i$ units in dimers that facilitates its own flow counteracting the opposite influence of the lower $V_m$ observed for this glass composition.

With regard to the glass transition temperature, it increases with the modifying oxides content. Two regions can be differentiated attending to the $T_g$ variation with composition. The behaviour in the ultraphosphate region can be explained based on the structural model presented by Hoppe. The higher covalent character and the consequent bond shortening of these later bonds gives rise to the increase of the overall covalent character of the glass network together with higher packing densities that cause the glass network strengthening, which balances the depolymerization effect and leads to the pronounced increase on $T_g$ with increasing modifying oxides content. On the meta- and polyphosphate compositional regions, the high concentration of modifiers, and thus of O-M-O bonds with higher covalent

character, balances the depolymerization effect and leads to a slight increase on $T_g$ with increasing modifying oxides content.

In both temperature ranges, Ea $^{low\text{-}T}$ and Ea $^{high\text{-}T}$ slightly increase with the increasing modifier content. The variation between compositions is the lowest shown for the phosphate glass series studied. As seen in the previous sections, the preferential arrangement of the $Q^2$ groups units in chains instead of rings is expected to cause a decrease on the Ea $^{low\text{-}T}$ with increasing modifier content. However, the reduction on the molar volume as a consequence of the lower connectivity degree may counteract this effect, hindering the cooperative flow of these structural units. Therefore, these two opposite factors would be responsible of the similar values observed.

In the high temperature range, when the breaking and re-forming of bonds occurs fast enough due to the high temperature, the connectivity degree of anionic network may not play an important role. A single-process action drives the $E_a^{high\text{-}T}$ to increase with the increase of the overall covalent character of the glass network and its rigidity.

### 4.6 References

[1] Q. Jiang, H. Zeng, Z. Liu, J. Ren, G. Chen, Z. Wang, L. Sun, D. Zhao, J. Chem. Phys. 139 (2013) 124502.

[2] H. Zeng, Q. Jiang, Z. Liu, X. Li, J. Ren, G. Chen, F. Liu, S. Peng, J. Phys. Chem. B 118 (2014) 5177.

[3] A.I. Fu, J.C. Mauro, J. Non-Cryst. Solids 361 (2013) 57.

[4] C. Hermansen, J.C. Mauro, Y. Yue, J. Chem. Phys. 140 (15) (2014) 154501.

[5] D.L. Sidebottom, T.D. Tran, S.E. Schnell, J. Non-Cryst. Solids 402 (2014) 16.

[6] S. Gaylord, B. Tincher, L. Petit, K. Richardson, Mater. Res. Bull. 44 (5) (2009) 1031.

[7] S. Striepe, J. Deubener, J. Non-Cryst. Solids 358 (12–13) (2012) 1480.

[8] D. Massiot, F. Fayon, M. Capron, I. King, S. Le Calvé, B. Alonso, J.O. Durand, B. Bujoli, Z. Gan, G. Hoatson, Magn. Reson. Chem. 40 (2002) 70.

[9] F. Liebau, in : M. O'Keefe, A. Novrotsky (Eds.), Structure and Bonding in Crystals II. Academic Press, New York, 1981, p. 197

[10] A. Dietzel, Glastechn. Ber. 22 (1948) 41

[11] R.K. Brow, J. Am. Ceram. Soc., 74 (6); (1991) 1287-90

[12] A.R. Grimmer, U. Haubenreisser, Chem. Phys. Lett. 99 (1983) 487.

[13] T.M. Duncan, D.C. Douglass, Chem. Phys. 87 (1984) 339.

[14] R.K. Brow, D.R. Tallant, S.T. Myers, C.C. Phifer, J. Non-Cryst. Solids 191 (1995) 45.

[15] B.N. Nelson, G.J. Exarhos, J. Chem. Phys. 71 (1979) 2739.

[16] S. Mamedov, D. Stachel, M. Soltwisch, D. Quitmann, J. Chem. Phys. 123 (2005) 124515.

[17] P.K. Gupta, J. C. Mauro, J.Chem. Phys. 130 (2009) 094503.

[18] Y. Yue, J. of Non-Cryst. Solids 355 (2009) 737-744.

[19] U. Hoppe, R. Kranold, A. Barz, D. Stachel, J. Neuefeind, D.A. Keen, J. Non-Cryst. Solids 293–295 (2001) 158.

[20] U. Hoppe, J. of Non-Cryst. Solids 183 (1-2) (1995) 85-91

[21] U. Hoppe U. Hoppe, G. Walter, R. Kranold, D. Stachel and A. Barz, J. of Non-Cryst. Solids 192-193 (1995) 28-31

[22] T.M. Alam, S. Conzone, R.K. Brow, T.J. Boyle, J. of Non-Cryst. Solids 258 (1999) 140

[23] V. Dimitrov, T. Kamatsu, Phys. Chem. Glasses 46 (5) (2005) 521.

[24] M.W. Barsoum, Fundamentals of Ceramics, CRC Press, Boca Raton, 2003.

[25] D. J. Green, An introduction to the Mechanical Properties of Ceramics, Cambridge University press, London, 1998

[26] P. Boch, J.C. Nièpce, Ceramic Materials, Iste Ltd, London, 2007.

[27] S. T. Martin, J. Am. Ceram. Soc., 74 (8) 1991 1767-84], $E_a$=0.95 eV Hezzat et al.

[28] M. El Hezzat, M. Et-tabirou, L. Montagne, E. Bekaert, G. Palavit, A. Mazzah, P. Dhamelincourt, Materials Letters, 58, 2003, 60-66.

[29] A. Bhide, K. Hariharan, Materials Chemistry and Physics, (105) 2007 213-221]).

[30] O.L. Anderson, D.A. Stuart, J. Ame. Ceram. Soc. 37 (12) (1954) 573.

[31] L. van Wüllen, H. Eckert, G. Schwering, Chem. Mater. 12 (2000) 1840.

[32] A. Moguš-Milanković, L. Pavić, S.T. Reis, D.E. Day, M. Ivanda, J. Non-Cryst. Solids 356 11-17 (2010) 715.

[33] J. F. Stebbins, Chem. Rev. 91 (1991) 1353-1373

[34] A I. Farnan, J. F. Stebbins, J. Am. Chem. Soc. 112 (1990) 32-39

[35] J.F. Stebbins, S. Sen, A.M. George, J. Non-Cryst. Solids 192 and 193 (1995) 298.

[36] J.F. Stebbins, S. Sen, I. Farnan, Am. Mineral. 80 (1995) 861.

[37] I. Farnan, J.F. Stebbins, Science 265 (1994) 1206.

[38] L. Van Wüllen, S. Wegner, G. Tricot, J. Phys. Chem. B 111 (2007) 7529.

[39] S. Wegner, L. Van Wüllen , G. Tricot, J. Phys. Chem. B 113 (2) (2009) 416.

[40] S. Wegner, L. Van Wüllen , G. Tricot, Solid State Sciences 12 (2010) 428.

[41] M. Eden, M. H. Levitt, J. Magn. Reson. **132**, 220–239 (1998). URL http://www.mhl.soton.ac.uk/research/software/Orientations.

[42] C. F. F. Karney, *Nearly optimal coverings of orientation space* (2006). URL http://charles.karney.info/orientation/

[43] D. B. Dingwall, S. L. Webb, phys. Chem. Miner. 16 (1989) 508-516

[44] G. W. Scherer, *Relaxation in Glass and Composites*; Wiley: New York, 1986.

[45] S. Brawer, *Relaxation in Viscous Liquids and Glasses*; American Ceramic Society: Columbus, OH, 1985.

[46] L. Koudelka, J. Jirak, P. Mosner, L. Montagne, G. Palavit, J. Mater. Sci., 41 (2006) 4636.

[47] E. Matsubara, Y. Waseda J. Non-Cryst. Solids, 103 (1988) 117.

[48] U. Hoppe, J. of Non-Cryst. Solids 195 (1996) 138.

# Chapter V

# Modelling of viscosity-temperature curves in phosphate glasses

## Chapter V: Modelling of viscosity-temperature curves in phosphate glasses

The prediction of properties with enough accuracy has been for many years one of the most important goals that the glass Science community wanted to achieve. This has been proved to be particularly difficult for glasses with complex compositions which contain a relatively large number of components, like industrial glasses, or glasses with limited industrial applications like phosphates. Several efforts have been made to study the composition–property relationships through traditional atomistic simulation techniques, such as molecular dynamics and other empirical macroscopic modeling methods in order to offer an alternative to the time consuming experimental studies.

The systematic study of the structure and properties carried out in the previous chapter has given rise to numerous experimental and adjustable data such as chemical shift anisotropy, glass transition temperature, kinetic fragility, Doremus ratio, activation energy of viscous flow and the extrapolated infinite temperature viscosity. This chapter will be devoted to the attempt of deriving a general relationship between the properties and structure for all the phosphate glass systems studied, specifically between kinetic fragility and the medium range order structure, as well as other correlations involving $T_g$ and the two concepts used in this work to study fragility in phosphate glasses.

On the basis of those relationships found, the first steps on viscosity-temperature curves prediction will be settled with the aim to give an alternative to the tedious and time consuming experimental determination of viscosity in the melt.

### 5.1 General relationships found between properties and structure in phosphate glasses

The glass transition temperature has been experimentally determined in this work by dilatometry and obtained as an adjustable parameter through the fitting of viscosity data points to VFT, AM and MYEGA models. A good correlation between both of them has been observed for all the phosphate glass systems under study as represented in Figure 5.1. This correspondence shows a good agreement between the definition of $T_g$ by DSC and the results obtained by dilatometry. A precise match between glass transition temperatures obtained from the best fitting of viscosity data to the AM equation and the glass transition temperatures determined using DSC, for 24 inorganic glasses has been reported by Yue [1]. It also constitutes a good evidence to validate the results obtained from the fits, such as kinetic fragility parameters.

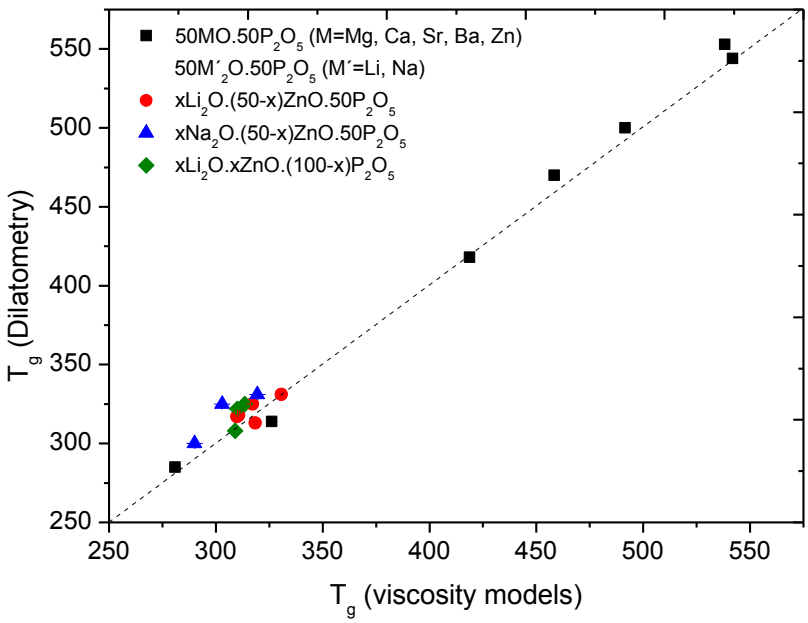


Figure 5.1: Linear correlation between glass transition temperatures ($T_g$) obtained by dilatometry and by VFT, AM and MYEGA models of a series of phosphate glasses. Dotted line is drawn as guide for the eyes.

Throughout this thesis the fragility concept has been studied by determining Angell's kinetic fragility and Doremus ratio for several series of phosphate glasses. Both parameters have been represented in Figure 5.2

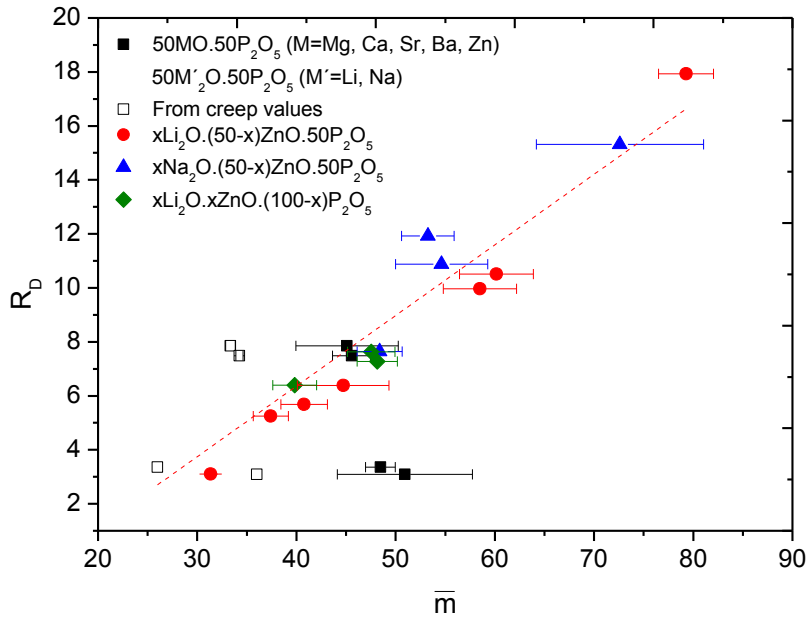


Figure 5.2: Correlation between Doremus ratio ($D_R$) and average value of kinetic fragility obtained by VFT, AM and MYEGA equations of a series of phosphate glasses. Dotted line is the least squares fit with equation $R_D$=-4.1+0.3m ($R^2$=0.90)

Despite some scattering on the data, it can be observed that both parameters correlate quite well taking into account that m values are the average value of those obtained by the three viscosity models. It is worth pointing out that the lower m values obtained through creep technique (i.e. void square symbols) approximate better to the linearity compared with those obtained by fitting beam bending data (i.e. filled square symbols) for the same glass compositions. On the other hand, since Doremus ratio is calculated from the relation between the activation energy of viscous flow in the low and high temperature ranges, i.e. $Ea^{low\ T}$ and $Ea^{high\ T}$, it can be deduced that, in general, the bigger is the gap between both activation energies, the greater is Doremus ratio and the change of viscosity with temperature occurs faster as reflected in the corresponding higher kinetic fragility values.

This linear relationship is not only important from the point of view of correlating two parameters that define the same concept, but also because it brings an equation from which $R_D$ can be calculated when m is previously known, or *vice versa*. For example, an approximation for the activation energy of viscous flow in the high temperature range can be obtained if m and $Ea^{low\ T}$ are known following $R_D=a+bm$ and $R_D= Ea^{low\ T}/Ea^{high\ T}$ equations.

One of the main challenges of this thesis has been to find a clear and general relationship between structure and properties in phosphate glasses through their composition. In this regard, after the study of the compositional dependence of the chemical shift anisotropy ($\delta_{CSA}$), as a value that gives an idea of the proportion of the different arrangements in the medium range order structure, and kinetic fragility, an attempt to correlate both of them has been done as represented in Figure 5.3.

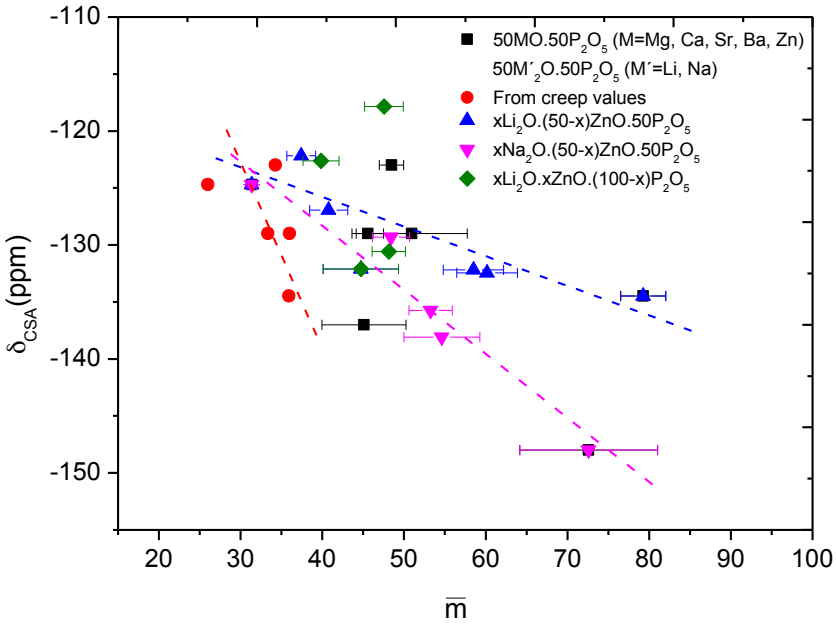


Figure 5.3: Correlation between chemical shift anisotropy ($\delta_{CSA}$) and average value of kinetic fragility obtained by VFT, AM and MYEGA equations of a series of phosphate glasses. Dotted lines are drawn as guide for the eyes.

Unlike the plot of $R_D$ *vs.* m, a grater scattering is observed and thus a clear correlation between both parameters cannot be found for all systems of composition. However, considering each metaphosphate glass system separately at least a tendency can be deduced (c.f. dotted lines in Figure 5.3). A greater proportion of rings in the glass network seem to lead to higher fragility values. In any case, the scattering and the dependence of fragility on M-O bond nature that was deduced in the previous chapter do not allow reaching a clear conclusion about the dependence of fragility on the prevalence of rings or chains arrangements in the glass network. Once more, this underlines the high difficulty of establishing a correlation between the local structure observed in phosphate glasses and fragility as a parameter that reflects an important macroscopic property.

## 5.2 Modelling of viscosity-temperature curves

Another parameter obtained from the fits is the extrapolated infinite temperature viscosity. Mauro et al. [2] have analysed a large number of silicate liquids and have approximated the extrapolated infinite temperature viscosity to about -4, obtained by VFT fittings, -3 by MYEGA and -1.5 by AM. From the systematic study of viscosity carried out in several phosphate glass systems throughout this work by fitting the experimental viscosity values to the three viscosity models, the extrapolated infinite temperature viscosity are -2.3±1.1 by VFT fittings, -0.2±0.6 by AM and -1.0±0.9 by MYEGA. These values are

significantly different and lower in absolute terms from those obtained for silicate glasses, which is in accordance with the more fragile character of phosphate glasses. In fragile glasses, the viscosity range between $T_g$ and the extrapolated infinite temperature viscosity gets shorter, thus the change of viscosity with temperature needs to take place faster.

As pointed out in Chapter II, the addition of kinetic fragility definition by Angell (2.8) to VFT, AM and MYEGA models leads to equations with three adjustable parameters expressed in terms of: kinetic fragility, $T_g$ as defined for a shear viscosity equal to $10^{12}$ Pa.s and the extrapolated infinite temperature viscosity (equations (2.9), (2.10) and (2.11)). As it has been corroborated, the temperature obtained by dilatometry is similar to the one obtained from the fits (c.f. Figure 5.1.), and the values taken for the extrapolated infinite temperature viscosity for phosphate glasses have been deduced, so the two last adjustable parameters can be substituted by fixed values. This approximation will lead to viscosity equations with only one fitting parameter, the kinetic fragility.

The hypothesis stated in this work is that it is possible to obtain the viscosity-temperature curve in the whole temperature range and thus the kinetic fragility value, by fitting only the experimental viscosity data in the low temperature range (i.e. the values obtained by beam bending measurements) and replacing $T_g$ and $\log \eta_\infty$ by fixed values as discussed above. In order to verify this assumption, a ternary metaphosphate glass with composition $25Li_2O.25Na_2O.50P_2O_5$, where the viscosity data has been determined by beam bending and rotation methods in the melt, has been selected for establishing a comparison with the suggested model. The determination of kinetic fragility in this glass will also be useful to study whether the mixed alkali effect is also observed on the kinetic fragility as it does in other transport properties of glasses.

In Figure 5.4 the experimental viscosity data obtained by beam bending and by rotation methods have been represented together with the bests fits to VFT, AM and MYEGA equations. One fit takes into account all the experimental viscosity data and $T_g$, $\log \eta_\infty$ and m as parameters to fit freely (in black). On the other hand, the second fit (in red) only takes into account the viscosity data obtained by beam bending while $T_g$ and $\log \eta_\infty$ have been fixed to the values obtained by dilatometry and by MYEGA fits in phosphate glasses, respectively (c.f. Figure 5.4 caption). Therefore, in this last fit m will be left as the unique parameter to fit freely. The same procedure has been followed for VFT and AM fittings and the fitted curves are represented in Figure 5.5.

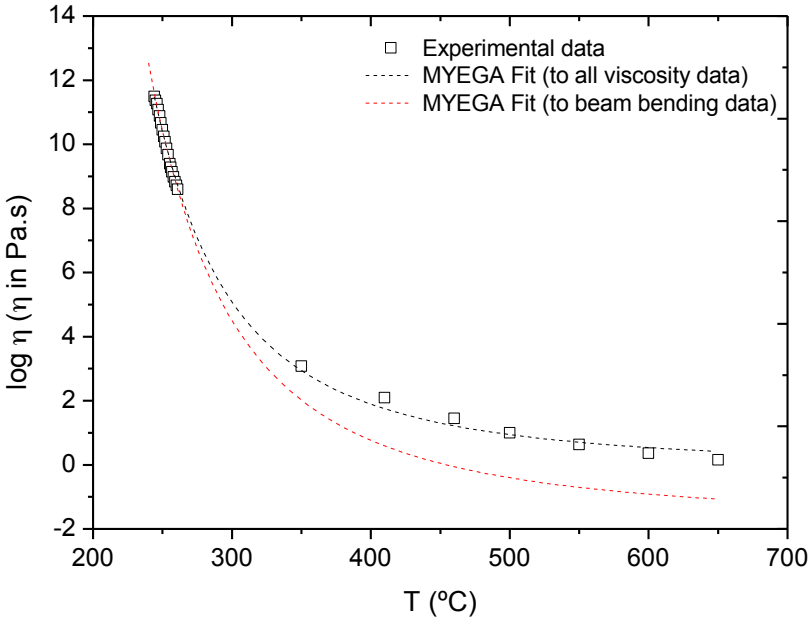


Figure 5.4: Experimentally determined viscosity data points of $25Li_2O.25Na_2O.50P_2O_5$ glass. The dotted line in black corresponds to the best fit of beam bending and rotation experimental data to MYEGA equation as a function of temperature. The dotted line in red corresponds to the best fit of beam bending data. For this last fit $T_g$ value has been fixed to 237ºC ±10 ºC and log $\eta_\infty$ to -1±0.9 Pa.s. Error bars are of the size of the points. The regression coefficient ($R^2$) obtained from the fits were 0.999 and 0.991 respectively.

The values obtained by the three viscosity models represented in Figure 5.4 and 5.5 are collected in Table 5.1 for ease of comparison between both fitting results.

Table 5.1: Kinetic fragility parameter (m), glass transition temperature ($T_g$) and the extrapolated infinite temperature viscosity (log $\eta_\infty$) of $25Li_2O.\ 25Na_2O.50P_2O_5$ glass obtained by VFT, AM and MYEGA models. In all cases the regression coefficient ($R^2$) is higher than 0.998.

| **Parameters** | **Fit to all viscosity data** | | | **Fit to beam bending data** | | |
|---|---|---|---|---|---|---|
| | **VFT** | **AM** | **MYEGA** | **VFT** | **AM** | **MYEGA** |
| **m** | 60 | 52 | 51 | 58 | 41 | 54 |
| **$T_g$** | 243 | 241 | 242 | 243 | 242 | 242 |
| **log $\eta_\infty$** | -1.3 | 0.3 | -0.2 | -2.3 | -0.8 | -1.9 |

As it can be observed, the biggest discrepancy between both fitting methods is found in the extrapolated infinite temperature viscosity. In all cases log $\eta_\infty$ value goes to the lower bound settled when fitting uniquely the beam bending data. As it might be expected, the absence of viscosity data in the high temperature range affects mainly to the log $\eta_\infty$, as the intercept of a rational function limited by a horizontal asymptote on the x axis. On the contrary, a good

agreement is found between both fitting methods on m and $T_g$, which corroborates the hypothesis initially formulated.

In order to try to reduce the difference in log $\eta_\infty$, the viscosity data in the high temperature range could be obtained from $E_a^{low\ T}$ and from equation (5.1) that relates Doremus ratio and kinetic fragility as described in the previous section.

$$R_D=-4.1+0.3m \qquad (5.1)$$

For example, taking the m value obtained by fitting the beam bending values to MYEGA (m=53, c.f. Table 5.1) and following equation 5.1, $R_D$ equals to 11.2. Through the relationship between activation energies from viscous flow that defines Doremus ratio and replacing the values obtained for $25Li_2O.25Na_2O.50P_2O_5$ glass, equation (5.1) turns into $E_a^{high\ T}$= 957 kJ.mol$^{-1}$/11.2 = 85.4 kJ.mol$^{-1}$.

Assuming that $E_a^{high\ T}$ follows an Arrhenian behaviour in the high temperature range and thus being constant with temperature, viscosity values can be deduced giving values to T between 450 ºC and 650ºC following the Arrhenius equation ($\ln \eta=\ln \eta_0 - E_a^{high\ T}/RT$), where $\ln \eta_0$ has been taken as the intercept of VFT, AM and MYEGA curves in the high temperature range (c.f. Figure 5.5 caption). The same procedure has been followed for VFT and AM fittings. The resulting viscosity points are shown coloured in Figure 5.5.

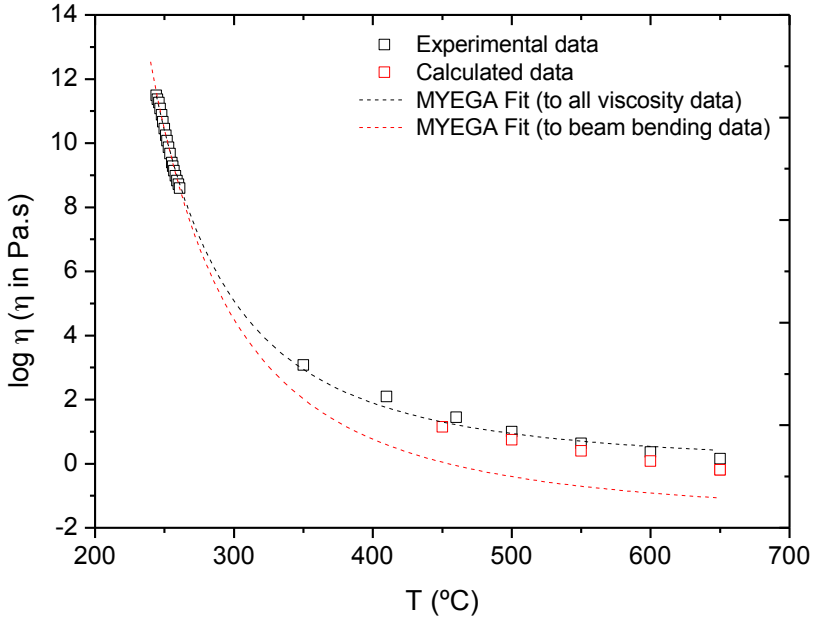

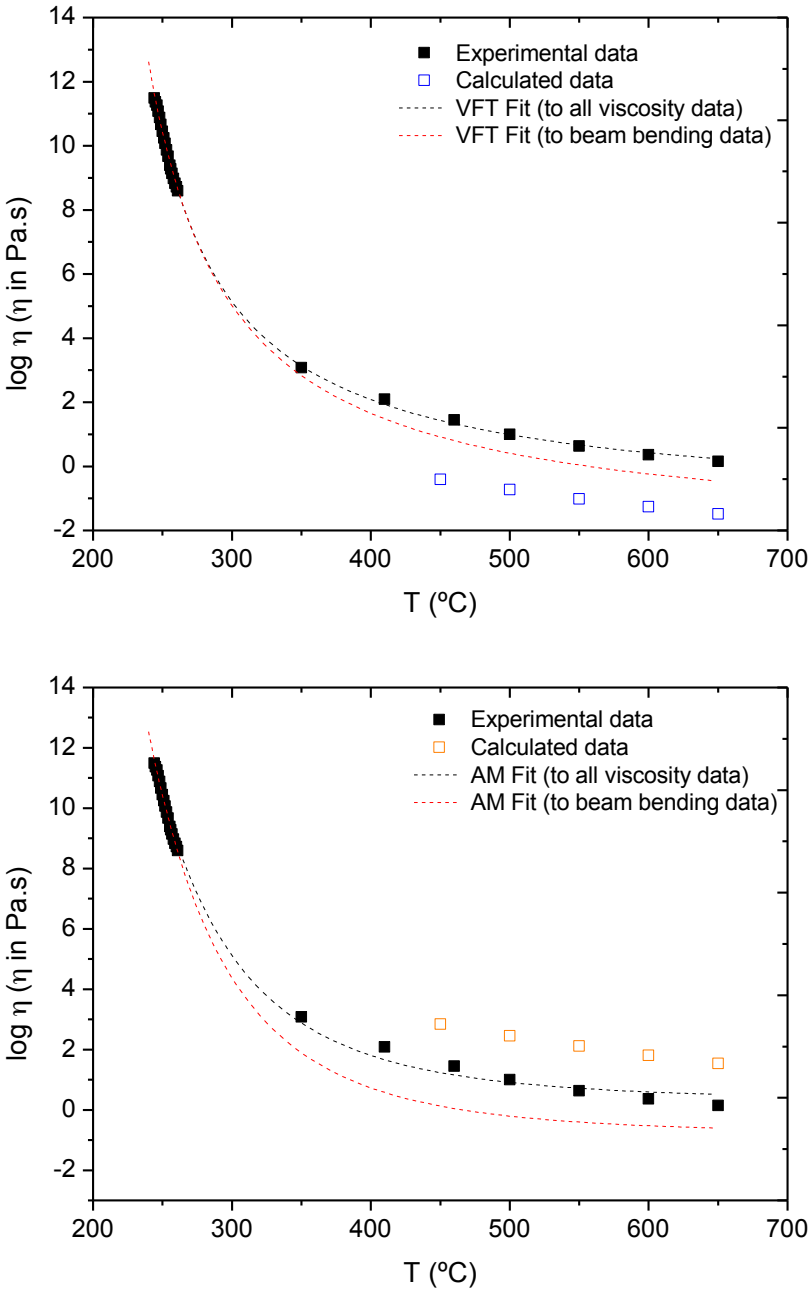


Figure 5.5: Experimentally determined (in black) and calculated (in colour) viscosity data points of $25Li_2O.25Na_2O.50P_2O_5$ glass. The dotted line in black corresponds to the best fit of beam bending and rotation experimental data to MYEGA, VFT and AM equations as a function of temperature. The dotted line in red corresponds to the best fits of beam bending data to the three viscosity models. The intercepts are taken as $\ln \eta_0^{MYEGA} = -11.6$ Pa.s, $\ln \eta_0^{VFT} = -12.4$ Pa.s, $\ln \eta_0^{AM} = -7.3$ Pa.s

As it can be observed now, the calculated viscosity values by MYEGA equation are the closest to the values experimentally determined in the melt, while the calculated values by VFT and AM equations show a greater deviation with respect to the experimental viscosity points. Even though, it is considered that the good agreement found by MYEGA validates the use of the relationship found between $R_D$ and m (equation 5.1) and establishes an alternative way to get the approximated viscosity values in the high temperature range.

It is possible to get an idea about the values that are going to be obtained by fitting now the experimental beam bending data together with the new calculated viscosity points for log $\eta_\infty$ just by looking at the graphs in Figure 5.5, and thus to predict that the most similar results will be obtained by MYEGA. The results collected in Table 5.2 corroborate this point.

Table 5.2: Kinetic fragility parameter (m), glass transition temperature ($T_g$) and the extrapolated infinite temperature viscosity (log $\eta_\infty$) of $25Li_2O.\ 25Na_2O.50P_2O_5$ glass obtained by fitting the calculated data to VFT, AM and MYEGA models. The results shown in Table 5.1 have been repeated here for ease comparison. The values used as inserts for Arrhenius equation (ln $\eta_0$) are -12.4 and -7.3 Pa.s respectively. In all cases the regression coefficient ($R^2$) is higher than 0.9990.

| **Parameters** | **Fit to all viscosity data** | | | **Fit to calculated data** | | |
|---|---|---|---|---|---|---|
| | **VFT** | **AM** | **MYEGA** | **VFT** | **AM** | **MYEGA** |
| **m** | 60 | 52 | 51 | 59 | 90 | 54 |
| **$T_g$** | 243 | 241 | 242 | 243 | 242 | 242 |
| **log $\eta_\infty$** | -1.3 | 0.3 | -0.2 | -3.8 | 2 | -0.5 |

The similarity between experimental and calculated viscosity data at high temperature lead to a better approximation of log $\eta_\infty$ values using MYEGA equation while AM model give rise to higher deviations on the extrapolated infinite temperature viscosity and fragility. Nevertheless, the addition of calculated viscosity data in the high temperature range by MYEGA equation has been proved to be a successful approach to reduce the dramatic deviation of log $\eta_\infty$ to lower values.

### 5.3 Study of the mixed alkali effect on fragility

One of the most widely studied interactions between components in glasses is the mixed-alkali effect, especially for properties based on diffusivity and that implies charge or matter displacement within the glass network, such as the electrical conductivity or viscosity, but its origin is still home for debate. This deviation from additivity is observed in glass compositions with two modifying cations having different ionic field strength (i.e. same valence but different ionic radius) that interact producing a decrease on the diffusion coefficients which leads to a minima on transport properties for molar relations between cations close to 1:1, and thus on a non-linear variation of properties on a glass compositional series.

In the previous section the fragility of the mixed alkali phosphate glass of $25Li_2O.25Na_2O.50P_2O_5$ composition has been deduced from experimentally determined

viscosity data in the low temperature range by fixing two of the three fitting parameters of MYEGA, AM and VFT viscosity models. The average value obtained together with the two binary lithium and sodium metaphosphate glasses ($LiPO_3$ and $NaPO_3$) have been represented in Figure 5.6

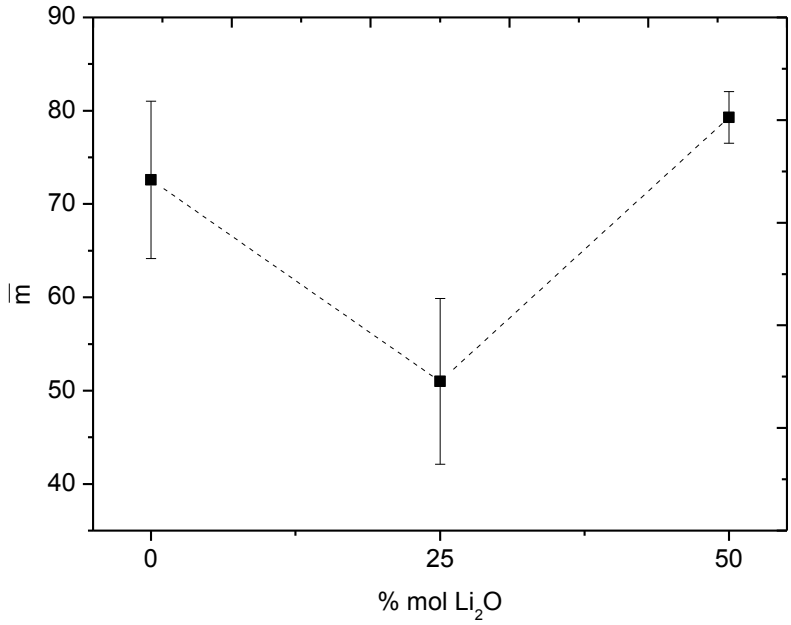


Figure 5.6: Kinetic fragility of $xLi_2O$. $(50-x)Na_2O.50P_2O_5$ glasses as a function of $P_2O_5$ content. Dotted lines are drawn as guide for the eyes.

A clear minimum is observed for the glass composition where the molar ratio between both alkali cations is 1:1. Therefore, the mixed-alkali effect also affects kinetic fragility in this compositional glass system as seen previously in other mixed-alkali metaphosphate glasses [3, 4], unlike in mixed alkali iron phosphate glasses where no maxima or minima is observed with composition [5].

### 5.4 Partial conclusions

The systematic study of viscosity carried out in several phosphate glass systems throughout this work has allowed taking the first steps towards the modelling of glass compositions with desired fragility. By fitting the experimental viscosity values obtained to VFT, AM and MYEGA viscosity models, the extrapolated infinite temperature viscosity has been deduced as well as the glass transition temperature.

A linear relationship has been found between $T_g$ values, as obtained through the viscosity models, and glass transition temperature determined experimentally by dilatometry, which constitutes a good evidence to validate the $T_g$ and m parameters obtained from the fits.

The results obtained have made possible to get the viscosity-temperature curve in the whole temperature range and the kinetic fragility value by fitting only the experimental viscosity data in the low temperature range and replacing $T_g$ and log $\eta_\infty$ of viscosity models by the fixed values found. The similarity with the viscosity curve that takes into account viscosity points in the low and high temperature ranges reveals that m and $T_g$ are mainly controlled by the viscosity data near the glass transition range, highlighting the importance of having enough experimental viscosity data, and the more accurate as possible, within this range.

Viscosity points in the high temperature range were calculated from Doremus ratio definition and the equation deduced from the linear correlation found between $D_R$ and m through $E_a^{high T}$. The calculated viscosity values were very similar to the values experimentally determined in the melt, which validates the use of the relation found between $R_D$ and m and establish an alternative way to get approximated viscosity values in the high temperature range. Thus, saving time and costs derived from the use of experimental techniques where high temperatures are needed for measuring viscosity in melts.

The determination of kinetic fragility through this method in a Li-Na metaphosphate glass with a molar ratio between modifying cations of 1:1 shows that mixed alkali effect can also be observed on kinetic fragility.

A general relationship between the local structure observed in phosphate glasses and kinetic fragility was not possible to achieve, which underlines the inherent difficulties to reach a clear conclusion about the dependence of fragility on the medium range order structure.

### 5.5 References

[1] Y. Yue, J. of Non-Cryst. Solids 355 (2009) 737–744

[2] J.C. Mauro, Y.Z. Yue, A.J. Ellison, P.K. Gupta, D.C. Allan, Proc. Natl. Acad. Sci. U. S. A. 106 (2009) 19780–19784.

[3] J. P. Poole, J. Am. Ceram. Soc. 32 (1949) 230

[4] S.V. Nemilov, J. Appl. Chem. URSS 42 (1969) 46

[5] X. Fang, C. S. Ray, D. E. Day, J. of Non-Cryst. Solids 319 82003) 314

# Chapter VI

# Study of fragility in mixed glass former glasses

## Chapter VI: Study of the mixed former effect on fragility

In recent years, borophosphate glasses have received increasing attention because of their interesting optical and electrical properties. It is well known that these glasses, where two glass formers are mixed, show a pronounced non-linear change in their properties, such as ionic conductivity [1-15], density [16], glass transition temperature [8, 14, 17-20] or chemical durability [21-24], which is commonly known as the so-called mixed network former effect (MGFE). In addition, these properties are generally enhanced in the mixed compositions when compared with to the pure borate or phosphate glasses, leading to improved chemical durability and thermal and mechanical stability [25-27] and making borophosphate glasses to find applications in batteries, glass seals and low melting glass solders [28, 29], in non-linear optical devices [30] or as degradable temporary implants [21, 22].

In the light of the wide literature found about structural studies in borophosphate glasses [3, 8, 9, 11, 13, 20, 31-43], it is noteworthy the effort made by the glass community to better understand the effect of composition on structure and on physical properties, and to bring some light to the MGFE in order to predict the compositional dependence of the properties. In this regard, the results achieved in the works that have been recently published are promising, where the MGFE has been quantitatively explained by the temperature dependent constraint theory and a topological model has been established for alkali and calcium borophosphate glasses [44], and where glass transition temperatures have been modeled for sodium borophosphate glasses through the topological constraint theory [45]. On the other hand, structural models have also been developed based on the obtaining 3D atomic structures from diffraction data by Reverse Monte Carlo (RMC) simulation [38, 46]. Nevertheless, to the best of the author´s knowledge just few works address a systematic study on the rheological properties of alkali borophosphate glasses through the determination of their fragility [44, 47]. However, a complete knowledge of the viscosity behaviour with temperature of these glasses is essential for the establishment of the parameters for applications such as fibre processing, where the prediction of the drawing point with enough accuracy is required. The next chapter will be entirely devoted to this aspect.

The aim of this work is to revisit the structural studies by means of $^{11}B$ and $^{31}P$ MAS-NMR measurements performed on a high field magnet (800MHz) on the one hand, and to complete the study on transport properties carried out by Muñoz *et al.* [14] on a series of lithium borophosphate glasses where the dependence of $T_g$ and ionic conductivity on boron

addition were studied, on the other. For this purpose, the effect of the addition of boron on the viscosity behavior on a series of lithium and sodium borophosphate glasses was studied through the determination of the activation energy for viscous flow and kinetic fragility. The structural changes in the short and medium range order structure caused by the mixing of two glass former network will be followed to elucidate whether they are the underlying cause of the mixed glass former effect, if observed on kinetic fragility.

## 6.1 Materials and methods

### 6.1.1 Glass melting

Lithium and sodium borophosphate glasses with compositions $50Li_2O.xB_2O_3.(50\text{-}x)P_2O_5$ (x= 5-15; 50) and $50Na_2O.xB_2O_3.(50\text{-}x)P_2O_5$ (x= 5-25), were prepared by conventional melt-quenching techniques. Reagent grade raw materials analytically pure, $Li_2CO_3$ (Sharlau, ACS), $(NH_4)_2HPO_4$ (Sharlau, ACS) and v-$B_2O_3$ ($B_2O_3$ previously melted at 800ºC) were mixed and the batches were calcined in porcelain crucibles up to 450ºC in an electric furnace and melted during 1 h at temperatures ranging from 800ºC to 900ºC depending on composition. The melts were poured onto brass moulds and annealed slightly above their glass transition temperature.

The compositional range was limited by the crystallization issues as observed by XDR experiments previously performed [14] and to avoid its influence on the determination of properties. Crystallization and phase separation occurs at 20 and 30 mol % $B_2O_3$ in lithium and sodium borophosphate glasses, respectively, compositions that have been neglected.

### 4.2.1.2 Structure characterization

Magic Angle Spinning (MAS) $^{31}P$ and $^{11}B$ Nuclear Magnetic Resonance (NMR) spectra were recorded on a 18.8 T *Bruker Advance III* spectrometer operating at 324 and 256.8 MHz, respectively. The experiments have been performed using a prototype 3.2 mm $^{11}B/^{31}P$ measurement probe equipped with a B free stator operating at a spinning frequency ($\nu_{rot}$) of 20 kHz. The $^{31}P$ MAS-NMR acquisitions have been recorded with a 2µs pulse length (π/6 pulse angle), a radiofrequency field (rf) strength of 40 kHz, 16-64 transients and a recycle delay (rd) of 120 s. The $^{11}B$ MAS-NMR experiments have been acquired with a 1 µs pulse length (π/12 pulse angle), a rf strength of 40 kHz, 1024-2048 transients and a rd of 2 s. The spectra have been simulated using the Gaussian/Lorentzian model available in the dmit

software. The $^{11}B$ and $^{31}P$ chemical shift values have been referred to liquid $H_3PO_4$ (85%) and solid $NaBH_4$ at 0 and -604.3 ppm respectively.

All the MAS-NMR spectra collected in this chapter has been performed in the facilities of Université de Lille 1, France in collaboration with the Laboratoire de Spectrochemie Infrarrouge et Raman in Lille, France.

Raman spectroscopy analyses were performed on a *WItec Alpha300RA* Raman-AFM confocal spectrometer with 532 nm laser wavelength excitation and 39 mW power in the range of 220-3800 $cm^{-1}$. The laser polarization angle was in x axis. Polished glass samples around 2 mm thick were used. The precision in the determination of the Raman shifts is ± 1 $cm^{-1}$.

#### 4.2.1.3 Properties characterization

Glass transition temperature ($T_g$) was determined from the thermal expansion curves of the glasses obtained in air with a *Netzsch Gerätebau* dilatometer, *model 402 PC/1* at a heating rate of 2 $K.min^{-1}$. Prismatic samples around 10 mm in length were used for the measurements. The estimated error in $T_g$ is ± 1K.

The density of the glasses was measured by helium pycnometry in a *Quantachrome Corp*. multipycnometer on bulk samples (±0.01$g.cm^{-3}$). The molar volume ($V_m$) was calculated from the relation between the molar mass (M) and the density ($\rho$) of the glass ($V_m$=M. $\rho^{-1}$).

The viscosity-temperature curves of the glasses were determined using the rotation and beam-bending methods at high and low temperature ranges, respectively. The viscosity of the melts in the range $10^3$–$10^1$ dPa.s was determined employing a high-temperature Haake viscometer of the cylindrical Searle type (*Haake, Karlsruhe, Germany*) equipped with a ME 1700 sensor. Rotation speeds of 3 to 15 rpm were used for 15 min, following the International Standard ISO 7884-2.

Within the viscosity range $10^{12.5}$–$10^9$ dPa.s viscosity was measured by bending glass beams heated at a rate of 2 $K.min^{-1}$ and using weights of 10 to 200 g. A viscometer *VIS401 (Bähr Thermoanalyse, Germany*) with a 40 mm open span in symmetric three point mode was employed. The viscosity was calculated according to the standard testing conditions DIN ISO 7884-4. For further details about the experimental procedure followed to determine the viscosity, the reader is referred to the Chapter III of this thesis.

## 6.2. Structural characterization

### 6.2.1 $^{31}$P and $^{11}$B MAS NMR spectroscopy

The addition of $B_2O_3$ is going to produce changes on the $^{31}$P local environment. On the other hand, it is expected that changes on the boron coordination number also occur when the boron concentration is progressively increasing in the glass systems where the modifying oxide content is kept constant, given rise to the coexistence of three and four-fold coordinated boron species, $BO_3$ and $BO_4$ species. This change on the speciation of phosphorus and boron atoms is depicted in Figures 6.1 and 6.2 for both lithium and sodium borophosphate glass series, respectively.

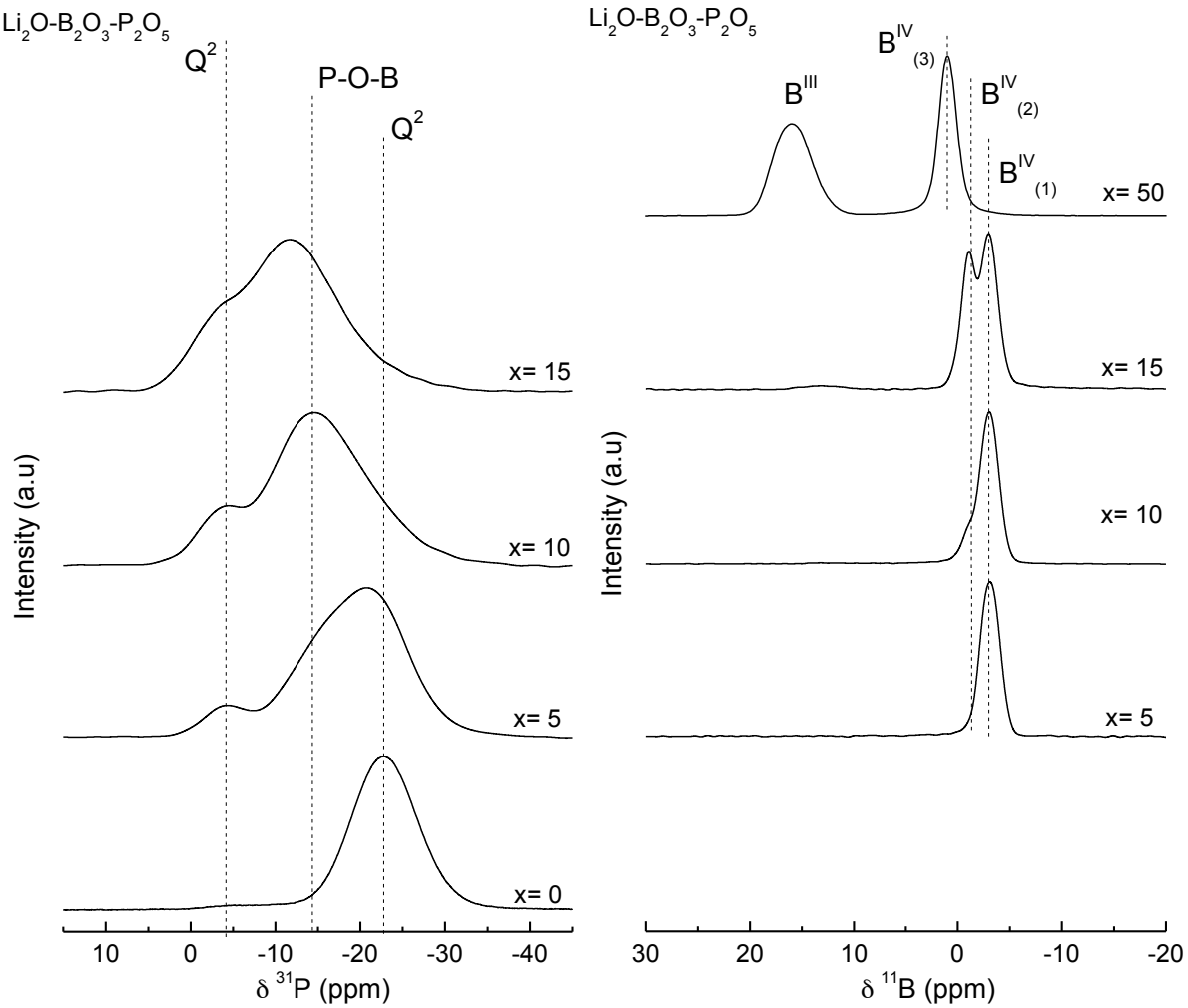


Figure 6.1: $^{31}$P MAS NMR spectra (left) and $^{11}$B spectra of $50Li_2O.xB_2O_3.(50\text{-}x)P_2O_5$ glasses (right) where x denotes the $B_2O_3$ content in each glass.

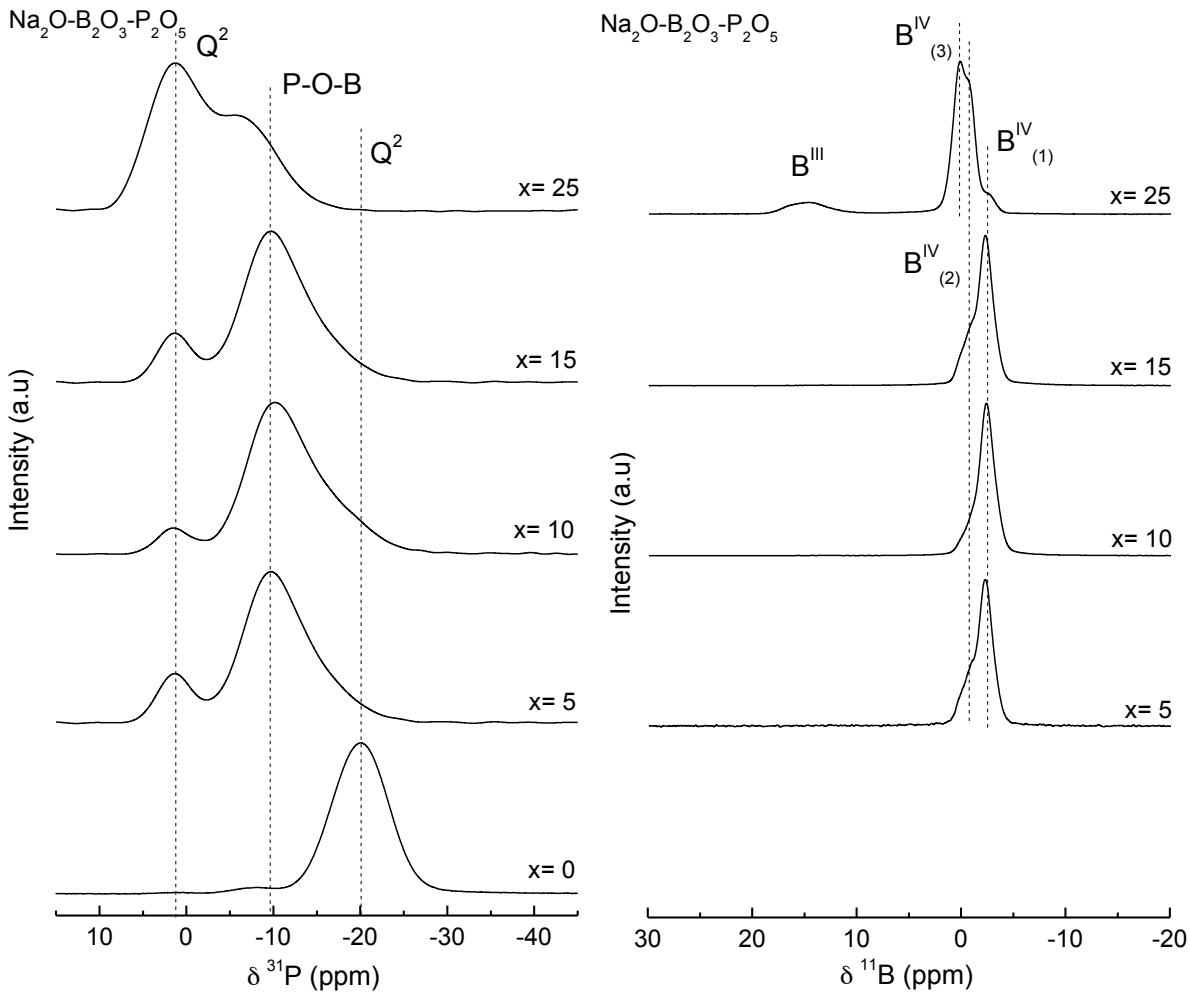


Figure 6.2: $^{31}P$ MAS NMR spectra (left) and $^{11}B$ spectra of $50Na_2O.xB_2O_3.(50\text{-}x)P_2O_5$ glasses (right) where x denotes the $B_2O_3$ content in each glass.

It can be observed that important changes on the $^{31}P$ environment take place with boron addition together with the broadening of the resonance bands. This provides limited information about the phosphate speciation, but with the naked eye it can be concluded from the spectral line shape that the addition of boron do not cause the same speciation on the lithium and sodium borophosphate glass systems. However, as phosphorous is substituted by boron in the network of the alkali ternary glasses, the resonance attributed to $Q^2$ units and the global chemical shift of the other resonances appears toward positive values. This shift indicates that the phosphorous nucleus is becoming less shielded by the electrons surrounding the nucleus.

The increase in $B_2O_3$ content leads to the increase in the intensity of the $Q^1$ units and to the broadening of the resonance that could be attributed to P-O-B groups and the decrease in the $Q^2$ units, bringing to light the depolymerization of the phosphate network.

But on the other hand, it is not clear to distinguish how many types of phosphate units, $Q^2$ and $Q^1$, and in which proportion, are bonded to either $BO_3$ or $BO_4$ boron groups. Therefore, a transition from a phosphate to a borophosphate glass network is expected to occur due to the affinity between boron and phosphorous, but it cannot be demonstrated by simple 1D spectra.

In a recent work, Tricot *et al*. [48] have shown for tin borophosphate glasses, that a deeper investigation of the B-O-P linkages can be performed using $^{11}B$ ($^{31}P$) D-HMQC sequences through the 2D maps obtained and that the transition from a pure phosphate to a borophosphate glass network is confirmed by the resulting correlations.

On the contrary, $^{11}B$ MAS-NMR spectra are highly resolved for both alkali phosphate systems, thus providing interesting information about the local order of the borate species. Compared with the spectra obtained in the previous work [14] it can be seen the improvements achieved with regard to the spectral resolution of a high magnetic field. Threefold boron ($B^{III}$) and fourfold ($B^{IV}$) can be easily distinguish through the chemical shift values. $B^{IV}$ resonance appears from -3 to 3 ppm while $B^{II}$ appears around 15 ppm in the glass with x=50 glass (c.f. Figure 6.1) and in x=25 glass in the sodium borophosphate glass system. $B^{III}$ groups appear at high boron contents, thus it is clear that boron enter first in the glass network as four-fold coordinated before being replaced by $BO_3$ groups. The high magnetic field employed to run the experiments allow also to distinguish between different $B^{IV}$ groups labeled in the figures as $B^{IV}_{(1)}$, $B^{IV}_{(2)}$, and $B^{IV}_{(3)}$, appearing each signal at -3, -1 and 1 ppm, respectively in the lithium borophosphate glasses and at -2, -0.7 and 0 ppm in the sodium borophosphate ones. In order to quantify and show clearly the evolution of the different borate species in all the compositional range in both glass systems, the spectra have been simulated and the evolution of the relative proportions of $B^{IV}$ groups as a function of $B_2O_3$ content has been represented in Figure 6.3.

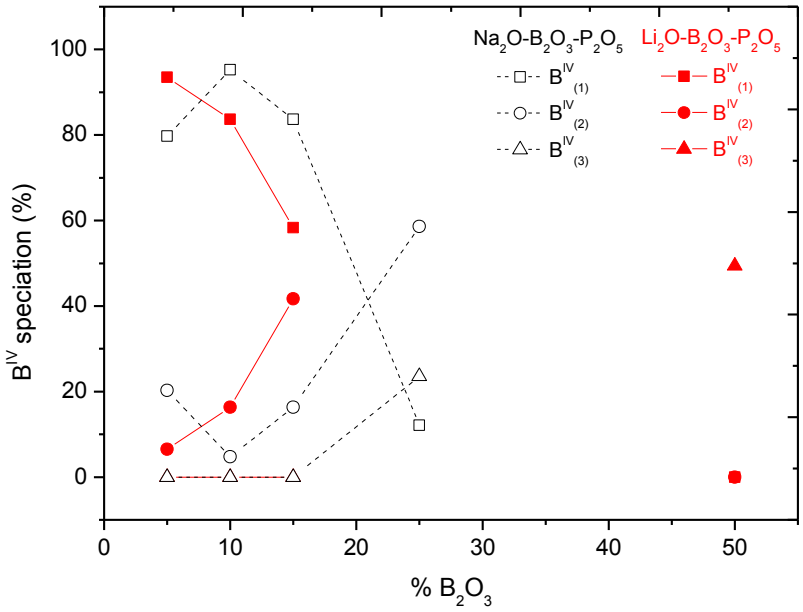


Figure 6.3: Evolution of the boron speciation of $50Li_2O.xB_2O_3.(50\text{-}x)P_2O_5$ (black) and $50Na_2O.xB_2O_3.(50\text{-}x)P_2O_5$ glasses (red) as a function of $B_2O_3$ content. Dotted lines are drawn as guide for the eyes.

As it can be observed in the graph, $B^{IV}_{(1)}$ is the main species that appear after the first addition of boron oxide and decreases from x=5 in the lithium borophosphate glass system. On the contrary, for sodium borophosphate glasses, $B^{IV}_{(1)}$ starts decreasing only after $B_2O_3$ in the glass network is higher (i.e. from x=10 glass composition). Therefore, it can be observed that the proportions of $B^{IV}_{(1)}$ and $B^{IV}_{(2)}$ are reversed in the compositional range between 5 and 10 mol% of $B_2O_3$, leading to a higher proportion of $B^{IV}_{(1)}$ for the compositions with Na than with Li.

### 6.2.2 Raman spectroscopy

The Raman spectra of lithium and sodium borophosphate glasses are summarized in Figure 6.4. The addition of boron to the binary phosphate glasses causes several modifications in the glass structure as the spectra show, in agreement with the results obtained by NMR.

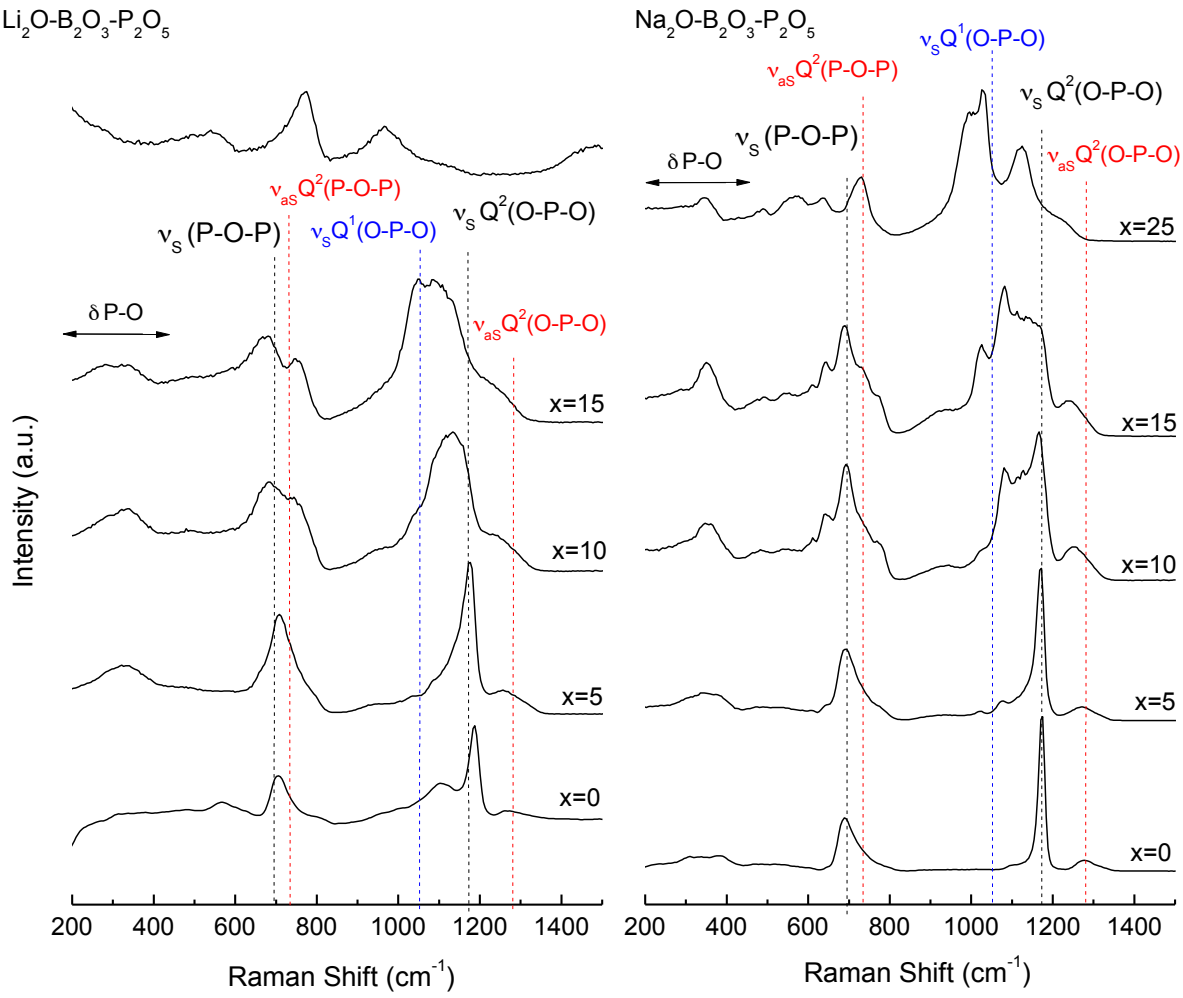


Figure 6.4 Raman spectra of $50Li_2O.xB_2O_3.(50-x)P_2O_5$ (left) and $50Na_2O.xB_2O_3.(50-x)P_2O_5$ glasses (right) where x denotes the $B_2O_3$ content in each glass.

The trends observed are in agreement with previous publications on these two glass systems with similar compositions found in the literature [13, 47]. For easier interpretation, the Raman spectra were scaling to the same intensity for the strongest peak due to the big intensity difference between the modes arising from the borate and phosphate structural units as a result of the stronger Raman scattering cross section of the last ones. The Raman spectra of the binary metaphosphate glasses (x=0) are both dominated by two main bands. The peaks appearing at 1174 $cm^{-1}$ for $NaPO_3$ glass and 1187 $cm^{-1}$ for $LiPO_3$ are attributed to the symmetric $PO_2$ stretching modes involving non-bridging oxygen atoms (O-P-O). The P-O bond symmetric vibrations that are part of P-O-P bridges arise at 690 $cm^{-1}$ for $NaPO_3$ glass and at 706 $cm^{-1}$ for $LiPO_3$. It can be also observed at 1270 $cm^{-1}$ in both metaphosphate glasses the band attributed to the asymmetric stretching mode of O-P-O bonds in $Q^2$ groups [49, 50, 51]. The glasses exhibit also a band with small amplitude around 350 $cm^{-1}$which has been attributed to the phosphate bending-network vibrations. As the $B_2O_3$ content is

increased replacing phosphorous, a new peak appears at about 1000 $cm^{-1}$ attributed to $Q^1$ units as an evidence of the introduction of the dominant fourfold coordinated boron atoms breaking the phosphate network. This band becomes progressively more intense as the band attributed to symmetric stretching mode of O-P-O bonds in $Q^2$ unit shifts toward lower frequency and decreases in intensity. These effects along with a gradual replacement by a broader signal near 1100 $cm^{-1}$ in both systems can be attributed to the boron linked to $Q^2$ and $Q^1$ units. The peak at 690 $cm^{-1}$ for $NaPO_3$ glass and at 706 $cm^{-1}$ for $LiPO_3$ decreases in intensity and develops shoulders at higher $B_2O_3$ contents that reveal the formation of B-O-P groups. These bands are transformed into a broad intense peak at the binary sodium borate glass composition around 800 $cm^{-1}$. This new band has been related to B-O-B stretching modes [52] involving bridging oxygen atoms that are associated to metaborate superstructural units composed of three trigonal boron units that form a six-membered ring called boroxol ring as found in vitreous-$B_2O_3$ [53]. The presence of threefold coordinated boron is confirmed in the $^{11}B$ MAS NMR spectra for glasses with more than 20 mol % of $B_2O_3$ in both alkali borophosphate glass systems. The pure sodium borate shows a strong band near 1400 $cm^{-1}$, which can be assigned to B-O stretching vibrations associated with non-bridging oxygen atoms. The absence of this vibrational mode from the spectra of all the other lithium and sodium borophosphate glasses suggests that there are no appreciable amounts of non-bridging oxygen species.

The analysis of the Raman spectra confirms that the incorporation of $B_2O_3$ leads to a depolymerization of the phosphate network through the incorporation of $BO_4$ structural units, breaking and shortening phosphate chains until a point where the preferred fourfold coordinated boron atoms begin to switch to threefold coordination leading to a decrease of B–O–P bonds [7, 18, 26, 52, 54]. In this current investigation it is observed for a B/(B + P) ratio higher than 0.4 which corresponds to x=20 glass composition.

### 6.3. Transport properties

#### 6.3.1 Viscosity

The temperature dependence of viscosity in the glasses under study was evaluated using the three viscosity models as in the previous chapters. The experimental results together with the best fits to MYEGA model as an example have been represented in Figure 6.5. As it can be noted, an increase of $B_2O_3$ content in both alkali borophosphate systems results in a clear shift of the log η to higher temperatures except for x=10 and x=15 glass compositions which both show similar viscosity values in the low temperature range. This behaviour is also

observed by Gaylord et al. in the same glass system between two similar glass compositions [47].

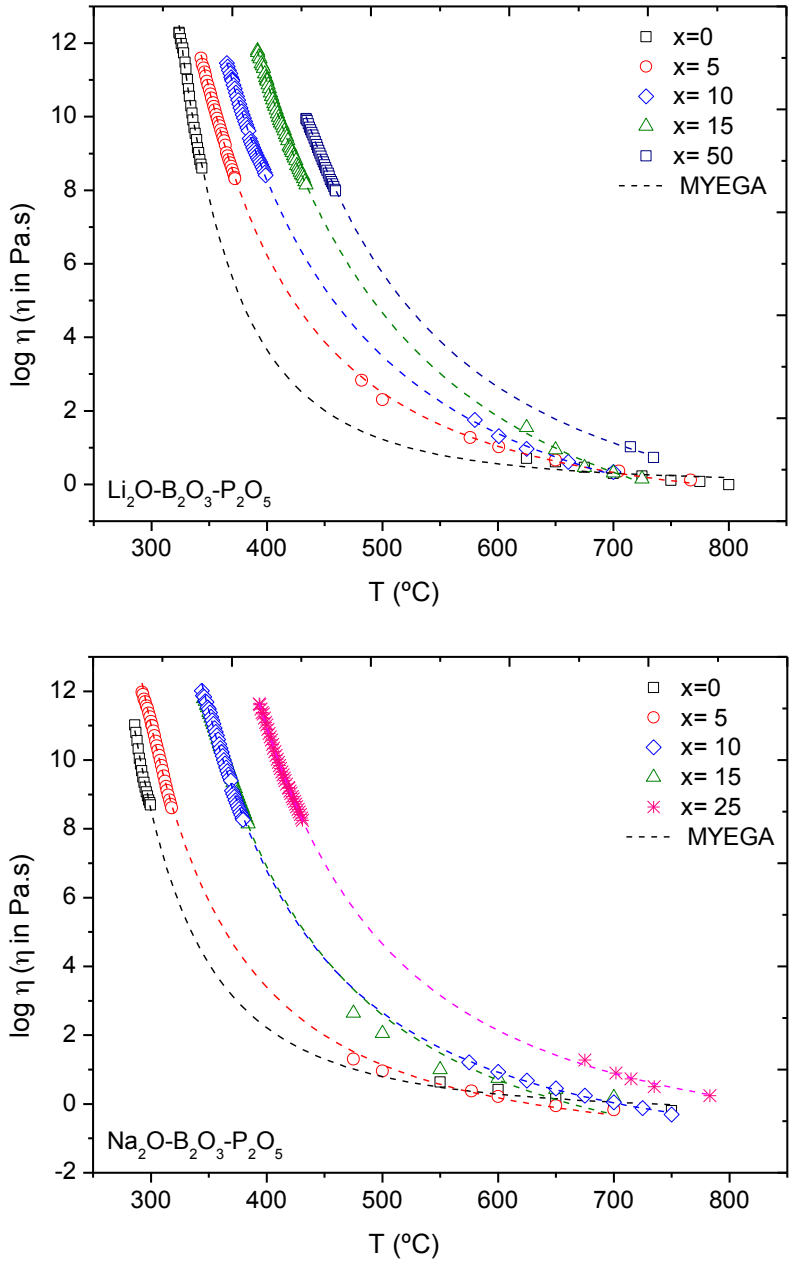


Figure 6.5: Viscosity data points of $50Li_2O.xB_2O_3.(50\text{-}x)P_2O_5$ (top) and $50Na_2O.xB_2O_3.(50\text{-}x)P_2O_5$ glasses (bottom) and best fits of the experimental values to MYEGA equation as a function of temperature. Error bars are of the size of the points. The regression coefficient ($R^2$) obtained from the fits to the three models was 0.999, or better.

The average of the kinetic fragility values obtained from VFT and MYEGA equations are collected in Table 6.1. It was considered not to include the values obtained from AM model to calculate m average value for all the glass compositions due to the high difference observed with the other two models that dramatically increases the standard deviation.

Table 6.1: Kinetic fragility parameter of $50Li_2O.xB_2O_3.(50-x)P_2O_5$ and $50Na_2O.xB_2O_3.(50-x)P_2O_5$ glasses obtained from VFT, AM and MYEGA models.

| Glass composition | Glass code | m | | |
|---|---|---|---|---|
| | | VFT | AM | MYEGA |
| **$50Li_2O.xB_2O_3.(50-x)P_2O_5$** | | | | |
| $50Li_2O.50P_2O_5$ | **x=0** | 78 | 100 | 83 |
| $50Li_2O.5B_2O_3.45P_2O_5$ | **x=5** | 54 | 42 | 50 |
| $50Li_2O.10B_2O_3.45P_2O_5$ | **x=10** | 43 | 22 | 43 |
| $50Li_2O.15B_2O_3.45P_2O_5$ | **x=15** | 44 | 10 | 43 |
| $50B_2O_3.50P_2O_5$ | **x=50** | 49 | 30 | 46 |
| **$50Na_2O.xB_2O_3.(50-x)P_2O_5$** | | | | |
| $50Na_2O.50P_2O_5$ | **x=0** | 72 | 81 | 65 |
| $50Na_2O.5B_2O_3.45P_2O_5$ | **x=5** | 51 | 37 | 49 |
| $50Na_2O.10B_2O_3.45P_2O_5$ | **x=10** | 49 | 30 | 47 |
| $50Na_2O.15B_2O_3.45P_2O_5$ | **x=15** | 46 | 21 | 45 |
| $50Na_2O.25B_2O_3.45P_2O_5$ | **x=25** | 48 | 33 | 46 |

The average value obtained for both alkali borophosphate glass systems is illustrated in Figure 6.6 as a function of $B_2O_3$ content.

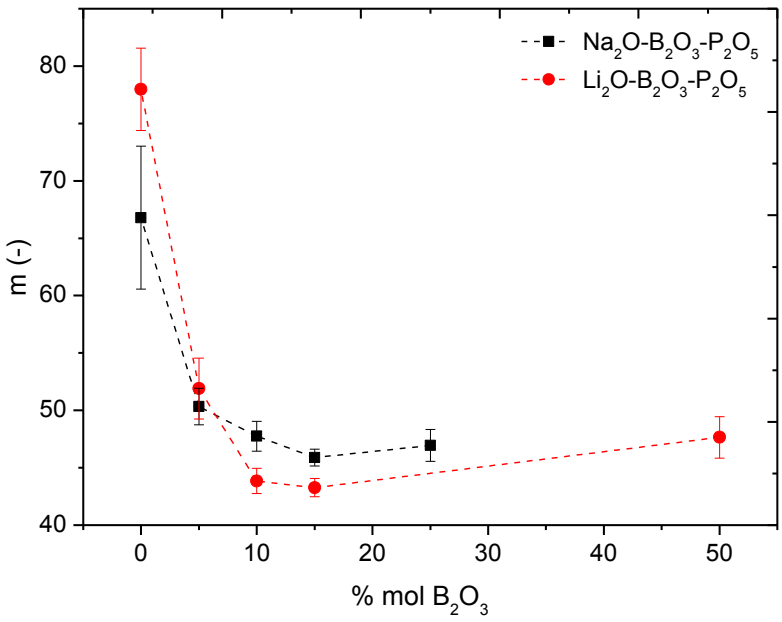

Figure 4.31: Kinetic fragility of $50Li_2O.xB_2O_3.(50-x)P_2O_5$ and $50Na_2O.xB_2O_3.(50-x)P_2O_5$ glasses as a function of $B_2O_3$ content. Dotted lines are drawn as guide for the eyes.

The kinetic fragility parameter, m, decreases for both alkali borophosphate glass systems suggesting that the glass network becomes stronger and therefore more rigid, with increasing $B_2O_3$ content until x reaches a value of x=15, as seen in Figure 4.31. This behaviour has been seen in previous works with similar glass systems [47]. From that glass composition onward, an increasing $B_2O_3$ content causes m to remain almost constant suggesting that the glass network has stabilized in a more rigid form.

This behaviour can be explained based on the evolution of the glass structure with $B_2O_3$ content as in the previous section. With the first additions of boron, this enters the glass network as fourfold coordinated, thus increasing the connectivity degree of the borophosphate glass network and leading to a more rigid glass network with a less pronounce variation of viscosity with temperature (i.e. lower kinetic fragility). By means of Raman and $^{11}B$ MAS-NMR experiments the presence of trigonal boron is confirmed for glass compositions with x=20 for both alkali borophosphate glasses. The change on coordination from B(IV) to B(III) is supposed to create a less reticulated network that counteracts the effect of replacing phosphorous by boron, and thus the increase of the overall covalent character of the glass network.

Comparing both alkali borophosphate glass systems, it can be observed that the tendency to present higher fragility values observed for the glasses with Na is reversed in the compositional range between 5 and 10 mol % of $B_2O_3$. This behavior has been also observed in B(IV) speciation. It seems that a higher proportion of $B^{IV}_{(1)}$ leads to higher kinetic fragility. From the 1D spectra it could not be extracted conclusions about the P-O-B linkage, either about the different local environments around boron that leads to different boron sites. Since $B^{IV}_{(1)}$ groups dominate the glass network with the first additions of boron, it could be expected that boron of the $B^{IV}_{(1)}$ type will be linked to $Q^2$, and thus this types of linkage is the one responsible of a less rigid network but, as discussed before, 2D spectra would be needed to confirm this point and to shed some more light into the dependence of fragility on the different B-O-P linkages.

### 6.4 Partial conclusions

The structural characterization of a series of alkali borophosphate glasses has been revisited by means of MAS-NMR experiments performed at a very high field. The field applied has allowed to distinguish between different types of B(IV) groups in the glass

network, contrary to the expectation of a single species with a changing environment. On the other hand, the broadness of the $^{31}P$ resonances does not allow confirming a borophosphate glass network. The presence of B(III) groups was confirmed by means of Raman and NMR.

The variation of kinetic fragility with increasing boron content has been related with the changes on boron coordination observed in the structure.

It has been observed that a higher proportion of $B^{IV}_{(1)}$ groups in the glass network leads to higher fragility values.

### 6.5 References

[1] R. V. Salodkar, V. K. Deshpande, and K. Singh, J. Power Sources 25 (1989) 257.

[2] A. Magistris, C. Gaetano, and M. Duclot, Solid State Ionics 9-10 (1983) 611.

[3] M. Storek, R. Böhmer, S. W. Martin, D. Larink, and H. Eckert, J. Chem. Phys. 137, (2012) 124507.

[4] S.Kumar, P.Vinatier, A. Levasseur, and K. J. Rao, J. Solid State Chem. 177 (2004) 1723.

[5] S. Lee, J. Kim, D. Shin, Solid State Ionics 178 (2007) 375–379

[6] T. D. Tho, R. P. Rao, and S. Adams, Eur. Phys. J. E 35 (2012) 8.

[7] P.S. Anantha, K. Hariharan Materials Chemistry and Physics 89 (2005) 428–437

[8] D. Zielniok, C. Cramer, H. Eckert, Chem. Mater. 19 (2007) 3162−3170

[9] M. Villa, M. Scagliotti, G. Chiodelli, J. Non-Cryst. Solids. 94 (1987) 101− 121.

[10] L. Koudelka, P. Mosner, M. Zeyer, C. Jager, J. Non-Cryst. Solids. 351 (2005) 1039−1045.

[11] M. Zeyer-Dusterer, L. Montagne, G. Palavit, C. Jager, Solid State Nucl. Magn. Reson. 27 (2005) 50−64.

[12] D. Qiu, P. Guerry, I. Ahmed, D. M. Pickup, D. Carta, J. K. Knowles, M. E. Smith, R. J. Newport, Mater. Chem. Phys. 111 (2008) 455−462.

[13] R. Christensen, G. Olson, and S. W. Martin, J. Phys. Chem. B 117 (2013) 16577−16586

[14] F. Muñoz, L. Montagn, L. Pascual, A. Durán, J. Non-Cryst. Solids 355 (2009) 2571–2577

[15] N.K. Karan, B. Natesan, R.S. Katiyar, Solid State Ionics 177 (2006) 1429–1436

[16] R. Christensen, J. Byer, G. Olson, S. W. Martin, J. Non-Cryst. Solids 358 (2012) 583–589

[17] B. Raguenet, G. Tricot, G. Silly, M. Ribes, A. Pradel, Solid State Ionics 208 (2012) 25.

[18] L. Koudelka, P. Mosner, Mater. Lett. 42 (2000) 194

[19] R. Christensen, J. Byer, G. Olson, S. W. Martin, J. Non-Cryst. Solids 358 (2012) 826

[20] D. Carta, D. Qiu, P. Guerry, I. Ahmedb, E. A. Abou Neel, J. C. Knowles, M. E. Smith, R. J. Newport, J. Non-Cryst. Solids 354 (2008) 3671–3677

[21] N. Sharmin, M. S. Hasan, A. J. Parsons, D. Furniss, C. A. Scotchford, I. Ahmed, C. D. Rudd, BioMed Res. Int. 902427 (2013).

[22] A. Saranti, I. Koutselas, M. A. Karakassides, J. Non-Cryst. Solids 352 (2006) 390.

[23] N.J. Kim, S. H. Im, D.H. Kim, D.K. Yoon, B.-K. Ryu, Electron. Mater. Lett. 6 (2010) 103.

[24] I. J. Hidi, G. Melinte, R. Stefan, M. Bindea, and L. Baia, J. Raman Spectrosc. 44, (2013) 1187.

[25] H. Takebe, T. Harada, M. Kuwabara, J. Non-Cryst. Solids 352 (2006) 709.

[26] J.F. Ducel, J.J. Videau, Mater. Lett. 12 (1992) 271.

[27] N. Sharmin, A. J. Parsons, C. D. Rudd, I. Ahmed, J. of Biomaterials Aplications 29 (5) (2014) 639-653.

[28] L. Koudelka, P. Mošner, M. Zeyer, C. Jäger, J. Non-Cryst. Solids 326&327 (2003) 72.

[29] R. K. Brow, D. R. Tallant, J. Non-Cryst. Solids 222 (1997) 396-406

[30] V. Nazabal, E. Fargin, C. Labrugère, G. Le Flem, J. Non-Cryst. Solids 270 (2000) 223

[31] D. Larink, H. Eckert, M. Reichert, S.W. Martin, J. Phys. Chem. C 116 (2012) 26162.

[32] B. G. Aitken, R. E. Youngman, Phys. Chem. Glasses: Eur. J. Glass Sci. Technol., Part B 47 (2006) [33] T. Feng, P. Linzhang, J. Non-Cryst. Solids 112 (1989) 142.

[34] S. Elbers, W. Strojek, L. Koudelka, and H. Eckert, Solid State Nucl. Magn. Reson. 27 (2005) 65.

[35] M. Villa, K. R. Carduner, J. Solid State Chem. 69 (1987) 19.

[36] R. K. Brow, J. Non-Cryst. Solids 194 (1996) 267.

[37] V. K. Michaelis, P. Kachhadia, S. Kroeker, Phys. Chem. Glasses: Eur. J. Glass Sci. Technol., Part B 54 (2013) 20.

[38] M. Schuch, R. Christensen, C. Trott, P. Maass, S. W. Martin, J. Phys. Chem. C 116, 1503 (2012).

[39] Y. Jin, X. Chen,, X. Huang, J. Non-Cryst. Solids 112 (1989) 147.

[40] M. T. Rinke , H. Eckert, Phys. Chem. Chem. Phys. 13 (2011) 6552.

[41] R. Christensen, J. Byer, T. Kaufmann, S. W. Martin, Phys. Chem. Glasses: Eur. J. Glass Sci. Technol., Part B 50 (2009) 237.

[42] Y. H. Yun, P. J. Bray, J. Non-Cryst. Solids 30 (1978) 45.

[43] D. Raskar, M. T. Rinke, H. Eckert, J. Phys. Chem. C 112 (2008) 12530.

[44] C. Hermansen, R. E. Youngman, J. Wang, Y. Yue, J. Chem. Phys. 142 (2015) 184503.

[45] Q. Jiang, H. Zeng, Z. Liu, J. Ren, G. Chen, Z.Wang, L. Sun, and D. Zhao, J. Chem. Phys. 139 (2013) 124502.

[46] M. Karlsson, M. Schuch, R. Christensen, P. Maass, S. W. Martin, S. Imberti, Al.Matic, J. Phys. Chem. C 119 (2015) 27275−27284.

[47] S. Gaylord, B. Tincher, L. Petit, K. Richardson, Materials Research Bulletin 44 (2009) 1031–1035

[48] G. Tricot, A. Saitoh, H. Takebe, Phys. Chem. Chem. Phys., 17 (2015) 29531

[49] M. Braun, Y. Yue, C. Rüssel, C. Jäger, J. of Non-Cryst. Solids 241 (2-3) (1998) 204

[50] B. N. Nelson, G. J. Exarhos, J. Chem. Phys. 71 (1979) 2739

[51] R. K. Brow, D. R. Tallant, S. T. Myers, C. C. Phifer, J. of Non-Cryst. Solids 191 (1995) 45

[52] J. F. Ducel, J. J. Videau, M. Couzi, Phys. Chem. Glasses 35 (5) (1993) 212-218

[53] B.N. Meera, A.K. Sood, N. Chandrabhas, J. Ramakrishna, J. Non-Cryst. Solids 126 (1990) 224–230.

[54] E.T.Y. Lee, E.R.M. Taylor, J. Phys. Chem. Solids 66 (2005) 47–51.

# Chapter VII

# Structure and viscosity relationship applied to fibre drawing of bioactive phosphate glasses

# Chapter VII: Structure and viscosity relationship applied to fibre drawing of bioactive phosphate glasses

## 7.1 Bioactive glasses

Bioactive glasses were the first synthetic biocompatible materials able to interact with the body tissue. Heretofore, implants made from metals and alloys were biotolerant but inert. Their ability to form a strong interfacial bond with the bone cells and to degrade in the body at a rate similar to the bone formation, allows their gradual replacement by the newly formed bone [1]. These excellent properties makes these materials good candidates to develop implants that stimulate bone regeneration instead of their merely replacement.

These biomaterials are mainly based on a silica network structure with ions such as calcium, sodium and phosphorous. In a physiological media, these $SiO_2$-rich glasses release calcium and phosphate ions as a consequence of their degradation and form a double layer consisting on silica gel and calcium phosphate. The ion exchange taking place between alkali and hydrogen ions produces an alkali deficient surface. The hydrolysis of Si-O-Si bonds in the glass results in a silica gel layer, while the calcium phosphate layer is then transformed on a biologically active hydroxyl carbonate apatite layer as a result of the absorption of calcium, phosphate and carbonate ions onto the glass surface and its later crystallization.

The first bioactive glass, Bioglass ® 45S5, was a quaternary glass developed by Larry Hench in 1969 [2] and has been in medical use for nearly thirty years [1]. This glass offers a good implementation *in vivo* for numerous medical and dental applications. Additionally, they degrade over time allowing a controlled release of therapeutically active ions previously incorporated into the glass network [3, 4]. However their high tendency to crystallize due to the highly disrupted silicate structure [5, 6] makes their further processing challenging [7]. On the contrary, glasses with higher working range (e.g. bioactive glasses with high silica content [8]), and therefore good candidates for sintering or fibre drawing without crystallization, show a minor bioactivity [9] and degrade very slowly, with remnants of glass that still being present in the patient after several years [10]. These compositional limitations, together with their poor mechanical properties have diminished so far the range of clinical applications to particulate bioactive glasses and to non-load-bearing uses.

The design of new compositions with improved mechanical stability and suitable for more clinical needs, will require a more structural approach to understand the role of each

component on the glass structure in order to keep unaltered the whole reactivity of the glass while new components are incorporated and/or substituted [11].

### 7.1.1 Phosphate bioactive glasses

Phosphate-based glasses have generated considerable interest due to their potential to be used as active materials for resorbable implants and for hard and soft tissue engineering applications [12]. Their ability to dissolve completely in aqueous media and the possibility to control their degradation rates through tailoring the glass composition is one of their unique properties.

The biocompatibility of phosphate glasses has been related to their dissolution rate, the associated pH variation and the ions release in the media. Several glass systems have been developed by addition of various modifier oxides such as $Fe_2O_3$, $Al_2O_3$, ZnO, $TiO_2$, SrO, $Ag_2O$ and CuO. They offer a great variety of biomedical applications such as dental, maxillofacial and orthopaedic implants or as scaffolds for bone tissue engineering. The highly controllable solution degradation rate of these glasses has also encourage a number of studies for the development of these materials, previously doped, as suitable carriers for *in vivo* antimicrobial ions release such as silver and cooper [12, 13], or for promoting osteoblast cells proliferation as is the case of strontium [14, 15].

### 7.1.2 Phosphate glass fibres

The optical properties of bulk phosphate based glasses and fibres have been the driving force in the development of these materials. Additionally, they present relatively high strength values (typically 500 MPa to 1.2 GPa [16]), and degrade in aqueous media through a surface erosion process that allows the maintenance of properties during degradation [17, 18]. These two last features make them suitable to be used for tissue engineering either directly or as reinforcement phase in completely degradable and anisotropic composite materials [12, 19, 20]. One of the advantages of using these glasses for composites, compared to conventional metallic implants, is the elimination of stress shielding. The similarity between bond and composite stiffness allows the gradual transfer of stress to the healing bone and thus eliminates the need for secondary surgeries to remove the implant in order to avoid a possible resorption of the bone with its associated weakening. Compared with stoichiometric additives, such as hydroxyapatite [21-25], due to a more variation in the composition of the glass phase, is it possible to tailor the mechanical properties and the overall dissolution rate of the composite.

In order to increase both, bending strength and elastic modulus, phosphate glasses as reinforcing phase of composites have to be in the form of fibres with a desirable diameter of 9–12 μm [26] and arranged in multi-filament threads. The process commonly used is melt drawing due to the difficulty to obtain thousands of individual filaments drawn from a pre-form. This process is well known and commercially scaled for silica fibres (e.g. E-glass) since the 1960s [27] because they can be drawn very effectively. However, a commercial melt drawing process for phosphate glass fibre production has never been achieved due to the lack of applications found for these glass fibres in the past and because of their particular properties that make them prone to crystallization. The drawing viscosity point for glass fibre production is typically assumed to be $10^2$ Pa.s and usually falls above the liquidus point for silica-based glasses [28]. However, phosphate glasses present a higher kinetic fragility compared with silicates and thus tend to crystallize when the glass is held at the appropriate fibre drawing temperature, usually below its liquidus point. That phenomenon occurs at viscosities much lower which narrows the drawing point temperature window and hinders a continuous glass flow due to an eventual blockage of the drawing equipment by gradual crystal growing, or decreases the quality of the resulting fibres.

### 7.1.3 Importance of viscosity and structure on the design of bioactive phosphate glasses suitable for fibre drawing:

In order to design new bioactive phosphate glasses suitable for continuous fibre production and industrial implementation, fundamental studies would be required. On one hand, it is necessary to determine the glass network structure to understand the role of each component on the glass network, but it is also essential a complete knowledge of the viscosity behaviour with temperature to predict the drawing point with enough accuracy and also to characterize the thermal properties. Accordingly, a big effort has been done so far to determine the structure in several bioactive phosphate glasses for fibre drawing by means of Nuclear Magnetic Resonance and Raman spectroscopies [29, 30, 31]. But just few works have been published about structural studies directly performed in the fibres due to the complexity of its determination [29]. More recently, several works have been published for the improvement of the processing conditions for fibre drawing based on kinetic fragility determination [32, 33], enhancing the important role of the structure to predict the behaviour of bioactive glasses during processing [11].

In this study four phosphate glass formulations in the system $Na_2O$-MgO-CaO-$P_2O_5$ with fixed magnesium and calcium content at 24 and 16 mol %, respectively, were selected according to previous formulations that present good cytocompatibility. This biocompatible

behaviour is due to the lower solution degradation rate of MgO containing glasses, which enhance their durability [34]. In a previous work, the thermal properties and the viscosity behaviour of these glasses were studied through combined quasi-static and bob-in-cup methods from above and below crystallization range in order to determine the theoretical fibre drawing points and fragility of the glasses [33].

This work is aimed to relate macroscopic properties such as kinetic fragility (m) and molar volume ($V_m$) with the structure determined by means of Raman and $^{31}P$ and $^{23}Na$ Nuclear Magnetic Resonance of the fibres. The structural features will be compared with those observed on the bulk glass to elucidate if changes on the glass network structure occur during fibre processing. Static $^{31}P$ nuclear magnetic resonance will be also employed to obtain experimental evidence of the anisotropy generated on the glass fibre due to the mechanical load applied during fibre drawing.

The structural results will also be related with empirical observations made during fibre drawing process, such as pulling temperature and the ease of pulling fibre continuously. Additionally, the mechanical properties of the fibres and the dissolution rate in phosphate buffered saline (PBS) media will be tested and related with the compositional changes on the glass network structure.

## 7.2. Materials and methodology

### 7.2.1 Glass production

Glasses with compositions $xNa_2O.16CaO.24MgO.(60-x)\ P_2O_5$ (x=5-20) were prepared by conventional melt-quenching technique. Reagent grade raw materials analytically pure, $NaH_2PO_4$, $CaHPO_4$, $MgHPO_4.3H_2O$ (Sigma Aldrich UK) and $P_2O_5$ (Fisher Chemicals) were mixed and the batches were place in a platinum-gold crucible and heated for 30 min at 350ºC in an electric furnace to drive off adducted water before melted at 1100ºC during 90 min. The melts were either cast directly onto a steel plate or poured into 9 mm graphite moulds. The glasses were annealed 10ºC above their glass transition temperature before sectioning into parallel faced ~10mm long rods for durability tests.

### 7.2.2 Glass characterization

Thermal analysis of the glasses was performed using a Texas Instruments SDTQ10 for Differential scanning calorimetry (DSC). Measurements of glass transition temperature were taken in triplicate at 10ºC/min using Aluminium pans containing powdered glass.

Glass density was measured by helium pycnometry in a MicromeriticsAccuPyc 1330 on bulk samples (±1 $Kg.m^{-3}$). The molar volume ($V_m$) was calculated from the relation between the molar mass (M) and the density ($\rho$) of the glass ($V_m=M.\ \rho^{-1}$).

Magic Angle Spinning (MAS) $^{31}P$ Nuclear Magnetic Resonance (NMR) spectra were recorded on a *Bruker Avance II* spectrometer operating at 161.96 MHz (9.4 T) . The pulse length was 2$\mu$s and 120 s delay time was used. A total number of 32 scans were accumulated with a spinning rate of 12.5 kHz for the bulk glass and 10 kHz for the fibres due to stability reasons. MAS NMR spectra were fitted to Gaussian functions, in accordance with the chemical shift distribution of the amorphous state. Solid $(NH_4)H_2PO_4$ was used as secondary reference with a chemical shift of 0.82 ppm with respect to $H_3PO_4$ (85 %). $^{23}Na$ MAS NMR was performed on a Bruker *Avance II* spectrometer operating at 105.87 MHz (9.4 T). The pulse length was 2 µs and 2 s delay time was used. A total number of 256 scans were accumulated under a spinning rate of 12.5 kHz on the bulk glass. NaCl 1M was used as reference.The quantitative $^{31}P$ and $^{23}Na$ spectra were deconvoluted with the Dmfit software [35] using the ss_band and Czjzek [36] distribution models, respectively. The error in the determination of the chemical shift is taken as ± 1 ppm.

Raman spectroscopy analyses were performed on both, bulk samples and single fibre on a *Witec Alpha300RA* Raman-AFM confocal spectrometer with 532 nm laser wavelength excitation and 39 mW power in the range of 220-3800 $cm^{-1}$. The laser polarization angle was located in x axis and microscope lent of 100 augments was used in all cases. The focus was adjusted well underneath the surface of a single fibre in order to avoid a possible degradation on the fibre surface due to ambient moisture. The precision in the determination of the Raman shifts is ± 1 $cm^{-1}$.

### 7. 2. 3 Degradation studies

Degradation tests via hydrolysis were performed on three glass samples per glass composition of ~ 9 mm diameter and 10 mm length according to the standard BS EN ISO 10993-13:2010. Specimens were placed (laid flat at the bottom of the vial) into 30 ml glass vials filled with phosphate buffered saline solution (PBS) (pH = 7.4±0.2) as degradation medium and maintained at a constant temperature of 37°C. The samples were extracted and blot dried before weighting and size measuring. Weight measurements were obtained at time points of 1, 3, 7, 14, 21, 28, 42, 56 and 84 days. The pH on PSB solution was controlled after each measurement in order to ensure that not big changes were taking place during degradation test. Fresh PBS solution was used before starting daily or weekly experiments.

Glass degradation has been expressed in terms of weight loss percentage ($M_L$) following equation (7.1) and dissolution rate ($D_R$) by equation (7.2):

$$M_L(\%) = \frac{m_d - m_i}{m_i} \cdot 100 \quad (7.1)$$

$$D_R(\%) = \frac{m_d - m_i}{SA \cdot t} \quad (7.2)$$

where $m_d$ is the mass of degrades sample, $m_i$ is the initial mass of the sample, SA is the sample area and t is the time.

### 7. 2. 4 Glass fibre production

Continuous fibres with diameters ranging from approximately 10 to 25 μm were produced via melt-draw spinning process using dedicated in-house facility. The speed was varied from 780 to 1620 rpm for each composition in order to obtain fibres with different diameter size. The pulling temperature was adjusted to approximately 150ºC above liquidus temperature in order to overcome the temperature gradient between the thermocouple controller and the actual temperature at the bottom of the platinum crucible.

### 7. 2. 5 Single Fibre Tensile Test (SFTT)

Tensile testing of single filaments was conducted in accordance with BS ISO 11566 by using a single fibre tensile tester *Diastron LEX-810* (UK) at room temperature with a load capacity of 0.2 N and a speed of 0.017 mm. $s^{-1}$. A laser scan micrometer *Mitutoyo LSM6200* attached to the tensile tester was employed prior to testing for the determination of the individual fibre diameter. The laser scan micrometer was calibrated with phosphate glass fibres of known diameters previously determined by SEM. The precision in diameter determination is considered to be ± 0.3*μ*m. At least 40 fibres were tested with a gauge length of 25 mm. Tensile strength ($\delta_f$) and tensile modulus ($E_f$) were calculated following equations (7.3) and (7.4):

$$\delta_f = \frac{F_f}{A_f} \quad (7.3)$$

$$E_f = \frac{\left(\frac{\Delta F}{A_f}\right)\frac{L}{\Delta L}}{1 - K\left(\frac{\Delta F}{\Delta L}\right)} \quad (7.4)$$

Where $\Delta F$ and $\Delta L$ are the difference in force and length corresponding to the strain limits selected according with BS ISO 11566, respectively, and depending on the nominal strain at break of the fibre. $A_f$ is the cross-section area of the filament, $F_f$ is the maximum tensile force, L is the gauge length and K is the system compliance.

The effect of composition on the tensile strength and tensile modulus was studied. Due to the brittle character of phosphate based glass fibres, Weibull distribution was employed to statistically characterize the failure mode of the fibres via the statistical software Minitab ® 15.

The strength distribution is usually represented using the two-parameter approach, also referred to a simple Weibull distribution, based on the weakest-link approximation. This assumes that the fibre is formed by *n* independent segments/links of arbitrary unit length, each segment failing or surviving at a given stress level, independently of its neighbours. The failure probability for a fibre is given by equation (7.5).

$$P(\sigma_l) = 1 - \exp\left[-n\left(\frac{\sigma_l}{\sigma_0}\right)\right] = 1 - \exp\left[-\frac{V_l}{V_0}\left(\frac{\sigma_l}{\sigma_0}\right)^m\right] \quad (7.5)$$

## 7. 3 Results and Discussion

### 7. 3. 1 Structural Characterization

#### 7. 3. 1. 1 Magic Angle Spinning Nuclear Magnetic Resonance (MAS-NMR)

Many efforts have been made to study the structure of phosphate glasses using different methods like X-ray and neutron diffractions, IR, X-ray photoelectron spectroscopy (XPS), solid state nuclear magnetic resonance spectroscopy (MAS-NMR) and Raman spectroscopy, but just these last ones were found to be the most useful in determining the structure of the glasses [37-39].

The $^{31}P$ and $^{23}Na$ MAS NMR spectra of the $xNa_2O.16CaO.24MgO.(60-x)P_2O_5$ glass series are depicted in Figure 7.1 a) and b) respectively. It can be observed the evolution of the isotropic chemical shifts of both nuclei with composition.

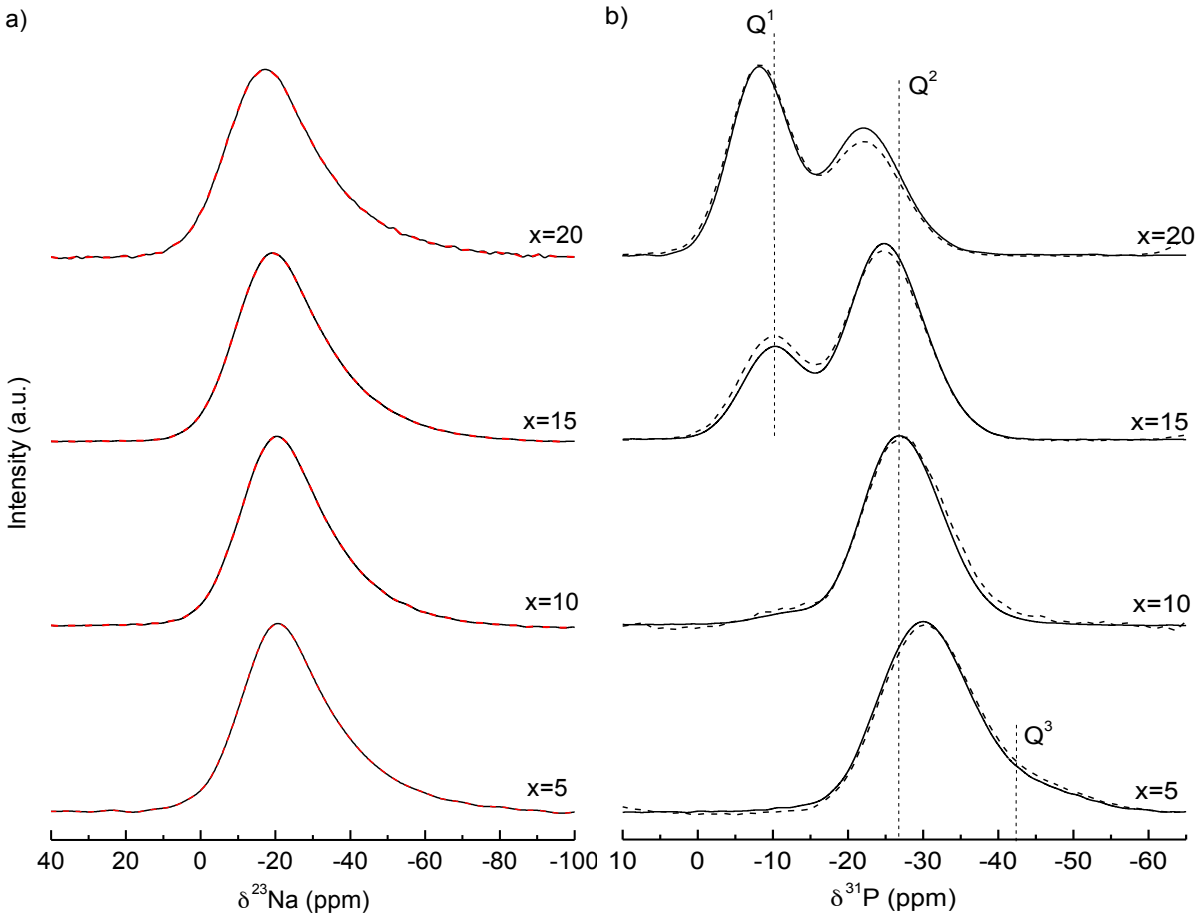


Figure 7.2: a) Isotropic signal of $^{23}Na$ MAS NMR spectra of $xNa_2O.16CaO.24MgO.$ (60-x) $P_2O_5$ glasses where x denotes the molar fraction of $Na_2O$ oxide, accompanied with simulations (red dotted lines).b) Isotropic signals of $^{31}P$ MAS NMR spectra of glasses in bulk (continuous lines) and fibres (dotted lines).

As $Na_2O$ content increases, the resonances attributed to different $Q^i$ sites are less shielded, which indicates a redistribution of the electronic density around phosphorous with changing bridging to non-bridging oxygen ratios with increasing modifier oxide content.

In order to study the evolution of $Q^i$ units as a function of composition and to compare them with the theoretical values, the relative fraction of each species has been plotted as function of $Na_2O$ mol percentage in Figure 7.2.

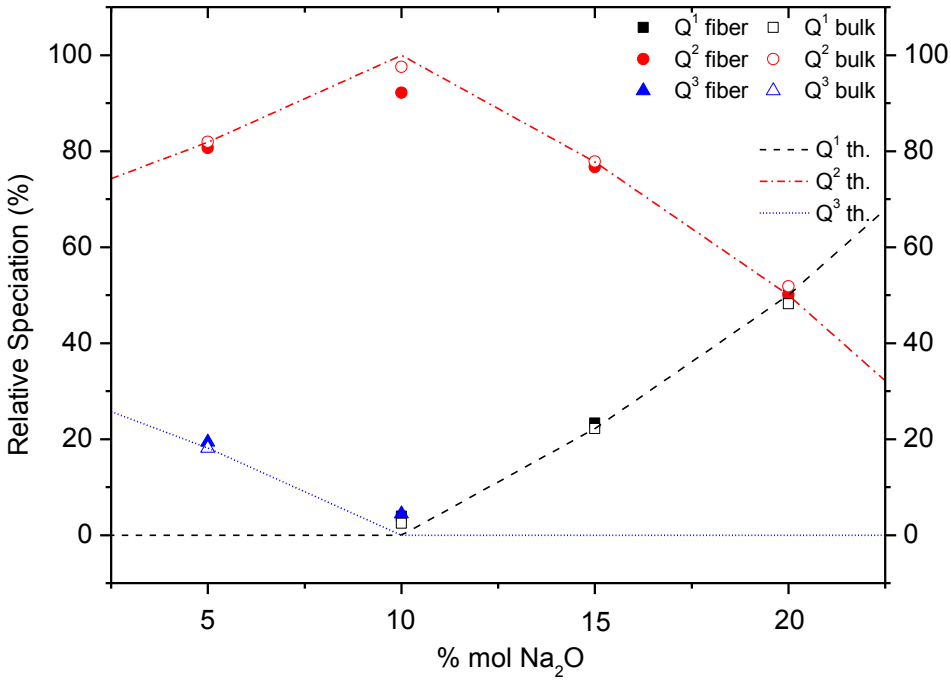


Figure 7.2: Relative speciation of $Q^i$ units as function of $Na_2O$ content. Dotted lines correspond to theoretical values obtained from equations (7.6 and 7.7). Note: $Q^1$ point in glass fibre x=10 and x=20 is not observed due to the overlap with other points.

It can be observed that $Na_2O$ content increases the glass network depolymerization. Progressively, the presence of $Q^i$ units with less bridging oxygens (i. e. $Q^1$) occurs at expense of $Q^2$ and $Q^3$ groups.

For both the bulk glass and the fibres, the relative speciation is very close to the theoretical values predicted by the structural model based on the nominal composition following equations (7.6 and 7.7)[7].

$$f(Q^2)=\frac{x}{1-x};f(Q^3)=\frac{1-2x}{1-x} \quad \text{where} \quad 0\leq x\leq 0.5 \qquad (7.6)$$

$$f(Q^1)=\frac{2x-1}{1-x};f(Q^2)=\frac{2-3x}{1-x} \quad \text{where} \quad 0.5\leq x\leq 0.67 \qquad (7.7)$$

In general, in all cases it can be observed that the glass network structure in the fibres slightly differs from that of the bulk. The proportion of $Q^1$ groups is slightly higher in the fibres than in the bulk glasses at expense of $Q^2$ groups' proportion. It is worth noting that for metaphosphate glass fibres composition (i.e. x=10), where the tetrahedral units should be of $Q^2$ type (except for a small proportion of $Q^1$ ending groups), a low but not negligible

[7]Equations (7.6) and (7.7) are already presented in Chapter I section 1.2 as equations 1.1 and 1.2 and have been replicated here for convenience.

proportion of $Q^3$ groups appears. The presence of these species could be caused by a disproportionation reaction of the type of $Q^2$ groups into $Q^1$ and $Q^3$ units responsible of the appearance of $Q^1$ and $Q^3$ units when compared with the bulk glass. The reaction is described in equation 7.8:

$$2Q^2 \leftrightarrow Q^1 + Q^3 \tag{7.8}$$

$Q^1$ site disproportionation reactions are usually observed in pyrophosphate glasses, thought it has also been reported a case of $Q^2$ disproportionation in calcium metaphosphate composition [40].

The relative speciation of $Q^i$ units has been used to calculate the experimental $P_2O_5$ molar fraction present in the glass trough equations 7.6 and 7.7. The values obtained are equal to the nominal ones, except for the x=10 where a deviation of 2 mol% on the $P_2O_5$ content has been observed. The experimental molar fraction of $P_2O_5$ has been used to calculate the network connectivity of the glasses (NC), defined as the number of bridging oxygens (BO) per network forming element [41] and the average chain length (ñ) according to Bunker et al. [41], as well as the oxygen packing density [O] in the glass [42]. NC, ñ and [O] were calculated according to equations (7.9), (7.10) and (7.11) respectively:

$$NC = \frac{3\left[P_2O_5\right] - \left[M_2^{I}O\right] - \sum\left[M^{II}O\right]}{\left[P_2O_5\right]} \tag{7.9}$$

$$\bar{n} = \frac{2}{\frac{\left[M_2^{I}O\right] + \sum\left[M^{II}O\right]}{\left[P_2O_5\right]} - 1} \tag{7.10}$$

$$\left[O\right] = \frac{1000.\rho.(O)}{M} \tag{7.11}$$

where $[M_2^{I}O]$, $[M^{II}O]$ are the molar fractions of the network modifiers and $[P_2O_5]$ is the molar fraction of phosphate. $\rho$ is the density of the glass, (O) is the number of oxygen atoms in the glass composition and M is the molecular mass of the glass.

The values obtained and represented in Figures 7.3 and 7.4 are closed to the nominal ones due to the similarity between the experimental and the nominal composition.

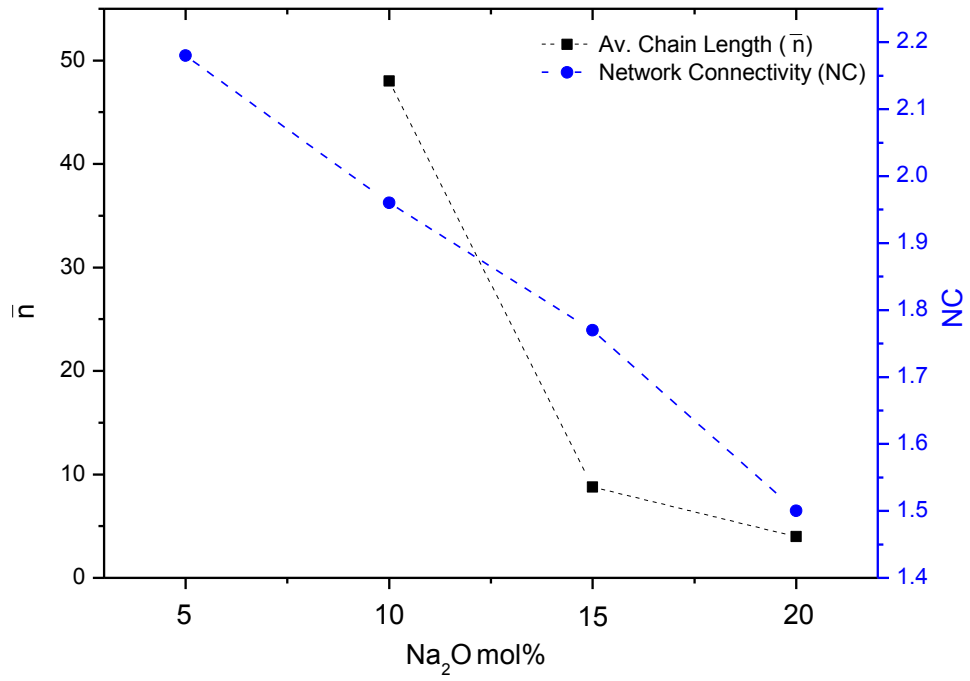


Figure 7.3: Network connectivity (NC) and average chain length (ñ) as function of $Na_2O$ content. Dotted lines are drawn as guide for the eyes. Note: equation 7.10 can be only applied for glasses containing 50 mol % or less of $P_2O_5$.

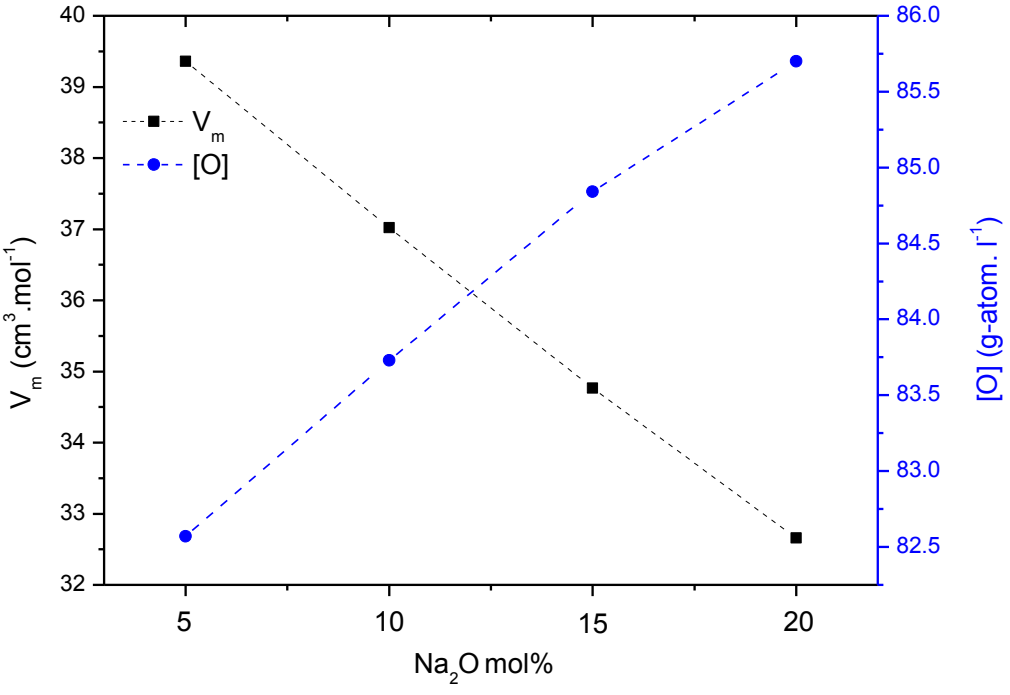


Figure 7.4: Molar volume ($V_m$) and oxygen packing density ([O]) as function of $Na_2O$ content. Dotted lines are drawn as guide for the eyes.

As seen in the $^{31}P$ MAS-NMR spectra, the replacement of $P_2O_5$ by $Na_2O$ causes the glass network depolymerization. Progressively, the increase on the $Q^i$ units with less bridging oxygens (i. e. from $Q^3$ to $Q^2$ and $Q^1$) results in shorter phosphate chains and lower network

connectivity as Figure 7. 3 shows the depolymerization caused by the addition of $Na_2O$ as modifier oxide, induces a contraction of the glass network that leads to the densification of the glass and thus to the decrease on the volume occupied by one mol of glass as depicted in Figure 7. 4. The subsequent increasing amount of $Na^+$ will force these ions to share the available NBO, resulting in coordination polyhedral that have to share corners and edges increasing the oxygen packing density (cf. Fig. 7.4).

The $^{31}P$ chemical shift anisotropy ($\delta_{CSA}$) provides information about the conformation of the $Q^n$ units. $\delta_{CSA}$ was determined from the integration of the MAS NMR spectra including the spinning sidebands using dmfit software [35]. Larger values of this tensor are found in structures in which there is a prevalence of rings arrangements instead of phosphate chains [43, 44]. In Table 7.1 are collected the $\delta_{CSA}$ values obtained for the fibres and bulk glasses for $Q^2$ units.

Table 7.1: Chemical shift anisotropy of Q2 units for bulk and glass fibres The errors on the values are estimated to ±0.2 ppm.

| Glass composition | Glass code | $\delta_{CSA}$ $^{31}P$ $Q^2$ (ppm) bulk glass | $\delta_{CSA}$ $^{31}P$ $Q^2$ (ppm) glass fibres |
|---|---|---|---|
| $5Na_2O.16CaO.24MgO.55P_2O_5$ | **x=5** | -139 | -136 |
| $10Na_2O.16CaO.24MgO.50P_2O_5$ | **x=10** | -131 | -130 |
| $15Na_2O.16CaO.24MgO.45P_2O_5$ | **x=15** | -131 | -130 |
| $20Na_2O.16CaO.24MgO.40P_2O_5$ | **x=20** | -123 | -123 |

According to our results, the chemical shift anisotropy is similar for the bulk and glass fibres and does not vary between the meta- and x=15 pyrophosphate glass. In both, the Na rich glass compositions seem to favour chain structures.

The distribution of $Na^+$ ions within the structure $xNa_2O.16CaO.24MgO.(60-x)$ $P_2O_5$ glasses can be analysed by means of $^{23}Na$ MAS NMR. The spectra present a characteristic shape associated to the Second Order Quadrupolar Effect (SOQE) in distributed structures. This system cannot be deconvoluted with a Gaussian model because it is not capable of reproducing this asymmetry coming from the quadrupolar parameters distribution. Deconvolutions have thus been carried out using the Czjzek model [36]. The NMR parameters deduced from the spectra deconvolution, such as chemical shift and quadrupolar

constant (CQ), are reported in Table 8.2. The evolution of the chemical shift towards higher frequencies (lower field) is usually related with small and continuous changes on the cation coordination sphere towards lower coordination number (CN), but investigations in binary lithium phosphate glasses [45] have discussed that correlations between the observed chemical shift and the structure usually does not depend only on one factor since the chemical shift ranges for different CN overlap. Thus, a variety of structural parameters such as coordination numbers, bond length and modifier ion nature should be involved. For example, $^{23}$Na NMR investigations of silicate and aluminosilicate crystals and melts have shown that decrease in the degree of network polymerization within the structure produce an increase in the $^{23}$Na chemical shift [46], as the phosphate glasses under study. On the contrary, the variation on CQ is not significant, suggesting that the chemical environment around sodium cations is constant. These results indicate that the $Na^+$ ions are distributed around the phosphate units independently of the former oxide content and thus of the glass composition.

Table 7.2: Chemical shifts and quadrupolar constant ($C_Q$) extracted from the 1D $^{23}$Na NMR spectra simulation. The errors on the values are estimated to ±0.2 ppm and ±0.1 MHz.

| Glass code | $\delta_{CS}$ $^{23}$Na (ppm) | CQ (MHz) |
|---|---|---|
| **x=5** | -12.20 | 2.32 |
| **x=10** | -11.83 | 2.27 |
| **x=15** | -10.81 | 2.29 |
| **x=20** | -8.53 | 2.32 |

Bulk glasses are isotropic materials with respect to their structure and physical properties. However, they can present a certain degree of anisotropy introduced in the glass as a result of the stress applied during its processing into glass fibres.

In the past, the orientation and alignment of the weakest bonds within the glass structure along the axis of the fibre have been discussed. Goldstein and Davies developed the concept of glasses as polymers consisting of glass forming atoms connected by oxygen that allows the formation of fibres with oriented linear chains [47]. They investigated the X-ray diffraction patterns of sodium metaphosphate glass fibres and found them very similar to those of organic fibres with oriented chain molecules. Subsequently, Milberg and Daly

investigated also the structure of fibres made from the same glass composition and the results indicate that the sodium metaphosphate fibres were made up of long chains that are preferentially orientated along the fibre main axis, thus a strong structural anisotropy results from the rearrangements of the structural units [48]. Muñoz *et al.* [49] have studied the anisotropy of phosphate glass fibres through the measurements of optical birefringence and have correlated it with the drawing stress and the diameter of the drawn fibre. A permanent birefringence is observed in the case of glass fibres drawn by applying high shear stresses as a consequence of the alignment of anisotropic flow units.

With the aim of studying if any favoured direction is taken by the chains present in the glass structure, and thus corroborate the studies mentioned above for these particular compositions, the anisotropy of the metaphosphate glass (i.e. x=10) was studied by Static Nuclear Magnetic Resonance of $^{31}P$. The spectra of both, the bulk glass and the fibres are depicted in Figure 8.5.

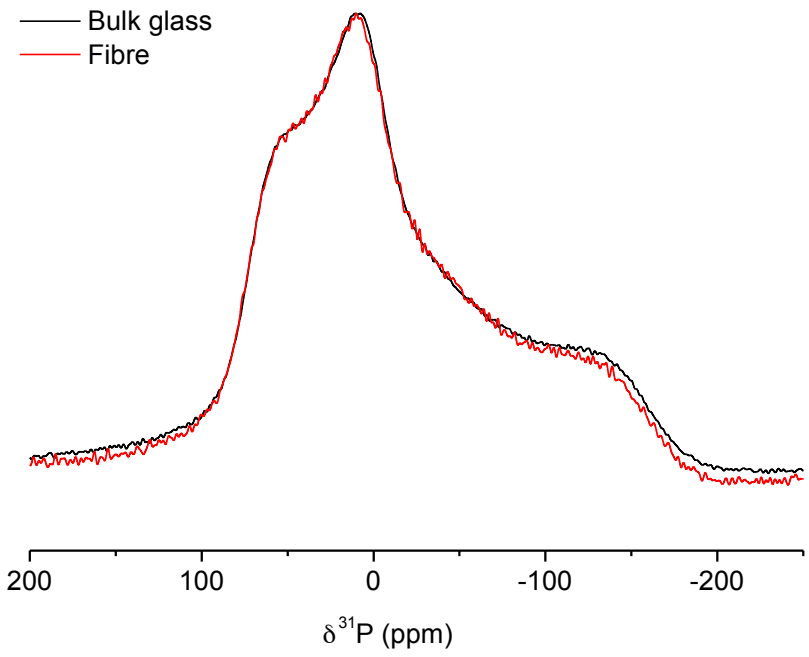


Figure 8.5: $^{31}P$ NMR spectra of $10Na_2O.16CaO.24MgO.50P_2O_5$ glass in bulk (black line) and fibres (red line).

It can be observed that there is almost no difference between both spectra, thus the variation on the chemical shift anisotropy ($\delta_{CSA}$) that should be observed as a consequence of the phosphate chains alignment seems not to be reflected on the phosphorous local environment. Additionally, the $\delta_{CSA}$ obtained from the simulation of the rotation bands in the $^{31}P$ MAS NMR spectra of the bulk glass and fibres, -131 ppm and -130 ppm respectively,

does not shed light on the discussion. On the other hand, the line shape of the minor amount of $Q^1$ units present in the glass, as discussed above, will overlap with the $Q^2$ dominating pattern. Braun et al. [50] have studied extruded calcium metaphosphate glasses by static and 2D MAS NMR. As in these glasses, they conclude that it is almost impossible to verify a noticeable local structural alignment of the phosphate chains in the glass fibres with ordinary static NMR. Therefore we cannot elucidate whether the chains of $PO_4$ tetrahedra present in the glass fibres are randomly distributed or lie along the fibre main axis direction. In any case, the good mechanical properties observed in these fibres, that will be discussed in detail in next section, leads to the conclusion that a structure orientation on the fibres is likely taking place.

#### 7. 3. 1. 2. Raman Spectroscopy

Raman spectroscopy was employed as a complementary method to study the structure on the bulk glass and on the fibres, specifically if any changes occurred regarding the nature and orientation of phosphorous to oxygen bonds. Figure 7.6 shows the Raman spectra collected for the bioactive glasses. All the spectra were normalized to the band with major intensity. The evolution of the structure as the modifier oxide content increases agrees with that observed by $^{31}P$ MAS-NMR. The spectra are all dominated by two main bands appearing at about 700 $cm^{-1}$ and 1170 $cm^{-1}$ and attributed to the symmetric stretching modes of phosphorous to bridging (P-O-P) and to non-bridging oxygen bonds (O-P-O) in $Q^2$ units, respectively [51, 52]. The corresponding asymmetric modes appear as shoulders around 790 $cm^{-1}$ and 1260 $cm^{-1}$ [50, 52]. The progression from a more cross-linked $Q^3$ network to a glass network based on chains or rings made of $Q^2$ units and a depolymerised glass with the presence of $Q^2$ units and $Q^1$ (not only as a chain terminal groups but forming pyrophosphate units) with decreasing [O]/[P] ratio, can be followed observing two significant bands. The band attributed to O-P-O bonds in $Q^1$ units (~1050 $cm^{-1}$) gradually increases in intensity and gets broader, while the band attributed to the symmetric stretching mode of P=O bonds in $Q^3$ groups (~1370 $cm^{-1}$) progressively disappears. Additionally, the P-O bond bending mode of $Q^2$ and $Q^1$ units appears as a broad signal in the range of 200 $cm^{-1}$ to 400 $cm^{-1}$ [51, 52]. If we look to the frequency of the dominant stretching modes of phosphorous linked to non-bridging oxygens, we can observe a decrease on the Raman shift from P=O bonds in $Q^3$ to O-P-O in $Q^2$ and $P\text{-}O^-$ in $Q^1$ as an indication of the progressive depolymerization of the phosphate network as well as the increase in the average bond length of phosphorous to non-bridging oxygens.

Comparing the structure on the bulk and fibres, it cannot be observed any significant difference between the main peaks, neither in Raman shift nor in intensity. Apart from the higher background present in all the fibres spectra compared with the bulk, the bands attributed to asymmetric modes and the O-P-$O_{sym}$ mode in $Q^2$ units seem to present a higher relative intensity on the fibres than on the bulk, but it is complex to extract a conclusions from that observation due to the difference on the background in all the Raman shift range mentioned before.

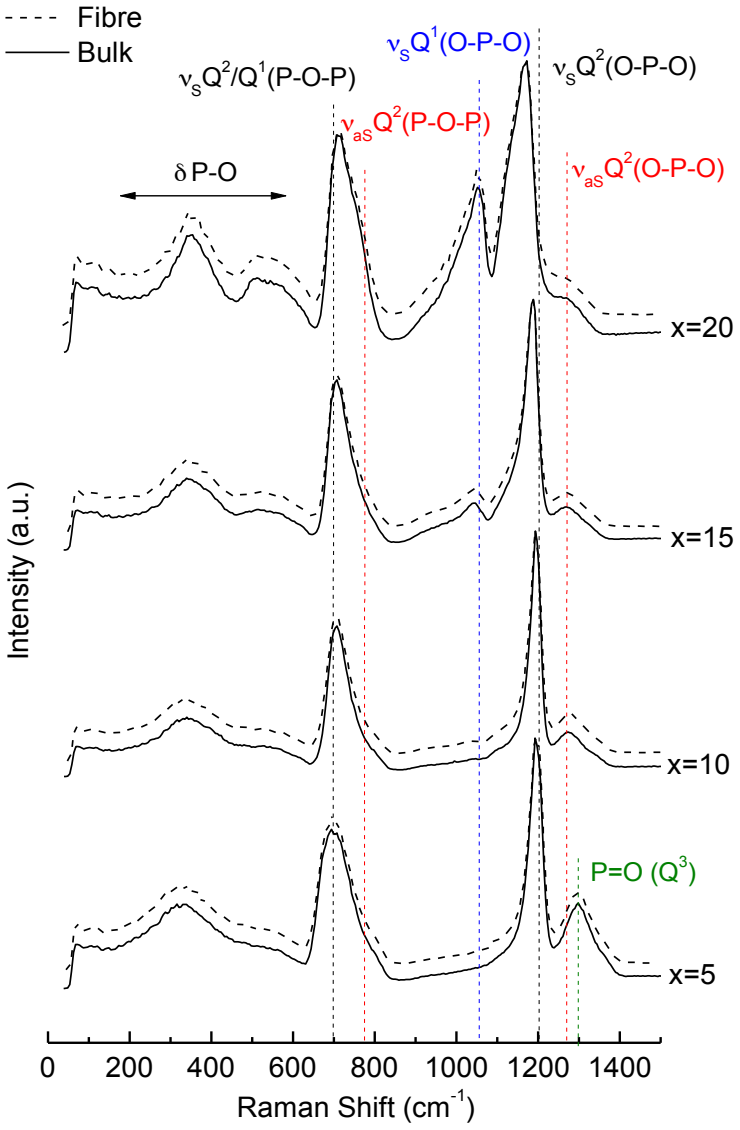


Figure 7.6: Raman spectra of $xNa_2O.16CaO.24MgO.(60-x)P_2O_5$ glasses in bulk (continuous lines) and fibres (dotted lines).Discontinuous coloured lines show the bands attributed to bending (δ) and stretching (ν) vibrational modes of P-O bonds.

### 7. 3. 2. Glass solubility

While the poor chemical durability of phosphate glasses in aqueous environments has restricted their industrial applications, it was one of the main motivations for their use as temporary bone fracture fixation devices. The dissolution rate of phosphate glasses depends on the chemical composition, the thermal history and the ratio of surface area to volume, but also on the pH of the degradation medium and the degradation temperature [53]. In this work the durability experiments have been carried out on annealed glass samples at a constant temperature of 37ºC and in a buffered aqueous media (PBS).

The pH of the immersion media was recorded after every measurement. Its variation *vs.* dissolution time has been represented in Figure 7. 7.

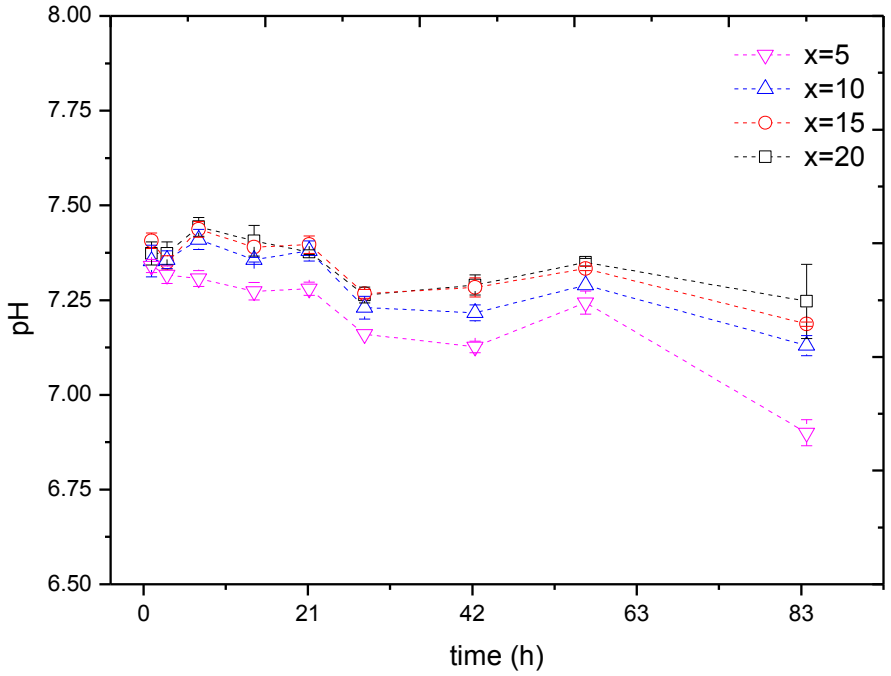


Figure 7.7: Evolution of pH of $xNa_2O.16CaO.24MgO.(60-x)P_2O_5$ glasses in PBS at 37 ºC for 84 days study. Dotted lines are drawn as a guide for the eyes. Error bars represents the standard error of mean value.

The starting value of the immersion solution (PBS) was 7.3 and the pH remained stable around this physiological value (i.e 7.3-7.4) during all the measurements, except for the durability tests carried out through one month (points at 83 days in Figure 7.7) that presents slightly lower pH values. For x=5 glass pH drops below 7. This increase in the acidity can be attributed to the formation of phosphoric acid due to the rapid release of phosphate ions into solution [54]. This more acidic media could in turn increase the dissolution rate of the glass as the network breakage reaction is highly sensitive to the $H_3O^+$ ion attack [55], thus giving

higher values of dissolution rate and mass loss than expected. Therefore, this value will not be taken into account to calculate de degradation rate.

The degradation process of phosphate glass occurs into two steps: a hydration process involving $Na^+/H^+$ ion exchange and the subsequent hydrolysis of the previously formed hydrated layer:

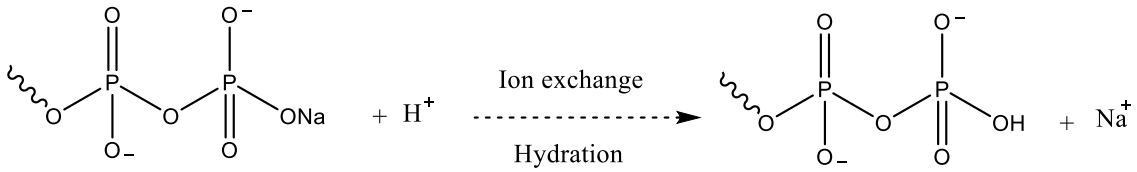


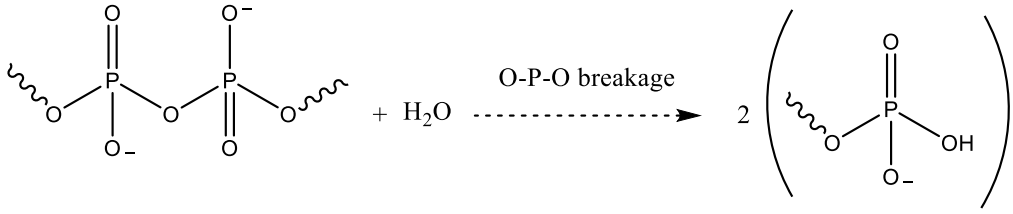


During this last step, the cleavage of P-O-P bonds takes place and thus the network structure breaks down into phosphate chains of different lengths that are released into the solution [53]. Bunker *et al.* [17] proposed that the theoretical ion exchange is the reaction rate limiting step in the dissolution process, whilst Gao *et al.* [53] reached the opposite conclusion considering the ion exchange reaction just an initiator of the network breakage as dominant reaction.

The mass loss percentage was calculated according to equation (7.1) and was plotted against immersion time in PBS at 37ºC in Figure 7. 8.

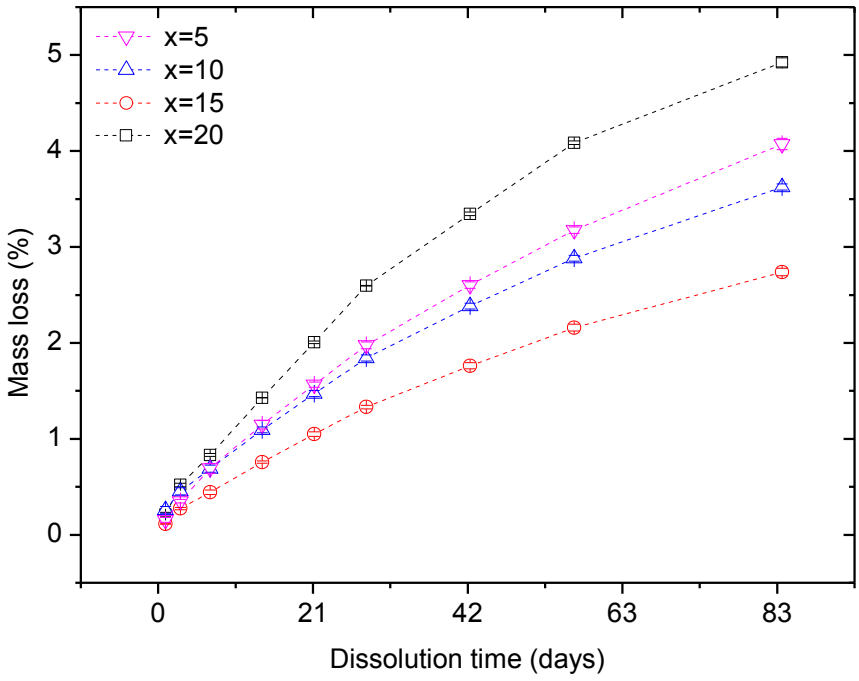


Figure 7.8: Mass loss of $xNa_2O.16CaO.24MgO.(60-x)P_2O_5$ glasses in PBS at 37 ºC for 84 days study. Dotted lines are drawn as a guide for the eyes. Error bars represent standard error of mean value.

In all cases, the rate of mass loss (%) increases with increasing immersion time. The glass x=15 presents the lowest values followed by x=10, x=5 and x=20, thus the mass loss increases with increasing former oxide content except for x=15. The difference in mass loss between the most durable glass (i.e. x=15) and x=20 is a 51%.

The dissolution rate (i.e. the mass loss per unit area and time) has been calculated by equation (7. 2) and plotted as function of dissolution time in Figure 7. 9.

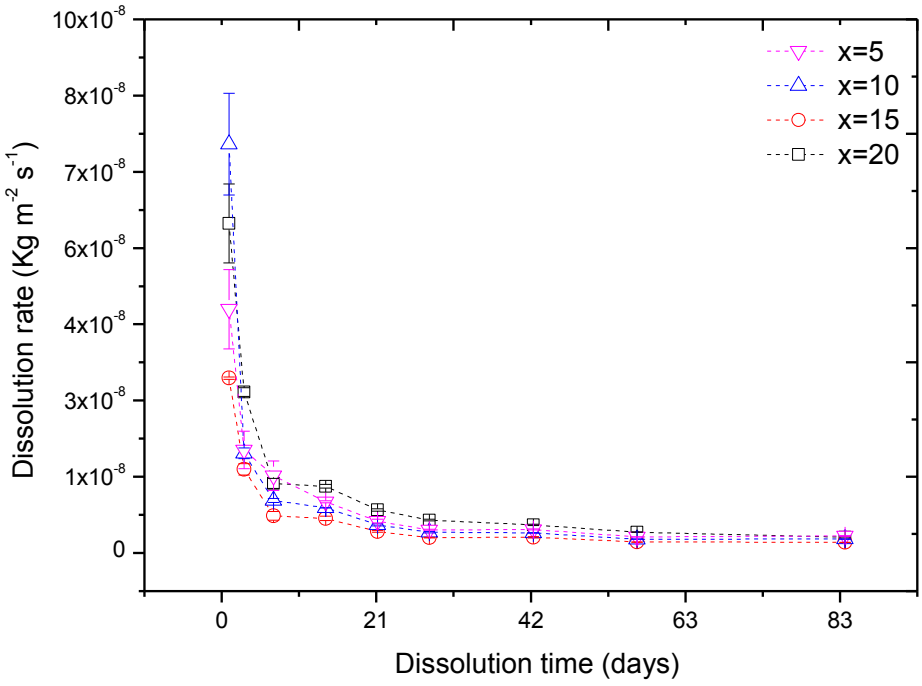


Figure 7.9: Degradation rate of $xNa_2O.16CaO.24MgO.\ (60\text{-}x)\ P_2O_5$ glasses in PBS at 37 ºC for 84 days study. Dotted lines are drawn as a guide for the eyes. Error bars represent the standard error of mean value.

For all the glasses, the dissolution rate was high at the beginning of the degradation experiments and decreased slowly, in an asymptotic manner, as dissolution time increases. According to the mass loss profiles, these variation shapes are consistent with a polymer hydration model, and have been attributed to a dissolution process divided into two kinetic periods by Bunker *et al.* [17]. In the first stage the dissolution rate is higher; glass samples lose weight as a function of $t^{1/2}$. This stage is controlled by the rate at which water diffuses into the glass surface. As the dissolution process continues, phosphate chains are entirely surrounded by water. Totally hydrated chains can then disentangle from partially hydrated chains still attached to the surface and float off into solution. The hydrated layer achieves a steady state resulting in uniform and linear with time kinetics glass dissolution.

After 84 days of experiment, a decrease in dissolution rate was observed with increasing $Na_2O$ content as depicted in Figure (7.10). The dissolution rate values are in the range of previously studied glasses with similar composition [16]. It is suggested by Parsons et al. that a degradation rate of around 5. $10^{-10}$ $Kg.m^{-2}.s^{-1}$ or lower is required for phosphate glass fibres for bone repair application [56]. The most durable glass found in this study, x=20, is in the range of the suggested optimum rate.

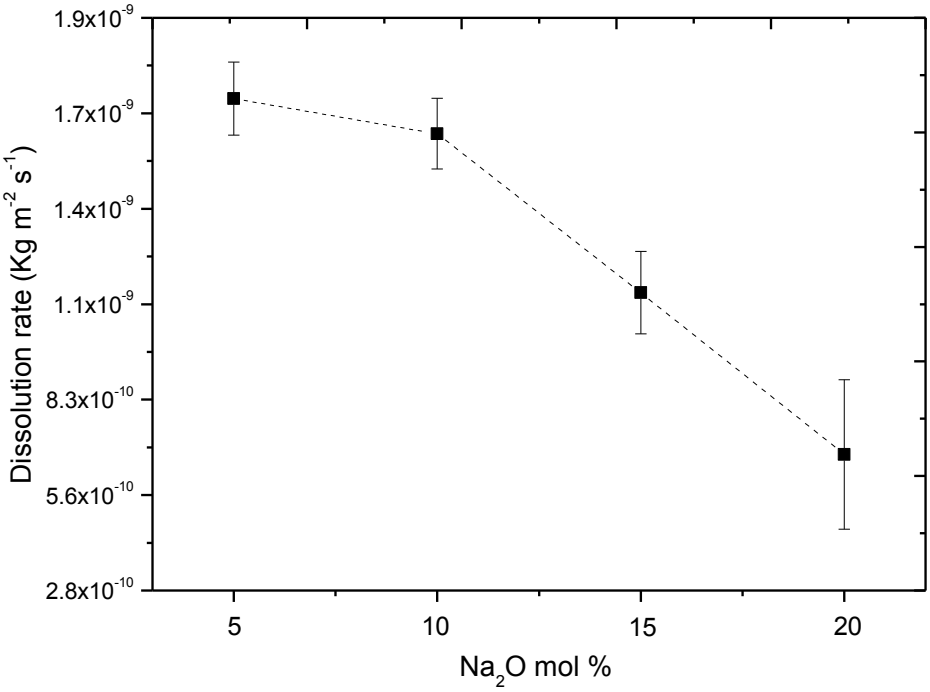


Figure 7.10: Degradation rate of $xNa_2O.16CaO.24MgO.(60-x)P_2O_5$ glasses in PBS at 37 ºC after 84 days. Dotted lines are drawn as a guide for the eyes. Error bars represent the standard deviation of mean value.

The chemical durability of phosphate glasses is strongly affected by the field strength of the modifying cations, and thus by the size and charge of the ions. Generally, the replacement of monovalent cation oxides by di-valent or tri-valent ion oxides (i. e. small ionic radius and high electrical charge) results in a decrease in the dissolution rate due to the strengthening of phosphate glass network via the cross-linking between phosphate chains by the modifier [55, 57]. However, the dissolution rate of the glasses is not only affected by the modifier oxides but also by the amount of $P_2O_5$. The glasses under study differ on the $P_2O_5$ content, replacing the glass former oxide by $Na_2O$ and keeping constant the CaO and MgO proportions in the glass. Brauer *et al.* [58] found that the degradation rate of phosphate based glasses is reduced by two orders of magnitude as the $P_2O_5$ content was reduced from 50 to 45 mol %. Solubility in both the polyphosphate and the pyrophosphate region was investigated by Vogel *et al.* [59-62]. Results suggested that phosphate invert glass[8] was more resistant to hydrolysis than the chain structure of meta- and polyphosphate glasses. In general, it is observed a reduction on degradation rate with decreasing $P_2O_5$ content due to depolymerization of the phosphate chain structure. Hydration energy in phosphates decreases for $Q^2>Q^1>Q^0$, since $Q^2$ units are more susceptible to hydration and the

[8] Phosphate glasses containing less than 40 mol % are often referred to as invert glasses, as their properties depend on the network modifier ions rather than on the network former [63]

subsequent hydrolysis compared with smaller $Q^1$ groups [31]. As seen in the structural characterization, with increasing $Na_2O$ content the glass network depolymerises. The proportion of $Q^1$ units increases at expenses of $Q^2$ and $Q^3$ groups, being the P-O-P bonds replaced by more resistant to hydration P-O-Na bonds. Phosphate glass with 55 $P_2O_5$ mol % (x=5) presents the highest dissolution rate with a value of 1.7 $10^{-9}$ Kg $m^{-2}$ $s^{-1}$, this can be explained based on the presence of potentially hydrolysable P=O bonds in $Q^3$ groups for this glass composition. In the meta- and polyphosphate region the dissolution rate decreases with decreasing former oxide. As discussed above, the decrease in the fraction of more hydrolysable $Q^2$ species, along with an increase on the oxygen packing density decreases the dissolution rate and thus enhances the chemical durability.

### 7. 3. 3 Mechanical properties of fibres

Phosphate glass fibres essentially present a brittle nature as it is seen by their little or no plastic deformation up to the point of failure when testing.

Figure 7.11 summarises the effect of increasing $Na_2O$ on the mechanical properties of glass fibres such as tensile fracture stress and modulus.

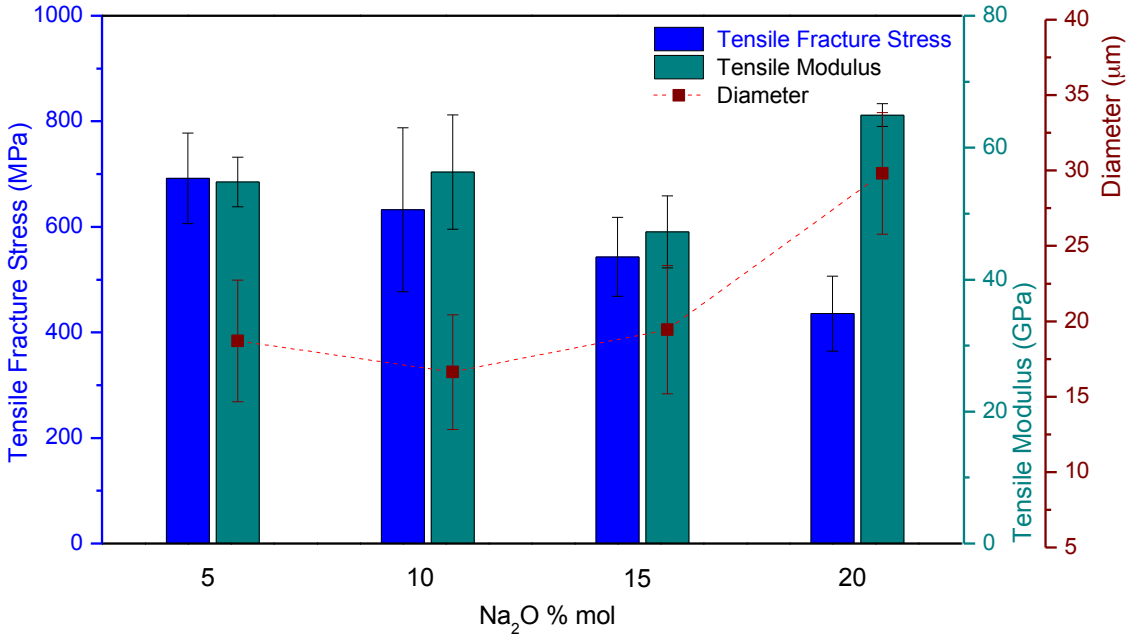


Figure7.11: Tensile fracture stress, tensile modulus and fibres diameter of the fibres in the glass system $xNa_2O.16CaO.24MgO.$ (60-x) $P_2O_5$ glasses in PBS at 37 ºC after 84 days. Error bars represent the standard deviation. Dotted lines are drawn as a guide for the eyes.

A decrease in tensile fracture stress was seen with increasing $Na_2O$ content. The best mechanical properties of the phosphate glass fibres tested are given by the glass with higher network connectivity and lower oxygen packing density that corresponds to the glass with higher phosphate content (x=5). This is consistent with previous results obtained in similar bioactive glass systems [16]. The tensile modulus of a material is an intrinsic property and should follow the same trend as tensile fracture, but in the glasses under study the modulus of x=20 shows the highest value. The shorter chains present in this glass composition, as ñ shows, will be able to pack together tighter and thus create a more durable glass with greater tensile modulus. As it can be seen in Figure 7.11, the average diameter of the fibres is quite similar for x=5 to x=15, being the glass fibres with 40 mol % of $P_2O_5$ (x=20) the thickest ones. Several speeds were tested for this glass, ranging from 780 to 1620 rpm, when drawing the fibres as explained in the experimental section. A total number of 68 single fibres were tested in order to select the ones with the closest diameters to the other glass compositions. Despite the average diameter is about 10 $\mu$m higher for x=20, and thus the most likely reason of a lower tensile fracture stress than expected, bigger diameter fibres should lead to lower strength values.

The Weibull distribution is a well-known and accepted statistical tool used to characterize the failure mode of brittle fibres [64]. Weibull modulus (m) statistically states the most probable strength of the fibres. If this parameter takes large values, then the stresses even slightly below the normalizing value ($\sigma_0$) would led to a low probability of failure. However, a low Weibull modulus would introduce uncertainty about the strength of the fibre [65]. The variation of failure stress mostly depends on the presence of flaws on the fibre surface that are usually observed after annealing treatment. In this work the fibres were tested as-prepared, thus a smaller variation in strength is expected. As for some glass formulations the number of fibres tested were fewer than 30, Student's t-test is used to elucidate if the population under study is statistically significant (i.e. $P<0.05$). Weibull modulus and normalising stress for the bioactive glass fibres are found statistically as the shape and scale factors in Figure 7.12.

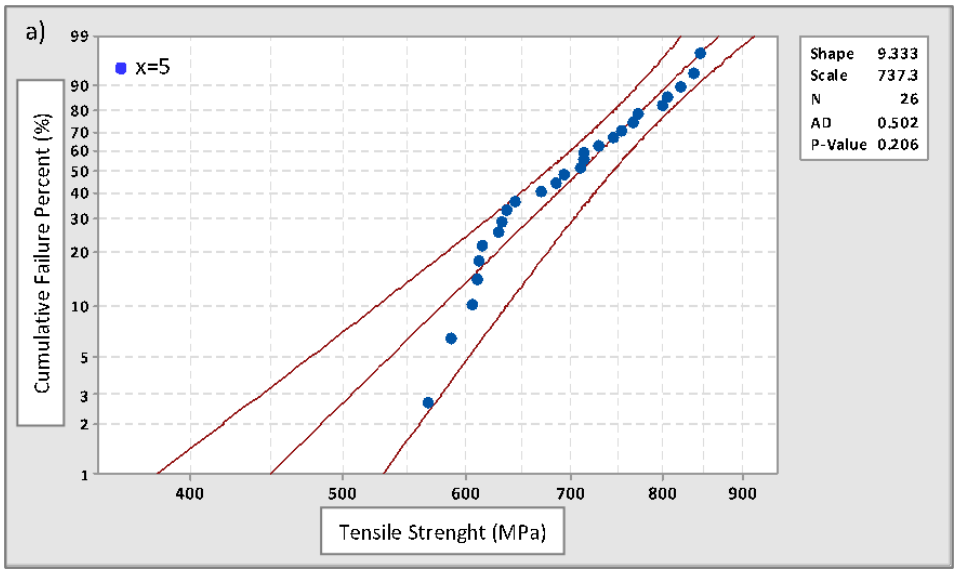
a)
x=5
Cumulative Failure Percent (%)
Tensile Strenght (MPa)
Shape 9.333
Scale 737.3
N 26
AD 0.502
P-Value 0.206

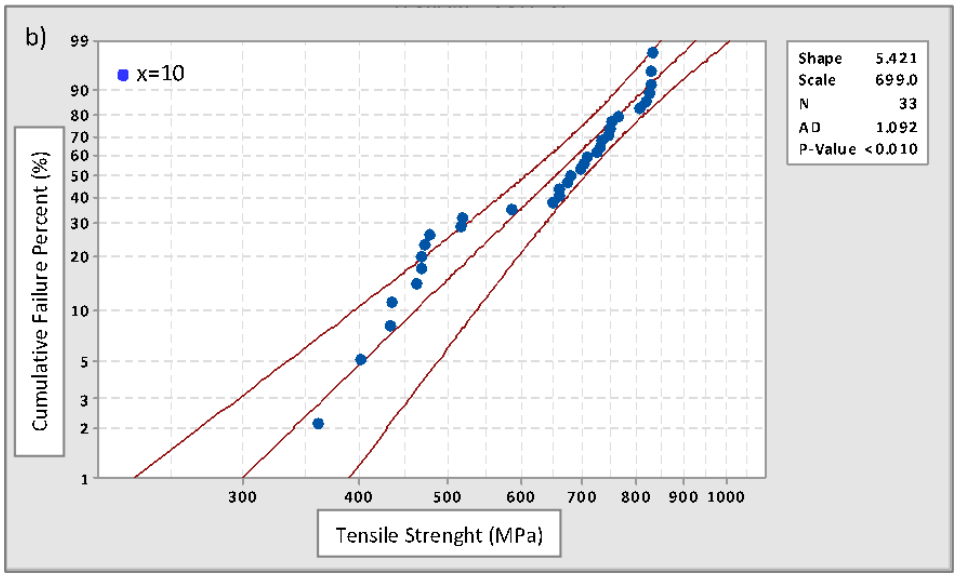
b)
x=10
Cumulative Failure Percent (%)
Tensile Strenght (MPa)
Shape 5.421
Scale 699.0
N 33
AD 1.092
P-Value <0.010

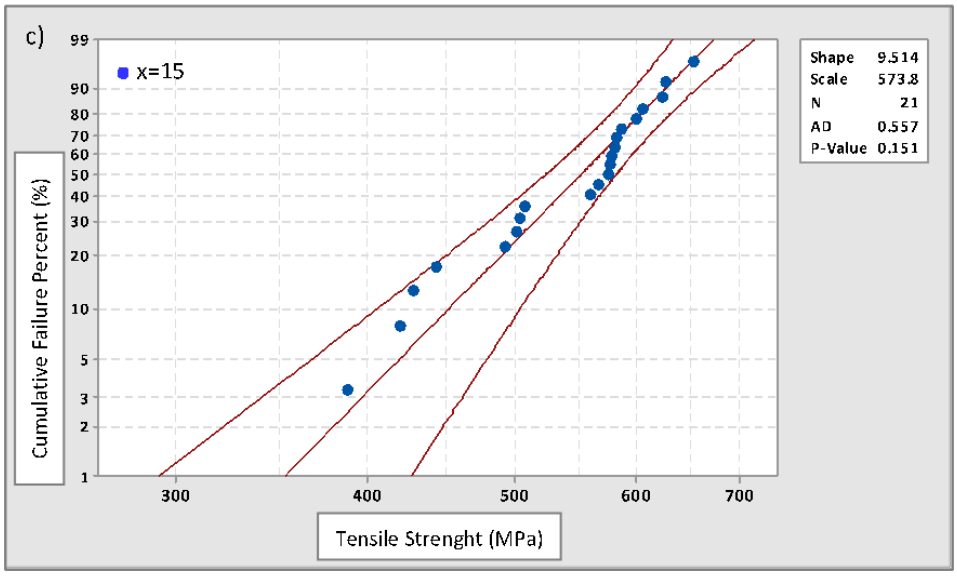
c)
x=15
Cumulative Failure Percent (%)
Tensile Strenght (MPa)
Shape 9.514
Scale 573.8
N 21
AD 0.557
P-Value 0.151

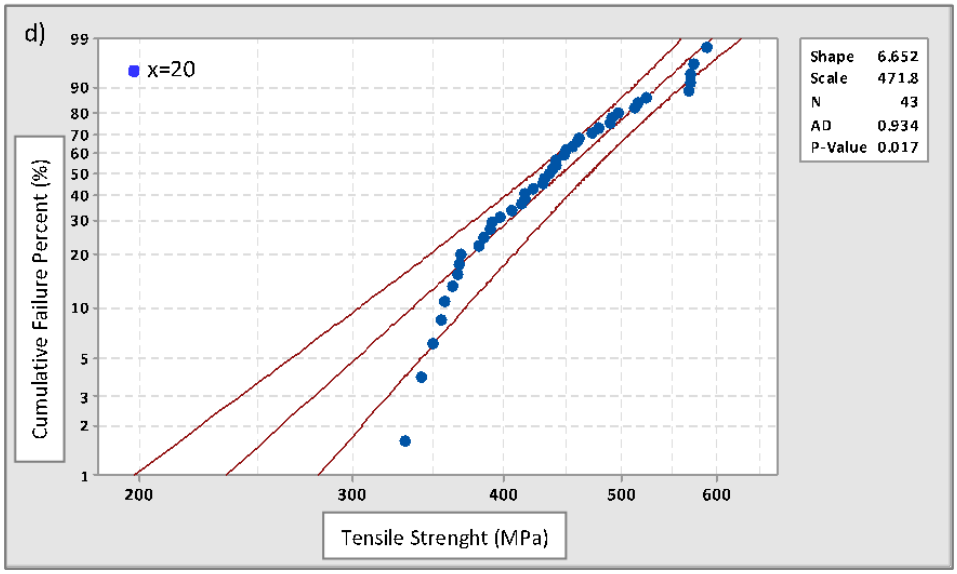


**Figure 7.12**: Weibull distributions for the glass system $xNa_2O.16CaO.24MgO.(60-x)P_2O_5$. a) for x=5, b) for x=10, c) for x=15 and d) for x=20 glasses. Shape term is referred to the Weibull modulus, Scale to the normalizing strength, N to the number of sample tested and p-value is the result derived from Student's test.

These parameters are collected in Table 7.3 together with the tensile fracture stress values for the ease of comparison.

As it can be observed, the trend of normalizing strength ($\sigma_0$) is consistent with the trend of average tensile fracture strength. The glass fibres of x=15 glass present the highest Weibull modulus among the glass systems under study, followed by x=5 glass fibres, therefore it is the material with highest reliability. Furthermore, attending to tensile fracture stress, the highest value is obtained for x=5 glass fibres (i.e. 55 mol % $P_2O_5$). Therefore, the glass composition that shows a better compromise between both, Weibull modulus and tensile fracture stress, is that of the glass fibres with higher former oxide content (i.e. x=5 glass).

Table7.3: Weibull distribution of fibres in the glass system $xNa_2O.16CaO.24MgO.(60-x)P2O5$.

| Glass code | Tensile Fracture Stress (MPa) | $\sigma_0$(MPa) | m (Weibull modulus) |
|---|---|---|---|
| **x=5** | 692±86 | 737 | 9.33 |
| **x=10** | 632±155 | 699 | 5.42 |
| **x=15** | 543±75 | 574 | 9.51 |
| **x=20** | 436±71 | 472 | 6.65 |

### 7. 3. 4 Kinetic fragility and fibre drawing ability

The fragility values that are going to be discussed here in terms of the structural features have been calculated from experimental viscosity data determined by rotation and quasistatic viscosity methods along the high and low temperature range, respectively [33]. The values are reproduced in Figure 7.13 for convenience.

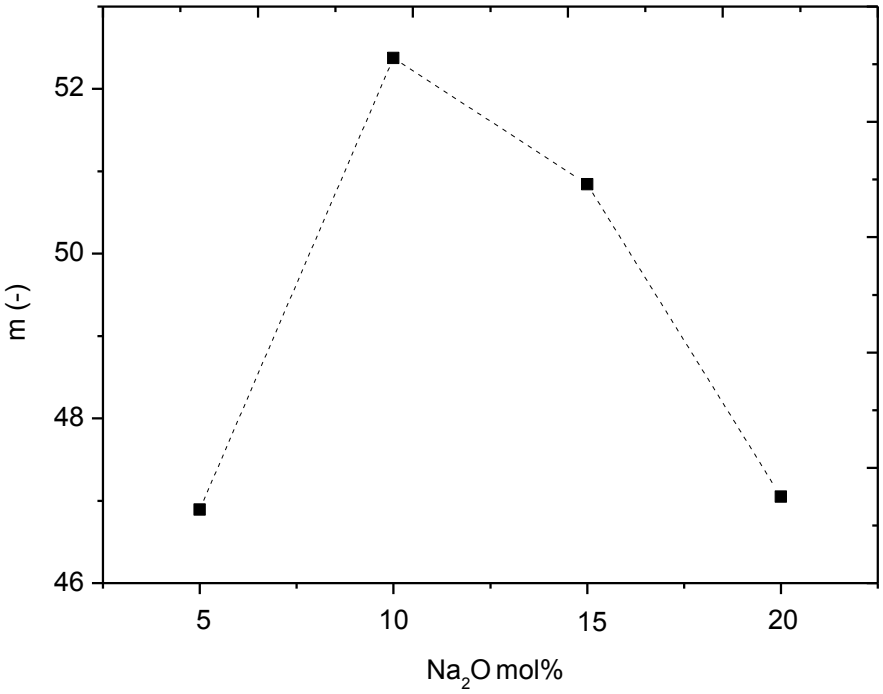


**Figure 7.13:** Kinetic fragility as function of $Na_2O$ content. Dotted lines are drawn as guide for the eyes.

The combination of these two techniques allows the experimental determination of viscosities within the processing range up to $10^8$ Pa.s and on the melt. Based on the conclusions obtained from the viscosity studies presented previously along this thesis, and on Angell's kinetic fragility definition (equation 2.9), the absence of viscosity data on the transition range may underestimate the fragility values obtained from the fits, in this case to VFT. However, the trend followed with composition is expected to be similar even if the values may vary. As discussed in the work where these data are published [33], fragility results are somewhat unexpected. Lower network connectivity and thus a larger concentration of NBO together with a decrease in the phosphate chain length with increasing modifier content, would be expected to increase the fragility since it would take less time for the shorter chains to rearrange and relax. Nevertheless, fragility decreases from metaphosphate composition to x=20. The variation observed with composition could be caused by the glass network compaction degree. A higher proportion of short chains arrangements as $\delta_{CSA}$ and ñ values show, would lead to denser glass network as the

increase on the oxygen packing density with increasing alkali content shows. The subsequent lower $V_m$ is going to hinder somehow the cooperative flow of the $PO_4$ units through the glass network and therefore cause a reduction on the kinetic fragility. Furthermore, the presence of $Q^3$ units in x=5 glass, as seen from the structural determination by spectroscopic techniques, give rise to a more branched and interconnected glass network that could be responsible of the significantly lower value of fragility. However, as suggested above, this value could be underestimated when taking into account experimental viscosity values nearby the transition range, and thus the drop on fragility less pronounced.

The fibre drawing ability of phosphate glasses strongly depends on the structure of the glass, in particular the $Q^i$ speciation within the glass [55]. As $^{31}P$ MAS NMR spectra have shown that not significant differences occur in the glass network structure during fibre drawing, especially regarding variations on $Q^i$ speciation, therefore the properties or structural features determined in the bulk glasses are applicable to the fibres structure, as is the case of kinetic fragility.

A less fragile behaviour will lead to a wider temperature window range for fibre drawing since the glass will have smaller tendency to crystallize. This extended temperature range together with glass compositions with elevated average chain length (i.e. glasses with structure heavily dominated by $Q^2$ species) are presumably easier to draw into fibres.

Fibre drawing was carried out varying the temperature to modulate the glass flow coming through the crucible filament. With increasing alkali content, the optimum temperature required to draw continuous glass fibres gets lower. Glass compositions x=10 and x=15 were the easiest to fibre because of their polymeric nature due to the high proportion of $Q^2$ groups. Fibre drawing was almost continuous and gave around 80% and 60% conversion of glass into fibre, respectively. However, it was also possible to draw fibres from x=5 and x=20 glass compositions, which present the lowest kinetic fragility values of the glass series under study (c.f. Fig. 7.13). It is worth noting that even challenging, it was possible to draw fibres continuously from x=20 glass composition (i.e. 40 mol % $P_2O_5$). In order to avoid crystallization around crucible filament, it was needed to enhance the temperature around 50 degrees above the optimum required to keep the glass flow under control. The greater flow achieved could be the main reason of the higher diameters observed on x=20 fibres, as discussed in section 7.3.3. Whereas, even if glass x=5 presents a lower proportion of $Q^2$ groups compared with metaphosphate composition, it presents a long-chain structure and a higher connectivity degree, responsible of a higher tensile strength. These glass network structure features may contribute to withstand the stress from the pulling process, even at

the high temperatures employed to draw fibres due to the higher viscosity of a glass with 55 mol% of $P_2O_5$.

### 7. 4 Partial conclusions

The structural studies performed in the bulk glasses and on the fibres by means of $^{31}P$ and $^{23}Na$ MAS NMR and Raman spectroscopies have shown that not significant differences occur in the glass network structure during fibre drawing, especially regarding to the $Q^i$ speciation and to the nature and orientation of P-O bonds.

The replacement of $P_2O_5$ by $Na_2O$ causes the glass network depolymerization and seems to favour the presence of chain arrangements in the glass network. Progressively, the increase on the $Q^i$ units with less bridging oxygens results in shorter phosphate chains and lower network connectivity. Also a contraction of the glass network that leads to the densification of the glass and thus to the decrease on the molar volume has been observed with increasing $Na_2O$ content.

By means of Static NMR of $^{31}P$ it was not possible to elucidate whether the chains of $PO_4$ tetrahedra in the glass fibres are randomly distributed or lie along the fibre main axis direction. In any case, the good mechanical properties observed in these fibres, leads to the conclusion that a structure orientation on the fibres is likely taking place.

A decrease in dissolution rate was observed with increasing $Na_2O$ content, being the glass with 40 $P_2O_5$ mol% (i.e. x=20) the most durable due to the presence of less hydrolysable $Q^1$ units in the glass network and an increase on the oxygen packing density. On the contrary, the glass with higher $P_2O_5$ content (i.e. x=5) shows the best mechanical properties with good reliability, according with Weibull distribution studies.

With increasing $Na_2O$ content, a denser glass network as a result of a higher proportion of short chains arrangements, will hinder somehow the cooperative flow of the $PO_4$ units through the glass network and therefore cause a reduction on the kinetic fragility. This less fragile behaviour leads to a wider temperature window range, facilitating fibre drawing processing.

### 7. 5 References

[1] L.L.Hench, J.Wilson, C.Greenspan, J.Aust. Ceram. Soc. 40 (1) (2004) 1

[2] L.L Hench, R. J.Splinter, W. C. Allen, T. K. Greenlee, J. Biomed. Mater Res. 5 (1971) 117

[3] D. L. Wheeler, K. E. Stokes, R. G. Hoellrich, D. L. Chamberland, S. W. McLoughlin, J. Biomed. Mater. Res. 41 (4) (1998) 527

[4] S. Froum, S. C. Cho, E. Rosenberg, M. Rohrer, D.Tarnow, J. Periodontol.73 (2002) 94

[5] A. Pendone, T. Charpentier, G. Malavasi, MC. Menziani, Chem. Mater 22 (2010) 5644

[6] R. G. Hill, DS Brauer, J. of Non-Cryst Solids 357 (2011) 3884

[7] J. R. Jones, Acta Biomater. 9 (2013) 4457

[8] M. Brink, T. Turunen, R.P. Happonen, A. Yli-Urpo, J. Biomed. Mater. Res. 37 (1997) 114

[9] M. Brink, J. Biomed. Mater.Res. 36 (1997) 109.

[10] N. C. Lindfors, I. Koski, J. T. Jeikkila, K. Mattila, A. J. Aho, J. Biomed. Mater . Res. B 94B (2010) 157

[11] D. S. Brauer, Angew. Chem. Int. Ed. 54 (2015) 4160

[12] J. C. Knowles, J, Mater. Chem., 13 (2003) 2395

[13] E.A. Abou Neel, D.M. Pickup, S.P. Valappil, R.J. Newport and J.C. Knowles, J, Mater. Chem., 18 (6) (2009) 690

[14] P.J. Marie, P. Ammann, G. Boivin and C. Rey, Calcif Tissue Int, 69 (3) (2001) 121

[15] S.C. Verberckmoes, M.E. De Broe, P.C. D'Haese, Kidney Int, 64 (2) (2003) 534

[16] N. Sharmin, A.J. Parsons, C.D. Rudd, I. Ahmed, J. Biomater. Appl. 29 (5) (2014) 639

[17] B.C. Bunker, J. Non-Cryst. Solids 64 (3) (1984) 291

[18] P. Haque, I. Ahmed, A.J. Parsons, R. Felfel, G.S.Walker, C.D. Rudd, J. Non-Cryst. Solids 375 (2013) 99

[19] A.J. Parsons, I. Ahmed, P. Haque, B. Fitzpatrick,M.I.K. Niazi, G.S.Walker, C.D. Rudd, J. Bionic Eng. 6 (2009) 318

[20] D.S. Brauer, C. Rüssel, S. Vogt, J.Weisser, M. Schnabelrauch, J.Mater. Sci.Mater.Med. 19 (2008) 121

[21] J. M. Taboas, R. D. Maddox, P. H. Krebsbach and S. J. Hollister, Biomaterials 24 (2003) 181

[22] P. Ylinen, R. Suuronen, R. Taurio, P. Tormala and P. Rokkanen, Int. J. Oral Maxillofacial Surg. 31 (2002) 405

[23] J. Ni and M. Wang, Mater. Sci. Eng. C—Biomimetic Supramol. Syst. 20 (2002) 101

[24] S. C. Rizzi, D. T. Heath, A. G. A. Coombes, N. Bock, M. Textor and S. Downes, J. Biomed. Mater. Res. 55 (2001) 475

[25] Z. B. Luklinska and W. Bonfield, J. Mater. Sci.- Mater. Med. 8 (1997) 379

[26] F.T. Wallenberger, J.C. Watson, H. Li, in: D.B. Miracle, S.L. Donaldson (Eds.), ASM Handbook, Vol. 21: Composites ASM International, Ohio (2001) 27

[27] J.M. Stickel,M. Nagarajan, Int. J. Appl. Glass Sci. 3 (2012) 122

[28] F.T. Wallenberger, in: F.T. Wallenberger, P.A. Bingham (Eds.), Fiberglass and Glass Technology, Springer, US (2010) 3

[29] J. Massera, I.Ahmed, L. Petit, V. Aallos, L. Hupa, Materials Science and Engineering C 37 (2014) 251

[30] J. Massera, M. Vassallo-Breillot, B. Törngren, B. Glorieux, L. Hupa, J. of Non-Cryst. Solids 402 (2014) 28

[31] D. S. Brauer, N. Karpukhina, R. V. Law, R. G. Hill, J. of Non-Cryst. Solids 356 (2010) 2626

[32] F. Döhler, D. Groh, S. Chiba, J. Bierlich, J. Kobelke, D. S. Brauer, J.of Non-Cryst. Solids (2015), 1–7. doi:10.1016/j.jnoncrysol.2015.03.009

[33] A.J. Parsons, N. Sharmin, S.I.S. Shaharuddin, M.Marshall, J. of Non-Cryst. Solids 408 (2015) 76

[34] M.S. Hasan, I. Ahmed, A.J. Parsons, G.S.Walker, C.A. Scotchford, J. Mater. Sci.Mater. Med. 23 (2012) 2531

[35] D. Massiot, F. Fayon, M. Capron, I. King, S. Le Calvé, B. Alonso, J. O. Durand, B. Bujoli, Z. Gan, G. Hoatson, Magn. Reson. Chem. 40 (2002) 70.

[36] G. Czjzek, J. Fink, F. Gotz, H. Schmidt, J.M.D. Coey, J.P. Rebouillat, A. Lienard, Phys. Rev. B 23 (1981) 2513

[37] R. K. Brow, J. of Non-Cryst. Solids 263-264 (0) (2000) 1-28

[38] U. Hoppe, G. Walter, R. Kranold and D. Stachel, J. of Non-Cryst. Solids, 263-264 (0) (2000) 29

[39] R. J. Kirkpatrick, R. K. Brow, Solid State Nuclear Magnetic Resonance 5 (1) (1995) 9

[40] J.P. Fletcher, R.J. Kirkpatrick, D. Howell, S.H. Risbud, J. Chem. Soc. Faraday Trans. 89 (17) (1993) 3297

[41] R. Hill, J. of Mat. Sci. Letters 15 (1996) 1122

[42] L. G. Baikova, Y.K. Fedorov, M. N. Tolstoi, Sov. J. Glass Phys. Chem. 16 (1991) 211

[43] A.R. Grimmer, U. Haubenreisser, Chem. Phys. Lett. 99 (1983) 487.

[44] T.M. Duncan, D.C. Douglass, Chem. Phys. 87 (1984) 339.

[45] T.M. Alam, S. Conzone, R.K. Brow, T.J. Boyle, J. Non-Cryst. Solids 258 (1999) 140.

[46] X. Xue, J. F. Stebbins, Phys. Chem. Miner. 20 (1993) 297

[47] M. Goldstein, T. H. Davies, J. Am. Ceram. Soc. 38 (1955) 223

[48] M. E. Milberg, M. C. Daly, j. Chem. Phys. 39 (1963) 2966

[49] F. Muñoz, O. Pritula, J. Sedlácek, C. Rüssel, Eur. J. Glass Sci. Technol. A, 49 (1) (2008) 47.

[50] M. Braun, Y. Yue, C. Rüssel, C. Jäger, J. of Non-Cryst. Solids 241 (2-3) (1998) 204

[51] B. N. Nelson, G. J. Exarhos, J. Chem. Phys. 71 (1979) 2739

[52] R. K. Brow, D. R. Tallant, S. T. Myers, C. C. Phifer, J. of Non-Cryst. Solids 191 (1995) 45

[53] H. Gao, T. Tan, D. Wang, J. of Controlled Release, 2004. 96 (1) 29

[54] J. R. Van Wazer, Interscience Publishers Ltd. (1958)

[55] I. Ahmed, M. Lewis, I. Olsen and J.C. Knowles, *Biomaterials*, 25 (3) (2004)
491

[56] A.J. Parsons, L.D. Burling, C.A. Scotchford, G.S. Walker, C.D. Rudd, J. of Non-Cryst. Solids 352 (50–51) (2006) 5309

[57] K. Franks, I. Abrahams, J.C. Knowles, J. of Mat. Sci.: Materials in Medicine 11 (10) 609

[58] D.R. Brauer, S. C. Kraft, J. Kraft, J. of Non-Cryst. Solids, 353 (3) (2007) 263-270.

[59] J. Vogel, P. Wange, P. Hartmann. Glastech Ber Glass Sci Technol 70 (1997) 23

[60] J. Vogel, P. Wange, P. Hartmann. Glastech Ber Glass Sci Technol 70 (1997) 220

[61] J. Vogel, P. Wange, S. Knoche, C. Rüssel. p. Glass Sci Technol 77 (2004) 82

[62] J. R. van Wazer, Interscience, New York (1958)

[63] G. Walter, J. Vogel, U. Hoppe, P. Hartmann, j. of Non-Cryst. Solids, 296 (2001) 212

[64] H.Y.L.S. Kobayashi, D.S. Brauer, C. Rüssel, Materials Science and Engineering: C, 30 (7) (2010)
1003

[65] D. Hull, T. W. Clyne, An introduction to composite materials. NY: Cambridge University Press (1996).

# Overall conclusions

The relationships between chemical composition, structure and dynamics of the processes taking place within the phosphate glass network have been studied in depth through the preparation and characterization of more than 35 different glass compositions ranging from binary and ternary phosphate glasses with different modifying oxides, to glasses with different $P_2O_5$ content, or more than one network former oxide.

A detailed study of the compositional influence on the short and medium range order structure has shown that for a constant $P_2O_5$ content, the presence of modifying cations with lower field strength in the glass network leads to less covalent $M^{n+}O^{m-}$ bonds. The decrease on the covalent character of the glass network and, therefore, the weakening and subsequent decrease of the overall network's rigidity are reflected on the short and medium range order structure. The qualitative study of the proportion of tetrahedral units in rings and chains arrangements has shown that the decrease on the overall covalent character of the glass network seems to favour rings arrangements. Therefore, the nature of the modifying cation to oxygen bonds plays an important role on the short and medium range order structure in phosphate glasses.

Thermal and transport properties have been characterized and possible relationships between the short and medium range order structure and the main glass properties have been suggested shedding some light on the mechanisms that govern their variation with composition. The main conclusions obtained in this regard are the following:

Throughout this thesis it has been carried out one of the most extensive experimental studies recently performed on viscosity in phosphate glass systems. A systematic analysis of viscosity through VFT, AM and MYEGA viscosity models, where the adjustable parameters have been expressed in terms of glass transition temperature ($T_g$), fragility (m) and extrapolated infinite temperature viscosity ($\log \eta_\infty$), has shown that the kinetic fragility takes different values depending on the model employed. In general, a good agreement has been found between the results obtained by VFT and MYEGA models, while AM has shown in some cases a high discrepancy compared to the other two models. Nevertheless, similar $T_g$ values are obtained independently on the viscosity model used being these values similar to those determined by dilatometry. This correspondence proves a good agreement between the definition of $T_g$ by DSC and the values obtained by dilatometry.

Additionally to the commonly employed viscosity methods, measurements by two no conventional techniques, *in situ* high-T NMR and creep, have been carried out within the processing and above and below the glass transition range. The viscosity points obtained fit remarkably well within the viscosity data as determined from conventional viscosity methods.

The rate of variation of viscosity with temperature in phosphate glasses has been studied through two approaches, Angell's kinetic fragility (m) and Doremus' ratio ($R_D$). In general, both parameters follow the same variation with composition. The flow of $PO_4$ units through the glass network seems to be governed by the degree of the covalent character of $M^{n+}O^{m-}$ bonds. The intermediate range order structure, based either in chains or rings, apparently does not influence the kinetic fragility.

The activation energy for viscous flow has been calculated in the low and high temperature ranges resulting in two activation energies ($E_a^{low\text{-}T}$ and $E_a^{high\text{-}T}$) that follow different trends with composition. This may imply two different mechanisms controlling the viscous flow through a different evolution of the structure with temperature in each of them. Therefore, the $E_a$ is thought to be influenced not only by composition and structure, but also by the temperature range in which is determined.

The variation on the activation energy for viscous flow observed at temperatures above $T_g$ ($E_a^{low\text{-}T}$) seems to be determined by cooperative motion of the medium range order structure (i.e. rings and chains). In contrast, in the melt, when the breaking and re-forming of bonds occurs fast enough due to the high temperature, a single-process action drives the $E_a^{high\text{-}T}$ to vary as a function of the overall covalent character of the glass network and its rigidity degree. Thus, it seems that the medium range order structure does not influence the activation energy in the melt.

The range of values obtained for activation energy of ionic conduction $E_a(\sigma)$ in the metaphosphate glasses studied indicates that conductivity is of the ionic hopping type. Following Anderson & Stuart model, it has been observed that a lower Z/a or field strength of the modifying cation and, therefore, a lower bond strength between the cation and the surrounding oxygens, gives rise to lower $E_a(\sigma)$. The higher mobility and easiness for the diffusion of the charge carriers through a weaker and less rigid glass network reduce the energy barrier that cations need to overcome for the hopping mechanism. Additionally, it has been observed the important role played by a higher molar volume ($V_m$) on the $E_a(\sigma)$ decrease.

Finally, the lower character of $M^+O^-$ bonds is going to be also reflected on the thermal properties. The weakening of the glass network with increasing alkali oxide content gives rise to a reduction of the temperature required to activate the rotational motions which make decrease the glass transition temperature. The medium range order structure, specifically the reorganization of the glass network from chains to rings may be responsible of the discontinuity shown with composition. Additionally, the influence of the coordination number

of the modifying ion on $T_g$ variation reveals in some cases the importance of the connectivity of the modifying ionic subnetwork.

The systematic study of structure and transport properties in phosphate glasses has been concluded studying the effect of the glass network connectivity on the structure and properties through the variation of the proportion of glass former oxide. An increase of the depolymerisation degree is observed with increasing modifying oxide content. The formation of $Q^1$ units in the glass network causes a more pronounced increase of NBO per tetrahedral unit, which seems to provoke a preferential arrangement of the $Q^2$ groups in chains instead of rings. Therefore the polymerization degree plays an important role on the medium range order structure in phosphate glasses. The main conclusions obtained from the possible relationships between the short and medium range order structure and the main glass properties are the following:

Unlike in metaphosphate glasses, the variation of kinetic fragility and Doremus ratio with composition seems to be influenced by the higher proportion of chains that would lead to a denser glass network, and thus by the medium range order structure.

With regard to the glass transition temperature, it increases with the modifying oxides content. Two regions can be differentiated attending to the $T_g$ variation with composition. The behaviour in the ultraphosphate region can be explained based on the structural model presented by Hoppe. On the meta- and polyphosphate compositional regions, the high concentration of modifiers, and thus of O-M-O bonds with higher covalent character, balances the depolymerisation effect and leads to a slight increase on $T_g$ with increasing modifying oxides content.

Like in metaphosphate glass compositions, two different activation energies of viscous flow have been found depending on the temperature range ($Ea^{low\text{-}T}$ and $Ea^{high\text{-}T}$), which would be governed by the same mechanisms than in a constant former oxide content series.

The addition of boron as another network former oxide causes important transformations on the phosphate glass network as a result of the different coordination environments adopted by boron (three and fourfold coordinated). Kinetic fragility has been seen to be affected by these structural changes.

It was not possible to obtain a common model for the viscosity-T curves through the study of the rheology of phosphate glasses when a certain composition is given. However, through the systematic study of viscosity in phosphate glasses it has been verified that experimental viscosity data can be fitted with enough accuracy by the current viscosity

models, i.e. VFT, AM and MYEGA. This has allowed the achievement of averaged values of extrapolated infinite temperature viscosity ($\log \eta_\infty$), as well as similar $T_g$ values to those obtained by dilatometry, which ultimately constitutes a good evidence to validate the $T_g$ and m parameters obtained from the fits.

On the other hand, the first steps towards the modelling of glass compositions with desired fragility have been taken. The viscosity-temperature curve in the whole temperature range together with the kinetic fragility value, were accurately obtained by only fitting the experimental viscosity data in the low temperature range and replacing $T_g$ and $\log \eta_\infty$ by the fixed values found. This has revealed that m and $T_g$ are mainly controlled by the viscosity data near the glass transition range, highlighting the importance of having enough experimental viscosity data, as accurate as possible, within this range.

Additionally, viscosity points in the high temperature range were calculated by the linear correlation found between $R_D$ and m through $E_a^{high\ T}$ closely to the values experimentally determined in the melt. This validates the use of the relation found and establishes an alternative way to get approximated viscosity values in the high temperature range saving time and means derived from the use of experimental techniques.

Despite the relationships found between $\delta_{CSA}$ and Raman band intensities attributed to rings ($I_{ring}$) with Doremus ratio, a general relationship between the local structure observed in phosphate glasses and the fragility was not possible to achieve, which underlines the inherent difficulties of modelling the transport properties from structural data in phosphate glasses.

To conclude, the relationships found between properties and structure in phosphate glasses have been applied to fibre drawing processing of bioactive phosphate glasses. In the first place, it has been observed that not significant differences occur in the glass network structure during fibre drawing, especially regarding to the $Q^i$ speciation and to the nature and orientation of P-O bonds. It has also been observed that with increasing $Na_2O$ content, a denser glass network as a result of a higher proportion of short chains arrangements, will hinder somehow the cooperative flow of the $PO_4$ units through the glass network causing a reduction on the kinetic fragility. This less fragile behaviour leads to a wider temperature window range, facilitating fibre drawing processing.

Therefore, some progresses has been made regarding to the full process that runs from the generation of basic knowledge, i.e. the relationships between glass properties and structure through composition, to its implementation on the processing of phosphate glasses in fibres.

# Conclusiones generales

Se ha estudiado en profundidad la relación entre la composición química, la estructura y la dinámica de los procesos que tienen lugar en el seno de la red vítrea en los vidrios de fosfatos a través de la preparación y caracterización de más de 35 vidrios de diferentes composiciones que van desde vidrios de fosfato binarios y ternarios con diferentes óxidos modificadores, a vidrios con diferente contenido en $P_2O_5$, o aquellos que contienen dos óxidos formadores en su composición.

El estudio detallado llevado a cabo sobre de la influencia de la composición en el orden estructural a corto y medio alcance en vidrios de metafosfato, ha mostrado que la presencia de cationes modificadores en la vítrea que presentan una menor intensidad de campo dan lugar a enlaces $M^{n+}O^{m-}$ de menor carácter covalente. La disminución en el carácter covalente total de la red vítrea y, por tanto, el debilitamiento y consiguiente pérdida de rigidez de la red vítrea influye tanto en el orden estructural a corto como a medio alcance. El estudio cualitativo de la proporción de unidades tetraédricas que se encuentran en ordenaciones en forma de anillos o cadenas, muestra que la disminución del carácter covalente total de la red vítrea parece favorecer estructuras de tipo anillo. Por lo tanto, la naturaleza de los cationes modificadores juega un papel importante en el orden estructural a corto y medio alcance en los vidrios de fosfato.

Se han caracterizado las propiedades térmicas y de transporte y se han sugerido posibles relaciones entre el orden estructural a corto y medio alcance y las propiedades principales de los vidrios arrojando cierta luz sobre los mecanismos que gobiernan la variación de dichas propiedades con la composición. Las conclusiones principales que se han obtenido en este aspecto se enumeran a continuación:

A lo largo de esta tesis se ha realizado uno de los trabajos experimentales más extensos llevados a cabo recientemente sobre viscosidad en vidrios e fosfato. El análisis sistemático de la viscosidad a través de los modelos VFT, AM y MYEGA, donde los parámetros ajustables se han expresado en términos de temperatura de transición vítrea ($T_g$), fragilidad (m) y la viscosidad extrapolada a temperatura infinita ($\log \eta_\infty$), ha demostrado que la fragilidad cinética toma diferentes valores dependiendo del modelo que se emplee. En general se ha obtenido una buena concordancia entre los resultados obtenidos mediante el ajuste a los modelos VFT y MYEGA, mientras que en algunos casos el modelo de AM ha mostrado una alta discrepancia comparado con los otros dos modelos. Sin embargo, se han obtenido valores muy similares de $T_g$ independientemente del modelo utilizado, siendo dichos valores a su vez muy semejantes a los obtenidos mediante dilatometría.

Además de las técnicas comúnmente utilizadas para determinar la viscosidad en vidrios, se han podido realizar medidas mediante dos técnicas no convencionales, RMN de alta temperatura y fluencia a temperaturas cercanas al intervalo de transición y en las que se lleva a cabo el procesamiento. Los puntos de viscosidad obtenidos mediante estas técnicas concuerdan de forma notable con los datos de viscosidad obtenidos mediante técnicas de mediad convencionales.

La velocidad de variación de la viscosidad con la temperatura en vidrios de fosfato se ha estudiado a partir de dos aproximaciones, la fragilidad cinética de Angell (m) y la relación de Doremus ($R_D$). En general, ambos parámetros siguen la misma variación con la composición. La fluencia de las unidades $PO_4$ a través de la red vítrea parecen estar influidas por el grado de covalencia de los enlaces $M^{n+}O^{m-}$. El orden estructural al medio alcance sin embargo, basado tanto en cadenas como en anillos, aparentemente no influye sobre la fragilidad cinética.

La energía de activación de flujo viscoso se ha calculado en los rangos de bajas y altas temperaturas, dando lugar a dos energías de activación diferentes ($E_a^{baja\text{-}T}$ y $E_a^{alta\text{-}T}$) que varían de forma diferente con la composición. Esto podría implicar que el flujo viscoso se encuentra controlado por dos mecanismos diferentes debido a una evolución también diferente de la estructura con la temperatura para cada una de ellas. Por lo tanto, se cree que la $E_a$ está influenciada no solo por la composición y la estructura, si no por el rango de temperaturas en el que es determinada.

La variación que se observa en la energía de activación a temperaturas por encima de $T_g$ ($E_a^{baja\text{-}T}$) parece estar determinada por movimientos cooperativos de las unidades estructurales a medio alcance (anillos y cadenas). Por el contrario, en el fundido, cuando la ruptura y formación de los enlaces tiene lugar lo suficientemente rápido debido a las altas temperaturas, un único proceso de activación parece ser el que lleva a la $E_a^{alta\text{-}T}$ a variar en función del carácter covalente total de la red vítrea y su grado de rigidez. Por tanto, cabría esperar que el orden estructural a medio alcance no influyese en la energía de activación del fundido.

El rango de valores en el que se encuentran los resultados obtenidos para la energía de activación de conducción $E_a(\sigma)$ en los vidrios de metafosfato estudiados, indican que la conductividad es de tipo iónico. En base al modelo de Anderson y Stuart, se ha observado que cuanto menor es el potencial catiónico (Z/a) o la intensidad de campo de los cationes modificadores, y por tanto, menor es la fuerza de enlace entre catión y oxígeno menor es también la $E_a(\sigma)$. Cuanto mayor sea la movilidad y facilidad para que la difusión de los

portadores de carga tenga lugar a través de una red más debilitada y menos rígida, menor es la barrera de energía que los cationes tienen que superar para que el mecanismo de salto entre vacantes tenga lugar. Además, se ha observado el importante papel que juega un mayor volumen molar ($V_m$) en la disminución de la energía de activación de conducción iónica.

Por último, el menor carácter covalente de los enlaces $M^{n+}O^{m-}$ se va a ver reflejada también en las propiedades térmicas. El debilitamiento de la red vítrea con el aumento del contenido en óxidos de metales alcalinos, da lugar a una reducción en la temperatura necesaria para activar los modos rotacionales que hacen que disminuya la temperatura de transición vítrea. El orden estructural a medio alcance, en concreto, la reorganización de la red vítrea de cadenas a anillos podría ser la responsable de las discontinuidades observadas con la composición. Además, la influencia del índice de coordinación de los cationes modificadores en la variación de $T_g$ revela en algunos casos la importancia de la conectividad de la subred iónica.

El estudio sistemático de la estructura y las propiedades de transporte se ha concluido con el estudio del efecto que ejerce la conectividad de la red vítrea en la estructura y las propiedades a través de la variación de la proporción de óxido modificador presente en el vidrio. Con el aumento del contenido en óxidos modificadores se observa a su vez el aumento en el grado de despolimerización de la red. La formación de unidades $Q^1$ produce un mayor aumento de los enlaces oxígeno no puente (ONP) por unidad tetraédrica, lo que parece provocar la organización preferencial de las unidades $Q^2$ en cadenas en vez de en anillos. Por tanto, el grado de polimerización de la red juega un papel importante en el orden estructural a medio alcance en los vidrios de fosfato. Las principales conclusiones que se han extraído de las relaciones entre el orden estructural a corto y medio alcance y las principales propiedades de los vidrios se recogen a continuación:

A diferencia de los vidrios de metafosfato, la variación de la fragilidad cinética y la relación de Doremus con la composición parecen estar influenciadas por la mayor proporción de cadenas que darían lugar a una red vítrea más densa, y por tanto por el orden estructural a medio alcance.

Atendiendo a la temperatura de transición vítrea, ésta aumenta con el aumento del contenido de óxidos modificadores en la red vítrea.

Como en el caso de los vidrios de metafosfato, se han encontrado dos energías de activación de flujo viscoso ($E_a^{baja\text{-}T}$ y $E_a^{alta\text{-}T}$) dependiendo del rango de temperaturas en el

que ésta se haya determinado, por lo que podrían estar controladas por los mismos mecanismos descritos para vidrios con un contenido constante de óxido formador.

La adición de boro como otro óxido formador de red provoca transformaciones importantes en la red vítrea de fosfato como resultado de los diferentes entornos de coordinación que adopta el boro (trigonal y tetraédrica). Se ha observado que estos cambios estructurales influyen en la fragilidad cinética de los vidrios de borofosfato.

No ha sido posible obtener un modelo común para las curvas de viscosidad-temperatura a través del estudio de la reología en vidrios de fosfato a partir de una cierta composición previa. Sin embargo, a través del estudio sistemático de la viscosidad en vidrios de fosfato, se ha verificado que los datos de viscosidad obtenidos experimentalmente para vidrios de fosfato se pueden ajustan con suficiente exactitud con los modelos de viscosidad ya establecidos (VFT, AM y MYEGA). Esto ha permitido al obtención de valores promedio de los valores de viscosidad extrapolados a temperatura infinita (log $\eta_\infty$), así como la obtención de valores de $T_g$ similares a los obtenidos por dilatometría, lo que en último lugar constituye una buena evidencia para la validación de los valores de $T_g$ y m obtenidos a partir de dichos ajustes.

Por otro lado, se han establecido los primeros pasos hacia la modelización de las composiciones vítreas con una fragilidad deseada. A través del ajuste de los datos de viscosidad obtenidos experimentalmente a bajas temperaturas y de la sustitución de los parámetros ajustables por valores fijos de $T_g$ y log $\eta_\infty$, las curvas de viscosidad junto con el valor de fragilidad cinética se han obtenido con suficiente exactitud en todo el rango de temperaturas. Estos ajustes han puesto de manifiesto que m y $T_g$ están principalmente controlados por los datos de viscosidad cercanos al intervalo de transición vítrea, destacándose de esta manera la importancia de tener suficientes valores experimentales de viscosidad, y tan exactos como sea posible, en ese rango de temperatura.

Además, se han podido calcular valores de viscosidad similares a los obtenidos experimentalmente en el rango de alta temperatura, a partir de la correlación lineal entre $R_D$ y m, a través de $E_a^{alta\text{-}T}$. Estos resultados validan el empleo de la relación encontrada y propone un método alternativo para la obtención de valores de viscosidad aproximados en el rango de altas temperaturas, ahorrando de esta manera tanto el tiempo como los costes derivados del empleo de técnicas experimentales.

A pesar las relaciones encontradas entre $\delta_{CSA}$ y la intensidad de las bandas de Raman atribuidas a anillos ($I_{anillos}$) con la relación de Doremus, no se ha podido conseguir una relación general entre el orden estructural a corto alcance y la fragilidad en vidrios de

fosfato, lo que pone de manifiesto las dificultades inherentes de la modelización de las propiedades de transporte a partir de datos estructurales en dichos vidrios.

Para concluir, se han aplicado las relaciones encontradas entre las propiedades y la estructura al fibrado de vidrios de fosfato bioactivos. En primer lugar, se ha observado que no hay variaciones significativas en la estructura de la red vítrea durante el procesamiento de los vidrios en fibras, concretamente atendiendo a la especiación de las unidades $Q^i$ y a la naturaleza de la orientación de los enlaces P-O. También se ha observado que el incremento en el contenido de $Na_2O$ produce una densificación de la red vítrea debido a una mayor proporción de ordenamientos en forma de cadenas de menor longitud que impiden de cierta forma la fluencia cooperativa de unidades $PO_4$ a través de la red vítrea, produciendo de esta forma una reducción en la fragilidad cinética. Esta menor fragilidad amplia el intervalo de temperaturas a las que se puede llevar a cabo el fibrado de los vidrios.

Por lo tanto, se han llevado a cabo avances en el proceso que va desde la generación de conocimiento fundamental, como es el caso de las relaciones entre las propiedades de los vidrios y su estructura a través de la composición, hasta la implementación de dichos conocimiento para el procesado de fibras de vidrios de fosfato.